CLOSING THE LOOP BY ENGINEERING CONSISTENT 4D SEISMIC TO SIMULATOR INVERSION

SEAN (SHUZHE) TIAN

SUBMITTED FOR THE DEGREE OF DOCTOR OF PHILOSOPHY
HERIOT-WATT INSTITUTE OF PETROLEUM ENGINEERING

SEPTEMBER 2014

Abstract

The multi-disciplinary nature of closing the loop (CtL) between 4D seismic and reservoir engineering data requires integrated workflows to make sense of these different measurements. According to the published literatures, this integration is subject to significant inconsistency and uncertainty. To resolve this, an engineering consistent (EC) concept is proposed that favours an orderly workflow to modelling and inverting the 4D seismic response. Establishing such consistency facilitates a quantitative comparison between the reservoir model and the acquired 4D seismic data observation. With respect to the sim2seis workflow developed by Amini (2014), a corresponding inverse solution is proposed. The inversion, called seis2sim, utilises the model prediction as *a priori* information, searching for EC seismic answers in the joint domain between reservoir engineering and geophysics. Driven by a Bayesian algorithm, the inversion delivers more stable and certain elastic parameters upon application of the EC constraints. The seis2sim approach is firstly tested with a synthetic example derived from a real dataset before being applied to the Heidrun and Girassol field datasets. The two real data examples are distinctive from each other in terms of seismic quality, geological nature and production activities. After extracting the 3D and 4D impedance from the seismic data, CtL workflows are designed to update various aspects of the reservoir model according to the comparison between sim2seis and seis2sim. The discrepancy revealed by this cross-domain comparison is informative for robust updating of the reservoir model in terms reservoir geometry, volumetrics and connectivity. After applying tailored CtL workflows to the Heidrun and Girassol datasets, the statistical istributions of petrophysical parameters, such as porosity and NTG, as well as intra- and inter-connectivity for reservoir compartments are revised accordingly. Consequently, the 3D and 4D seismic responses of the reservoir models are assimilated with the observations, while the production match to the historical data is also improved . Overall, the proposed seis2sim and CtL workflows show a progression in the quantitative updating of the reservoir models using time-lapse seismic data.

HERIOT WATT UNIVERSITY

ACADEMIC REGISTRY

Research Thesis Submission

Name	SEAN (SHUZHE) TIAN		
School/PGI	INSTITUE OF PETROLEUM ENGINEERING		
Version	FIRST	Degree Sought	Ph.D RESERVOIR GEOPHYSICS

Declaration

In accordance with the appropriate regulations I hereby submit my thesis and I declare that:

1) the thesis embodies the results of my own work and has been composed by myself
2) where appropriate, I have made acknowledgement of the work of others and have made reference to work carried out in collaboration with other persons
3) the thesis is the correct version of the thesis for submission and is the same version as any electronic versions submitted*.
4) my thesis for the award referred to, deposited in the Heriot-Watt University Library, should be made available for loan or photocopying and be available via the Institutional Repository, subject to such conditions as the Librarian may require
5) I understand that as a student of the University I am required to abide by the Regulations of the University and to conform to its discipline.

* *Please note that it is the responsibility of the candidate to ensure that the correct version of the thesis is submitted.*

Signature of Candidate	田書哲	Date	

Submission

Submitted By	Sean TIAN
Signature of Individual Submitting	田書哲
Date Submitted	

For Completion in the Student Service Centre (SSC)

Received in the SSC by			
Method of Submission			
E-thesis Submitted			
Signature		Date	

This thesis is dedicated to my parents,

田詩柯　張伊勤

to whom I am indebted for living.

But to my teacher

Colin MacBeth

I am indebted for living well.

Acknowledgements

It was the afternoon of 21^{st} March 2010, when , for the very first time in my life, I was asked to make a presentation about 4D inversion to Prof. Colin MacBeth, as a Ph.D studentship applicant. At the beginning of the presentation, of which most contents were scrambled up according to the relevance level suggested by search engines, I wrote "*I am after truth*.", with the boldest courage and passion. Yes, truth about the subsurface is all he inversion looks for, as I believed. After four and a half years' study, I am no longer as ignorant as I was, but questions I dared to ask and answer seem to be getting harder instead of easier. Nonetheless, by answering some of the "easy" ones, I am actually finding myself led into more and more waiting unknowns. It is like an adventure into space – one can only tell the origin, without knowing where it terminates.

In addition to the scientific findings in the next two hundred-ish pages, I am very keen to share with you some "side views", which I believe are equally important. The most often asked and answered question during my study encompasses the meaning of a Ph.D. Over the years, I have come across degree seekers who are merely after the titles, or the utility of the titles. I have also met people pursuing the degree out of curiosity and interest in the subject. Investigating the notion of "good" and "right" of a Ph.D study can be rather dependent on the individual and their social stance, just as I cannot clearly tell what my initial drivers were. However, in the first year, I learned to embrace and study the terrifying unknowns, when every single thing seemed overwhelming; later, I learned to communicate with others when the ideas were being put into shape; I learned to transfer my learning from one context to another, science to life; I also learned to accept differences and adapt to them. Most importantly, by studying, I understand myself better, which lead to a better respect of others. So, to me, the experience is a mental cure, making one tougher and more aware, and freer.

My utmost respect and gratitude goes to my teacher and supervisor Prof. Colin MacBeth who has been forever patient and supportive. It is his exceptional trust and help that has made my growth possible. His inspired attitude to work and life will motivate me throughout my lifetime. Great teachers are rare, and it is my fortune to be guided by him during these invaluable years.

My heartfelt appreciation also goes to my friends, advisors and office mates Dr. Hamed Amini, Dennis Obidegwu and Ming Yi Wong with whom my happiness and pain (mostly is brought about by myself), achievements and failures were understood. Technically, the seis2sim inversion would never have been achievable without Hamed's extraordinary development of sim2seis. Dennis's timely shortbread hospitality energizes me in hunger and sadness, from time to time. My use of English has been greatly sharpened since Ming's arrival and her vivacity is always cheery. I hope this friendship goes on for good.

My sincere thanks go to all the Edinburgh Time Lapse Project colleagues: Asghar Shams, Valery Rukavishnikov, Dhiman Mondal, Yi Huang, Alejandro Garcia, Erick Alvarez, Olarinre Salako, Zhen Yin, Lu Ji, Sergey Kurelenkov, Veronica Omofoma, Ricardo Rangel, Mathieu Chamberfot, Maria Mangriotis, Romain Chassagne and Niki Obiwulu. It is you who all make ETLP such a friendly, international group. Especially, I acknowledge Dr. Weisheng He, for initiating this 4D inversion project. I would like to express my gratitude to Pierre Thore and Andrew Wilson for showing their interest and support since the beginning of this study, as well as for the subsequent arrangements to visit the TOTAL Geoscience Research Centre in Aberdeen and BG office in Reading. I acknowledge the help from Ole Petter Dybvik, Ulrich Theune and Milana Ayzenberg and the Geophysics Reservoir Monitoring Group during and after my internship with Statoil in Trondheim. Without their advice, the seis2sim could not be as solid as it is. In addition, my wholehearted appreciation goes to Sean Ferris for taking to me on board with Chevron, where I could continue exploring the 4D business in the industry. I thank all the ETLP Phase IV and V sponsors for their financial support and, more importantly, for commuting to Edinburgh and commenting on the project every half year. I also thank the wider faculty of the Heriot Watt Institute of Petroleum Engineering for providing extraordinary facilities and academic support.

The completion of this thesis was fuelled and accompanied by Yi-Fan Chen, with whom the days I spent in writing-up became enchanted.

I am forever indebted to my parents. Although you do not read English, everything I am doing leads to my way home.

Last, I am indebted to Dr. Jing Ye, from whom I am always benefitting. She put me in fear of nothing, and knew me better than anyone else at the early time of this study.

Table of Contents

List of figures

List of symbols and acronyms

Symbols

ΔP	Pressure difference
ΔS	Saturation difference
ΔV_P	P-wave velocity difference
ΔV_S	S-wave velocity difference
$\Delta \rho$	Density difference
V_P	P-wave velocity
V_s	S-wave velocity
I_P	P-wave impedance
I_s	S-wave impedance
S_w	Water saturation

Greek letters

ϕ	Porosity
K	Bulk modulus
K_{dry}	Dry rock bulk modulus
K_{fl}	Fluid bulk modulus
K_m	Mineral bulk modulus
K_{sat}	Saturated rock modulus
μ	Shear modulus
ρ	Density

$\boldsymbol{\rho_m}$	Mineral density
$\boldsymbol{\rho_w}$	Water density
$\boldsymbol{\rho_o}$	Oil density
$\boldsymbol{\rho_{sat}}$	Saturated rock density
$\boldsymbol{\sigma}$	Stress
$\boldsymbol{\sigma_{eff}}$	Effective stress

Acronyms

AVO	Amplitude versus offset
CI	Coloured inversion
CtL	Closing the loop
CPG	Corner-point geometry
EC	Engineering consistent
FWI	Full waveform inversion
HR	High resolution
MCMC	Markov chain Monte Carlo
MH	Metropolis-Hastings
NRMS	Normalized root-mean square
NCC	Normalized correlation coefficients
NNC	Non-neighbour connection
NTG	Net-to-gross
OWC	Oil-water contact
OOWC	Original oil-water contact
PEM	Petro-elastic model

POWC	Produced oil-water contact
PRM	Permanent reservoir monitoring
PV	Pore volume
RMS	Root mean square
sim2seis	Simulator to seismic modelling
seis2sim	Seismic to simulator modelling
SHM	Seismic history matching
TRANS	Transmissibility
TWT	Two way time

List of publications

Part of this work is presented in the following publications:

- Tian, S., 2011. Towards Engineering-Consistent 4D inversion. SEG Inverting the reservoir workshop, Quebec, Canada.

- Tian, S., MacBeth, C. and Shams, A., 2012. An Engineering-consistent inversion of time-lapse seismic data. 74th EAGE conference & exhibition, extended abstract.

- Huang, Y., Alsos, T., Sørensen and Tian, S., 2013. Proving the value of 4D seismic data in the late-life field – case study of the Norne main field. First Break, Vol 31, No 9, pp. 57-67.

- Tian, S., MacBeth, C. and Shams, A., 2013. Closing the loop using engineering-consistent 4D seismic inversion. EAGE/SPE joint workshop on beyond closed loop integrated monitoring, extended abstract.

- Tian, S., MacBeth, C. and Shams, A., 2013. Closing the loops using engineering-consistent 4D seismic inversion. The Leading Edge, v. 33, p. 182-187, doi: 10.1190/tle33020182.1.

- Tian, S., MacBeth, C. and Shams, A., 2013. Closing the loop using engineering-consistent 4D seismic inversion. EAGE/SPE joint workshop on beyond closed loop integrated monitoring, extended abstract.

- Tian, S., MacBeth, C. and Shams, A., 2014. Updating the reservoir model using engineering-consistent 4D Seismic Inversion. 76th EAGE conference & exhibition, extended abstract.

Chapter 1

Seismic-to-simulator inversion for 4D seismic closing-the-loop

“Who knows his manhood’s strength, yet still his female feebleness maintains; as to one channel flow the many drains, all come to him, yea, all beneath the sky. Thus he the constant excellence retains.”

「知其雄，守其雌，爲天下溪。爲天下溪，常德不離。」

Lao Tze, *Chapter. 28, Tao Teh Ching, 400 BC to 700 BC*

This chapter gives a high level review of the methods used for 4D seismic reservoir monitoring, in conjunction with relevant reservoir engineering practices. This integration prompts the development of an efficient workflow to close the loops (CtL) between the geophysical domain and the reservoir engineering domain. Practically, the loops are closed by combining the simulator-to-seismic and seismic-to-simulator processes into a consistent workflow, leading to the development of an engineering-consistent (EC) approach to inverting the 4D seismic data. Attempts to assist the data interpretation and assimilation across disciplines make the inversion a key driver in designing a consistent CtL workflow.

Traditionally called four-dimensional (4D) seismic, time-lapse seismic data has been used to make a visual representation of what happens to the reservoir in space and time during the production activities. Since the birth of the 4D idea in the 1980s (Nur, 1982; Nur et al., 1984; Nur and Wang, 1987), the oil and gas industry has relied on it and extended its application to a diverse range of geology and production mechanisms. From the early 1990s, the technical focus on 4D seismic has drifted from the early applications and studies of its economic viability (Jack, 1998) to implementations dedicated to improving its reliability (Calvert, 2005; Barkved, 2012), and towards the quantitative integration across related disciplines (Johnston, 2013). Although 4D seismic is primarily regarded as a geophysical tool, it is essentially entailed by reservoir engineering activities, and tied closely to production management and optimisation. Nevertheless, the evolution of the 4D technique itself is fundamentally driven by the financial gains of avoiding possible losses of placing dry wells without 4D illumination. Therefore it is almost impossible to isolate 4D and its associated technologies from the context of reservoir engineering and the ultimate philosophy of this thesis is to maximise the value by "flowing these many drains into one channel" as quoted from *Tao Teh Ching*. In other words, the aim is to integrate multi-disciplinary information.

It is rather interesting to review the evolution of both the reservoir geophysical techniques, in particular, the seismology, with the development of the reservoir engineering, in a coupled time stream. Reservoir engineering, as a branch of petroleum engineering, consists of a sophisticated series of principles and tools in subsurface geology, applied mathematics and the laws of physics and chemistry governing the behaviour of liquid and vapour phases of the in-situ fluids of crude oil, natural gas and water in the porous media. The search for numerical simulations of these laws has initiated the development of theories, whereas, evolution in the reservoir engineering domain was aligned with the advances in the geophysical domain (see Figure 1.1). According to Coats (1987), most of the reservoir simulation before the 1960's was performed by approaches such as the analytical method (Muskat, 1946), zero-dimensional material balances (Muskat, 1945) and one-dimensional Buckley-Leverett calculations (Buckley and Leverett, 1942). In the early 1960's, with the advent of the integrated circuit, GSI introduced the first digital recording system for the oil and gas exploration geophysics industry (Barkved, 2012) and, at the same time, the reservoir engineers set out the idea of solving finite-difference equations describing two- and three-dimensional (2D and 3D), transient, multiphase flow in heterogeneous porous media with sophisticated computer programs (Coats, 1987). Here, the history matching problem was raised associatively as an inverse validation of the numerical models. In the late 1960's, the geophysicists managed to acquire the first onshore 3D seismic survey, while a number of reservoir engineers proposed the formulations for 2D/3D two-phases/three-phases flow simulation. During the 1970's, the picture changed markedly. The simulations for miscible, chemical and other unconventional processes started to appear, while the first marine 3D seismic data was acquired in 1975.

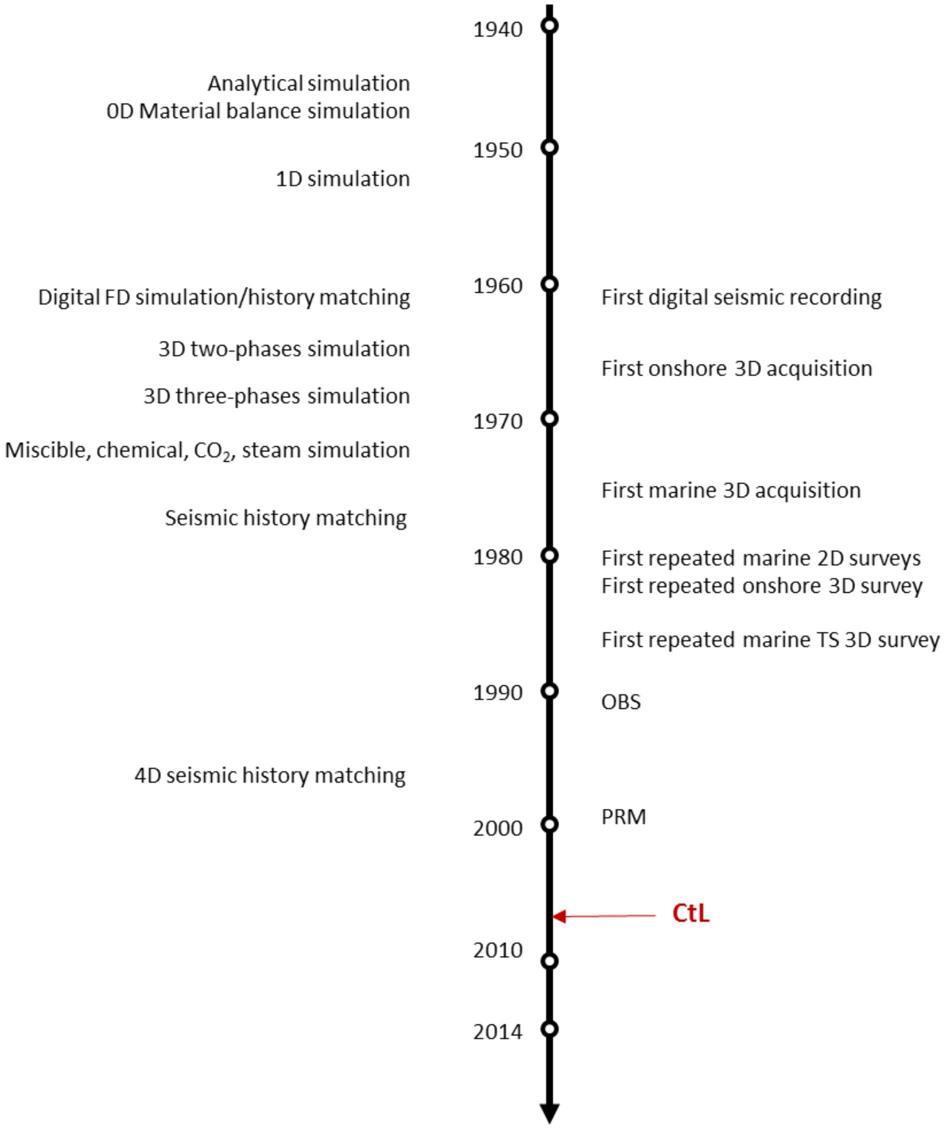

Figure 1.1 *Some selected milestones of seismic technology and reservoir engineering practices from the 1940's to recent times.*

Notably, Willcox and Riley (1975) tried to link the seismically interpreted faults into the pressure matching process in a North Sea gas field, which could be regarded as one of earliest attempts to incorporate seismic in the history matching process. Seismic technology achieved many successes in the 1980s during which surveys were repeated in 2D and 3D from onshore to offshore (Barkved, 2012). The ocean-bottom-seismic (OBS) firstly appeared in the beginning of the 1990's while a number of authors started to investigate the integration of 4D seismic and seismic history matching a few years later, including Landa and Horne (1997), Huang et al. (1998, 1999), Fanchi (1999), and Waggoner et al. (1999). With the advent of the permanent reservoir monitoring (PRM) system at Foinaven and Valhall in 1995 and 2002, the ever improving quality of the time-lapse seismic data gradually moved the focus of 4D applications from the qualitative end to the quantitative end. It was under these contexts that the concept of closing-the-loop (CtL) was proposed to the 4D community in the mid 2000's, which seeks the match of a subsurface model to data from a variety of disciplines.

1.1 The use of 4D seismic in reservoir management and optimisation

In the life cycle of an oil and gas field, modelling the subsurface has been a routine exercise throughout the development and management process. Data acquired by geologists, petrophysicists, geophysicists and reservoir engineers is sent to various models, in order to understand and predict the corresponding behaviours prior to any management decision. Among the models, the geological or reservoir simulation model is constructed as a comprehensive representation of the multi-disciplinary data that are mostly production-related. It is used to simulate the production-induced changes inside the reservoir with pre-set petro-physical parameters. Because the 4D seismic data is difficult to interpret without a reservoir engineering context, this model is regarded by reservoir geophysicists as an ideal assistant to make sense of the time-lapse signals. In addition, the reservoir engineers are the ultimate beneficiaries, as the 4D seismic provides them with realistic, in-space "snapshots" of the reservoir changes over time, to calibrate their models.

Johnston (2013) illustrated the ideal workflow for 4D-orientated projects in order to maximise the value from the repeated surveys, which is slightly modified in Figure 1.2. In the high level picture of this business, the life cycle of a field can be divided into three stages: exploration, development and production/optimisation. In the exploration stage, which primarily consists of discovery and appraisal activities, the operator has to carefully obtain wireline logs and core samples. These data are the fundamental items of evidence for the assessment of 4D applicability. In the development stage, a static reservoir model is usually constructed with the acquired 3D seismic, prior to the start of production, with which the field development plan is designed. A more detailed 4D feasibility study can be carried out based on this development plan and the simulation of this static reservoir model. Additionally, the feasibility study also helps to plan the seismic surveillance during the future production. Tasks in the production/optimisation stage focus on enhancing the predictability of the reservoir model by matching its dynamic predictions to the observed 4D seismic data. This process involves lots of effort in processing the acquired seismic data, such as dedicated imaging, petro-physical modelling, seismic modelling and inversion. In addition, the revision process can be iterated every time a new seismic survey is acquired.

This optimisation stage is where the focal points of this thesis fall. In order to optimize the reservoir model rationally and efficiently, the use of the acquired 4D seismic data as “hard or soft” evidence must be a very careful process. Reasonable interpretation of the 4D seismic data is the premise of and the ultimate destination towards which all of the acquisition, processing, rock-physics analysis, seismic modelling and reservoir engineering lead. A conceptual framework for 4D interpretation proposed by Johnson (2013) is shown in Figure 1.3. The key points in his workflow are, firstly that the both the presence and lack of 4D signals are equally informative, and secondly, that the interpretation of the 4D signals must be validated by tying them to the reservoir engineering context. Therefore, the interpretation of the 4D attributes has to be an integration exercise in which the knowledge in geophysics and reservoir engineering are reconciled.

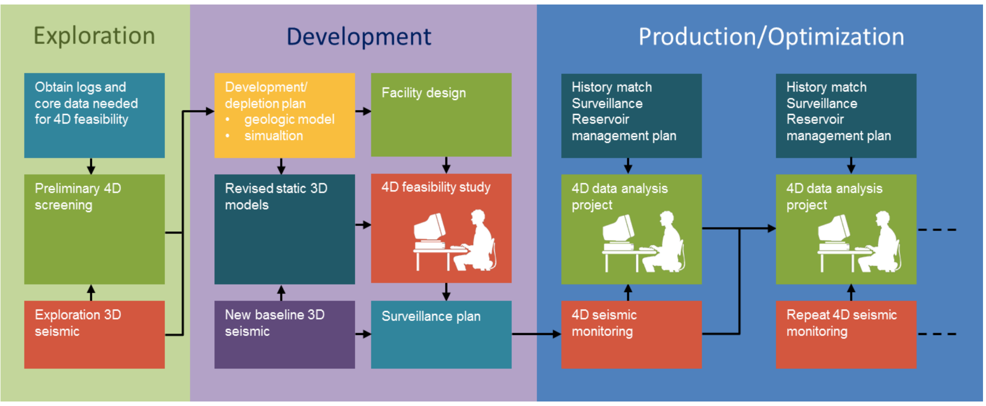

Figure 1.2 *4D-orientated activities during the life cycle of a field (from Johnson, 2013).*

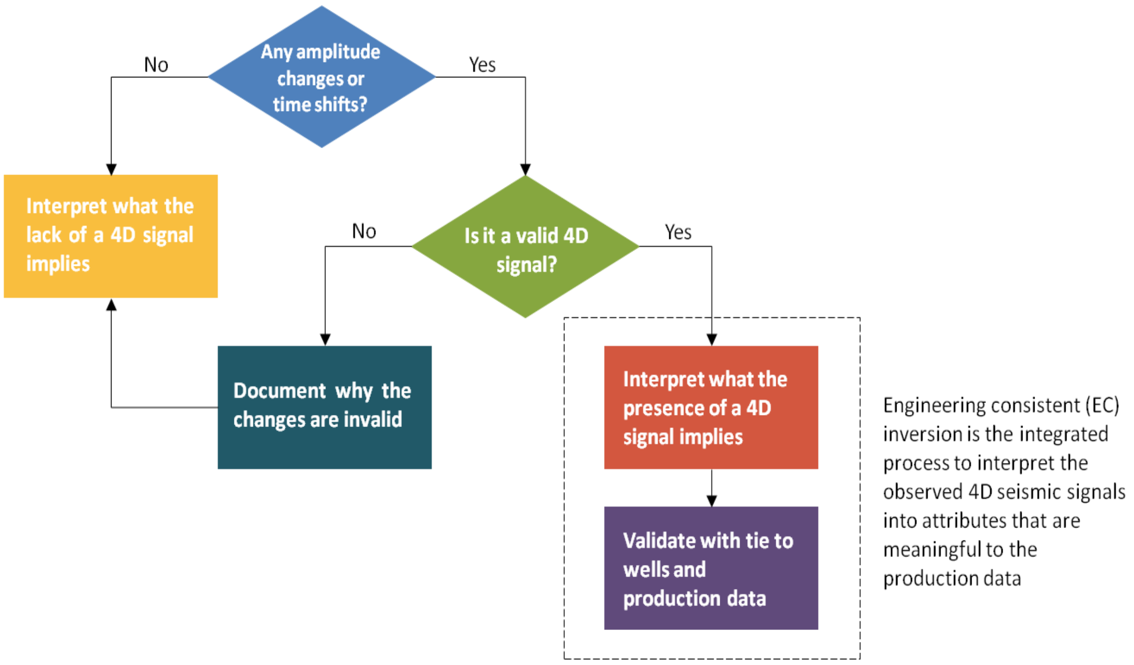

Figure 1.3 *The conceptual workflow for 4D seismic interpretation. The inversion of the observed primary 4D signal is actually a reconciling process during interpretation (modified from Johnson, 2013).*

1.2 Interpreting 4D seismic data by multiple attributes

The attributes of the 4D seismic that are subject to this integrated interpretation process can be classified into three typical levels (Figure 1.4), each of which can be synthesised or inverted from either the reservoir engineering or the seismic end. Starting from the inversion end, the acquired 4D amplitudes (which are generated by subtracting the amplitudes of the baseline and monitor surveys) are considered as the original form of the 4D seismic data. In practice, processing plays an important role in preserving the genuine amplitude differences, because the results it delivers will affect almost every single process during the interpretation. The amplitude differences are a combination of the reflectivity changes and time shifts induced by the production inside the reservoir. Also, the amplitude differences are in fact relative attributes, and mainly used as interfacial rather than volumetric data during the interpretation, because the reflection amplitudes are dependent on the seismic contrast above and below a certain interface. Inversion of the amplitude differences yields secondary representations of the reservoir changes, in the form of 4D elastic parameters. These parameters include the changes of P-wave velocity (V_P), S-wave velocity (V_S), density, P-impedance (I_P), S-impedance (I_S) and V_P/V_S ratio. Time shift inversion is different from elastic inversion, and is not the main scope of this thesis. In fact, the inversion process will inevitably embed uncertainties in the results, because inverting the noisy seismic data by itself is an ill-posed problem and subject to non-uniqueness. Furthermore, the essential causes of the 4D seismic signals, namely, the pressure and saturation changes (ΔP and ΔS) inside the reservoir, can be inverted either implicitly from the amplitudes (MacBeth et al., 2006) or indirectly from the elastic changes (e.g. Buland and El Quair, 2006). They are considered as “higher order” attributes than the elastic changes; therefore, their inversion and decomposition are subject to more uncertainties (MacBeth et al., 2006). In contrast to the inversion route, the ΔP and ΔS can be directly obtained by running the simulation of a reservoir model, which is, ideally, but not always, conditioned to the geological, seismic and production data. A reservoir model is usually gridded to a different lateral resolution to that of the seismic survey, and therefore, the simulated ΔP and ΔS, although satisfying all the reservoir engineering laws, may be inherently

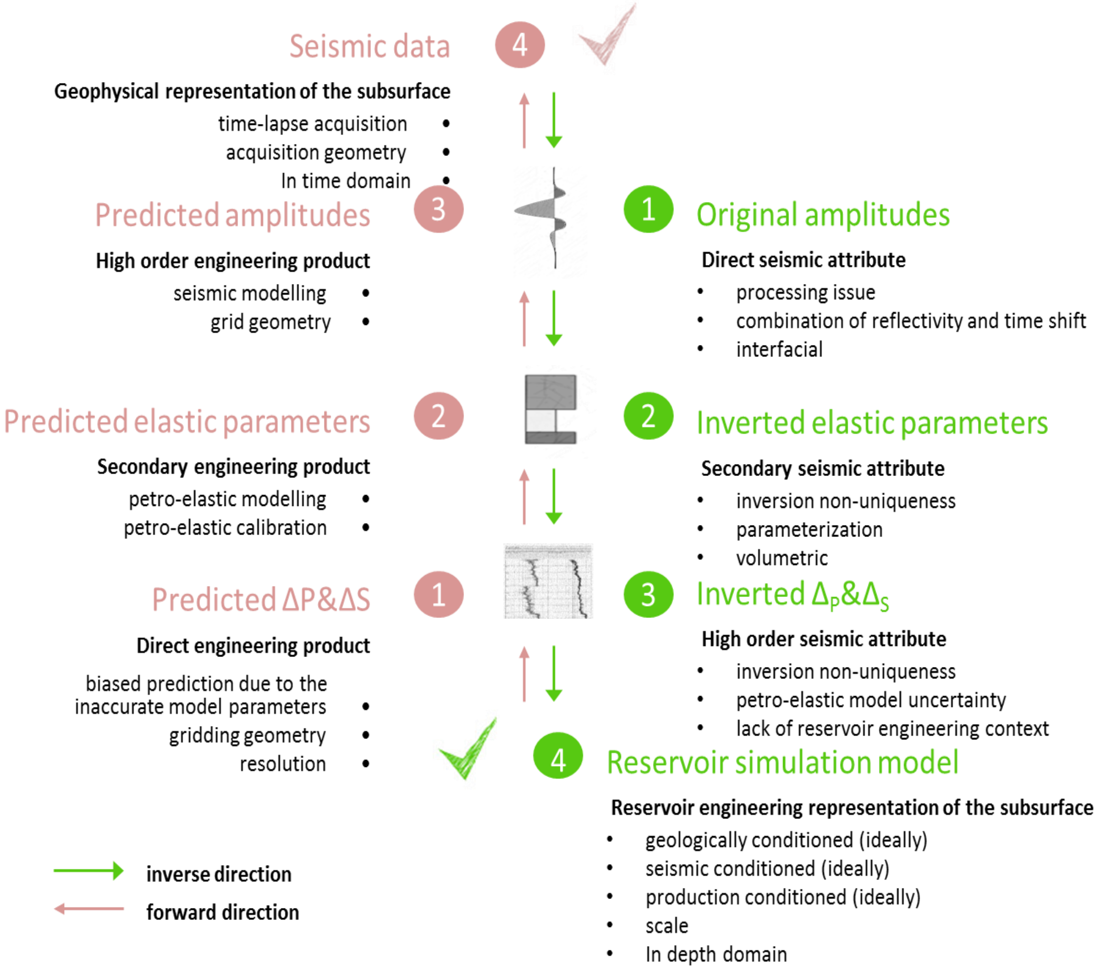

***Figure 1.4** Multiple attributes that bridge between the reservoir model and seismic data. The cross-domain comparison can be performed in any of the domains.*

unrealistic due to an inaccurate model. Elastic parameters can also be synthesized from the model predictions by employing a petro-elastic model. The petro-elastic model can be uncertain too, due to the simplification of physics and the lack of calibration data (Amini, 2014). This implies that the consequent synthetic seismics, either 3D or 4D, are inherently subject to uncertainties. Nevertheless, the grid geometry may be discernible in the synthetic seismic, due to differences in both lateral and vertical resolutions.

All of these attributes can be obtained and interpreted in either qualitatively or quantitatively. For instance, the 4D amplitude maps can be extracted along a reservoir surface, while the pseudo 4D impedance cubes can be approximated by processing the seismic volumes using the phase shift or “coloured inversion” technique (Lancaster and Whitcombe, 2000). These qualitative attributes are often relative, and the interpretation of them can sometimes adequately indicate the lateral sweep, bypassed reservoir, fluid baffles, reservoir compartments, contact movements and so on. In contrast to the qualitative uses, the 4D quantitative interpretation tends to answer different questions. For instance, the pressure and saturation changes quite often overlap on top of each other, making the qualitative interpretation ambiguous. To address this, techniques were developed to quantitatively segregate those (Landrø, 1999; Meadows, 2001; MacBeth et al., 2006). In contrast to ΔP and ΔS, the elastic changes provide a chance to depict the reservoir changes in terms of 4D I_P, I_S, density and so on. These 4D elastic properties can be used as intermediate attributes which lead to implicit inference of ΔP and ΔS. Although the quantitative interpretations require careful calculation and constraints to deliver meaningful solutions, one overwhelming benefit of going quantitative is the ease of cross-domain comparison, which will simplify the model updating process.

1.3 Closing-the-loop in reservoir management

When the closing-the-loop (CtL) idea was brought to industry, it was initially a general concept rather than a technology. By the early 1990’s, this idea had been around for many years in different forms, in which it was mostly centred around enhancing the understanding of the reservoir characterization from a geosciences perspective (Chierici, 1992). More recently, the activities in optimising production have been given innovative names such as ‘real-time’, ‘smart fields’, ‘i-fields’, ‘e-fields’, ‘self-learning reservoir management’, ‘integrated operations’ (Jansen et al., 2005), or ‘closed-loop reservoir management’ (Jansen et al., 2009). “Closing the loop” primarily refers to the process of improving the model match to the observed data whereas "closed loop" emphasises the completeness of workflows. Nevertheless, the essential practice of each retains the same frame. The underlying hypothesis of the CtL practice, according to Jansen et al. (2009), is that

"It will be possible to significantly increase life-cycle value by changing reservoir management from a batch-type to a near-continuous model-based controlled activity."

This statement highlights the importance of "timely feedback" to the models in order to control production. Chierici's reservoir management flowcharts, the framework of which did not include 4D seismic by the time it was published, can be referred as the prototype of CtL practice (Figure 1.5). The first rectangular area corresponds to the development stage in Johnson's workflow, discussed earlier (Figure 1.2). The loops closed at this stage primarily revise the modelled static geology by matching the model to wireline logs, 3D seismic and other geological concepts. The second rectangular area corresponds to the production/optimisation stage, within which the dynamic data starts to appear, such as the production histories, 4D seismic, production logging and so on. The dynamic CtL is here defined as the "real-time" data assimilation process. For the interests of this thesis, the detailed roles of the static and dynamic seismic data throughout the process are summarized in Table 1.1. It can be concluded at this stage that the 3D or static seismic is primarily used as an imaging tool in the exploration and development stage, while the surveillance value of the dynamic (4D) seismic is considered in the dynamic production stage.

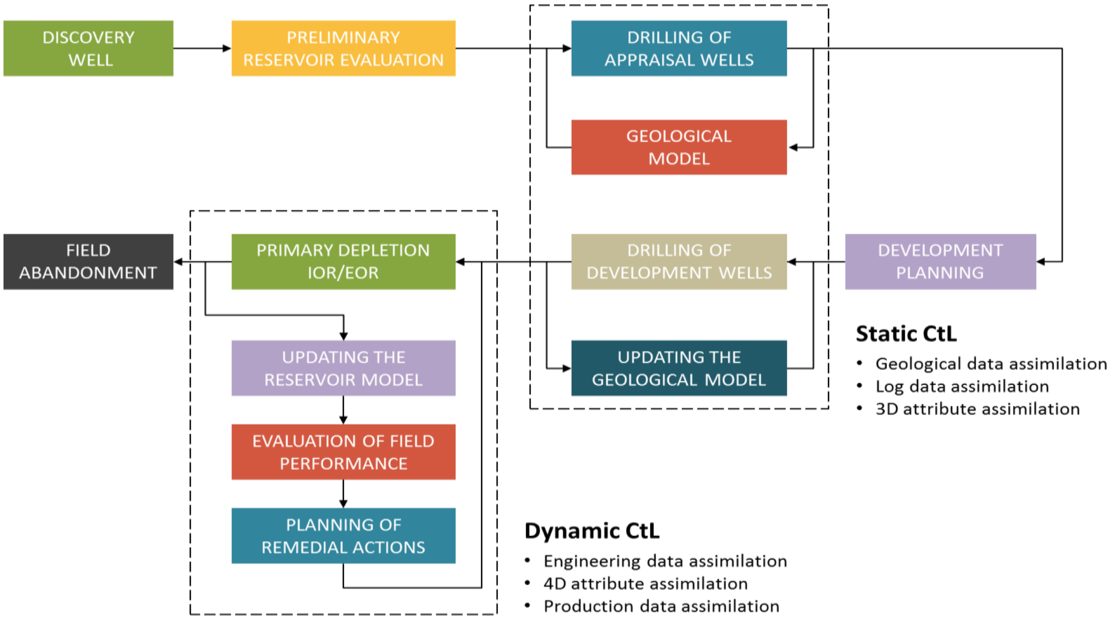

Figure 1.5 *Closing-the-loop in reservoir management (modified from Chierici, 1992).*

Exploration stage

- Build the basin scale seismic stratigraphy
- Locate the petroleum plays
- Image the reservoir structures
- Plan the exploration wells
- Detect the fluid boundaries
- Volumetric calculation

Development – 3D seismic in the static loop

- Build static geological/reservoir model
- Static petro-physical modelling
- Population of petro-physical properties
- Reservoir compartmentalization
- Static model updating

Production – 4D seismic in the dynamic loop

- Qualitative uses
    - Sweep pattern
    - Flood fronts and contact movement
    - Fluid baffles
    - Reservoir compartmentalisations
- Quantitative uses
    - 4D elastic inversion
    - ΔP and ΔS inversion
    - Dynamic model updating

Table 1.1 *The role of static (3D) and dynamic (4D) seismic technology at different stages of field life cycle.*

The inputs that are expected by the engineers in building reservoir models are summarized in Figure 1.6 by MacBeth (1999) and shared as a “wish list” within the Edinburgh Time-Lapse Project. Although it is possible to make indirect inferences for some laboratory based parameters, such as relative permeability, the seismic data are primarily capable of delivering more confident estimations about the reservoir geometry, porosity, NTG, transmissibility (Villegas et al., 2009) and reservoir compartments (Almaskeri and MacBeth, 2005). These are the focal elements that one

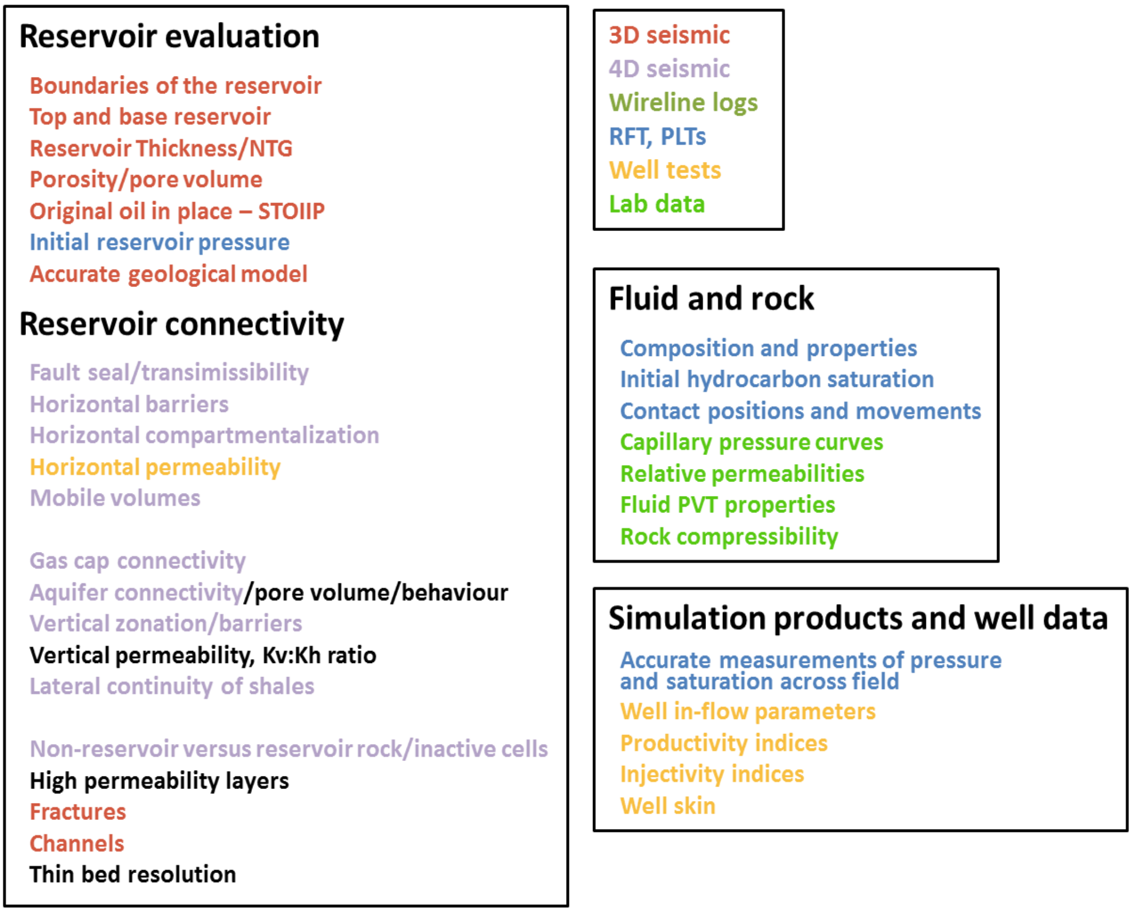

Figure 1.6 *The "wish list" of the reservoir engineering, among which the seismic could be used to provide spatial information for reservoir characterization over the life time of a field (MacBeth, 1999).*

should expect from performing a seismic driven CtL update. In practice, there are two main categories of approaches to close the loop, as depicted in Figure 1.7. In the seismic history matching (SHM) workflow, the 4D seismic and production data are used as conditions during the data assimilation process, while in the seismic to simulator workflows, fundamental parameters with which the reservoir model is built are directly or indirectly estimated from 3D and 4D seismic data, leaving the production history data as the only type of condition in the optimisation procedure.

1.3.1 CtL by seismic history matching

The current implementation of the CtL can be classified into two major groups, of which one is the incorporation of seismic data into the history matching process. The seismic history matching (SHM), which is developed on the basis of conventional production history matching, aims to tune the model in order to be consistent with the field performance as well as the seismic input. The underlying assumption for SHM is that a reservoir model which can capture the past life of a reservoir is more likely to make accurate predictions (Hajizadeh, 2011). The SHM process can be regarded as a non-unique inverse problem similar to the seismic inversion technique, in which the data kernel converts the modelled geological and engineering parameters into reservoir responses. The search for the numerically consistent inputs of these parameters, which is usually associated with one or more types of optimisation algorithms, constitutes the core of SHM. Because of the high dimensionality of the input model – which is usually defined by tens to hundreds of input parameter types that are stored in millions of cells – the inversion for these is never unique and the solution may make sense in one discipline while not in the others.

There has been a large amount of research probing into the possibility of reducing the non-uniqueness of the SHM problem by improving the optimisation algorithms. The methods used for searching in solution space have evolved from some basic regression (Coats et al., 1968) to a number of gradient based local optimisation approaches (Slater and Durrer, 1970, Thomas et al., 1971, Watson and Lee, 1986, Anterion et al., 1989), to some statistical approaches (Gavalas et al., 1976, Shah et al., 1978, Marsily et al., 1987). The more advanced "global" searching methods were introduced later into the industry; these include simulated annealing (Ouenes, 1992), genetic algorithms (Sen et al., 1995), particle swarm optimisation (Mohamed et al., 2009) and ensemble Kalman filters (Liu and Oliver, 2005). For a review of different applications of algorithms, interested

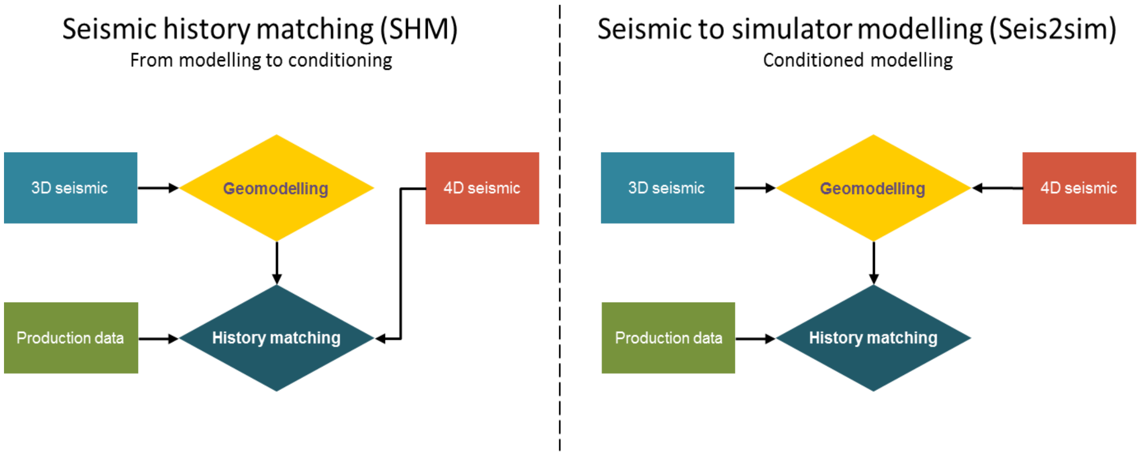

Figure 1.7 *The schematic workflows for seismic history matching (SHM) and seismic to simulator modelling (seis2sim) approaches.*

readers can refer to Hajizadeh (2011). Nevertheless, in order to speed up tefficiency, efforts were also spent in reducing the dimensionality of the history matching problem by upscaling (Christie and Blunt, 2001), or using some “cheaper” simulation methods, such as proxy models (Mohaghegh, 2006, Christie et al.) or streamline simulation (Stephen et al., 2009).

The integration of 4D seismic into the history matching process helps reduce the non-uniqueness during the optimisation process. Unlike the production data, which is only available at well locations, the 4D seismic serves as a spatial constraint to regulate the model behaviour. Gosselin et al. (2001) initially proposed a representative workflow to incorporate 4D seismic into the history matching workflow. They closed the dynamic loop by converting the simulated ΔP and ΔS into elastic impedance differences through a PEM and optimising the assimilation by a Gauss-Newton method. Kretz et al. (2002, 2004) used streamline simulation to match the flood front extracted from the 4D amplitudes by perturbing the permeability model in a North Sea field. Stephen and MacBeth (2006, 2007) utilised a Bayesian framework and streamline simulation to update the NTG and vertical permeability of the reservoir model by comparing synthetic 4D impedance maps with the observed one. Their use of pilot points and the Neighbourhood approach reduced the uncertainties in the reservoir models for the Schiehallion and Nelson fields. Fahimuddin et al. (2010) compared the use of amplitudes and impedance attributes in an EnKF-based history matching and suggested the advantages of the impedance cubes in stabilizing the optimisation. Tolstukhin et al. (2012) history matched the Ekofisk reservoir model by matching the time strain with a PSO algorithm, which led to an update of the fracture system in the chalk reservoir. Unlike the others, Castro et al. (2006) established a probabilistic workflow to incorporate 4D seismic into the geo-modelling process. The analysis and assimilation of 4D data is integrated in a probabilistic way, such that multiple realisations could be generated. Reservoir models that satisfy the production data could be found among these realisations directly, through a later history matching process.

CtL using SHM tends to provide an automatic solution to update the reservoir models. However, the lack of efficiency and non-unique solutions – even if with the assistance of the most advanced algorithms – remain as the two major challenges for SHM. In particular cases, the incomplete or incorrect parameterisation of the inverse problem may impose some meaningless updates to the model in order to achieve the numerical match.

1.3.2 CtL by Seismic-To-Simulator inversion

Watkins et al. (1992) highlight the importance of user interaction in the history matching process. In their context, the reservoir engineer's decision in updating the reservoir model may need to be added as an updated too. These strategic changes in updating the model are usually caused by the advances in understanding the fundamental geology, geophysical or reservoir engineering data. Driven by the 3D seismic data, the interpretation and modelling of this information is traditionally implemented in an integration workflow called 3D seismic-to-simulator modelling (3D seis2sim). The prototype of 3D seis2sim can be seen in Figure 1.8, in which the 3D seismic data is processed, interpreted, and inverted into petro-physical parameters for reservoir modelling. The 3D seis2sim modelling had become a standard exercise in the industry by the mid 2000's with the maturation of quantitative 3D seismic interpretation techniques, while most of the case studies were carried out under names such as "seismic reservoir characterizations" or "integrated reservoir modelling". However, one major drawback of the 3D seis2sim process is the lack of ability to validate the resultant model in terms of the correctness in replicating the original seismic data. The lack of

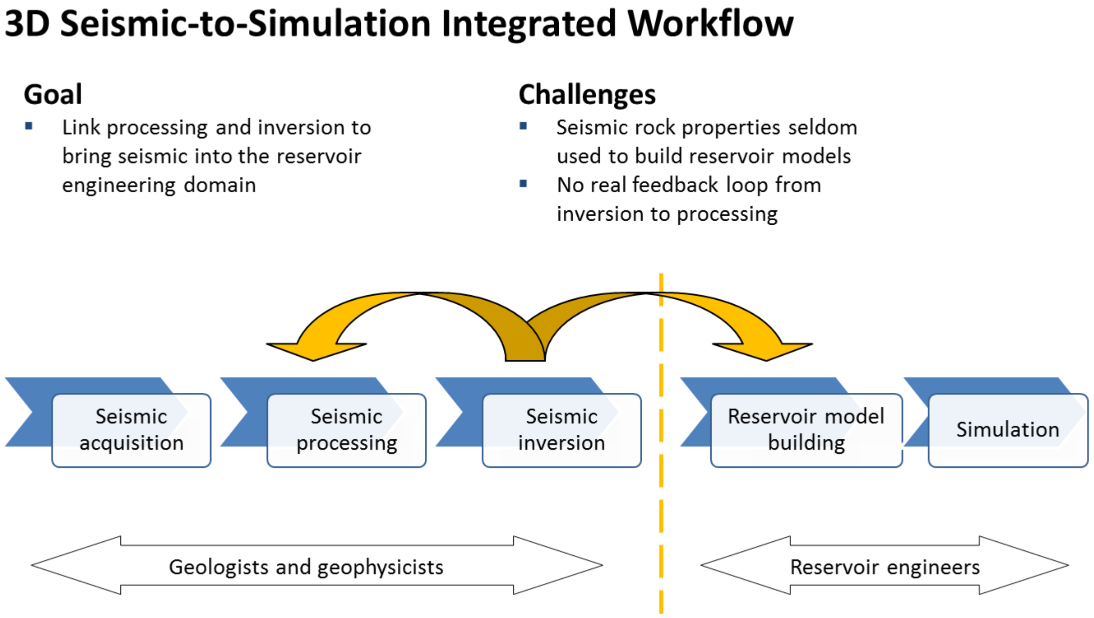
3D Seismic-to-Simulation Integrated Workflow

Goal
- Link processing and inversion to bring seismic into the reservoir engineering domain

Challenges
- Seismic rock properties seldom used to build reservoir models
- No real feedback loop from inversion to processing

***Figure 1.8** The 3D seis2sim workflow proposed by Boutte (2007).*

this feedback mechanism leads to a loophole, which cannot be closed without introducing a 3D simulator-to-seismic modelling workflow (3D sim2seis). Practically, the 3D sim2seis can generate synthetic 3D seismic responses of the reservoir model, based on its initial set-ups. The calculation of sim2seis includes the rock-physics modelling via the Gassmann substitution, stress modelling and the seismic modelling. The synthetic results from sim2seis can be compared to the seismic observation. Moreover,t he discrepancy highlighted in this comparison can lead to efficient 3D CtL updates of the reservoir model, since the observed 3D seismic data have captured the realistic distributions of reservoir properties such as porosity, NTG (net-to-gross) and possibly the permeability estimations.

Nonetheless, a natural expansion of the 3D CtL with sim2seis and 3D seis2sim is to incorporate the 4D data (Figure 1.9). Unlike the 3D seismic, 4D data capture the dynamic changes of the reservoir which mainly lead to the update of dynamic-performance-related parameters, such as flow barriers and permeability, in the reservoir model. The 4D loop is jointly closed by 4D sim2seis and 4D seis2sim workflows, where 4D sim2seis forward models the synthetic 4D elastic and seismic responses according to the simulated pressure and saturation variations, while the 4D seis2sim aims to invert the 4D seismic into more meaningful elastic differences. 4D CtL is established only if the inversion and forward modelling are designed in a consistent scheme, otherwise their results are not compatible. Nevertheless, 4D CtL is particularly robust in detecting the fundamental discrepancy across the domains, leading to a more target-orientated model-updating strategy.

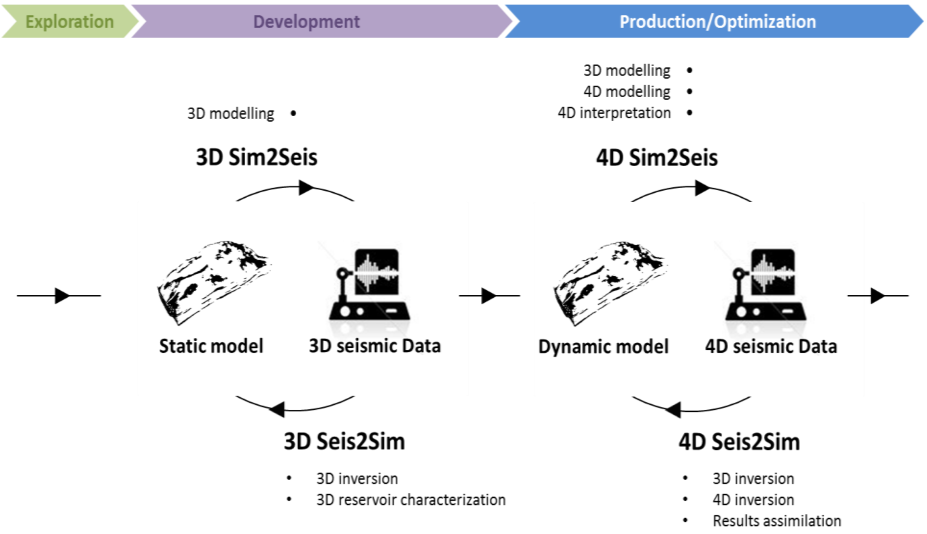

Figure 1.9 *The expansion of 3D seis2sim to 4D seis2sim and CtL.*

The potential of the seis2sim exercise has been applied to many fields. In the literature, most of the relevant case studies are not directly under the name of CtL, but in fact they all tend to close some of the selected loops by pre- or post-processing the 3D and 4D seismic data. Zachariassen et al. (2006) conducted the 3D and 4D elastic inversion for the Oseberg field, the results of which led to a probabilistic classification of the reservoir sand and various facies according to the 3D and 4D data (Figure 1.10). Model realisations generated from the sand probability cubes are ranked according to the visual comparison between the synthetic and observed 4D seismic responses. Nonetheless, their 4D seis2sim work was only validated by checking the 4D and production matches, leaving the static loop loosely closed. Ingrid et al. (2009) extended the 3D inversion work of Wijngaarden et al. (2007) to 4D and applied it to the Troll West field. The porosity and clay distribution of the geomodel were updated by the 3D inversion results, while the initial and produced oil-water contacts were inferred by the inversion of 3D and 4D seismic. They also updated the depth location of the model accordingly (Gjerding et al., 2010). However, their 4D seis2sim work did not show the “feedback loop”, therefore the update was not verified. Leguijt (2001, 2009) introduced a probabilistic Bayesian approach to invert for 3D static reservoir properties. Floricich et al. (2010, 2011) applied the method to the Schiehallion field and one other North Sea field to update the NTG and facies distributions in the reservoir models, which led to better static seismic responses. They carried out the inversion of the Schiehallion 4D data, in which the eight time-lapse vintages were simultaneously inverted into pressure and saturations over time and compared with the model predictions. This series

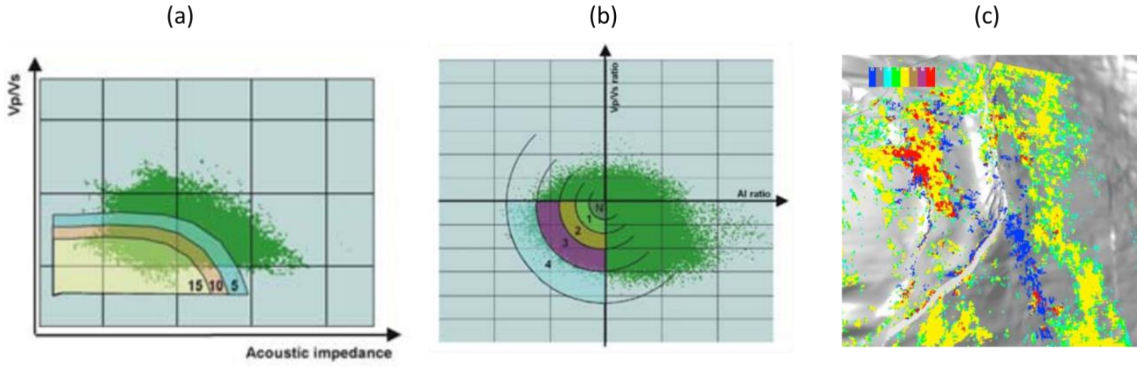

Figure 1.10 *Conceptual sketch of the 3D (a) and (4D) classification. In (a) low AI and low VP/VS ratio is classified as sand while in (b) decrease in both AI and VP/VS reflect gas flooding sand. (c) shows the final groups of sand, according to the 3D and 4D classification (modified from Zachariassen,2006).*

of advances have depicted the modern evolution of the seis2sim methodology. In addition, Kleemeyer et al. (2012) utilised the same technique for the Astokh field. The inverted pressure and saturation were thresholded to highlight the essential 4D changes which were to be used for the next level of the history matching process. In addition, the dynamic loop can also be closed by extracting unique geomechanical attributes (e.g. time-shifts, time-strain, or relative velocity changes) from 4D seismic. De Gennaro et al. (2008) and Dutry (2013) discuss the workflow through which the seismic geomechanical data can be incorporated into the reservoir model, detecting the fluid barriers and updating the fault transmissibilities.

1.4 Developing an EC inversion for 4D seis2sim

Figure 1.11 summarises the pros and cons of the SHM and 4D seis2sim approaches. In short, the SHM is a powerful tool to improve the numerical match to the production data. However, SHM is challenged when the reservoir model or the parameterisation of the inverse problem is fundamentally inadequate or insensitive. This means the optimisation will not converge to solutions that make sense. Sagitov and Stephen (2013) show a synthetic example where the inadequate parameterisation of a channelised reservoir led to an impossible history matching. In contrast, the seis2sim workflow is capable of addressing these fundamental issues by performing pinpoint updates. The updates are made according to the realistic understanding of the 3D and 4D seismic data.

1.4.1 The need of an Engineering-Consistent 4D inversion

According to Zhdanov (2002), implementing the 4D seis2sim inversion has inherent challenges from the data, because the input seismic has been acquired and processed with noises. Moreover, the inversion is non-unique and unstable, hence the search for existing solutions that can be understood by the reservoir engineers is of great importance. The need for this cross-domain consistency prompts the development of a reservoir engineering consistent (EC) 4D inversion method, which will give compatible seismic solutions that are in tune with the forward 4D sim2seis process. The non-uniqueness problem of a 4D inversion can be severe, as the 4D seismic signal can be quite often relatively subtle. Blanchard and Thore (2013) presented an inversion study showing various 4D solutions with and without proper constraints (Figure 1.12). In their example, the unconstrained inversion

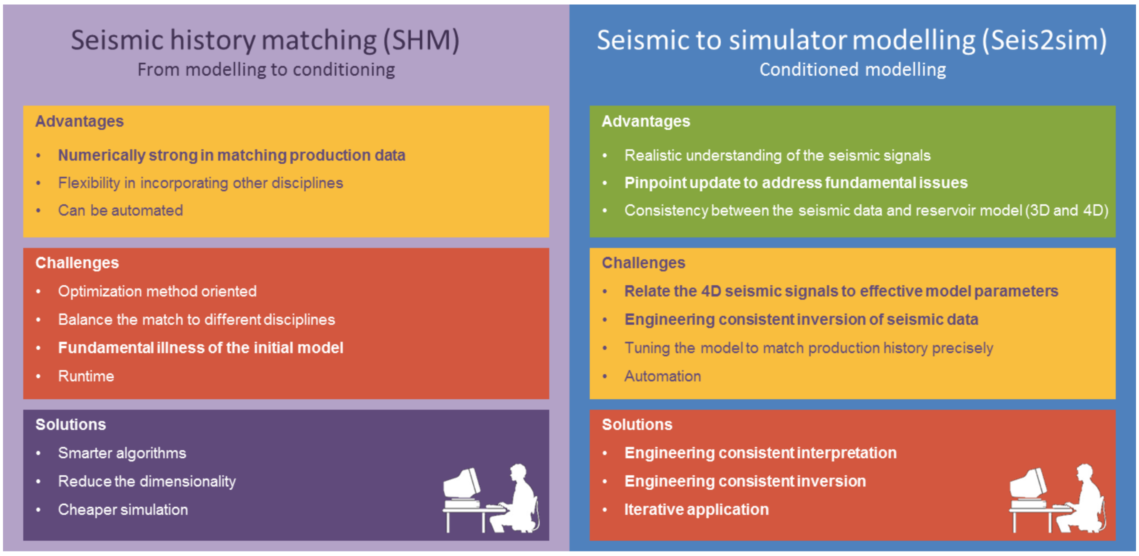

Seismic history matching (SHM)
From modelling to conditioning

Advantages
- **Numerically strong in matching production data**
- Flexibility in incorporating other disciplines
- Can be automated

Challenges
- Optimization method oriented
- Balance the match to different disciplines
- **Fundamental illness of the initial model**
- Runtime

Solutions
- Smarter algorithms
- Reduce the dimensionality
- Cheaper simulation

Seismic to simulator modelling (Seis2sim)
Conditioned modelling

Advantages
- Realistic understanding of the seismic signals
- **Pinpoint update to address fundamental issues**
- Consistency between the seismic data and reservoir model (3D and 4D)

Challenges
- **Relate the 4D seismic signals to effective model parameters**
- **Engineering consistent inversion of seismic data**
- Tuning the model to match production history precisely
- Automation

Solutions
- **Engineering consistent interpretation**
- **Engineering consistent inversion**
- **Iterative application**

Figure 1.11 *The advantages, challenges and possible solutions for the seismic history matching methods and seis2sim approaches.*

led to elastic changes that can be neither correlated to the production wells, nor rationalized in terms of reservoir engineering. For instance, the central area in Figure 1.12 corresponds to scenarios of water replacing oil, while the unconstrained solution presents an unrealistic density increase. However, with a dedicated dynamic constraint, the inversion solution shows higher coherency and the elastic changes are better understood under the context of reservoir engineering.

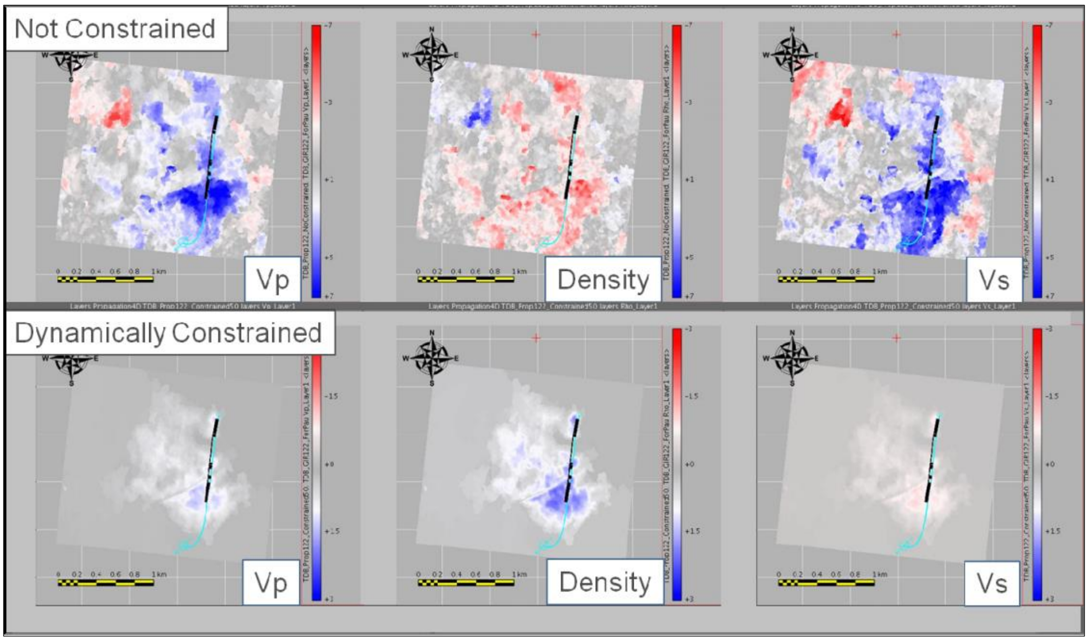

Figure 1.12 *Map view of the unconstrained (top) and constrained (bottom) 4D inversion solutions (Blanchard and Thore, 2013).*

1.4.2 Existing approaches in 4D seismic inversion

In theory, any changes inside the reservoir, large or small, will prompt a difference in the seismic signal. These changes include but are not limited to the contents (oil, gas, brine, injected solvent etc.), condition (pressure, temperature, salinity etc.) of the reservoir fluids, as well as other geomechanics -related changes in the reservoir rocks. These changes can be sensed by one or more seismic attributes, as shown in Figure 1.4. In order to inductively forward model the consequent seismic changes, or to deductively invert for the causes, a reliable kernel is needed. This kernel requires not only the mathematic functions to solve for the modelling and inversion, but also the physics to meet the reservoir engineering context. Therefore, the existing literature in both acoustic and elastic seismic inversion is reviewed according to the different aspects of implementation, in terms of data coupling, inversion algorithms and associative uncertainty, cross-domain integration and constraints, with respect to the possibility of their adaption to the CtL workflow.

1.4.2.1 The 4D inversion schemes

The modelling and inversion of 3D seismic data has been extensively reviewed by Barclay et al. (2008). The inversion for a single seismic vintage (e.g. a 3D seismic inversion) works as a basic function unit in a 4D inversion workflow. Sarkar et al. (2003) categorise the general workflows for conducting 4D inversion as an uncoupled inversion, coupled inversion and inversion of difference data (Figure 1.13). The uncoupled schemes invert different seismic surveys separately and subtract the results to

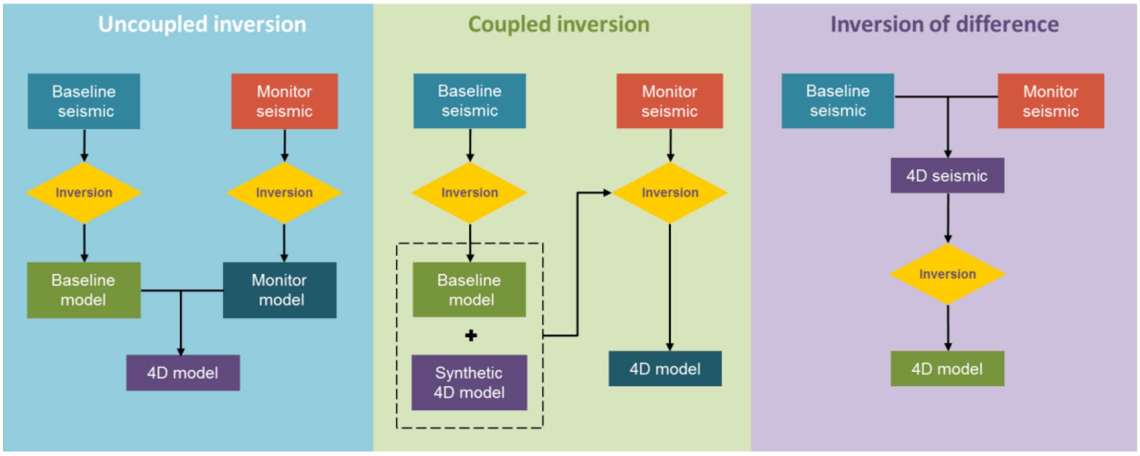

Figure 1.13 *Schematic options in inverting for 4D difference.*

obtain the 4D difference. It does not require additional effort to alter the existing 3D inversion approach, but the resultant difference is subject to the non-uniqueness of the inverse problem. Zhang (2005), Leguijt (2009) and Floricich (2012) developed this scheme further to simultaneously invert multiple time-lapse vintages. During the inversion, the vintages share a common initial model and usually a regularisation term is introduced into the cost function to stabilise the solution. However, consistency among the vintages is difficult to secure. In contrast, the coupled scheme uses the reservoir model estimated from the baseline seismic data as the initial state for the monitor inversion. Based on the initial state, the inversion looks for a suitable 4D change that can generate the observed monitor seismic data. Essentially, the coupled scheme mimics the physical process of a reservoir undergoing a production change, while the inversion algorithm works on the 4D changes directly. This facilitates the application of 4D constraints, and maximises the consistency between the baseline and monitor. However, error in the baseline inversion can propagate into the 4D inversion, which may introduce additional uncertainty. For example, Buland and More (2003) developed a linearised AVO seismic inversion approach, which was further extended and applied to the 4D difference data (Buland and El Ouair, 2006). The direct inversion of the difference data has a different formulation in the seismic modelling, because the popular Zoeppritz equation is not able to deal with the negative changes in 4D directly. Thus, the logarithm of the ratio between the monitor and baseline models has been used to tackle this problem (Buland and El Ouair, 2006; Ayzenberg and Theune, 2010; Thore and Hubans, 2012; Theune, 2013). The direct inversion of the difference data can lead to relative reservoir changes. However, the inversion has to process the input time-lapse seismic vintages carefully, and this necessitates dedicated pre-processing work, such as cross-equalisations.

1.4.2.2 The algorithms for 4D inversion

Strictly speaking, any algorithm that is applicable to 3D inversion can be adapted to 4D, as they are all essentially similar inverse problems. Pillar (2012) reviewed the modern techniques that exist for 3D inversion, and these approaches are summarized in Table 1.2. The deconvolution-based sparse spike methods are rarely used for 4D seismic data. Lancaster and Whitcombe (2000) proposed the coloured inversion (CI), which designs a spectual operator according to the well log derived earth model. The CI was applied to the Valhall field to perform a “fast-track” 4D interpretation. However, the CI needs to

Algorithm	Data type	Implementation	Results	Comments
Sparse spike	Pre-stack/Post-stack	Deterministic	Relative	Deconvolution based
Coloured	Pre-stack/Post-stack	Deterministic	Relative	Wavelet free, spectrum operation
Model based	Pre-stack/Post-stack	Deterministic	Absolute	Initial model is required
Stochastic/ Geostatistic	Pre-stack/Post-stack	Probabilistic	Absolute	Statistical information is required from logs
Simultaneous	Pre-stack	Deterministic/ Probabilistic	Absolute	AVO based
Bayesian	Pre-stack/Post-stack	Deterministic/ Probabilistic	Absolute	Prior information is required
FWI	Pre-stack	Deterministic	Absolute	Wave equation based
Time shift inversion	Pre-stack/Post-stack	Deterministic	Absolute	Geomechanics related

Table 1.2 *Modern seismic inversion algorithms.*

have adequate noise attenuation prior to the inversion and the reservoir thickness should be relatively thin. Apart from the fact that the zero phase assumption is hard to secure in reality, the inverted solutions are relative changes, therefore it is impossible to use CI for quantitative characterization. In fact, both the stochastic and geostatistical inversions are model-based approaches, for which the initial models are supposed to contain the low-frequency information. The solutions obtained from them are absolute values of the reservoir properties which honour the geostatistical features observed at the well locations. The inversion is typically solved by stochastic simulation methods such as Monte Carlo procedures; therefore, the uncertainty of the solution could be estimated by analysing the resultant realisations (Haas and Dubrule 1994, Dubrule 2003), at the cost of a longer computing time than the deterministic approaches. Because the geostatistical inversion is primarily used to characterise the static reservoir geology, the geological constraints it uses are not directly relevant for 4D inversion, though it is still valuable for the baseline inversion in a coupled scheme.

It comes as no surprise that all the above methods transfer readily to the pre-stack data domain. The 3D simultaneous inversion is able to jointly invert for elastic reservoir properties such as P-velocity, S-velocity and density by matching the seismic data at various offsets or angles. Compared to the conventional post-stack techniques, the elastic parameters can perform better at sand and shale discrimination, when the lithological difference between reservoir and non-reservoir is blurred (Pendrel, 2006). The 4D expansion of this approach is the “4D global” or “4D simultaneous” inversion, which computes multiple offsets and vintages concurrently (El Ouair and Stronen, 2006; Haaland et al., 2008; Lafet et al., 2009).

When the integration of information becomes vital, most of the inversion practitioners concede that the best way to approach the non-uniqueness and data-integration problem in seismic inversion is via a Bayesian formalism, because of its flexibility to introduce cross-domain information as well as the ability to handle data uncertainties. The examples of such work are studies by Omre and Tjelmeland (1997), Gunning (2000), Leguijt (2001), Eidsvik et al. (2002), Eide et al. (2002), Buland and Omre (2003) and Buland et al. (2003). In addition, Buland and El Ouair (2006) furthered their Bayesian approach for the inversion of 4D seismic data, in which the inverse problem is linearised and solved in a deterministic fashion. With the assistance of a petro-elastic model and Monte Carlo simulation, they could also estimate the saturation changes in a probabilistic manner. However, the linearised approach searches for local solutions, which requires the prior information to be relatively accurate.

The time-shift effect in 4D seismic has also been noticed by the inversion practitioners as an informative attribute to improve the solution of the elastic inversion approaches discussed above. Lafet et al. (2005) proposed a coupled angle-stack stochastic inversion method that includes the time-shift information by updating the P-wave velocity and reservoir thickness in time. Landrø (2002), Williamson (2007) and Haalland (2008) proposed inversion workflows in which the time-shift is directly inverted into relative velocity changes, with assumptions such as P-wave velocity-dominated 4D changes. A newer version of this approach, proposed by Thore (2011), performs such inversion at well locations first, and then extends it to the full field. Chu et al. (2011) used the time-shift-derived relative velocity change as a low frequency background model to image areas where the gas exsolution has caused seismic absorption.

Apart from these convolution-based inversion techniques, the more recent full waveform inversion (FWI) uses the full wave equation to simulate the wave propagation and match the observed seismic by updating the velocity model. Indeed, it is currently used as an imaging tool rather than for reservoir monitoring, but its potential for 4D is promising (Lu et al., 2013).

1.4.2.3 Cross-discipline integration and constraints

As discussed previously, sensible solutions of the 4D inversion lie in the joint domain of reservoir geophysics and engineering. Therefore, the integration of prior knowledge in reservoir engineering is the key to a successful inversion. Essentially, the seismic data is acquired in the time domain, while the reservoir engineering practices are primarily defined in depth. This raises domain conversion as a fundamental issue when the information goes across the disciplines. Ideally, the geometric frames (top, base and intra units as horizons) of a reservoir are initially picked out in the seismic domain, which are later converted to the depth domain via a velocity model that is dedicated to perform domain conversion. However, this velocity model is firstly subject to higher degree of uncertainty, as it is built in the early stage of the field development; secondly, the legacy may actually go missing, due to the data management of assets. To tackle this problem, a number of authors have tried to bypass this problem via alternative options. Thore (2005) suggested a "painting" algorithm, with which the gridded reservoir property in depth could be mapped onto a different gridded system. This idea could be used to map the depth domain data to the time domain, with structural constraints defining the corresponding boundaries in each. This approach does not require an accurate velocity model, and when the availability of the constraints and the smoothness of the grid system are guaranteed, it transfers data from one to the other with reasonable accuracy. In contrast, Lafet et al. (2005) and Thore (2011) included the time-to-depth relationship as one of the parameters to be inverted. They updated the thickness and positions of the modelled grids according to the inverted P-wave velocity. The inverted reservoir properties, static or dynamic, could then be transferred across the domains freely.

A reliable domain conversion is the prerequisite to almost every attempt in data integration. As discussed before, inversion of the noisy seismic data is by its nature ill-posed and there are non-unique solutions. In addition, the inherent errors in the 4D data, as well as the imperfect modelling process will make the inversion unstable. Therefore, collaboration among the disciplines is the key for a 4D inversion to qualify, particularly when it is designed for the CtL workflows. Sarkar et al. (2003) investigated the impact of coupling in a model-based 4D inversion. This coupling scheme is by itself a constraint to ensure the consistency in the inversion results. Gouveia et al. (2004) implemented the same comparison with the Jotun field, in which they concluded that, for model-based 4D inversion, the constraints for the low frequency component were of significant importance, because the seismic data is band limited and the first few hertz of the bandwidth has to rely on the initial model, especially when the inversion is conducted by a local optimisation algorithm. Chu et al. (2011) extended this low frequency concept by merging the coloured inversion results with the time-shift derived low frequency velocity changes (Figure 1.14). Zhang (2005) discussed the stabilisation of the simultaneous 4D inversion by applying sparseness, impedance and structural constraints. The sparseness constraint regulates the inversion problem by introducing prior models that are either exponential or Cauchy. The sparseness constraint works in a way that is similar to the correlation function proposed by Bulland et al. (2003) in their linearised AVO inversion. The impedance constraints are derived from well log data which reflect the realistic continuity of the impedance distribution. The structural constraints are based on the assumption that the 4D changes are confined by the interpreted reservoir intervals. Therefore, vertically varying weights can be applied during the search for 4D changes in and outside the reservoir zones. This approach has been implemented by a number of authors, such as Bulland and El Ouair (2006), Ayzenberg and Theune (2010 and 2013).

A further advance in designing the 4D constraints is to take the petro-elastic model (PEM) into account. A PEM can convert the given pressure and saturation changes into seismic elastic properties such as P-wave velocity, S-wave velocity and density by the

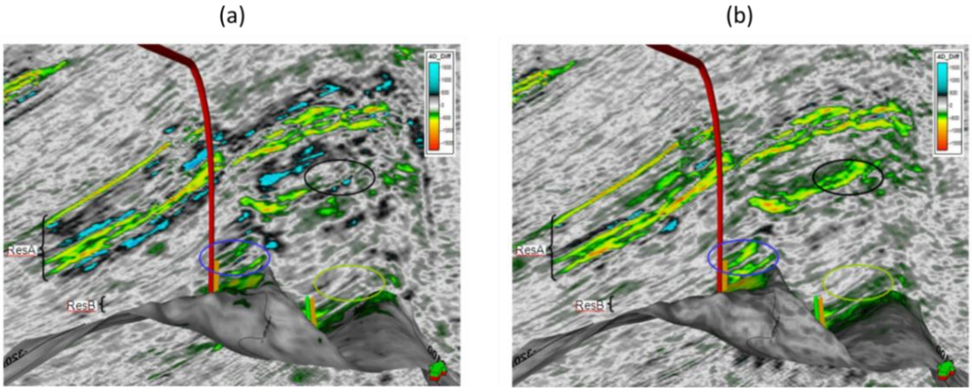

Figure 1.14 *4D difference of coloured inversion results in a West African field. (a) a conventional difference volume after cross-equalization and (b) the difference after spectral shaping and merging with the relative velocity changes (after Chu et al. 2011) .*

Gassmann substitution and stress modelling. 4D differences can also be predicted but the reliability cannot be examined unless the PEM is calibrated against an elusive dynamic measurement such as a PLT. The PEM predictions are based on reservoir simulation – hence, they provide the 4D seismic inversion with engineering expectations. The "global inversion" scheme by El Ouair and Stronen (2006) and Lafet et al. (2009) combines these constraints with stratigraphic constraints, forming a "4D mask" which honours the reservoir zonation, expected production effects and rock-physics (Figure 1.15). The risk of the constraints lies in the uncertainty during the petro-elastic modelling and the accuracy of the reservoir model itself. Therefore, it is not recommended to utilise the PEM predictions directly as "hard" constraints or "bounds" to limit the inversion. However, when the reservoir model is built consistently with the 3D seismic data, and history matched, the PEM predictions have a stronger degree of confidence. Nevertheless, the PEM is the heart of the sim2seis forward modelling. In order to close the loops, the PEM used in the forward loop (sim2seis) and the inverse loop (seis2sim) has to be identical. Only if the inversion has been constrained in a consistent PEM, are the results compatible and the discrepancy highlighted informative.

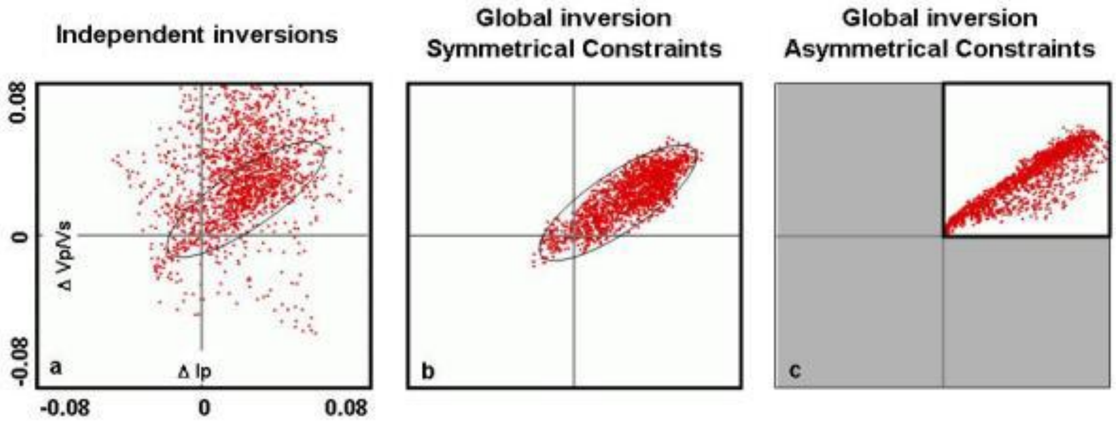

__Figure 1.15__ Cross plots of VP/VS vs IP (in %) for a water flooding area by independent inversions of base and monitor data (a), and global 4-D inversion with a symmetrical search window of ±8% (b) and with a non-symmetrical search window of 0 to 8% (c) as constraints. The white area corresponds to the limits of the imposed 4D constraints (after Lafet et al., 2009).

1.5 Thesis structure and outcomes

Despite the maturing 4D inversion mechanisms as reviewed above, the need for developing a 4D CtL workflow with an open source inversion package motivated an initial investigation of possible schemes to maximise the consistency, not only among datasets, but also among the sub-workflows. As is widely recognized, consistency is the key to every successful 4D project. This has to be maintained from the early stage of data processing, to the quantitative interpretation/inversion of the data, and to the updating part, which ultimately closes the loops among the disciplines. To close the loops, compatible workflows of 4D sim2seis and seis2sim must be developed to efficiently address the problems in the reservoir model. Secondarily, extracting reservoir engineering information from seismic is of fundamental interest in this thesis. As discussed, the nature of the non-unique solutions may prevent the 4D seis2sim workflow from yielding informative reservoir characterizations during production. The causes and solutions to this problem are therefore intriguing and challenging. In addition, it is necessary to probe into the uncertainties and technical obstacles during the data integration. The integration requires a large effort in interpreting data from various disciplines, such as petro-physics, structural geology, geophysics, and reservoir engineering. Approaches that allow the practical transfer of data from one domain to the other are of equal importance for CtL as an integrated process. In addition, the value of 4D CtL is also attractive. Its advantages over the other updating approaches can be revealed only by experiencing the journey through the loops.

The remainder of this thesis is divided into six chapters:

Chapter 2 discusses the development of the reservoir engineering consistent 4D inversion scheme which is to be used in my CtL workflow. It will highlight the unique issues that are raised in 4D inversion in contrast to 3D, = followed by a demonstration with a synthetic 1D example. In the example, the baseline and monitor seismic data are coupled in a Bayesian scheme in which the modelling errors are propagated from baseline to monitor to ensure the consistency. Unique engineering-consistent constraints are derived from the continuous 4D sim2seis predictions as correlations which allow the inversion to converge to the true solutions.

Chapter 3 implements the proposed inversion technique in the context of the Heidrun field. The time-lapse dataset consists of towed streamer seismic shot over a long period of production. A PEM model is calibrated for the field, with which a forward sim2seis modelling is performed. The application of EC 4D inversion is illustrated in both 1D and 3D, which is regulated by dedicated constraints derived from the prediction.

Chapter 4 brings the inversion results from Chapter 3 into the 4D seis2sim workflow, which aims at closing the static and dynamic loops of the Heidrun dataset by comparing the results from 4D sim2seis predictions. In the dynamic loop, the uncertain fault compartmentalisation is revised according to the discrepancy highlighted in the comparison.

Chapter 5 illustrates the application of the EC 4D inversion to the Girassol field. The 4D seismics are of much higher resolution than those for the Heidrun field, which raises a bigger challenge to the inversion. With the near, mid and far offset stacks, a pre-stack inversion was performed. This is important because the P-impedance alone cannot discriminate sand from shale in the field. Also, the constrained inversion results were benchmarked with the unconstrained ones.

Chapter 6 is about the CtL exercise in the Girassol field. Because of the uncertainty in reservoir extension, volumetrics and transmissibility, an additional reservoir loop is designed in the CtL strategy, which closes the loops in a sequential manner. The reservoir layout is jointly determined by combining 3D and 4D attributes together, while the modelled transmissibility field is fine-tuned iteratively, to improve the match to the observed 4D seismic.

Chapter 7 presents a summary and conclusions for this thesis. In addition, recommendations are suggested for the future improvement of the proposed workflow, as well as the research that lies ahead beyond this thesis.

Chapter 2

An Engineering-Consistent seis2sim approach for 4D inversion

“In the nature, all sharpness is blunted, all tangles untied, all glare tempered, all dust smoothed.”

「挫其銳，解其紛，和其光，同其塵。」

Lao Tze, *Chapter. 4, Tao Teh Ching, 400 BC to 700 BC*

With particular concern of integrating the reservoir engineering into seis2sim, an engineering-consistent (EC) workflow is proposed to extract information from a synthetic time-lapse dataset. The seis2sim adaptively honours the seismic and reservoir engineering according to the “strong” or “weak” contrast between the observed data and sim2seis predictions. The sim2seis-derived constraints take into account the modelled geology and simulated fluid flow changes, which ensures the seis2sim convergence to a joint solution between geophysics and reservoir engineering, with less uncertainty.

In order to investigate the potential issues in integrating the reservoir engineering data into seis2sim in a flexible system, a one dimensional dataset that contains a synthetic baseline and monitors is created. The term “inversion” is used in contrast to “forward theory”, which is defined as the process of predicting the results of measurements (predicting data) on the basis of some general principle or model and a set of specific conditions relevant to the problem at hand (Menke, 1984). An inversion workflow is proposed in Figure 2.1 to implement the seis2sim with this synthetic example, in order to validate the inversion method before applying it to the observed datasets. In the workflow, prior knowledge such as bounds and 3D sim2seis predictions is derived and embedded in the 3D seis2sim inversion to deliver the baseline 3D elastic model. This model is then used as the baseline reference model for the 4D seis2sim inversion, which is constrained by the analytical statistics from the 4D sim2seis predictions. By introducing EC constraints, the seismic solutions are expected to be more stable, and in tune with the reservoir engineering – just as nature harmonises conflicts.

2.1 Synthetic dataset and scenarios

Traditionally, seismic inversion is conducted in the time domain. However, the objective of proposed inversion is to provide the reservoir model with information from the seismic domain. It is thus important to define a new parameterisation scheme with which the information can get across efficiently. The geological models or fluid-flow simulation models usually grid the reservoir in compliance with the geological layers, flow units, and fault planes. As a result, the model grids are often built using non-vertical pillars and irregular cells. For example, corner-point geometry (CPG) is one of the typical structures used in reservoir models. To generate a realistic 1-D dataset for the seis2sim test, a vertical pseudo-log is created at the seismic trace location. The pseudo-log penetrates through the reservoir model vertically, forming a blocky log of the gridded model parameter along its trajectory (Figure 2.1). This log consists of the same number of modelled cells that are encountered by the vertical seismic trace. In order to forward model the corresponding seismic response, reflection coefficients are calculated at the interfaces of the model cells along the pseudo-log. By doing so, the model cells are directly parameterised as inputs for seis2sim. In addition, extracting the intersecting interfaces through oblique pillars and pinch-outs calls for extra care, because they complicate the parameterisation at “side-wall” locations (Amini, 2014).

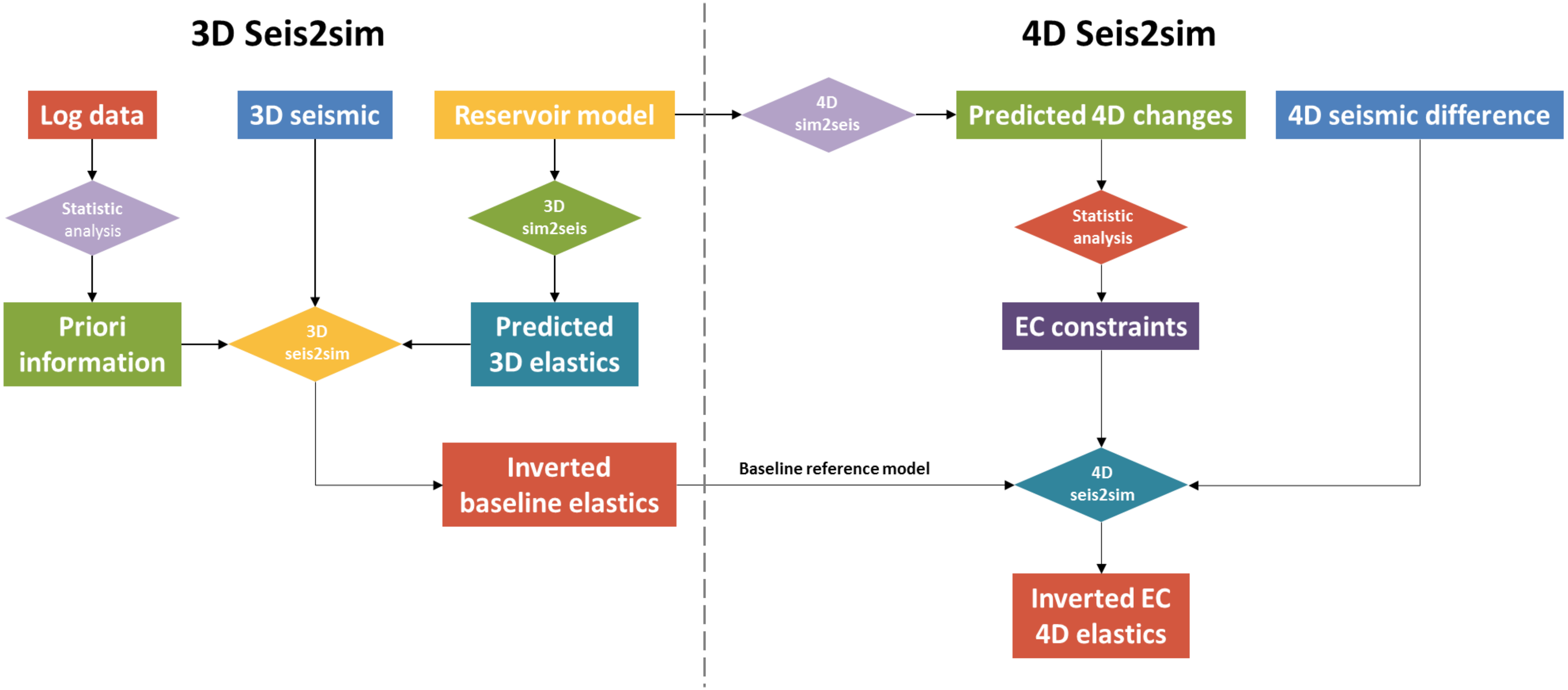

Figure 2.1 *The conceptual workflow for 3D and 4D seis2sim inversion.*

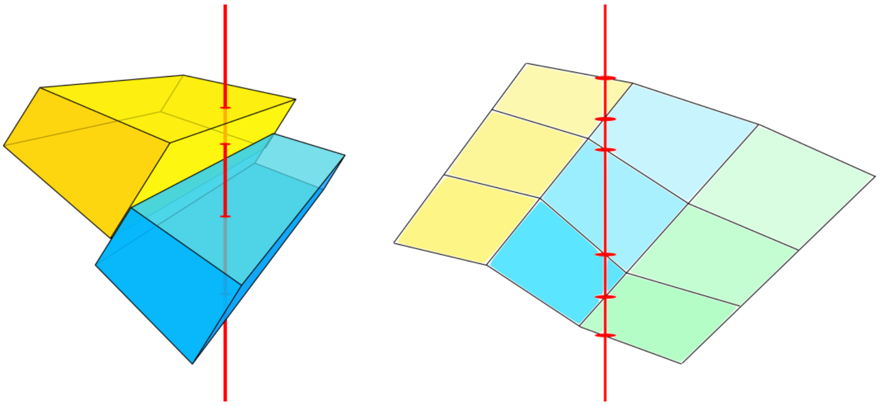

Figure 2.2 *The 3D (left) and 2D (right) illustration of the 1D vertical pseudo log extraction in models with corner-point geometry and non-vertical pillars (Amini, 2014).*

The synthetic dataset, as displayed in Figure 2.2, is based on the turbidite geology background from the real dataset used in Chapters 5 and 6. The sim2seis predictions of the P-velocity, S-velocity and density are superimposed onto the realistic reservoir model grids, as depth domain “true answers” to be inverted for. The vertical thicknesses of the reservoir model grids vary from 50 metres in the overburden, to about 4 metres in the reservoir and are additionally reduced to 1 metre in the underburden. The varying thickness results in non-uniform resolution, in contrast to the seismic data, which are often evenly sampled in time. The overburden of the reservoir is modelled by the first three layers of the gridded cells, while layers 4 to 10 are defined as the active reservoir interval.

In the example, the initial model for seis2sim inversion is assigned with constant P-velocity, S-velocity and density in the reservoir, overburden and underburden. The velocity of the reservoir cells is generally greater than the non-reservoir ones, whilst the density contrast between them is weak. To model the seismic response, the reflection coefficients at the near offset angles (0° to 10°), mid offset angles (10° to 20°) and far offset angles (20° to 30°) are calculated and stacked at the intersections for all 32 layers, by the modified Zoeppritz equation (Aki and Richards, 1980). The reflection coefficients are converted into the time domain by the P-velocity and convolved with a realistic wavelet to generate the synthetic, partially-stacked offset gathers. In the time domain, the reservoir interval lies between the peak at 2.98 seconds and the trough at 3.01s second. In terms of 4D changes, an elastic “softening” scenario resulting from

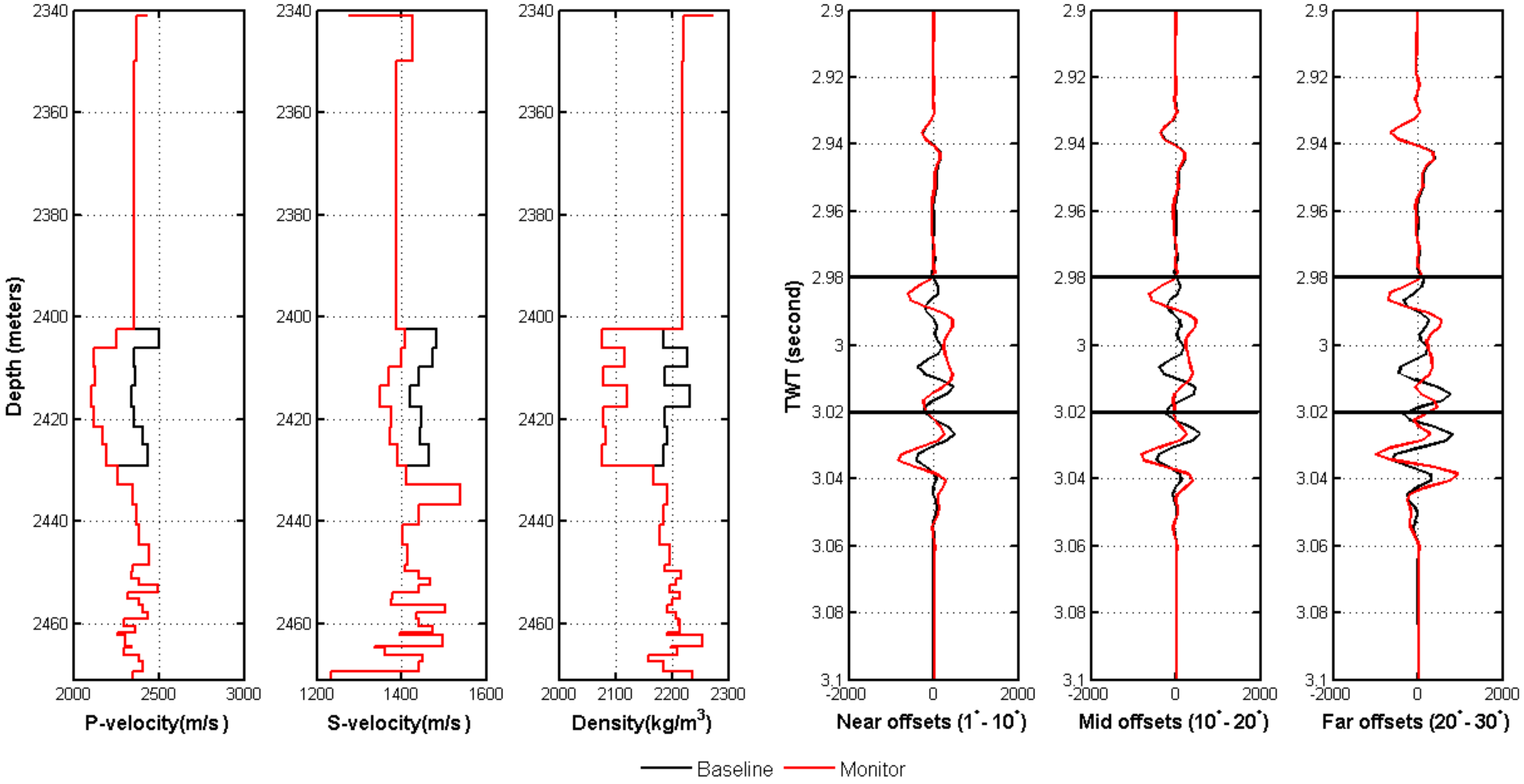

Figure 2.3 *The "true model" for the synthetic example with which the seis2sim inversion method is illustrated. The reservoir interval lies between 2.98 seconds to 3.02 seconds in the time domain.*

gas injection is designed, which causes a 10% decrease in P-velocity, S-velocity and density respectively inside the reservoir layers. The synthetic gathers of monitor seismic are generated in the same manner, which include the time-shifts caused by velocity difference and the amplitude differences due to the variation in elastic contrasts. After "production", the interface between the top reservoir and the overburden has a reversed elastic contrast, therefore the top reservoir event on the baseline and the monitor seismic have different polarities. Amplitude differences are found outside the reservoir interval, which are the results of side-lobe effects of the wavelet in the overburden and the cumulative time shifts in the underburden.

To develop and validate the inversion methodology, the synthetic baseline and monitor seismic gathers are used as "observed" data to invert for the elastic parameters that are employed to generate them.

2.2 Non-uniqueness and the necessity of coupling

As discussed previously, there are schematically three categories of approaches in the implementation of 4D inversion: the uncoupled, coupled and the direct inversion of the difference data (Sarka and Johnston, 2003, Lafet et al., 2008, Anno and Routh, 2007, Buland and EI Ouair, 2006). In order to provide the model updating workflow with the static and dynamic reservoir information in a consistent manner, the coupled scheme is selected. In the coupled scheme, the inverse problem can be formulated as below,

$$d_b = G \cdot m_b + e_b \tag{2.1}$$

$$\Delta_d = d_m - d_b = G \cdot (m_b + \Delta_m) + e_m - d_b, \tag{2.2}$$

where the baseline seismic, monitor seismic and their difference are denoted as d_b, d_m and Δ_d respectively. The elastic parameters such as P-velocity, S-velocity and density models at the baseline are denoted as m_b, while the production-created changes are denoted as Δ_m. G denotes the seismic modelling operator while e_b and e_m are the residual error of the baseline modelling and the cumulative error in calculating of the 4D difference seismic data. Because of the coupling scheme, e_m takes account both e_b and the 4D noise, which can include seismic modelling errors, non-repeatable 4D noise and the change in the wavelet through time. In general, the baseline inversion for m_b provides the volumetric characterisation of the reservoir in a static way, while the inversion for Δ_m, with a baseline of m_b, calculates for consistent dynamic reservoir changes under the given production activities.

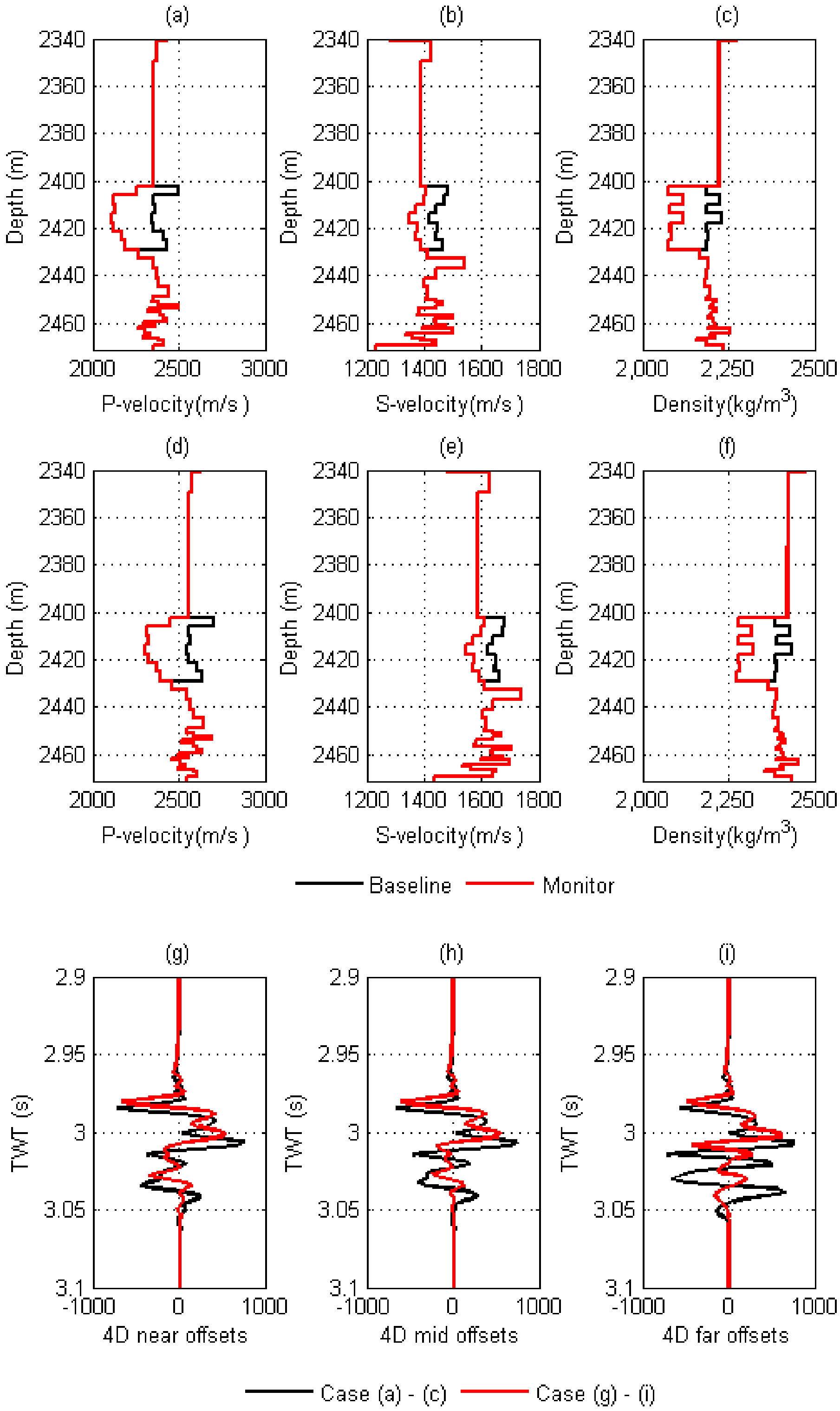

Figure 2.4 *A synthetic test of the impact of the baseline accuracy. (a) to (c) are the P-velocity, S-velocity, density values at the baseline (black) and the monitor (red) time. (d) to (f) represent the other case, in which the base numbers are 10% larger than (a) to (c).*

In a coupled scheme, the accuracy of estimated m_b is important for the inversion of Δ_m. This may be not as critical a problem as that for the uncoupled inversion schemes, because the calculations for different vintages are independent. Figure 2.3 illustrates an example highlighting the importance of a high quality baseline inversion. In the example, another set of 4D elastic models is built (Figure 2.3 (d) to (f)), in which the values at the baseline are 10% higher than those of the original dataset (Figure 2.2 (a) to (c)). However, the 4D differences in P-velocity, S-velocity and density are exactly the same. In other words, the answer to be estimated by seis2sim inversion are the same for both cases. However, after calculating the synthetic 4D amplitudes for the two cases at the near, mid and far offsets (Figure 2.3 (g) to (f)), it is noticed that their 4D seismic responses are very different. Visually, there is a remarkable time-shift at the near and mid offsets, without significant waveform changes. However, at the far angles offset, the 4D differences for the two cases are very different. Therefore, it can be inferred that when the 4D inversion starts the search with an inaccurate baseline estimation, it is almost impossible to find the true answers, because the true difference yields a different 4D seismic response with the wrong baseline. This coupling error can get severe when the baseline inversion gets more and more inaccurate. Figure 2.5

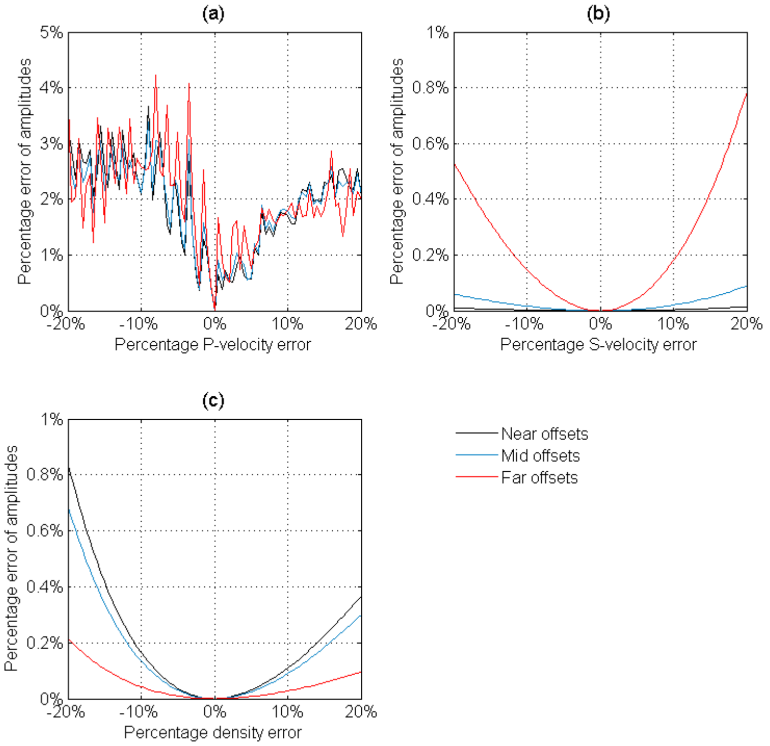

Figure 2.5 *A synthetic test of the impact caused by inaccurate (a) P-velocity, (b) S-velocity and (c) density at near offsets (black), mid offsets (blue) and far offsets (red).*

shows the results of a test for the sensitivity of this error, based on the synthetic data. In the test, the P-velocity, S-velocity and the density of the baseline models are individually altered by between 80% and 120% of their initial values. Constant 4D changes are then given to the different baseline models to calculate the monitors. The new 4D seismic traces are then compared to the original by summing up the L2-norm errors over the trace samples. The L2-norm errors are then normalized by the sum of the squared true 4D amplitudes to show the errors as percentages. In general, the mis-prediction of P-velocity tends to be more sensitive than that of the S-velocity and density, as it controls not only the reflectivity but also the time to depth relationship, as shown in Figure 2.4 (a). The fluctuations in the errors reflect the nature of 4D responses as a composite of time-shift and reflectivity. Nevertheless, the S-velocity error seems less severe than the other two, and it is because of the lack of sensitivity that inversion for the shear wave properties is more difficult during the optimisation/sampling process. In addition, the errors caused by the P and S-velocities are larger at the higher angles, while density shows the opposite trend. This indicates that the density related changes in 4D are better determined in the high angle offsets.

2.3 Bayesian inference for 3D and 4D seis2sim inversion

The Bayesian inference, in which the uncertainties associated with the unknowns are expressed in the form of probability distributions, updates the target model by jointly assessing its posterior probability, given the *a priori* estimations and observed evidence. The underlying theory estimates the posterior distribution of the hypothesis (in our case the values of m_b or Δ_m), given the observation ($d_b$or Δ_d) for baseline or 4D seis2sim inversion respectively, using the combination of prior probability over the hypothesis and the likelihood of the observed data. The posterior distribution is conditional on the relevant evidence, which takes into account both the prior guess of the model without any evidence, and the likelihood, which measures the compatibility of the observed data with the hypothesis. The Bayesian inference suits the proposed inverse problem most by virtue of its flexibility in integrating all available prior knowledge from different disciplines (Tarantola and Valette, 1982; Duijndam, 1988; Ulrych et al., 2001; Scales and Tenorio, 2001). To estimate m_b and Δ_m in Equations 2.1 and 2.2, the inverse problem can be formulated in a Bayesian framework as:

$$p(m_b|d_b) = \frac{L(d_b|m_b)\cdot p(m_b)}{\int L(d_b|m_b)\cdot p(m_b)\mathrm{d}m_b} \propto L(d_b|m_b)\cdot p(m_b) \tag{2.3}$$

$$p(\Delta_m|\Delta_d) = \frac{L(\Delta_d|\Delta_m)\cdot p(\Delta_m)}{\int L(\Delta_d|\Delta_m)\cdot p(\Delta_m)\mathrm{d}\Delta_m} \propto L(\Delta_d|\Delta_m)\cdot p(\Delta_m)\ , \tag{2.4}$$

where $p(m_b|d_b)$ and $p(\Delta_m|\Delta_d)$ are the target posterior probability distributions for the baseline reservoir model and so for the 4D changes, $L(d_b|m_b)\cdot p(m_b)$ and $L(\Delta_d|\Delta_m)\cdot p(\Delta_m)$ are the 3D and 4D joint probability distributions of the random variables of the model ($V_p\ /\Delta V_P$, $V_S/\Delta V_S$ and $\rho/\Delta\rho$ respectively); $L(d_b|m_b)$ and $L(\Delta_d|\Delta_m)$ are the likelihood functions of the model given the observed seismic data and $p(m_b)$ and $p(\Delta_m)$ are the prior distribution of the variables based on the sim2seis predictions. The terms $\int L(d_b|m_b)\cdot p(m_b)\mathrm{d}m_b$ and $\int L(\Delta_d|\Delta_m)\cdot p(\Delta_m)\mathrm{d}\Delta_m$ are normalising constants based on the given inversion problems, known as the marginal densities of m_b and Δ_m. The Bayesian approach is selected to make discrete choices between a set of models with high dimensionality. The solution is dependent on the evidence provided. In this problem, the model vectors comprise of three categories of model, say the P-velocity, S-velocity and density, each of which has a varying dimension based on the reservoir model grid that is penetrated by a given seismic trace. The detailed formulations of the prior terms will be discussed in the later sections with the synthetic examples.

Generally, the inversion of seismic data is complicated, as the relationship between the elastic parameters and the seismic responses is, by nature, nonlinear. It is possible to linearise the problem by assuming a time continuous reflectivity series in the seismic modelling, and perform a linearised inversion (Smith and Gidlow, 1987; Lortzer and Berkhout, 1993). However, the target distributions of Equations (2.3) and (2.4) are intractable and difficult to express analytically in mathematical forms. Therefore, the assistance of stochastic sampling approaches, such as Monte Carlo method and Markov Chain Monte Carlo (MCMC), is considered, to simulate the inversion process and to conclude the posterior distributions from the sample trajectories. Monte Carlo methods approximate the population mean of a given probability distribution by drawing a number of samples randomly from a target distribution. When the samples are independent, the law of large numbers ensures that the approximation is sufficiently accurate when the number of samples is large enough. MCMC is a way to generate such series of samples. With MCMC, the complex posterior distribution of the Bayesian inversion can be constructed implicitly by samples drawn directly from the unknown itself (Mosegaard and Tarantola, 1995; Sen and Stoffa, 1996; Mosegaard, 1998; Eide et al., 2002). The Metropolis-Hastings (M-H) algorithm (Metropolis et al., 1953) and Gibbs sampling (Geman and Geman, 1984) methods are two of the most popular recipes to construct such a Markov chain. The detailed derivation and implementation of the MCMC for inversion are explained in Appendix 1.

2.4 Seis2sim for baseline inversion

As discussed in Equations (2.1) and (2.2), the first step of inverting for the 4D difference is to obtain as accurate a baseline estimation of m_b as possible, where

$$m_b = [v_P, v_S, \rho] \ . \tag{2.5}$$

The modelling for seismic response is based on a weak contrast approximation to the PP reflection, as expressed in the approximation to the full Zoeppritz Equations by Fatti et al. (1994),

$$R(V_P, V_S, \rho, \theta) = (1 + \tan^2\theta) \cdot r_p - 8\bar{\gamma}^2 \cdot \sin^2\theta \cdot r_s + (4\bar{\gamma}^2 \cdot \sin^2\theta - \tan^2\theta) \cdot r_d \tag{2.6}$$

where, θ is the reflection angle, $r_P = \frac{1}{2} \cdot \frac{\Delta I_P}{\overline{I_P}}$, $r_S = \frac{1}{2} \cdot \frac{\Delta I_S}{\overline{I_S}}$, $r_\rho = \frac{1}{2} \cdot \frac{\Delta_\rho}{\bar{\rho}}$, $I_P = v_P \cdot \rho$, $I_S = v_S \cdot \rho$, $\Delta I_P, \Delta I_S$ are the corresponding contrasts of impedance over the interface, $\overline{I_P}$ and $\overline{I_S}$ are the average of the impedances above and below, and $\gamma = \frac{v_P}{v_S}$. Hence, the m_b in Equation (2.5) consists of v_P, v_S and ρ, which are directly sampled from the reservoir model grid as the target model parameters (illustrated in Figure 2.1). In the synthetic example, the 32 layers of the reservoir model, together with two additional layers in the overburden and underburden have formed 102 input parameters for the inversion to determine as statistical combinations.

The prior model $p(m_b)$ of Equation 2.3 for the baseline inversion defines the statistical model of the prior information for v_P, v_S and ρ. The distributions for each are assumed to be multivariate Gaussian and each of their elements is assumed to be independent, representing the statistical randomness of the subsurface geology. Therefore the joint prior probability

$$\begin{aligned} p(m_b) &= p(v_P)\cdot p(v_S)\cdot p(\rho) \\ &= \frac{1}{(2\pi)^{\frac{n}{2}}\left|\Sigma_{v_P}\right|^{\frac{1}{2}}} \exp\left[-\frac{1}{2}\left(v_P-\mu_{v_P}\right)^T\Sigma_{v_p}^{-1}\left(v_P-\mu_{v_P}\right)\right] \\ &\times \frac{1}{(2\pi)^{\frac{n}{2}}\left|\Sigma_{v_S}\right|^{\frac{1}{2}}} \exp\left[-\frac{1}{2}\left(v_S-\mu_{v_S}\right)^T\Sigma_{v_S}^{-1}\left(v_S-\mu_{v_S}\right)\right] \\ &\times \frac{1}{(2\pi)^{\frac{n}{2}}\left|\Sigma_{\rho}\right|^{\frac{1}{2}}} \exp\left[-\frac{1}{2}\left(\rho-\mu_{\rho}\right)^T\Sigma_{\rho}^{-1}\left(\rho-\mu_{\rho}\right)\right], \end{aligned} \tag{2.7}$$

where μ_{v_P}, μ_{v_S} and μ_ρ are the corresponding means of sim2seis predictions and Σ_{v_P}, Σ_{v_S} and Σ_ρ are the covariance matrices. Since v_P, v_S and ρ are assumed independent, $v_P^1, v_P^2, \dots, v_P^{32}$, $v_S^1, v_S^2, \dots, v_S^{32}$ and $v_\rho^1, v_\rho^2, \dots, v_\rho^{32}$ in the synthetic example are not correlated. Therefore, the Σ_{v_P}, Σ_{v_S} and Σ_ρ are simplified to diagonal matrices in which the elements are the positive defined variance and zeros. Thus covariance matrices not only capture the variation range of the solutions from the prior background models but also the uncertainties observed in any prior knowledge.

Given a zero mean Gaussian noise $e_b \sim \mathrm{N}(0, \sigma_{\mathrm{e_b}})$, the likelihood function $L(d_b|m_b)$ in Equation (2.3) is assessed by,

$$L(d_b|m_b) = \frac{1}{\left(2\pi\sigma_{e_b}^2\right)^{\frac{n}{2}}} \exp\left[-\sum\frac{\left(d_b-d_{\mathrm{syn}}\right)^2}{2\sigma_{e_b}^2}\right], \tag{2.8}$$

where d_b is the observed baseline seismic vector, d_{syn} is the synthetic seismic vector calculated based on m_b. The misfits between them are summed up over all trace samples. In the synthetic example, three synthetic stacks are calculated at different offsets. In order to obtain the posterior probability distribution of $p(m_b|\, d_b)$, the Markov chain is generated using the Metropolis-Hastings sampling method, and the proposal is a uniform distribution defined as,

$$q(m_i, m^*) \sim U(m_i - \Delta, m_i + \Delta), \tag{2.9}$$

where m_i represents the current combination of v_P, v_S, ρ, and m^* represents the next possible combination of v_P^*, v_S^*, ρ^*. Δ is determined adaptively, according to the acceptance ratio of the current performance of the Markov chain, using the scheme proposed by Corana (1987) to help the convergence rate. Hence, the transition probability from m_i to m^* is,

$$\begin{aligned} a(m_i, m^*) &= \min\left\{1, \frac{L(d_b|m^*) \cdot p(m^*) \cdot q(m^*, m_i)}{L(d_b|m_i) \cdot p(m_i) \cdot q(m_i, m^*)}\right\} \\ &= \min\left\{1, \frac{L(d_b|m^*) \cdot p(m^*)}{L(d_b|m_i) \cdot p(m_i)}\right\} \end{aligned} \tag{2.10}$$

and samples generated after the simulation reaches a detailed balance can be used to infer the posterior probability distribution of the target parameters of v_P, v_S and ρ at the baseline time. (See Appendix 1 for details of MCMC). Once the posterior samples are simulated, any features of the posterior distribution, such as moments and the highest posterior density solutions, are in accordance with Bayesian inference,. Indeed, all the posterior samples are equally probable and analysing the variances among them leads to uncertainty. The inversion of the synthetic dataset is conducted in the procedure below:

- Initialize the $m_b = m_{initial}$
- Repeat:
  1. Adaptively adjust Δ according to the current acceptance ratio.
  2. Choose a random element from $m_{initial}$.
  3. Propose m^* by applying a perturbation Δ to $m_{initial}$.
  4. Calculate the reflectivity by the approximated Zoeppritz Equation.
  5. Convert the reflectivity series to the time domain, according to the current velocity values.
  6. Calculate the synthetic seismic response d_{syn} at different angles.
  7. Calculate $a(m_{\text{initial}}, m^*)$ by assessing the cost function.
  8. Sample u from a uniform distribution $U\sim(0,1)$.
  9. If $u \leq a(m_{\text{initial}}, m^*)$, accept m^* and set $m_{\text{initial}} = m^*$; otherwise set $m_{\text{initial}} = m_{\text{initial}}$.
  10. Check the convergence diagnostic.
- Analyse the results.

In practice, three angle stacks are calculated by the Zoeppritz Equation. The near offset stack is equivalent to the gathers with incident angles from 0° to 10°, the mid offset stack is equivalent to the gathers with incident angles from 10° to 20° and the far offset stack is equivalent to the gathers with incident angles from 20° to 30°. To reduce the computational load, the reflectivity traces are generated every 5°, which means nine traces of reflectivity are generated in each iteration, before being stacked together and convolved with the wavelet. When the Markov chain converges (see Appendix 1 for details about the convergence diagnostic), 50 realisations are kept to reconstruct the posterior probability distribution. The realisations are selected from those in which the auto- correlation is lower than 0.3, to ensure the representation of the posterior probability distribution.

Inversion of the synthetic dataset converges quickly after 1,000 iterations, and the 1-D results are shown in Figure 2.5. The posterior mean values (thick red lines) of v_P, v_S and ρ are equal to the maximum *a posteriori* solution, according to the Gaussian assumption (Buland, 2002). The *a posteriori* solution is generally smoother than a single realisation. Theoretically, when the noise level σ_b increases, the solution converges to the *a priori* predictions as the confidence in the observed data drops. The largest uncertainty is found in the overburden cells (Layer 1), because their thicknesses are much bigger than the ones beneath, therefore their velocity values dominate the synthetic seismic more than the other cells. The thick cells with heights between 4m and 5m are also subject to larger uncertainties than the thinner ones in the underburden. This is possibly because the resolutions of these cells are not fine enough to provide the details in the high resolution seismic, while the finer ones lead to a better match to the observation. Nevertheless, the S-wave velocity is least determined, as its uncertainty range is much higher than the P-wave velocity and density after inversion. The match to the different angle stacks is controlled by the individual SNR, where the preset noise level is actually realistic to represent the origin of this example.

Figure 2.6 summarises the statistical results of the inversion by looking into one sample selected at the reservoir depth. The trajectory plotted in (a) to (c) are the evolutions ofv_P, v_S and ρ throughout the iterations. According to the misfit plotted in (g), the

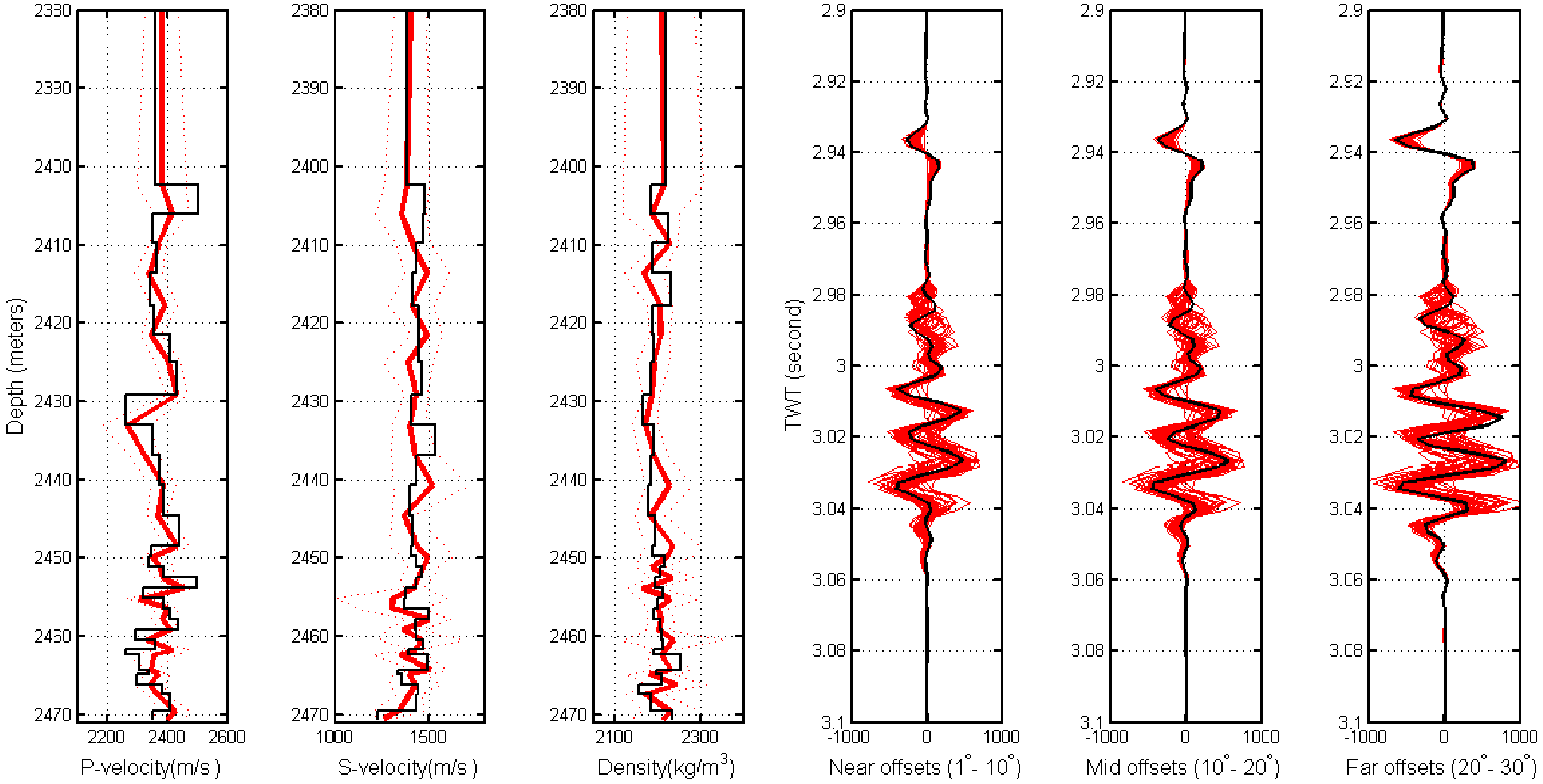

Figure 2.6 *The inversion results for the baseline calculated. The blocky black lines represent the true answer in the model, and the black traces are the "observed" input seismic observations. The thick red line represents the posterior mean from the MCMC simulation, while the dashed lines depict the 0.95 uncertainty range. The red traces on the right are the realisations of the synthetic seismic.*

convergence is achieved shortly after the first 2,000 iterations, when the random search for probable v_P, v_S and ρ starts to converge to about 2365 m/s, 1425 m/s and 2280 kg/m^3 respectively. A comparison of the 0.95 confidence regions between the prior and the posterior models depicts the information in the seismic data. The standard deviation of P-wave velocity is reduced from 300 m/s to about 40 m/s after seis2sim, indicating a 85% reduction of the uncertainty, as shown in (d). The same measurements for S-wave velocity and density are 73% and 81% respectively ((e) and (f)). The S-wave velocity could be better determined when the v_P/v_S ratio is higher, which corresponds to a higher AVO sensitivity in the far offset stacks. With particular concern regarding the impact to the 4D inversion, the baseline inversion quality is examined in Figure 2.7,

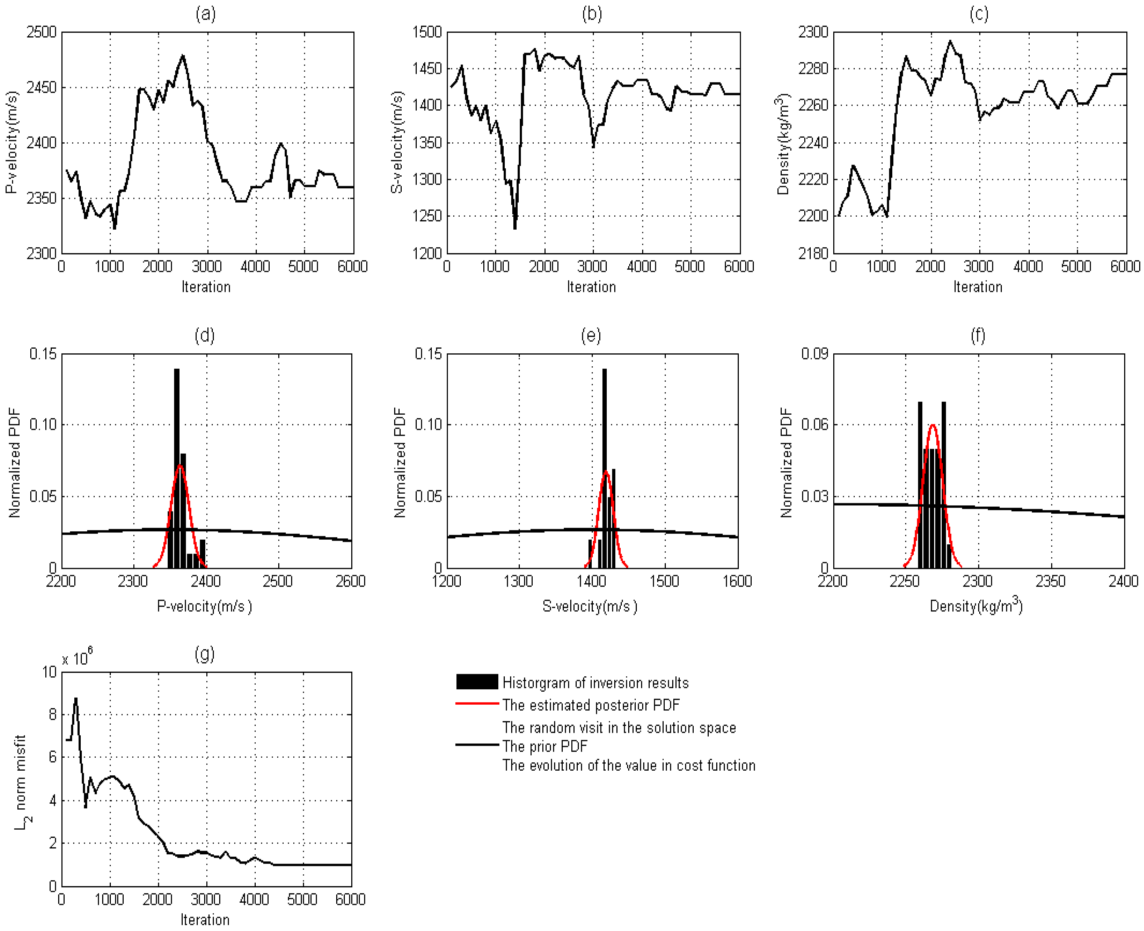

Figure 2.7 *The plots of the baseline statistical results from a selected cell at the reservoir level. (a) the evolution of the P-velocity, (b) the evolution of the S-velocity, (c) the evolution of the density changes; (d) to (f) are the posterior (red) and prior (black) distribution of the seis2sim results of P-velocity, S-velocity and 4D density respectively; (g) the cost function values in each iteration.*

by cumulatively summing up the $L_2 -$ norm misfits in time. The errors of the posterior mean v_P, v_S and ρ at the near, mid and far angle stacks are plotted in (a), (b) and (c) respectively. In between the two dashed dark lines, the 4D signal may not be visible if the residual error of the baseline is too severe. At all angles, the first peaks in the errors arise at the interface of the overburden cells at 2.94 seconds, due to the large uncertainties discussed above. Inside the reservoir interval, the amplitude errors accumulate slowly in the near and mid offsets, but increase dramatically in the far offsets. As previously discussed, the far angles could be better inverted when the AVO effect is more prominent. According to Equations (2.1) and (2.2), this error will be propagated to the 4D inversion as an additional source of noise, together with noise in the 4D dataset, due to the non-repeatability.

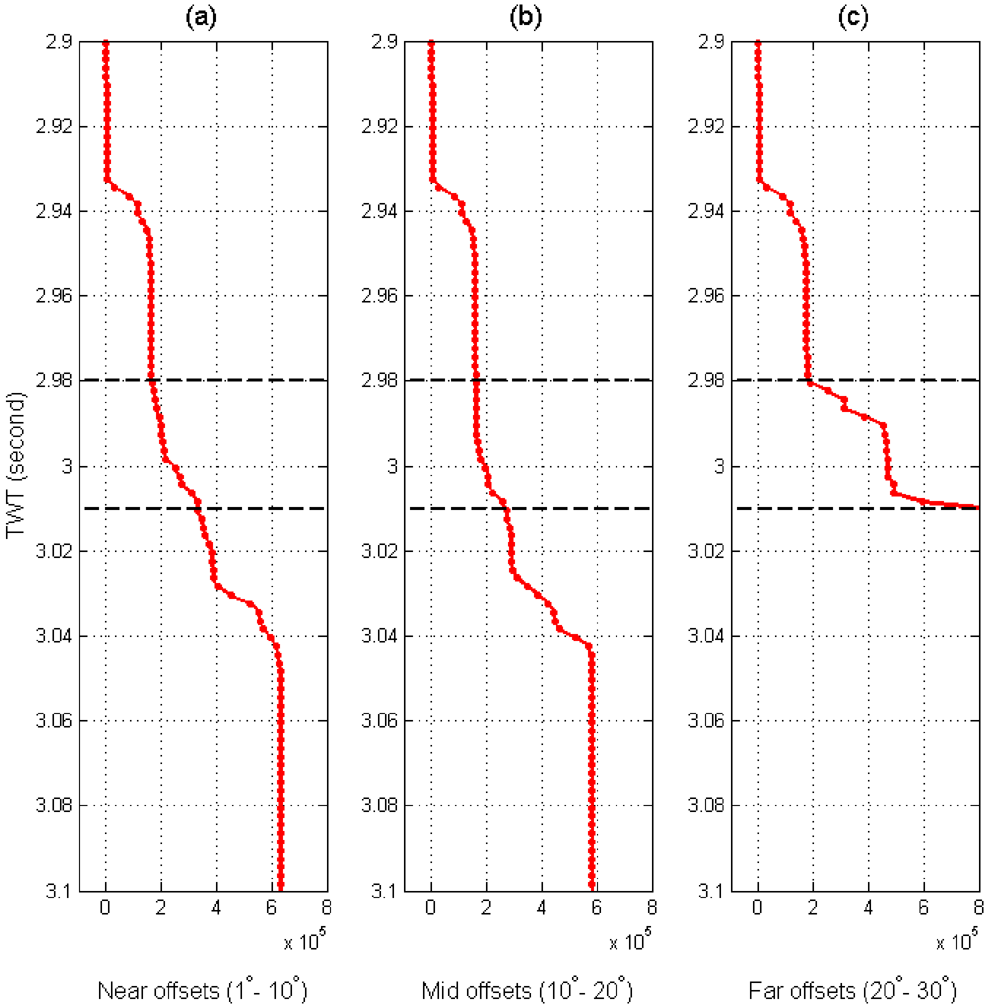

Figure 2.8 *The cumulative amplitude errors (x-axis) of baseline seis2sim as a function of TWT for (a) near offsets, (b) mid offsets, and (c) far offsets. The two dashed dark lines mark the top and base of the reservoir interval.*

2.5 4D seis2sim inversion

In contrast to the uncoupled and direct inversion of the 4D data, the coupled scheme could avoid a number of problems. Firstly, the Zoeppritz Equation cannot directly handle the negative 4D changes of absolute quantity. To address this, we to use indirect forms, such as the ratio between $m_{\text{monitor}}/m_{\text{baseline}}$ to represent the relative changes (Buland and EI Ouair, 2006). The potential risk of doing so is the lack of baseline background. Given a constant percentage of elastic changes, different baseline solutions lead to variant 4D seismic observations (see the examples in Figure 2.3 and Figure 2.4). Secondly, the 4D amplitude difference, which is usually generated by subtracting the baseline seismic from the monitor seismic, is responding to both the time-shift and reflectivity. Inverting such data in the time domain does not provide a solution to segregate them, because the TWTs of the input parameters, such as v_P, v_S and ρ, are usually fixed during calculation. Therefore all the visual amplitude differences are regarded as responses to reflectivity changes. Inversion in such a scheme, without careful constraints, will lead to artificial solutions. With the coupled scheme proposed in Equation (2.2), the inversion could not only provide a reliable baseline solution for static reservoir characterisation, but also relay the consistent 4D changes in the reservoir model domain.

2.5.1 The 4D data uncertainty

The first requirement for the 4D inversion is to understand the quality of the data. As discussed previously, the 4D noise can be sourced from a number of measurements and processes. In Equation (2.2), e_m denotes the total data uncertainty, which can be expanded as,

$$e_m = e_{\text{residual}} + e_{\text{data}} \tag{2.11}$$

where e_{residual} is the residual misfit from the baseline inversion, representing the error in coupling. The distribution of errors in the different offset stacks are separately recorded for the synthetic example, in which $e_{\text{near}} \sim N(0{,}96)$, $e_{\text{mid}} \sim N(0{,}91)$, and $e_{\text{near}} \sim N(0{,}187)$ as shown in Figure 2.8. e_{data} measures the data noise caused by processing or any other kind of non-repeatability, and is estimated from the overburden area, where the 4D changes are assumed to be negligible. In the synthetic example, $e_{\text{data}} = 0$, but in the later chapters, examples are given to quantitatively integrate it into the inversion.

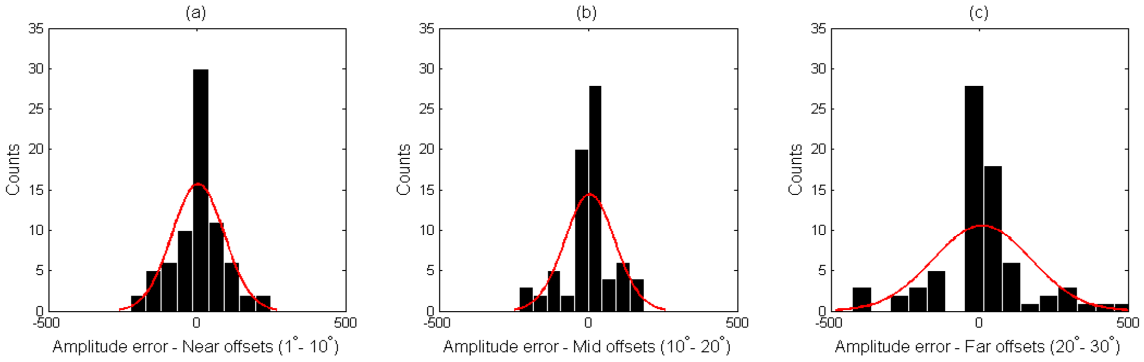

Figure 2.9 *The distributions of the 3D residual errors in terms of seismic amplitudes, at (a) the near offsets, (b)the mid offsets, and (c) the far offsets.*

The 4D detectability is essentially all about the competition between signal and noise; therefore, the 4D inversion needs to incorporate these inherent errors as part of the data uncertainty, also. For a more visual understanding of the 4D noise level in the example, the residual errors of amplitudes generated by the posterior mean solution are plotted, with the 4D difference data in Figure 2.9. The standard deviations of the red and black traces represent the strength of 3D residual errors and the 4D signals respectively. The $\mathrm{SNR} = \frac{\sigma(\Delta_{\mathrm{d}})}{\sigma(\Delta_{\mathrm{d}} - e_{\mathrm{residual}})}$ for the near offsets, mid offsets and far offsets are 2.88, 2.74 and 1.39 respectively. When the SNR approaches unity, the signal itself cannot stand out and the inversion can converge with large uncertainty. Hence the 4D inversion at the far angle offsets needs more prior information to help the convergence and additional constraints are required to be present in the prior model.

2.5.2 Constructing the 4D constraints

As discussed in the previous section, reservoir engineering activities are in fact the cause of the observed 4D seismic signal. Therefore, it is a natural choice to refer to the reservoir simulation for additional information. A reservoir simulator honours reservoir engineering laws in predicting the fluid evolution and the pressure distributions in a complete time series, while time-lapse seismic captures only a limited number of snapshots over the field at some particular points in time. Therefore, what the reservoir engineering tool can provide is the time-continuous patterns of reservoir changes under given production mechanisms. The patterns can be used to fill the information gaps between time lapse seismic surveys as they are the results of the similarities in lithology, connectivity, and production activities, and ideally, similar

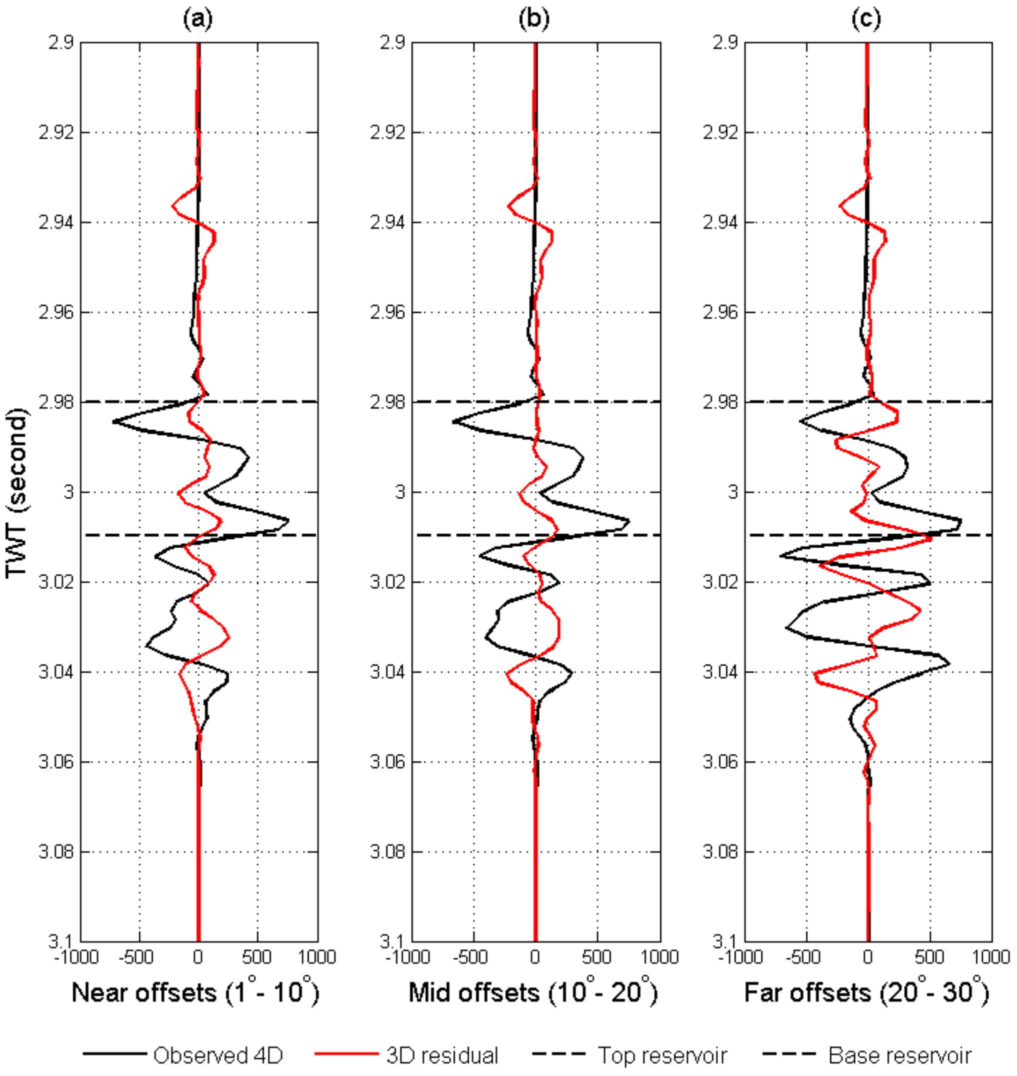

Figure 2.10 *The comparison between the 3D inversion residuals and the 4D amplitudes at (a) near offsets, (b) mid offsets and (c) the far offsets.*

reservoir rocks close to each other will share similar elastic responses given the same production triggers. These elastic changes can be simulated by sim2seis modelling programs (Amini, 2014), which convert the simulated pressure and saturation fields into elastic property fields, at any time during the simulation. The benefit of doing such modelling is to derive the patterns discussed above, in order to group different parts of the reservoir by correlating the patterns in both space and time domains. Huang et al. (2012) have applied this philosophy to the frequently acquired time-lapse seismic data to investigate the connectivity between different reservoir compartments. It is believed the way this time-lapse information is extracted is also

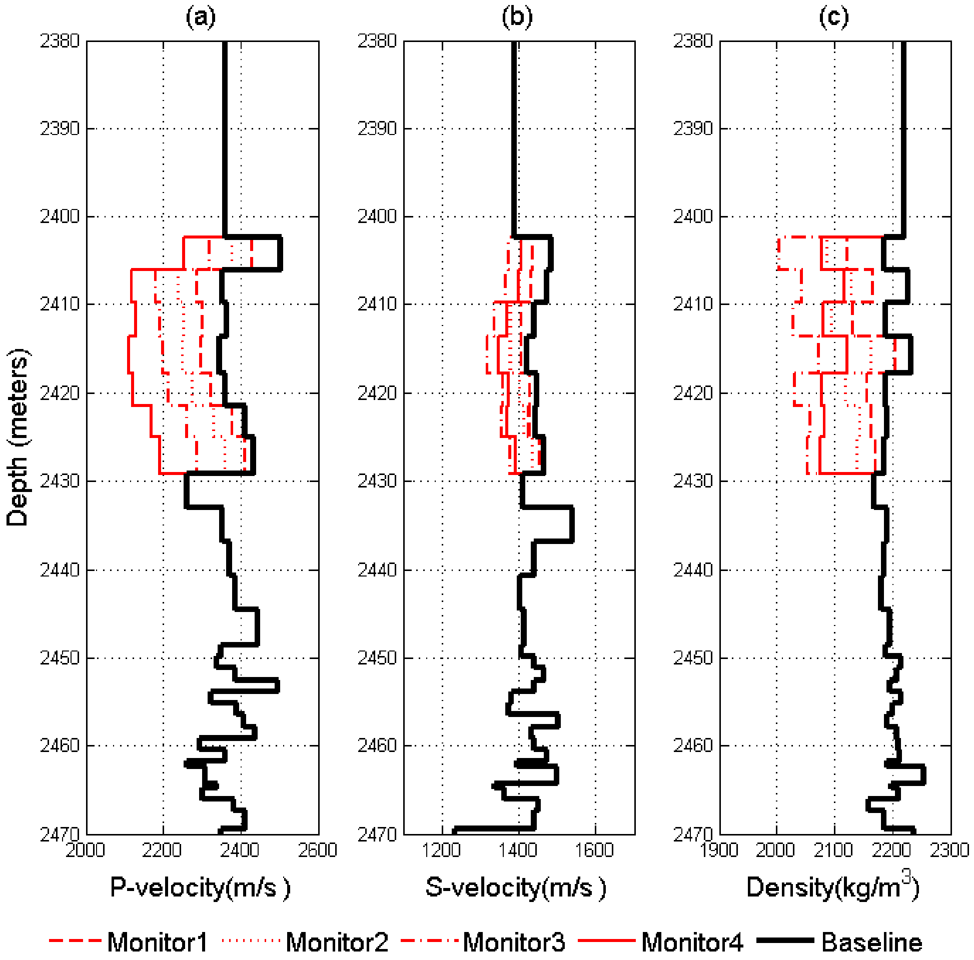

Figure 2.11 *Intermediate scenarios of (a) P-velocity, (b) S-velocity and (c) density for the synthetic example, with which the constraints are derived.*

applicable in the seis2sim domain. The correlations derived from these patterns are beneficial for the inversion, as they implicitly capture the reservoir engineering consistent geology layering, reservoir activity and the production responses. The correlation is capable of stabilising the seis2sim inversion in looking for the reservoir engineering consistent solutions in the joint domain.

Three time lapse snapshots of elastic properties, m'_1, m'_2 and m'_3, are added to the initial sim2seis prediction of 4D pair m'_b and $m'_4$to serve as the intermediate results between the baseline state m'_b and the final state m'_4 (Figure 2.10). These models are created based on the conceptual scenario of gas injection. As a result, the predicted v'_P in m'_1,

m_2', m_3' and m_4' are reduced progressively, while the predicted value of v_S' and ρ' reduces in m_1', m_2' and m_3', but increases at the final monitoring time m_4'.

Practically, the predicted elastic difference Δ_{v_P}', Δ_{v_S}' and Δ_{ρ}' of the 32 cells of the reservoir model at all available time steps m_1', m_2', m_3' and m_4' can be written as

$$\Delta_{v_P}' = \begin{bmatrix} \Delta_{v_P}^{m_b}(1) & \Delta_{v_P}^{m_1}(1) & \cdots & \Delta_{v_P}^{m_4}(1) \\ \Delta_{v_P}^{m_b}(2) & \Delta_{v_P}^{m_1}(2) & \cdots & \Delta_{v_P}^{m_4}(2) \\ \vdots & \vdots & \vdots & \vdots \\ \Delta_{v_P}^{m_b}(32) & \Delta_{v_P}^{m_1}(32) & \cdots & \Delta_{v_P}^{m_4}(32) \end{bmatrix} \tag{2.12}$$

$$\Delta_{v_S}' = \begin{bmatrix} \Delta_{v_S}^{m_b}(1) & \Delta_{v_S}^{m_1}(1) & \cdots & \Delta_{v_S}^{m_4}(1) \\ \Delta_{v_S}^{m_b}(2) & \Delta_{v_S}^{m_1}(2) & \cdots & \Delta_{v_S}^{m_4}(2) \\ \vdots & \vdots & \vdots & \vdots \\ \Delta_{v_S}^{m_b}(32) & \Delta_{v_S}^{m_1}(32) & \cdots & \Delta_{v_S}^{m_4}(32) \end{bmatrix} \tag{2.13}$$

$$\Delta_{\rho}' = \begin{bmatrix} \Delta_{\rho}^{m_b}(1) & \Delta_{\rho}^{m_1}(1) & \cdots & \Delta_{\rho}^{m_4}(1) \\ \Delta_{\rho}^{m_b}(2) & \Delta_{\rho}^{m_1}(2) & \cdots & \Delta_{\rho}^{m_4}(2) \\ \vdots & \vdots & \vdots & \vdots \\ \Delta_{\rho}^{m_b}(32) & \Delta_{\rho}^{m_1}(32) & \cdots & \Delta_{\rho}^{m_4}(32) \end{bmatrix}. \tag{2.14}$$

The evolution of m_1', m_2', m_3' and m_4' can be plotted against the time steps in Figure 2.11, in which the time-lapse patterns of the active cells are shown in (a), (c) and (e), while the inactive cells (non-reservoir) are shown in (b), (d) and (f). Since the activation of reservoir model cells is decided according to the interpretation of the stratigraphy, fluid and pressure changes are supposed to take place only inside the active cells. Hence the active part of the reservoir will stand out from the inactive ones, showing ever-changing profiles. In contrast, the inactive parts of the reservoir stay idle and cannot correlate to the active ones. To transform this information into a statistic, the covariance matrices of their 4D differences are calculated. Therefore Equations (2.12) to (2.14) can be compactly written as

$$\Delta_{v_P}' = [\Delta_{v_P}^{*}(1), \dots, \Delta_{v_P}^{*}(32)]^T \tag{2.15}$$

$$\Delta_{v_S}' = [\Delta_{v_S}^{*}(1), \dots, \Delta_{v_S}^{*}(32)]^T \tag{2.16}$$

$$\Delta_{\rho}' = [\Delta_{\rho}^{*}(1), \dots, \Delta_{\rho}^{*}(32)]^T, \tag{2.17}$$

from which the covariance matrices $\Sigma_{\Delta_{v_P}}$, $\Sigma_{\Delta_{v_S}}$ and Σ_{Δ_ρ} can be written as

$$\Sigma_{\Delta_{v_P}} = \begin{bmatrix} \mathrm{Cov}(\Delta^*_{v_P}(1),\Delta^*_{v_P}(1)) & \cdots & \mathrm{Cov}(\Delta^*_{v_P}(1),\Delta^*_{v_P}(32)) \\ \vdots & \ddots & \vdots \\ \mathrm{Cov}(\Delta^*_{v_P}(32),\Delta^*_{v_P}(1)) & \cdots & \mathrm{Cov}(\Delta^*_{v_P}(32),\Delta^*_{v_P}(32)) \end{bmatrix} \tag{2.18}$$

$$\Sigma_{\Delta_{v_S}} = \begin{bmatrix} \mathrm{Cov}(\Delta^*_{v_S}(1),\Delta^*_{v_S}(1)) & \cdots & \mathrm{Cov}(\Delta^*_{v_S}(1),\Delta^*_{v_S}(32)) \\ \vdots & \ddots & \vdots \\ \mathrm{Cov}(\Delta^*_{v_S}(32),\Delta^*_{v_S}(1)) & \cdots & \mathrm{Cov}(\Delta^*_{v_S}(32),\Delta^*_{v_S}(32)) \end{bmatrix} \tag{2.19}$$

$$\Sigma_{\Delta_\rho} = \begin{bmatrix} \mathrm{Cov}(\Delta^*_{\rho}(1),\Delta^*_{\rho}(1)) & \cdots & \mathrm{Cov}(\Delta^*_{\rho}(1),\Delta^*_{\rho}(32)) \\ \vdots & \ddots & \vdots \\ \mathrm{Cov}(\Delta^*_{\rho}(32),\Delta^*_{\rho}(1)) & \cdots & \mathrm{Cov}(\Delta^*_{\rho}(32),\Delta^*_{\rho}(32)) \end{bmatrix}, \tag{2.20}$$

where the diagonal elements of the matrices are in fact the variance of the cells themselves, and the off-diagonal members are symmetric and show how similar the patterns are over different cells, vertically. In the synthetic example, the covariance matrices are shown in Figure 2.12 (a), (c) and (e).

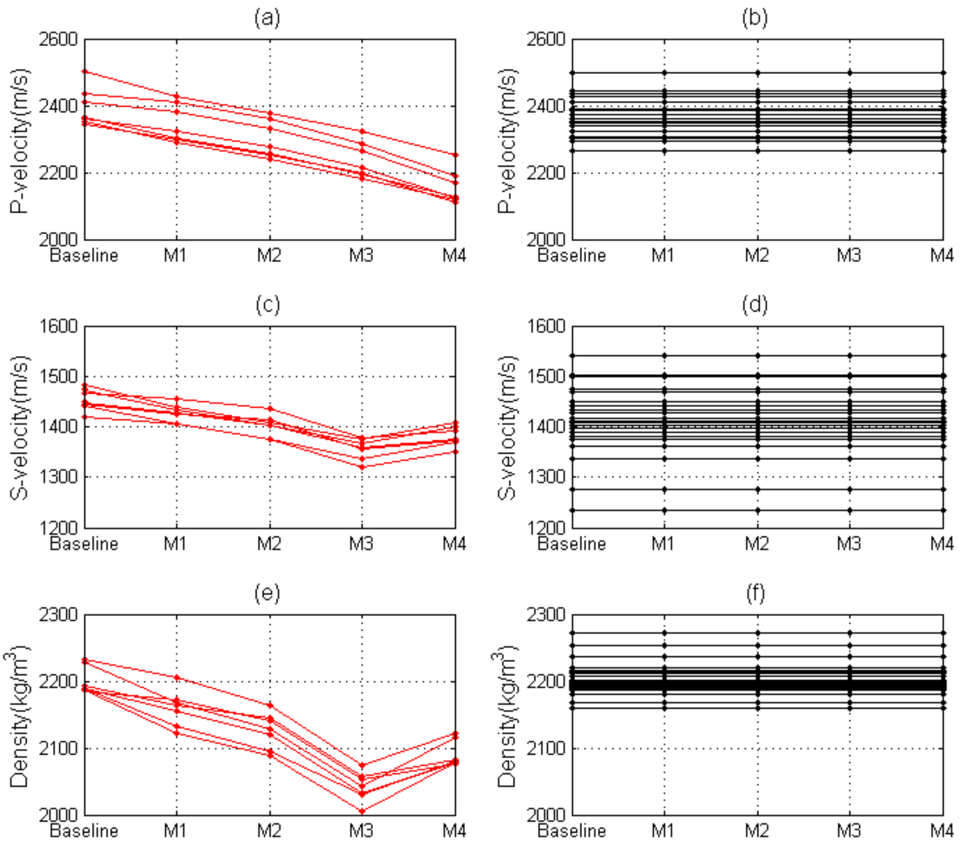

Figure 2.12 *The values of P-velocity, S-velocity and the density at different monitoring steps, assumed as the results of predictions by the sim2seis calculation; (a), (c) and (e) are the active reservoir cells while (b), (d) and (f) are the inactive ones.*

The covariances not only reflect the expected level of changes, but also implicitly show the similarities over different cells, because the neighbouring cells share a similar range of change. Furthermore, the correlation coefficients displayed in Figure 2.11 (b), (d) and (f), which are the normalised version of the covariance, show more direct information about the vertical connectivity, compared with the covariance matrices. In the data, layers 4 to 10 are defined as active, and therefore a patch of high correlation presents in

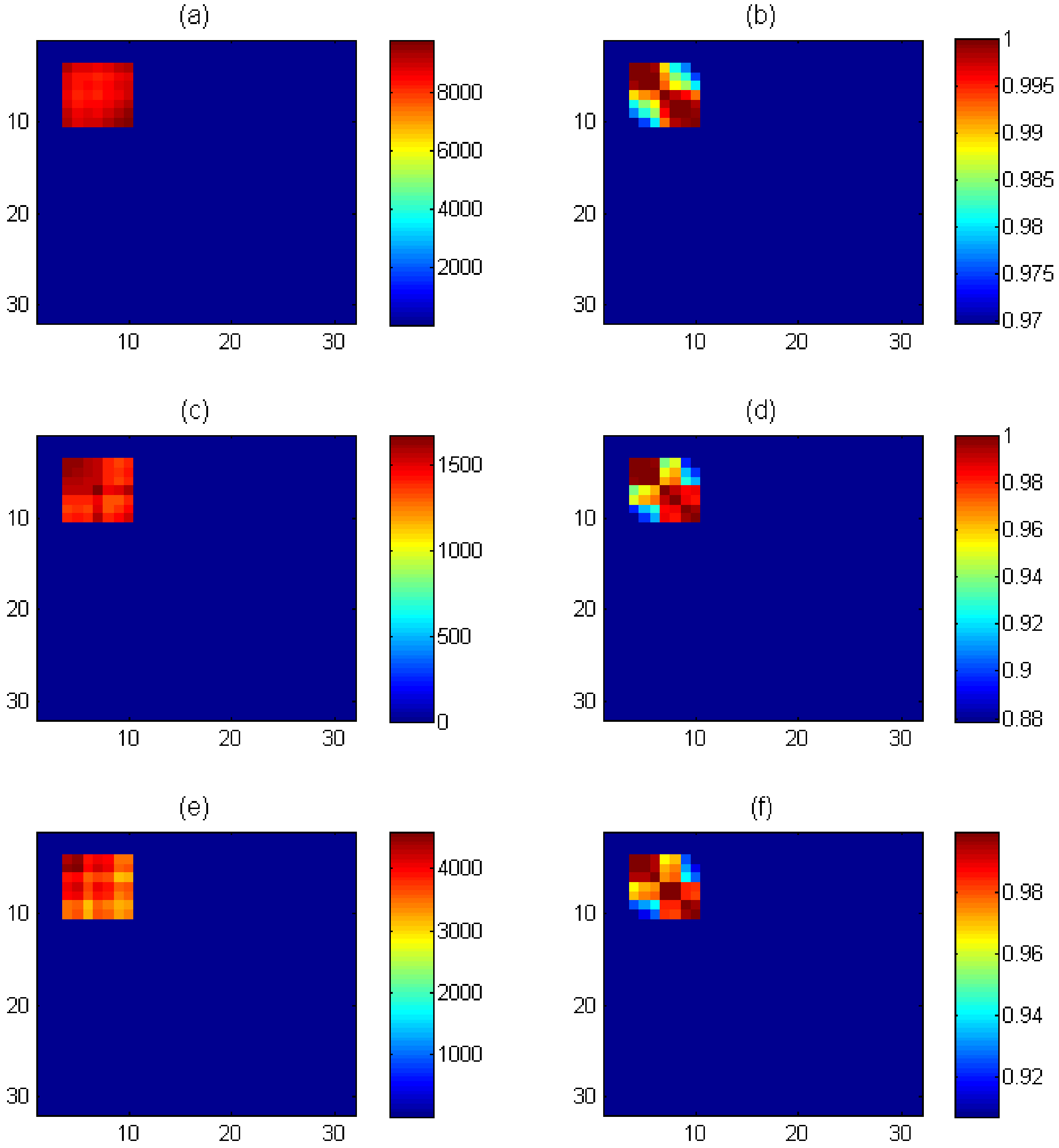

Figure 2.13 *The covariance matrices of the model prediction in terms of (a) 4D P-velocity, (c) 4D S-velocity and (e) 4D density, in contrast to the correlation coefficients in (b), (d) and (f).*

the upper left corner, which immediately stops at the eleventh member, indicating the change from reservoir to non-reservoir.

2.5.3 The Bayesian 4D seis2sim inversion

Similar to the 3D formulas, the 4D difference Δ_m to be inverted is defined as,

$$\Delta_m = [\Delta_{v_P}, \Delta_{v_S}, \Delta_\rho] \tag{2.21}$$

With such engineering-consistent information, the multivariate prior model for the 4D Bayesian inversion can be written as

$$\begin{aligned} p(\Delta_m) &= p(\Delta_{v_P}) \cdot p(\Delta_{v_S}) \cdot p(\Delta_\rho) \\ &= \frac{1}{(2\pi)^{\frac{n}{2}} \left|\Sigma_{\Delta_{v_P}}\right|^{\frac{1}{2}}} \exp\left[-\frac{1}{2}\left(\Delta_{v_P} - \mu_{\Delta_{v_P}}\right)^T \Sigma_{\Delta_{v_P}}^{-1} \left(\Delta_{v_P} - \mu_{\Delta_{v_P}}\right)\right] \\ &\times \frac{1}{(2\pi)^{\frac{n}{2}} \left|\Sigma_{\Delta_{v_S}}\right|^{\frac{1}{2}}} \exp\left[-\frac{1}{2}\left(\Delta_{v_S} - \mu_{\Delta_{v_S}}\right)^T \Sigma_{\Delta_{v_S}}^{-1} \left(\Delta_{v_S} - \mu_{\Delta_{v_S}}\right)\right] \\ &\times \frac{1}{(2\pi)^{\frac{n}{2}} \left|\Sigma_{\Delta_\rho}\right|^{\frac{1}{2}}} \exp\left[-\frac{1}{2}\left(\Delta_\rho - \mu_{\Delta_\rho}\right)^T \Sigma_{\Delta_\rho}^{-1} \left(\Delta_\rho - \mu_{\Delta_\rho}\right)\right] \end{aligned} \tag{2.22}$$

where $\mu_{\Delta_{v_P}}$, $\mu_{\Delta_{v_S}}$ and μ_{Δ_ρ} are the *a priori* means of the 4D changes and $\Sigma_{\Delta_{v_P}}$, $\Sigma_{\Delta_{v_S}}$ and Σ_{Δ_ρ} are the covariance matrices calculated. Since $\Delta_{v_P}, \Delta_{v_S}$ and Δ_ρ, unlike the baseline prior model, are assumed correlated and calculated according to Equations (2.12) to (2.20). $\left|\Sigma_{\Delta_{v_P}}\right|$, $\left|\Sigma_{\Delta_{v_S}}\right|$ and $\left|\Sigma_{\Delta_\rho}\right|$ are the determinants of the matrices. In the 4D inversion, the likelihood function is

$$L(\Delta_d|\Delta_m) = \frac{1}{(2\pi\sigma_{e_m}^2)^{\frac{n}{2}}} \exp\left[-\sum \frac{\left(\Delta_d - \Delta_{d_{\mathrm{syn}}}\right)^2}{2\sigma_{e_m}^2}\right], \tag{2.23}$$

where Δ_d is the vector of the observed 4D seismic difference between the baseline and monitor; $\Delta_{d_{\mathrm{syn}}}$ is the vector of synthetic 4D seismic difference caused by $\Delta_{v_P}, \Delta_{v_S}$ and Δ_ρ, based on the synthetic baseline of the posterior mean solution from baseline seis2sim (see d_{syn} in Equation (2.8)); e_m is the uncertainty in the data, which has been discussed above and defined in Equation (2.11). In order to obtain the posterior probability distribution defined in Equation (2.4), the same MCMC and M-H approach is used, and the proposal function is uniformly distributed as

$$q\left(\Delta_{m_i}, \Delta_m^*\right) \sim U\left(\Delta_{m_i} - \Delta, \Delta_{m_i} + \Delta\right), \tag{2.22}$$

where Δ_{m_i} represents the current combination of $\Delta_{v_P}, \Delta_{v_S}, \Delta_\rho$; Δ_m^* represents the next possible combination of $\Delta_{v_P}^*, \Delta_{v_S}^*$ and Δ_ρ^*. Δ is again determined and adapted according to the acceptance ratio of the current performance of the Markov chain. In addition, the transition probability from Δ_{m_i} to Δ_m^* is

$$\begin{aligned} a\left(\Delta_{m_i}, \Delta_m^*\right) &= \min\left\{1, \frac{L(\Delta d|\Delta_m^*) \cdot p(\Delta_m^*) \cdot q(\Delta_m^*, \Delta_{m_i})}{L\left(\Delta d\middle|\Delta_{m_i}\right) \cdot p\left(\Delta_{m_i}\right) \cdot q(\Delta_{m_i}, \Delta_m^*)}\right\} \\ &= \min\left\{1, \frac{L(\Delta d|\Delta_m^*) \cdot p(\Delta_m^*)}{L\left(\Delta d\middle|\Delta_{m_i}\right) \cdot p\left(\Delta_{m_i}\right)}\right\}. \end{aligned} \tag{2.24}$$

The inversion for the engineering consistent 4D solution is carried out in a similar way to the baseline, with these exceptions:

- Initialise the $\Delta_m = \Delta_{m_\mathrm{i}}$, $m_{\text{monitor}} = m_{\text{baseline}}$
- Repeat:
  1. Adaptively adjust Δ according to the current acceptance ratio.
  2. Choose a random element from m_{monitor}.
  3. Propose Δ_m^* according to the distribution $q\left(\Delta_{m_i}, \Delta_m^*\right)$.
  4. Calculate the reflectivity of $m_{\text{monitor}}^* = m_{\text{monitor}} + \Delta_m^*$ by the Zoeppritz Equation.
  5. Convert the reflectivity series to time domain according to the current velocity values.
  6. Calculate the synthetic 4D seismic response $\Delta_{d_{\text{syn}}} = d_{m_{\text{syn}}}^* - d_{b_{\text{syn}}}$ at different angles.
  7. Calculate $a(\Delta_{m_i}, \Delta_m^*)$ by assessing the cost function.
  8. Sample u from a uniform distribution $U \sim (0,1)$.

9. If $u \leq a(\Delta_{m_i}, \Delta_m^*)$, accept Δ_m^* and set $\Delta_{m_\mathrm{i}} = \Delta_m^*$, $m_\mathrm{monitor} = m_\mathrm{monitor}^*$; otherwise set $\Delta_{m_\mathrm{i}} = \Delta_{m_\mathrm{i}}$, $m_\mathrm{monitor} = m_\mathrm{monitor}$.
10. Convergence diagnostic.

- Analyse the results.

In the synthetic example, the same sets of angle stacks are calculated to infer the 4D changes at the near, mid and far offsets. In addition, a benchmark is designed to compare the results with and without the engineering constraints. The unconstrained inversion has uniform prior models with a large searching range, in which $\Delta_{v_P}, \Delta_{v_S}, \Delta_\rho$ are assumed to be independent. In other words, no correlations are specified to segregate the reservoir from the non-reservoir. In addition, the data uncertainty e_m is set to smaller values, to make the 4D SNR at the near, mid and far offsets equal to 6, which is the same level as the baseline inversion, while the EC inversion has the SNR discussed earlier. The results of the unconstrained inversion are shown in Figure 2.13, in contrast to the EC constrained results in Figure 2.14.

Because of a high level of confidence in the data, the unconstrained inversion matches the observed 4D difference very well (Figure 2.13 (a), (b) and (c)). Particularly, the 4D amplitudes within the reservoir interval (between the dashed lines) are resolved with few residual errors. However, the inverted $\Delta_{v_P}, \Delta_{v_S}, \Delta_\rho$ in Figure 2.13 (d), (e) and (f) are very different from the true solution (thick black lines). Visually, the solutions have artificial changes in the overburden and underburden, which are both assumed inactive. Nevertheless, the inverted 4D changes inside the reservoir interval are featured with unrealistic seismic-like trends. This problem is extremely severe for Δ_{v_S}, where the inverted changes are oscillatory, with a wider uncertainty range compared with the other two properties.

Figure 2.14 shows the EC constrained seis2sim results. With a larger uncertainty in the data (SNR is equal to 2.88, 2.74 and 1.39 at near, mid and far offsets), the inversion matches the observed data less rigorously than the unconstrained results. This tolerance is much bigger in the underburden of the far angle stacks, because of the large residual errors from the baseline inversion. In fact, none of the amplitude differences outside the reservoir interval are genuine 4D signals, as explained earlier. The match to these time-

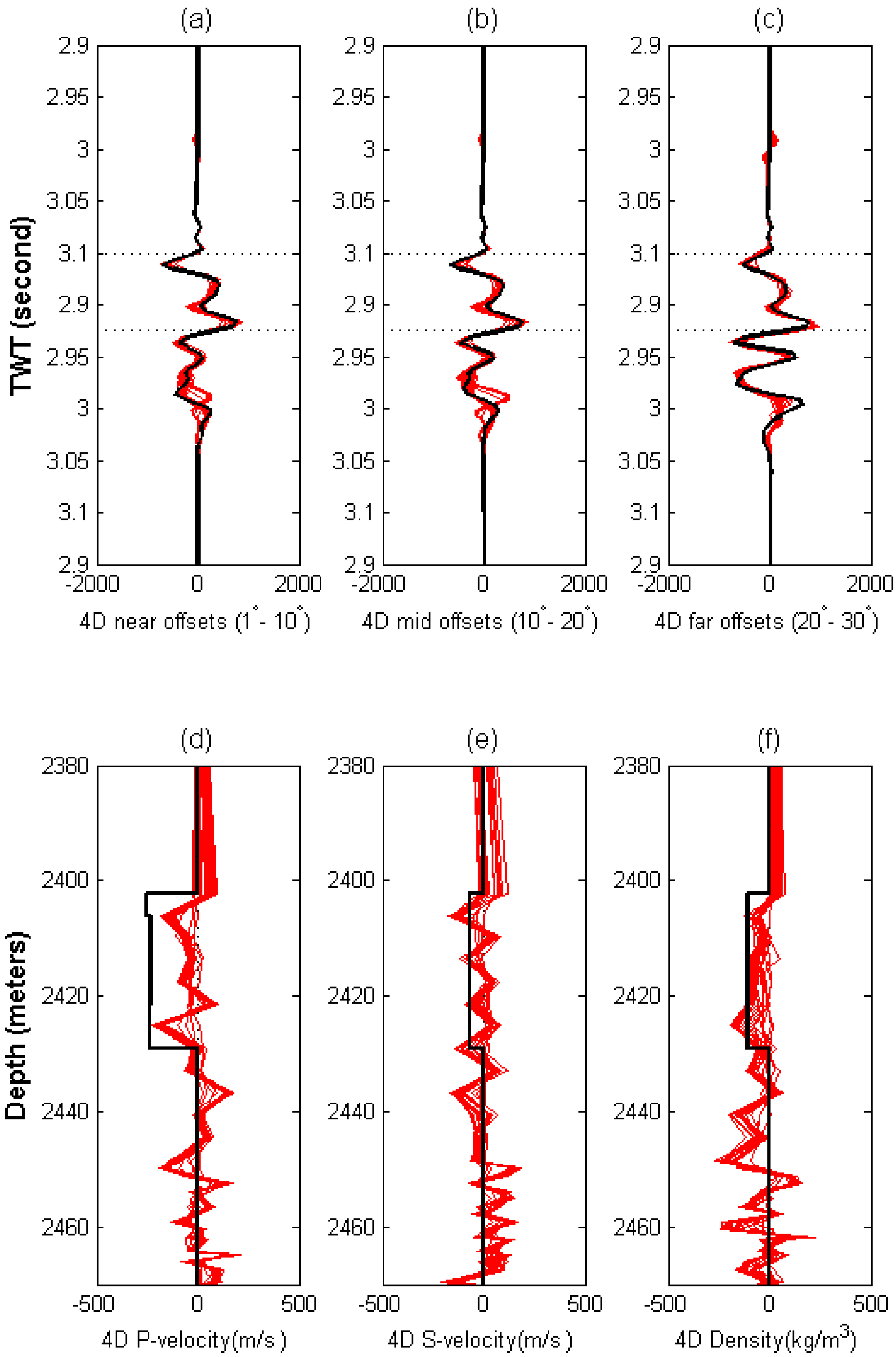

Figure 2.13 *The results of the unconstrained 4D inversion. (a) to (c) the amplitude matches at the near, mid and far offsets; (d) to (f) the equiprobable realisations (red lines) and the "true" 4D changes (black line) in terms of 4D P-velocity, 4D S-velocity and 4D density.*

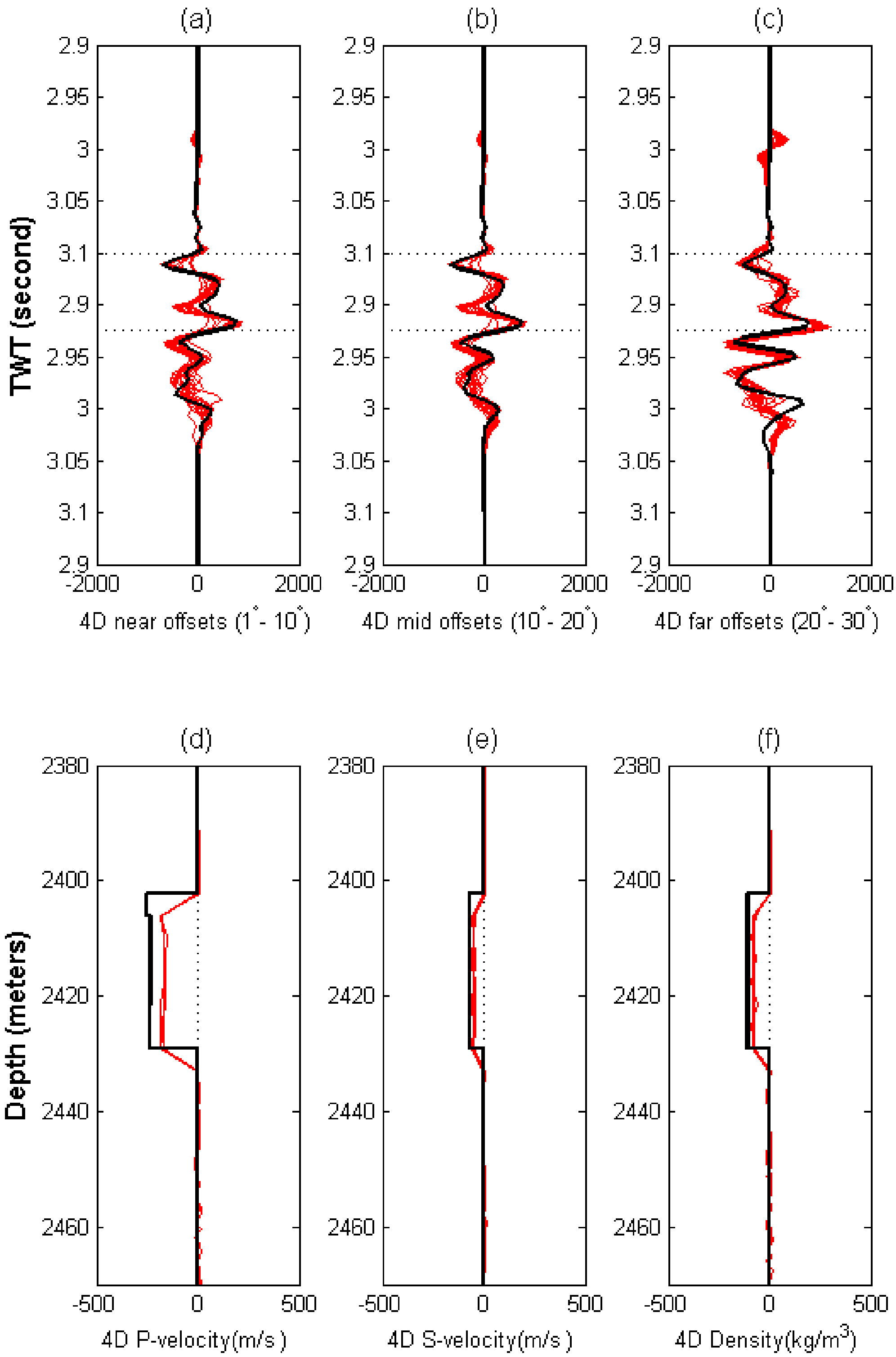

Figure 2.14 *Results of the EC 4D inversion. (a) to (c) the amplitude matches at the near, mid and far offsets respectively; (d) to (f) the posterior realisations (red lines) and the "true" 4D changes (black line) in terms of 4D P-velocity, 4D S-velocity and 4D density.*

shift related amplitudes would be sensible only if the inversion distributed the $\Delta_{v_P}$to the true locations inside the reservoir. With the prior model and noise tolerance, the EC solutions of $\Delta_{v_P}, \Delta_{v_S}, \Delta_\rho$ are subject to small posterior uncertainties, as shown by the realisations (red lines) in Figure 2.14 (d), (e) and (f). Negligible 4D changes are resolved in the overburden and underburden area while $\Delta_{v_S}, \Delta_\rho$almost reconstruct the true 4D changes (black log).

Statistically, the performances of the two methods are shown in Figure 2.15. The evolutions of $\Delta_{v_P}, \Delta_{v_S}, \Delta_\rho$ of a selected cell are plotted in Figure 2.14 (a), (b) and (c), for unconstrained inversion (black line) and EC constrained inversion (red line). The prior expectations of the EC inversion are plotted as thick blue dashes with the 0.95 range in blue dots. Generally, the unconstrained inversion has a slower convergence rate relative to the EC constrained one. Both of them converge after 500 iterations of "burn-in" and the range they cover afterwards represent the possible solution space. The EC solution reaches the steady period with the guidance of the prior expectation, which is the "true" model it is inverting for, with a narrower uncertainty. This is because the M-H sampler favours combinations of $\Delta_{v_P}, \Delta_{v_S}, \Delta_\rho$ which have the expected correlations among the members, and thus rejects the ones that are less likely, although the seismic response may match the observation. In Figure 2.14, (d), (e) and (f) show the corresponding normalized probability density functions of the selected cells by the unconstrained inversion. The unconstrained inversion is supposed to cover all possible solutions, given the observed data, and the distribution represents the full solution space according to the 4D seismic. Figure 2.14 (g), (h) and (i) are the histograms of the EC constrained results. In contrast to the unconstrained ones, the solutions tend to converge to a narrower window, with reduced uncertainty. The prior distributions (blue curves) with means as "true" answers in our example, have guided the algorithm to reasonable posterior distributions (red curves). The constrained expectations fall inside the "full solution space" covered by the unconstrained seismic solution, which means the non-uniqueness issue of the inverse problem is addressed better with the engineering information. The standard deviations at the near, mid and far offsets have been reduced by 68%, 81% and 74% respectively.

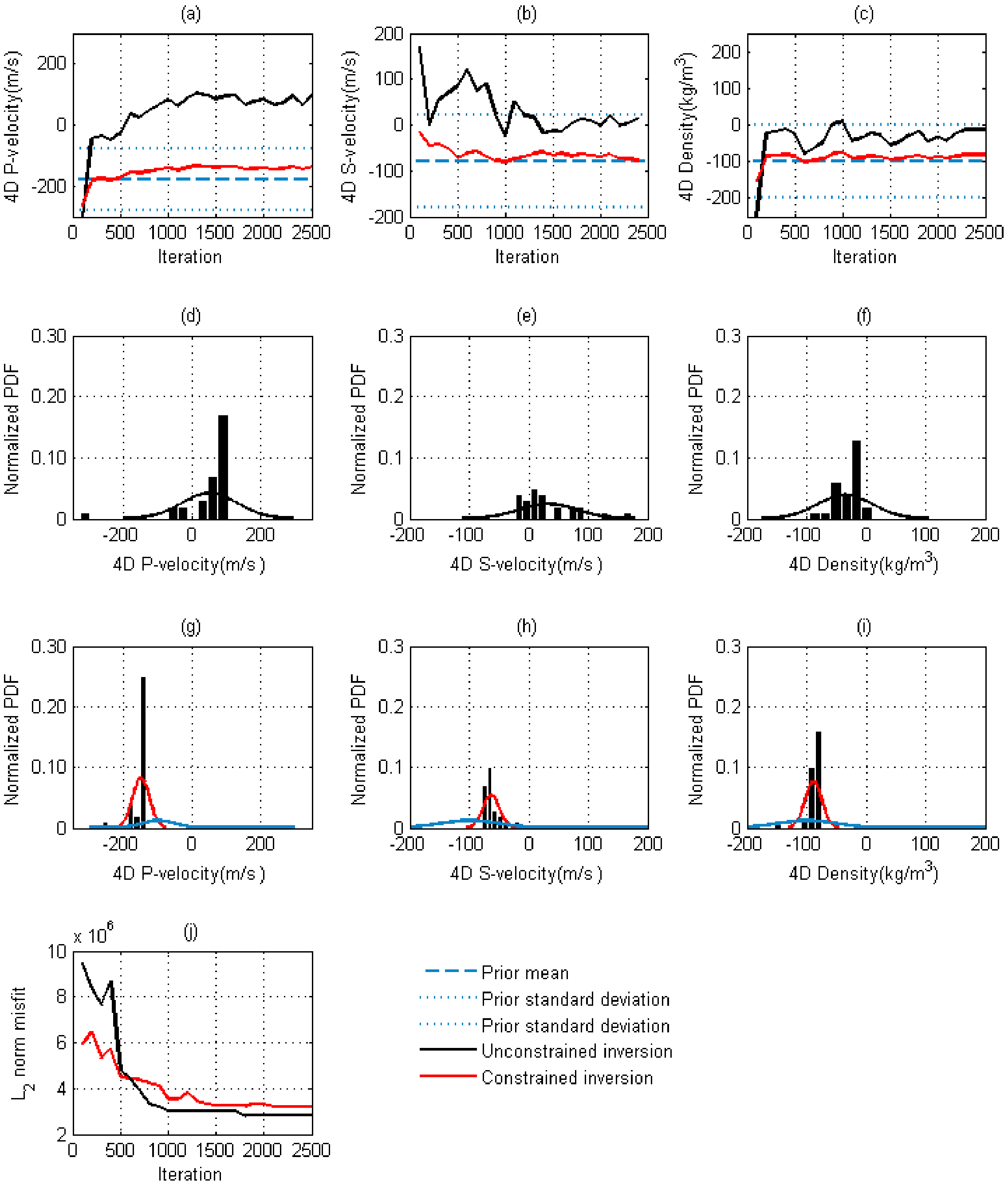

Figure 2.14 *The plots of the statistical results from a selected cell in the reservoir level. (a) the evolution of the 4D P-velocity, (b) the evolution of the 4D S-velocity, (c) the evolution of the 4D density changes; (d) to (f) the distributions of the unconstrained inversion results of 4D P-velocity, 4D S-velocity and 4D density respectively; (g) to (i) the posterior distributions of the EC constrained inversion results of 4D P-velocity, 4D S-velocity and 4D density respectively; (i) the comparison between the cost functions of the unconstrained (black line) and the constrained (red line) inversion.*

2.6 An alternative domain conversion

One practical challenge in applying this model grid-based inversion to the observed dataset is the domain transformation between TWT and depth. In the synthetic example, the overburden is modelled by only one thick cell, and its velocity dominantly determines the location of the seismic signals in time. In the real data, it is almost impossible to represent the overburden by one single value. To compensate for this error, an "alignment" is needed to line up a reference layer of the model to the corresponding seismic event (Amini 2014). The layer is ideally chosen at the top reservoir, by which the overburden effect can be eliminated. However in some models there is no single horizon that can be aligned on the seismic, due to pinch-out or any other type of unconformity structure (Figure 2.16). An alternative way to convert the seismic-derived attributes in the time domain to the model domain in depth is to map the attribute from one to the other, e.g. seismic samples 1 to 40 are linearly interpolated onto cells 1 to 32 (Thore, 2006). By doing so, markers from both domains need to be paired up (the thick red lines indicating the top and base of the reservoir in Figure 2.17 (a) and (b)) before the attributes are linearly interpolated onto each other. One significant advantage of doing this is the independence of the velocity model, which is quite often unavailable or problematic. The inversion could be carried out in the time domain, in which the time-to-depth conversion is not required, resulting in a more stable inversion. However, the more robust impedance attribute, which is the product of velocity and density, can be directly inverted for post-stack data, to speed up the data interpretation.

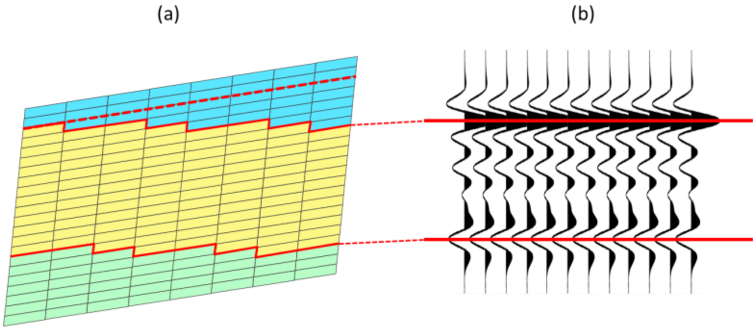

Figure 2.15 *The schematic illustration of the difficult alignment, when there is a pinch-out structure. The top and base reservoir (solid red lines) in the model cannot be directly correlated to the corresponding (b) seismic interpretation, because the layer index does not represent the geological boundaries, as shown by the red dashed line in (a).*

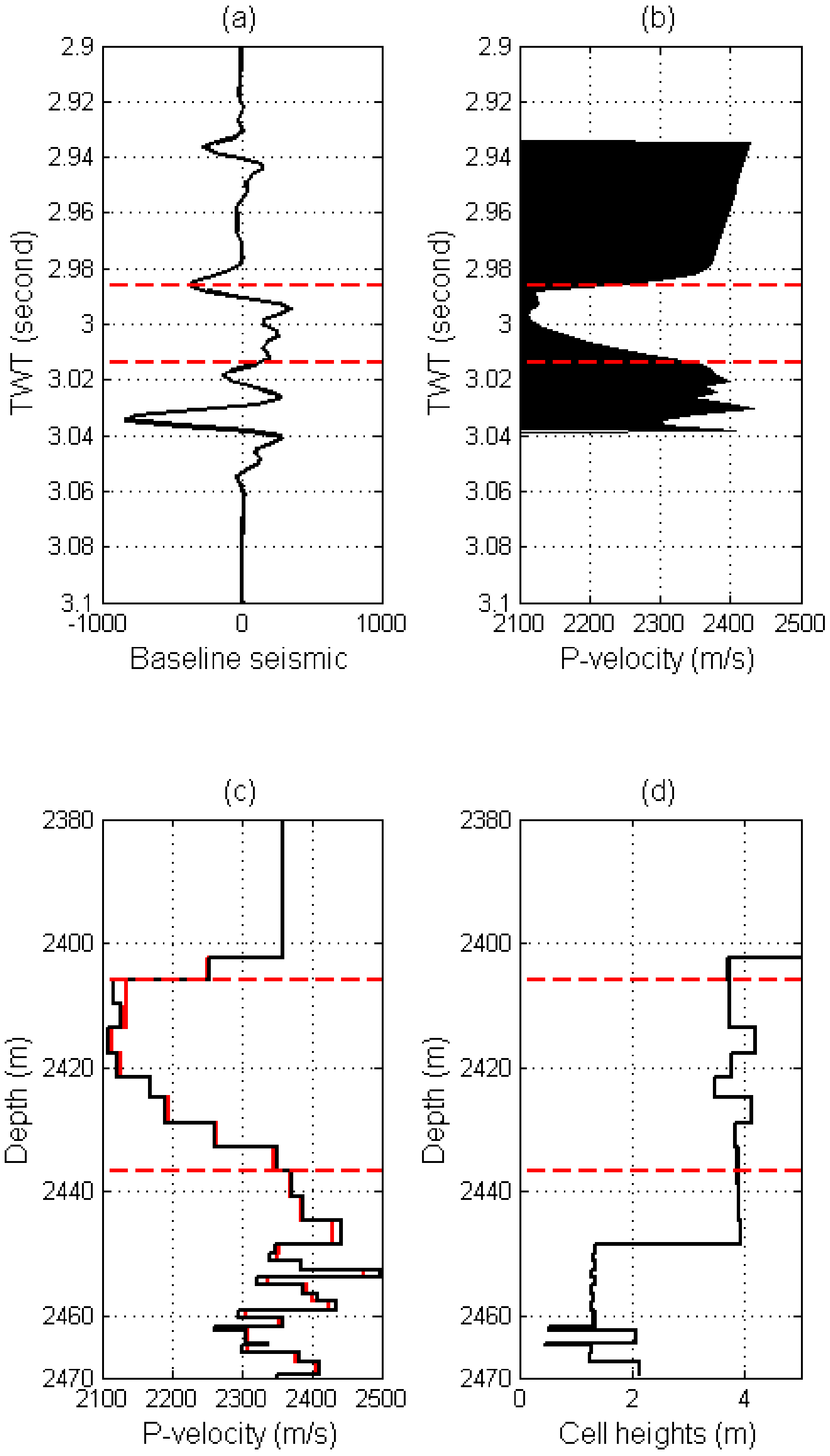

***Figure 2.16** The results of mapping (a) 3D amplitudes derived (b) velocity model in TWT, onto the (c) reservoir model cells, which have varying thicknesses (d). The red dashed lines indicate the top and base of the reservoir.*

However, an accurate mapping is based on the grid geometry. Vertically, if the cell heights vary dramatically, the mapping based on the indices may misplace the corresponding seismic attribute to a different cell, due to the uneven increments in depth. To improve this, the time domain attribute is mapped onto a uniformly spaced depth axis, and then resampled into the cells, according to their depth. The results of this mapping technique are shown in Figure 2.17.

2.7 Computational complexity

One general concern about the MCMC simulation is the insurmountable obstacle of the intensive computation cost. Usually, for a single trace inversion, a long Markov chain is needed to fully explore the posterior solution space, particularly when the inverse problem is heavily non-linear with high dimensionality. Nevertheless, a large number of posterior samples are required to be stored in the memory, given the high inherent autocorrelations, to extract the statistical moments of the posterior distributions. In addition, the seismic data is acquired at a much finer geometry, resulting a large volume of data in 3D, and for the particular interest of 4D, the data loads will double. Therefore, parallelising the computing tasks, which splits the whole workload into a set of tasks assigned to multiple computers, is the most efficient solution.

Although the MCMC method can be parallelised in a number of ways (Crane and Lemonie 1977, Whiley and Wilson 2004, Ye, 2011), the MCMC method, by nature, is a serial problem. According to Flynn’s Taxonomy (Flynn, 1972), the Single Instruction, Multiple Data Streams (SIMD) suits our problem most, as the inversion for different traces over a seismic volume follows the same computation process. The infrastructure of the proposed parallel scheme for inversion is demonstrated in Figure 2.18. Except the control flow, which is done by the master processor alone, most of the instruction streams are independent and parallel to each other. Thus, the *speedup* or *efficiency* ($\mathrm{Speedup}(p)=\frac{T_{\mathrm{serial}}}{T_{\mathrm{parallel}}(p)}$), can be maximised. In addition, the SIMD scheme does not require shared memory among the processors, and the coupling of the baseline and monitor seis2sim is secured by these remaining in serial. Practically, the runtime for an inversion of the 4D volume of 20,000 traces is reduced from weeks to less than a day by parallelising the tasks among 250 processors.

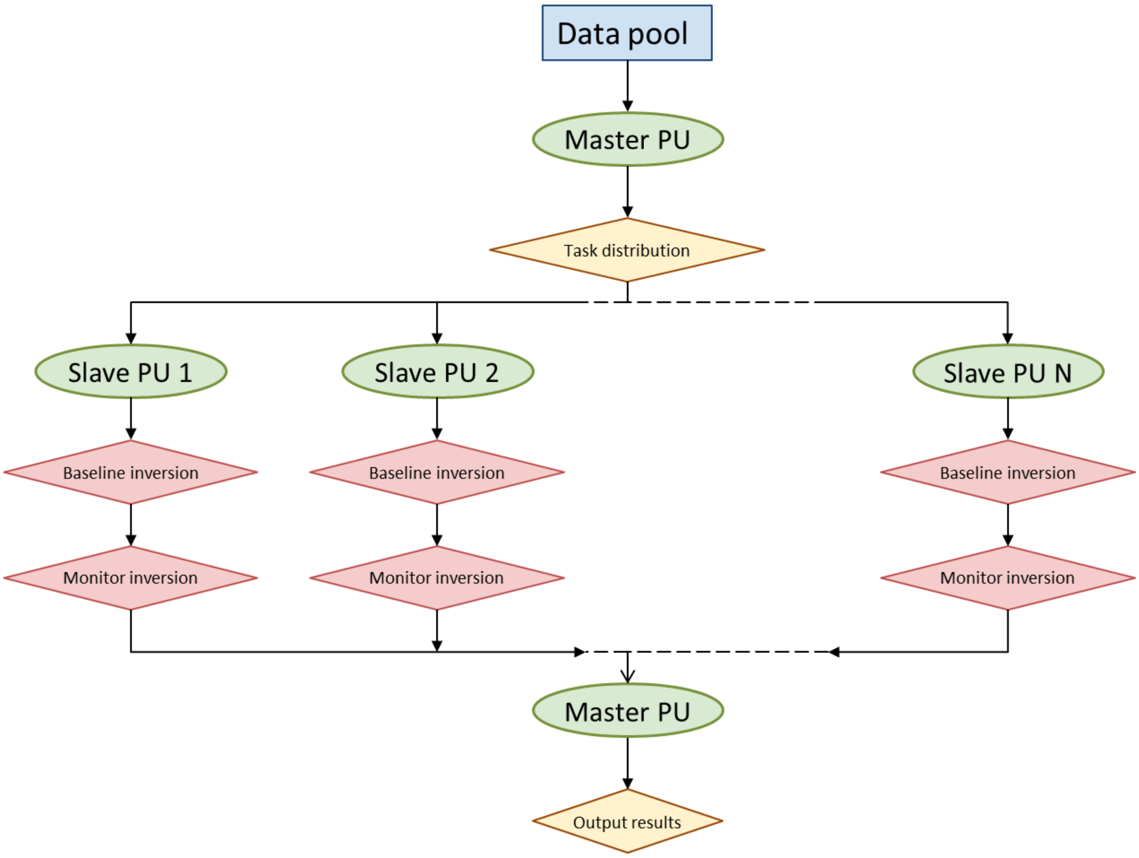

Figure 2.17 *The infrastructure of the parallelization scheme of the proposed EC inversion workflow in a SIMD scheme. The data pool represents the 3D dataset and 4D dataset, which are loaded and distributed to the slave processors by the master node. The key instructions are denoted in the diamond shape boxes, while the computing units are labelled by the circles.*

2.8 Summary

Inverting for the 4D difference can be implemented in a number of ways, as reviewed in the previous chapter, among which the consistency between the baseline and monitor solutions has drawn most of our attention. This feature is particularly guaranteed by inverting the baseline and monitor in a coupled scheme. The accuracy of the baseline inversion turns out to be fairly important for the 4D difference in this coupled method. Constraints derived from the reservoir engineering domain are needed to help the ill-posed seis2sim to converge to sensible solutions, with which the Bayesian framework is capable of integrating this information. In addition, the coupled scheme provides the static and dynamic information about the reservoir, which suits the ultimate goal of updating the reservoir model for multiple perspectives.

Chapter 3

Application of EC seis2sim to the Heidrun field

> “So the strong must guide the weak, for the weak are raw material to the strong. If the guide is not respected, or the material is not cared for, confusion will result, no matter how clever one is.”
>
> 「故善人者，不善人之師；不善人者，善人之資。不貴其師，不愛其資，雖智大迷。」
>
> Lao Tze, *Chapter. 27*, *Tao Teh Ching, 400 BC to 700 BC*

In this chapter, the proposed EC seis2sim technique is applied to the the Heidrun field. The Heidrun reservoir is characterised by a large number of fault-compartmentalised blocks, hence the assessment of fault sealing properties is a critical task for the 4D interpretation. Two towed streamer seismic surveys were selected for the seis2sim to invert for production-related changes between 1995 and 2008. The long period between the surveys results in poor repeatability, which raises great challenges in the data uncertainty. This chapter focuses on the implementation of seis2sim – with the assistance from the EC constraints, the “weak” seismic signal becomes stronger, and more interpretable.

The Heidrun field is operated by Conoco and partners offshore from Mid-Norway since March 1985 (Figure 3.1). The field lies in the Haltenbanken area, which comprises of blocks 6507/7 and 6507/8, with a total area of 38 km^2. The field was developed with a Tension Leg Platform (TLP). which is anchored to the seabed at about 350 metres water depth. The hydrocarbon accumulates primarily in the unconsolidated sands with an average reservoir depth of 2375 metres subsea, and initially contained an estimated 186 million standard cubic metres of oil and 41 billion standard cubic metres of gas (Koenig, 1986).

Figure 3.1 *The location of the Heidrun field.*

3.1 Introduction to the Heidrun field

The Heidrun field is formed by a large fault-bounded horst block dipping towards the south, and this structural closure is dissected by minor normal faults with typical displacements ranging from 30 m to 80 m (Figure 3.2). Kinematically, the northeast–southwest trending horst blocks and the secondary fault planes observed in the east-west

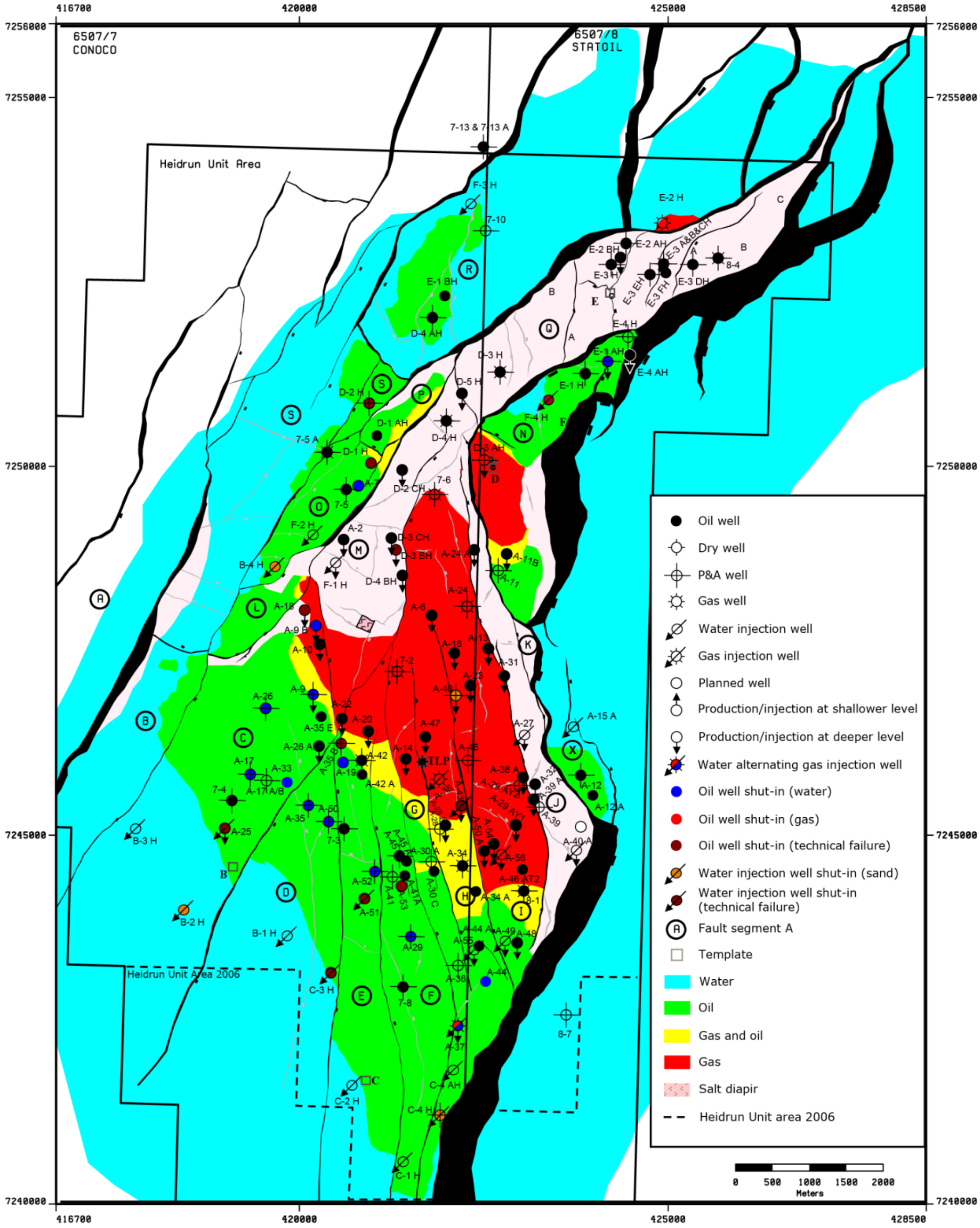

***Figure 3.2** Structural and fluid distribution map for the Heidrun field (Benguigui, 2010).*

directions are the consequence of the extensional evolution in Mid-Late Jurassic times. The Jurassic reservoir section was formed in a sequence ranging from continental to open marine sediments. These deposits were then overlain by the Cretaceous sands which were subject to partial erosion due to a posterior uplifting in the Late Cretaceous time. This global-scale sedimentation hiatus is often referred to as "Base Cretaceous

Unconformity", forming the topography of the most of the Heidrun field. The erosion increases from the central part of the field to the north, which causes a considerable variation in the seismic character of the top reservoir, depending on the lithology and fluid contrast below the unconformity. Geologically the Heidrun reservoirs are divided into the following main groups: Åre, Tilje and the Fangst, among which the Middle Jurassic Fangst Group is selected to be the object of this study.

3.1.1 Fangst group

The Fangst Group regionally comprises three sub-group formations - the Ile, Not and Garn, which are further subdivided into 10 zones, as shown in Figure 3.3. The total thickness of the Fangst Group can be up to 110 metres in the southern flank of the field and is recorded as an average of 50 ms on the seismic data. The erosion in the crestal part of the field has thinned the Fangst dramatically, and in some areas completely removed it. The entire group contains approximately 34% of the total oil in place, and 32% of the gas reserve for the Heidrun field. With its excellent reservoir properties, the Fangst Group provides the initial plateau production from the field.

The Lower Fangst Group is equivalent to the IIe Formation, in which the bottom part is composed of sediments deposited in a prograding, tidally-dominated delta, varying in thickness from 10 to 25 metres. It has a heavily cemented subzone (1-4 metres) at the base. The overlying sandstones are fine grained and coarsening upwards, without apparent internal barriers. The upper part of the Lower Fangst Group, with an average thickness of 34 metres, was deposited in a prograding wave-dominated coastline, with shoreface to beach deposits in the uppermost part. Grain size coarsens upward, which is considered as a main control on the reservoir properties. The fine laminations found in this part may restrict the vertical flow. The coarser grained uppermost part has little variation in porosity, vertically, but because of the upward increase in grain size, there are significant variations in permeability (Reid, 1996). The Not and Garn Formations which compose the Upper Fangst Group are separated by a layer of marine-origin shale in the Lower Not Formation. In the lowermost part of the Upper Fangst Group there is a set of shallow marine deposits, with thickness varying between 1 and 23 metres due to

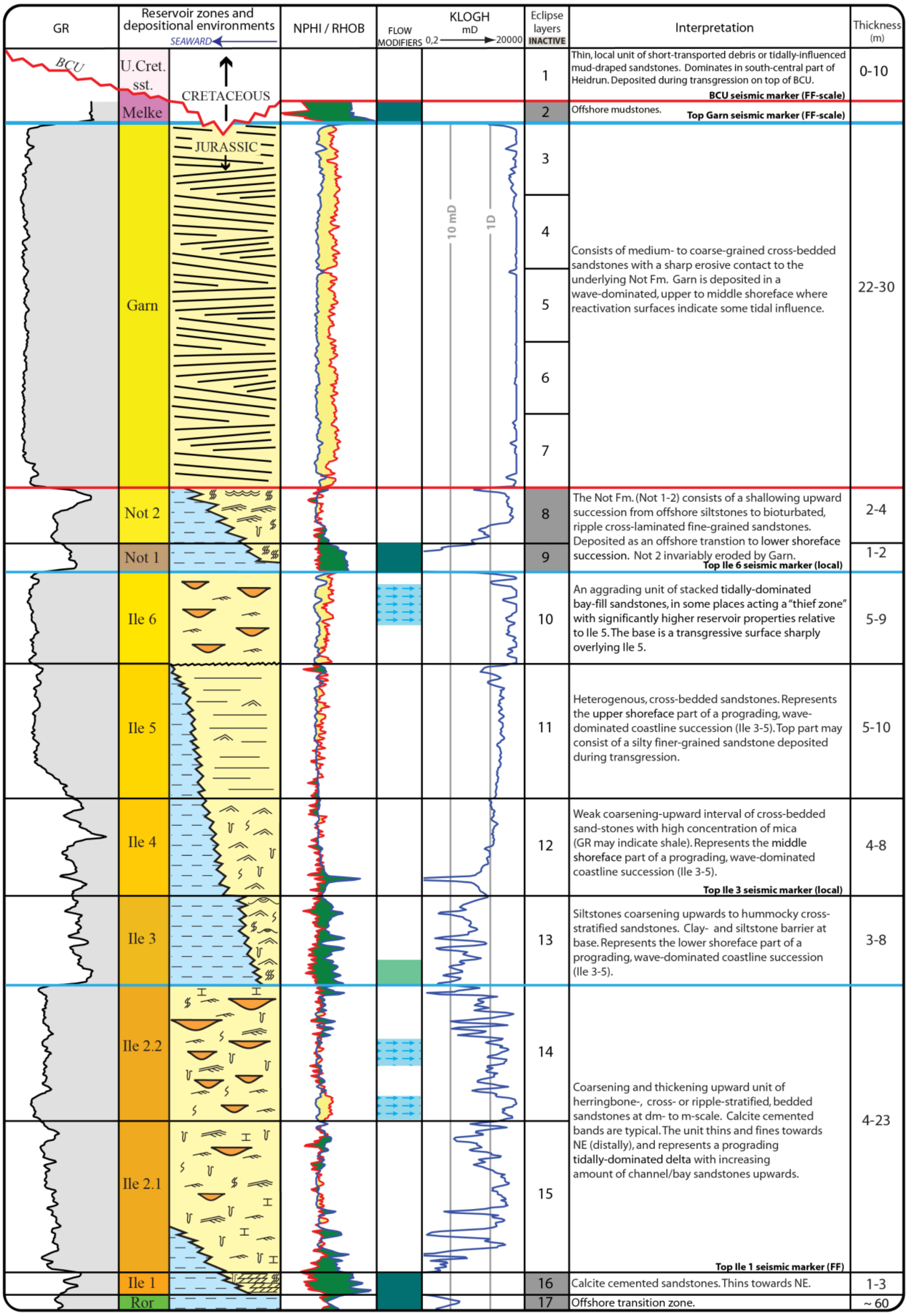

Thin, local unit of short-transported debris or tidally-influenced mud-draped sandstones. Dominates in south-central part of Heidrun. Deposited during transgression on top of BCU.

Offshore mudstones.

Consists of medium- to coarse-grained cross-bedded sandstones with a sharp erosive contact to the underlying Not Fm. Garn is deposited in a wave-dominated, upper to middle shoreface where reactivation surfaces indicate some tidal influence.

The Not Fm. (Not 1-2) consists of a shallowing upward succession from offshore siltstones to bioturbated, ripple cross-laminated fine-grained sandstones. Deposited as an offshore transtion to lower shoreface succession. Not 2 invariably eroded by Garn.

An aggrading unit of stacked tidally-dominated bay-fill sandstones, in some places acting a "thief zone" with significantly higher reservoir properties relative to Ile 5. The base is a transgressive surface sharply overlying Ile 5.

Heterogenous, cross-bedded sandstones. Represents the upper shoreface part of a prograding, wave-dominated coastline succession (Ile 3-5). Top part may consist of a silty finer-grained sandstone deposited during transgression.

Weak coarsening-upward interval of cross-bedded sand-stones with high concentration of mica (GR may indicate shale). Represents the middle shoreface part of a prograding, wave-dominated coastline succession (Ile 3-5).

Siltstones coarsening upwards to hummocky cross-stratified sandstones. Clay- and siltstone barrier at base. Represents the lower shoreface part of a prograding, wave-dominated coastline succession (Ile 3-5).

Coarsening and thickening upward unit of herringbone-, cross- or ripple-stratified, bedded sandstones at dm- to m-scale. Calcite cemented bands are typical. The unit thins and fines towards NE (distally), and represents a prograding tidally-dominated delta with increasing amount of channel/bay sandstones upwards.

Calcite cemented sandstones. Thins towards NE.

Offshore transition zone.

Figure 3.3 *The reservoir zonation of the Fangst Group for the Heidrun Field (Modified from Statoil internal report).*

the down cutting and erosion caused by the overlying fluvial sediments. The base of the Upper Fangst Group is a 1 to 2.5 metres thick claystone (non-reservoir) with good lateral continuity. It only forms local barriers to vertical flow between the Upper and Lower Fangst, as the faults offset this claystone, allowing vertical communication between the Upper and Lower Fangst. The uppermost Garn formation is a set of fluvial deposits with coarse- to medium-grained sandstones near the base, fining upwards to a medium to fine grained sandstone at the top. The reservoir quality here is excellent. However, as a consequence of different degrees of channel erosion, the thickness varies considerably. The maximum thickness is found in the eastern part of the field where this unit is up to 34 metres thick, while in the west, a minimum thickness of 5 metres is found (Reid, 1996).

3.1.2 A priori statistical rock physics of the Fangst group

The seismic imaging brings indirect, but spatially extensive information about reservoir properties that are not available from well data alone. However, the seismic-derived attributes are interpretable only if the links between seismic and reservoir properties are established. For example, the relation between the impedances and porosity is the key to bridging the two domains (Castagna and Smith, 1993).

In the petrophysical domain, Figure 3.4 shows a common set of acoustic wire-line logging data measured from an appraisal well for the Heidrun Field prior to the production start-up. The target Fangst group is between 2335 and 2430 m in measured depth, in which there is a thin layer of intra-reservoir shale at approximately 2360m. However, the log measurements are less reliable outside the Fangst group, as the caliper log suggests distinctive borehole rugosity. This rugosity can have an adverse effect on the response of logging devices which require borehole contact with the tool, such as those used to obtain the primary porosity, the lithology, the density and the neutron tools (Nieto et al. 1995). Therefore, the log measurements outside the Fangst group formation are subject to higher uncertainty during the later analysis. Different sets of elastic data are cross-plotted and their origins (reservoir or non-reservoir) are differentiated by colour, in Figure 3.5. In the V_P and V_S cross-plot the data stays loosely clustered while different trends are captured for Fangst sands and non-reservoir shale. In

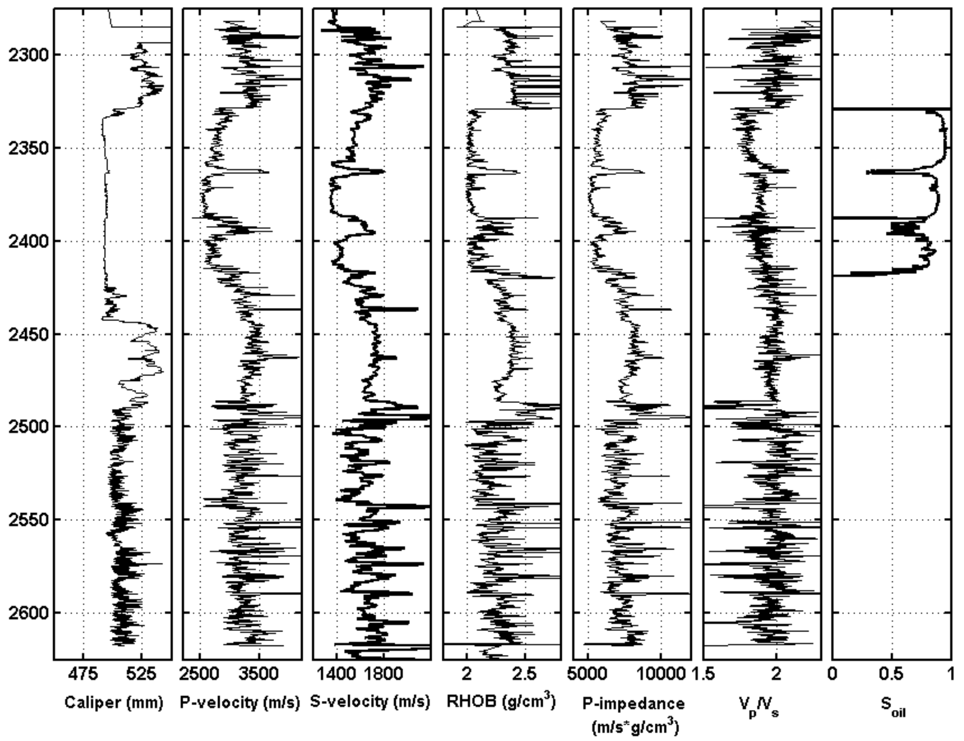

Figure 3.4 *The acoustic well logs measured in the depth interval 2275-2625m. The Fangst group is approximately between 2335 and 2430 m.*

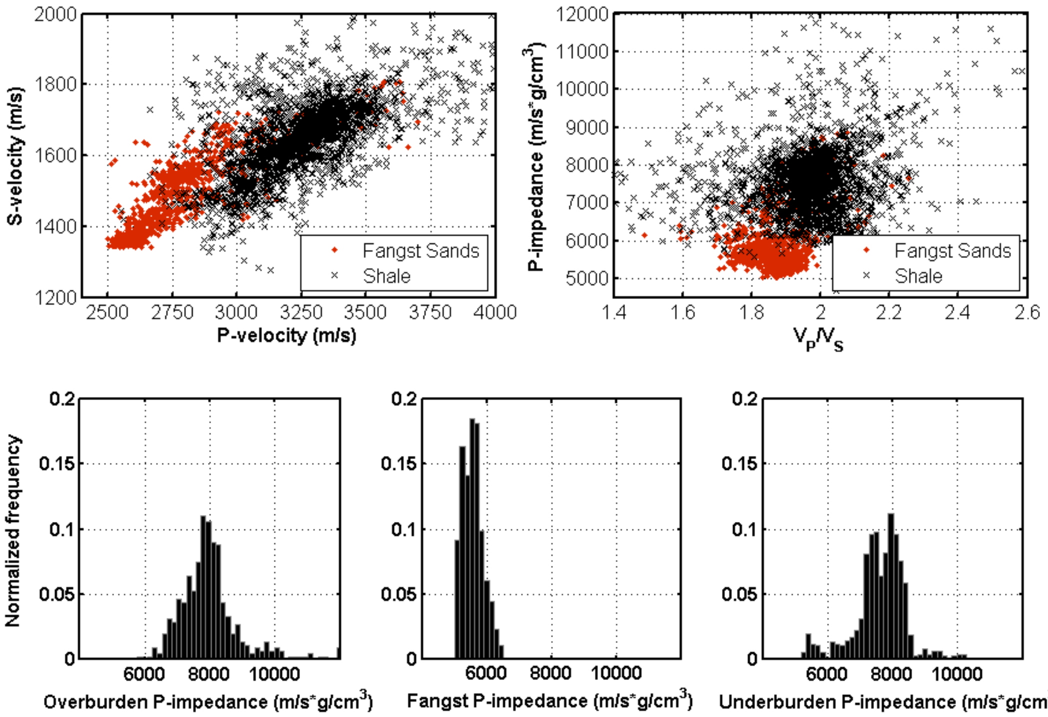

Figure 3.5 *Rock physics and statistics read from the Figure 3.4. The red samples are from the Fangst sands while the black crosses represent the overburden and underburden shale.*

the V_P/V_S and impedance cross-plot, the sands sit in the low P-impedance area while the shale shows higher P-impedance. This geological information needs to be honoured during the inversion, and thus *a priori* statistics are read from the three histograms in Figure 3.5 for the reservoir and non-reservoir accordingly. The reservoir sands have a mean of P-impedance of 5800 m/s*g/cm^3, which is associated with a standard deviation about 400 m/s*g/cm^3, while the overburden and underburden shale has a higher mean of about 8000 m/s*g/cm^3 and larger standard deviation, around 900 m/s*g/cm^3. These observations should be respected in the posterior probability distributions which are to be inferred by the Bayesian approach designed after inversion.

3.2 The seismic data and pre-inversion interpretation

The very first seismic survey conducted by Connoco in 1986 included a single gun and two-cable configuration. The result was merged and reprocessed with a later Statoil survey covering the Heidrun North, in 1991. In order to understand the fluid distribution in the Fangst and Upper Tilje, the time-lapse (4D) seismic monitoring project was carried out in 2001. The main target for the time-lapse study was the south-flank Fangst reservoir, which had proved promising for time-lapse seismic in a feasibility study (Brevik, 1997) and in a time-lapse pilot study (Jørstad et.al., 2000). The high porosity sand of the Fangst Group, as well as its long production history (since 1995); seem to be the dominant factors contributing to the observed changes in the 4D seismic response.

The first 4D seismic survey was acquired in August-September 2001 using Q – marine technology, which was later repeated in 2004. These surveys were conducted by a towed streamer with an identical single source and six-cable configuration. Subsequent processing between the 2001 and 2004 data resulted in normalized root-mean-square (NRMS) values of 21% and 34%, with reference to the 1986 baseline survey. Analysis of the time-lapse seismic data revealed fluid movement information and the character of the seismic attributes is consistent with the initial fluid contacts and main faults (Hanssen et al., 2004). Following the success of the first two monitoring surveys, new repeated surveys were acquired in 2006, 2008 and 2011, which were all processed against the 1986 baseline. All these vintages from the current version of the Heidrun seismic dataset, among which the 1986 baseline and 2008 monitor are then paired up to

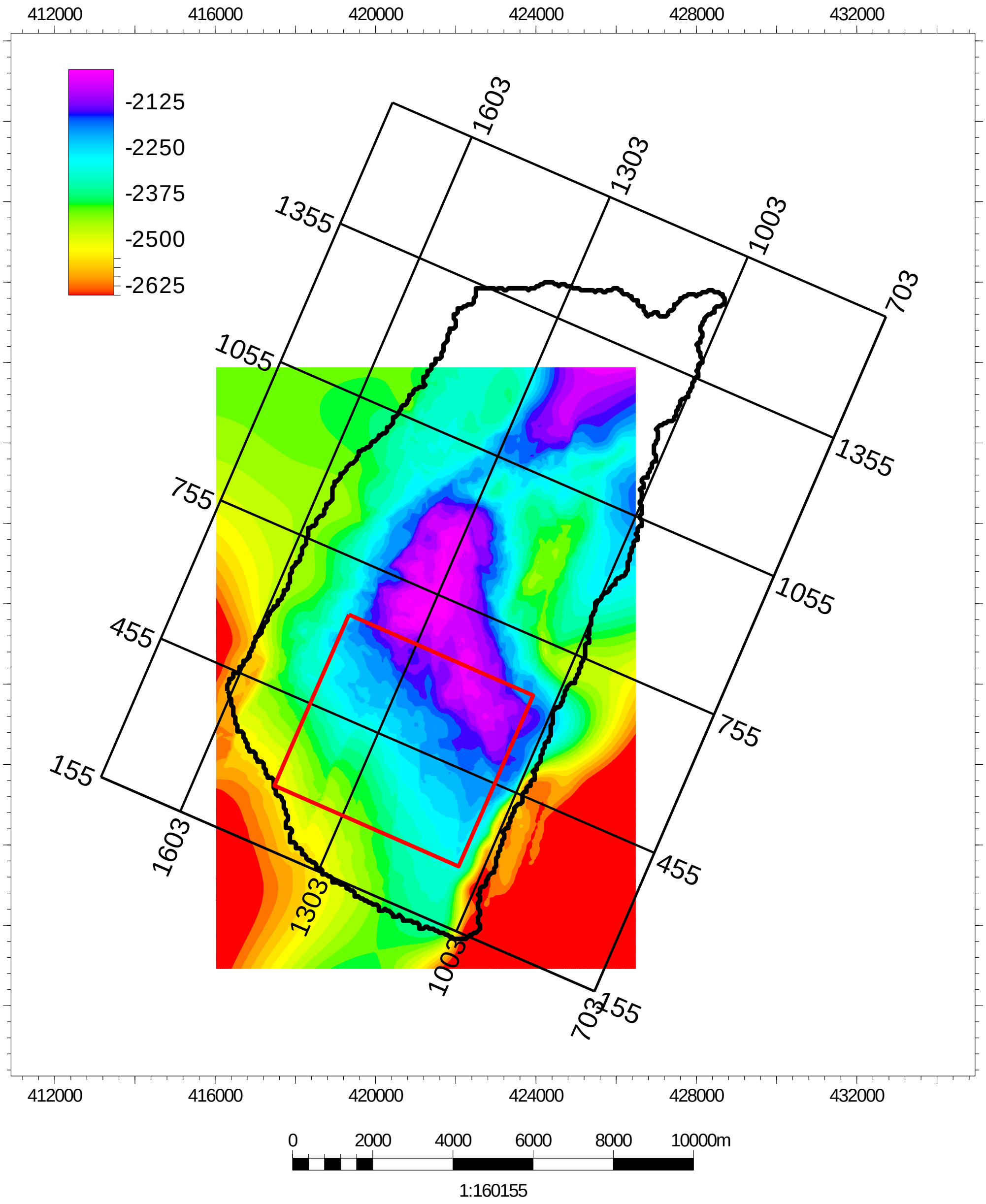

Figure 3.6 *The large black rectangle indicates the seismic data coverage, while the thick black line is the layout of the associated simulation model, showing where the main reservoir is. The red square is the inversion area of interest. Background colour map is the TVDSS of the top reservoir.*

implement the proposed inversion method, due the interests of data consistency and signal strength. The chosen seismic pair covers most of the Heidrun field; however, the only the south flank was decided to be the area of interest (Figure 3.6). The original seismic vintages have a consistent bin size of 12.5m by 12.5m, ranging from inline 277 to 645 and cross-line 1051 to 1447. Due to the lateral dimensions of the reservoir cells, which are about 100m by 100m, the seismic data was cropped at an increment step of 4 in both inline and cross-line directions. This results in a significant reduction for the seis2sim workload (from 146493 traces per survey to 9300 traces per survey), while preserving the maximum resolution of the reservoir model. A 40 ms window over the top horizon for the Fangst group was employed to calculate the NRMS value and the repeatability map is shown in Figure 3.7. The average NRMS for the area of interest is around 0.28, which is consistent with the report from Fürre et al. (2003). The north-western corner has a relatively poor repeatability, as it is close to a platform situated nearby. Additionally, streaks of poor repeatability are found along the fault panels, as the seismic data was subjected to higher uncertainty during the processing.

Two RMS seismic maps were generated from the 1991 baseline and 2008 monitor surveys using a 20ms window sitting at the top of the Fangst group. The monitor map was then subtracted by the baseline map to reveal the amplitude changes during the 13 years production and injection (Figure 3.8). Despite the noisy details, the 4D RMS amplitude map seems to honour the faults (black segments) and indicates the original fluid contact down to the south. A laterally continuous amplitude decrease is observed mainly in the southern oil leg, while a cross-block amplitude increase is seen further up to the north. Here, the reservoir rock (sandstones in the Fangst Group) has lower P-impedance values relative to the overlying layers, the intra-reservoir and underlying shales. So the water flooded oil-bearing reservoir would present a decrease in amplitude,

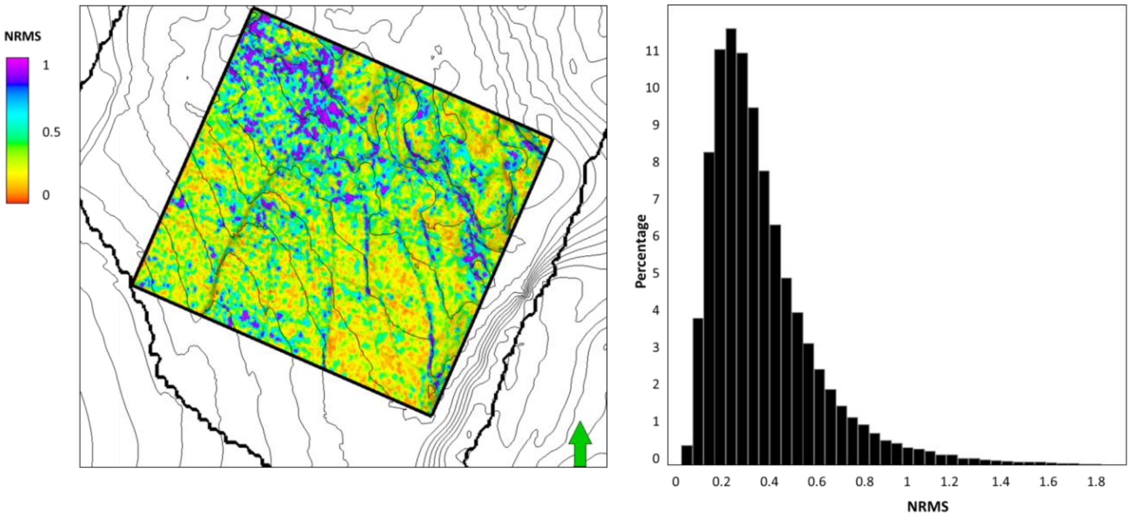

Figure 3.7 *Left, the NRMS repeatability map calculated using a 20ms window at the top of Fangst group, at a scale of 0 to 2. Right, histogram of the left, which has a mean NRMS repeatability of 0.28.*

as the contrast between "soft" sand and "hard" shale is reduced, while the increase in gas saturation would result in a bigger impedance contrast at the top Fangst formation, and a consequent amplitude increase in 4D. Although the 4D signature is able to be identified in most areas of the map, non-repeatable noise is an intrinsic issue in quantitative interpretations of the 4D data. Further qualitative inspection on low-angle stacks indicates that the noise could be related to the presence of multiples in the baseline data (Fürre et al., 2003). Moreover, gas withdrawal influenced by the gas injectors in the north-east sector, combined with the water-flooding effect of water injectors in the south-east, complicates the separation of pressure and saturation changes from the time-lapse seismic, due to the lack of signal strength. In order to quantify the production-related changes, the inversion to be performed needs to handle these data uncertainties, while honouring the reservoir engineering principles.

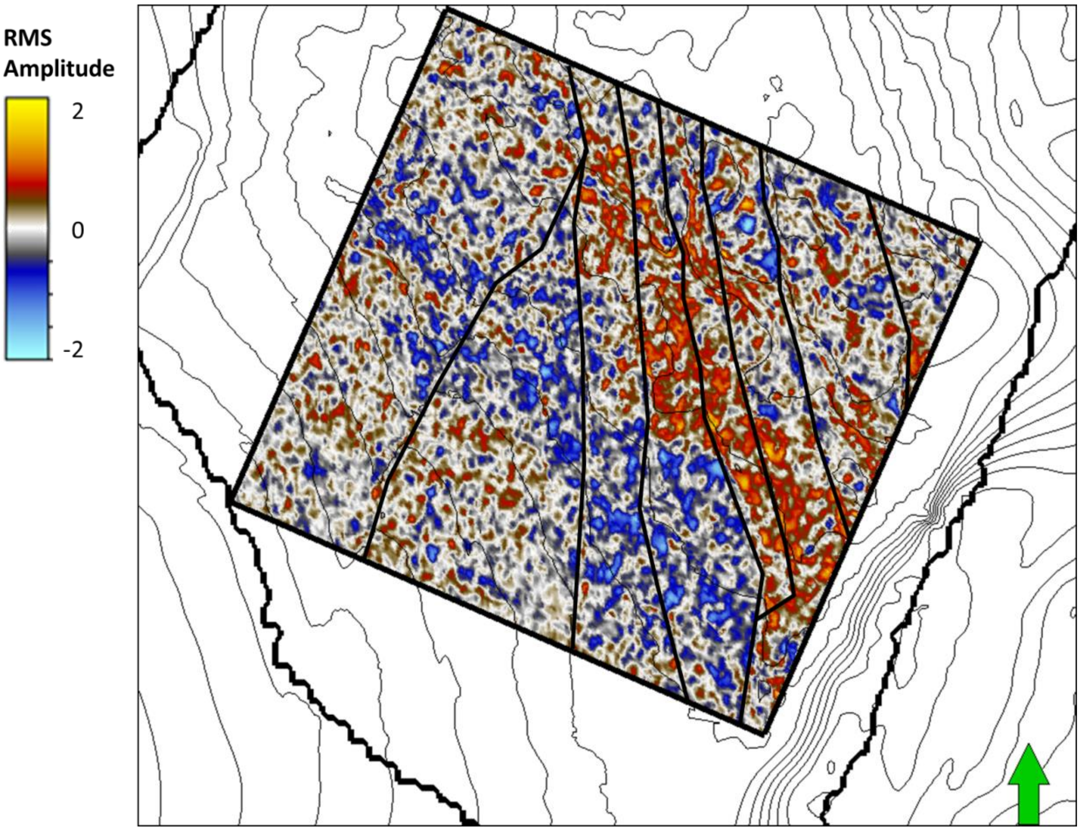

***Figure 3.8** RMS amplitude map generated by subtracting the 1991 baseline map from the 2008 monitor map. The 4D differences are confined within the fault blocks. The amplitude increase is related to the gas saturation increase present in the central crescent while the amplitude decrease reflects the water flood area in the oil leg.*

3.3 The reservoir engineering predictions

Predictions of the fluid distribution and pressure field from sim2seis are expected to bring deductive information that respects the fluid flow physics. The realistic transformation of reservoir engineering products, such as pressure and saturation, into petro-elastic properties will provide the 4D seis2sim with a cross-disciplinary reference to honour the geophysics domain. For this purpose, it is vital to accurately adjust the parameters involved in the petro-elastic model (PEM) as a necessary process to generate mutually reliable solutions. The PEM parameters are calibrated from a forward modelling perspective, using well log data. It is also important to adapt the PEM parameters according to the reservoir definition at the simulation cell scale, which is different from the log scale.

The same set of well logs displayed in Figure 3.4 is used to perform the calibration, and the entire Fangst group is assumed as a single facies. The density log is considered as a measurement of the saturated rock density and the mineral density of the reservoir can be calculated by inverting

$$\rho_{sat} = \rho_m(1 - \phi) + \phi[\rho_w \cdot S_w + \rho_o(1 - S_w)], \tag{3.1}$$

where ϕ and S_w refer to the observed porosity and water saturation log respectively. ρ_w and ρ_o are calculated using the experimental equation derived by Batzle and Wang (1992) in the initial reservoir conditions. The reservoir temperature is set to 85 °C and 27 for the oil API. The initial in-situ reservoir pressure log is created by extracting the cellular pressure values along the well trajectory. The Gassmann equation (Avseth et al., 2005; Kumar, 2006) is re-written for the dry bulk modulus as

$$K_{dry} = \frac{K_{sat}\left(\phi \cdot \frac{K_m}{K_{fl}} + 1 - \phi\right) - K_m}{\phi \cdot \frac{K_m}{K_{fl}} + \frac{K_{sat}}{K_m} - (1 + \phi)} \ , \tag{3.2}$$

where K_m is the mineral bulk modulus, K_{dry} is the rock bulk modulus without fluids inside; the saturated bulk modulus K_{sat} is directly calculated from the V_P, V_S and RHOB logs, and the fluid modulus K_{fl} is calculated by mixing gas, oil and water properties using the inverse bulk modulus averaging (Kumar, 2006).

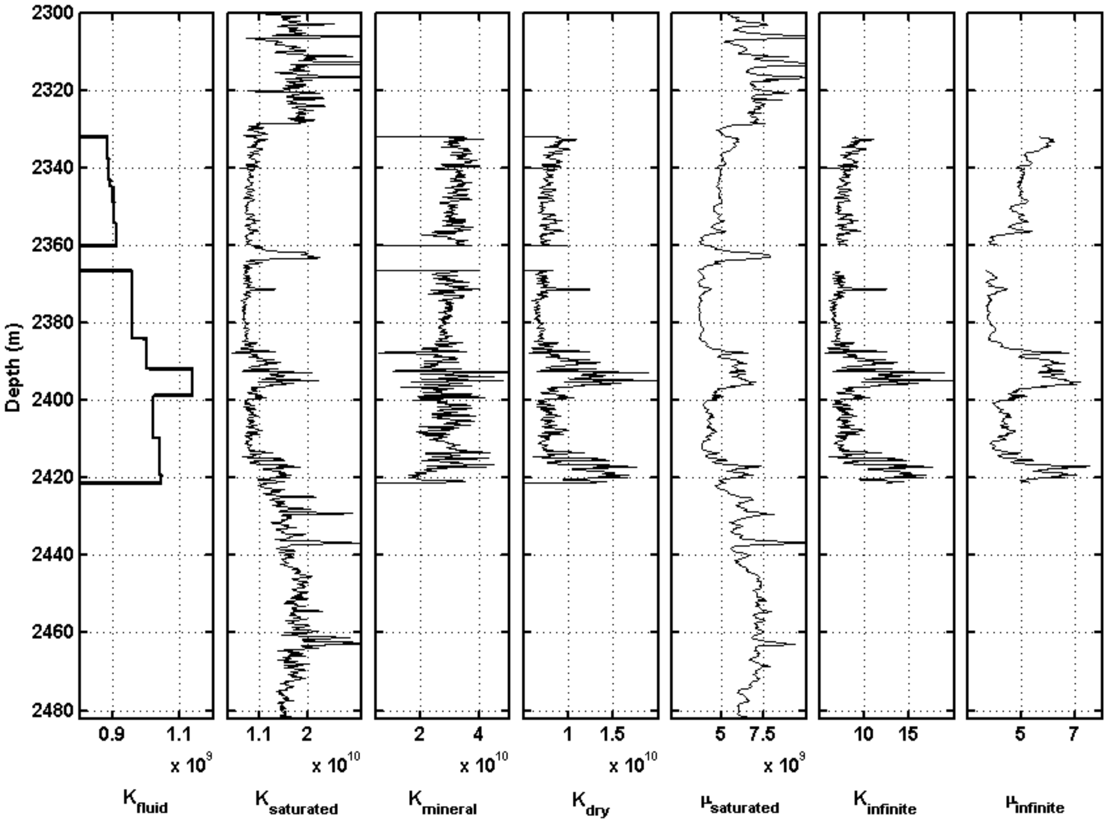

Figure 3.9 *Calculated pseudo modulus logs for the Fangst group.* $\boldsymbol{K_{fluid}}$ *is blocky log, as it reflects the resolution of reservoir cells vertically. The gap in the middle of the reservoir represents the inactive cells modelled for the intra-reservoir shale layer.*

Equation (3.2) is underdetermined, as both K_m and K_{dry} are unknown. Therefore an empirical relationship (Han and Batzle, 2004) between K_m and K_{dry} is employed as

$$K_{dry} = (1 - D \cdot \phi)^2 \cdot K_m, \tag{3.3}$$

where D is equal to 1.52 for a sand and shale system (Amini, 2014). Combination of equation (3.2) and equation (3.3) gives the calculated K_m and K_{dry} in Figure 3.9. The average K_{dry} over the Fangst is 9.3 GPa, while the shear modulus μ_{sat} has an average around 5.2 GPa. For the pressure effect, the stress sensitivity curves are modelled using

$$K_{dry} = \frac{K_\infty}{1+E_K \cdot e^{-P_{eff}/P_K}} \tag{3.4}$$

$$\mu_{dry} = \frac{\mu_\infty}{1+E_\mu \cdot e^{-P_{eff}/P_\mu}} \tag{3.5}$$

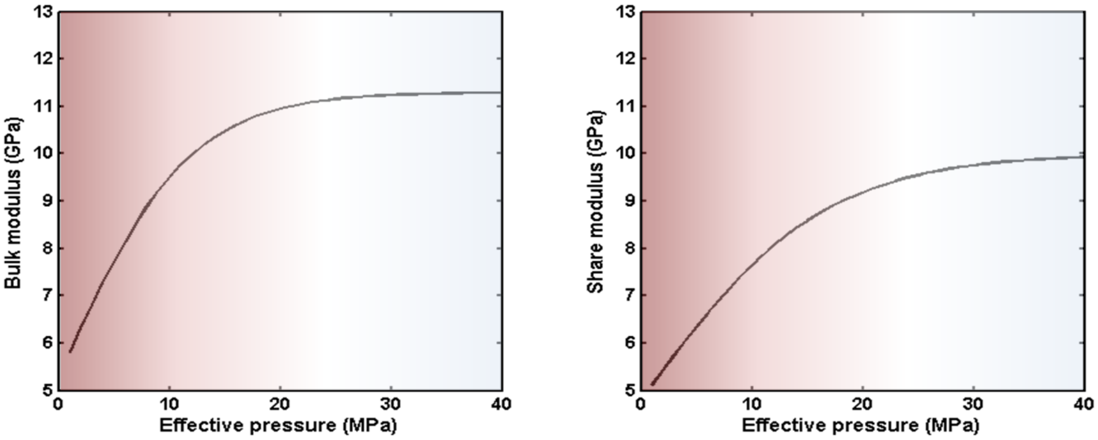

__Figure 3.10__ Calculated stress sensitivity curves for bulk modulus and shear modulus. The initial effective pressure is about 26 MPa. According to the gradients, reservoir pressure depletion (effective pressure increase) will have a smaller impact than reservoir pressure build-up.

proposed by MacBeth (2005). In equation (3.4) and (3.5), the K_∞ and μ_∞ will control the asymptote of the stress sensitivity curves, and they are believed to have a significant effect on the behaviour of the curve. So E_K and P_K are set equal to 1.12 and 5.62, while E_μ and P_μ are set equal to 1.08 and 7.97, for an oil and water system (Amini, 2010). In order to calculate K_∞ and μ_∞ with the average K_{dry} and μ_{dry} read from Figure 3.9, the resultant pressure sensitivity models are plotted in Figure 3.10. The shale properties are read from the well logs for the inactive cells inside the reservoir model, as well as for the overburden and underburden (Table 3.1).

With the PEM parameter sets calibrated from the observed well logs, synthetic predictions of P and S velocities and bulk density are generated using the pre-set values

	P-velocity (m/s)	**S-velocity (m/s)**	**Density (kg/cm^3)**
Overburden/underburden	3340	1680	2380
Intra-reservoir shale	3300	1650	2350

__Table 3.1__ The shale properties for PEM modelling. The values are the arithmetic averages from the corresponding reservoir intervals.

assigned to the reservoir model, to check the accuracy of the calibrated PEM. Pseudo logs are extracted from the reservoir model grid and superposed with the observed well log data in Figure 3.11. The initial values of effective porosity and oil saturation (the last three panels) are reasonably close to the well log measurements, except for the interval between 2390 to 2400 m, and the predicted logs generally show good matches to the wireline log data. However, the vertical heterogeneity in the predictions is not as detailed as in the wireline logs, due to the resolution of the reservoir grid. The cell heights range from 5m to 15m for the Fangst group, while the logging samples are spaced by less than a metre. In addition, synthetic 3D and 4D seismic volumes are generated by convolving a realistic wavelet extracted from the same well with the predicted impedance volumes over different survey times. The wavelet was extracted using the sonic logs (Hampson and Galbraith, 1981). An overlap of the results is displayed in Figure 3.12 to compare with the observed data. The 3D synthetic seismic shows consistent reflection events with the observed data, in which the top Fangst group is

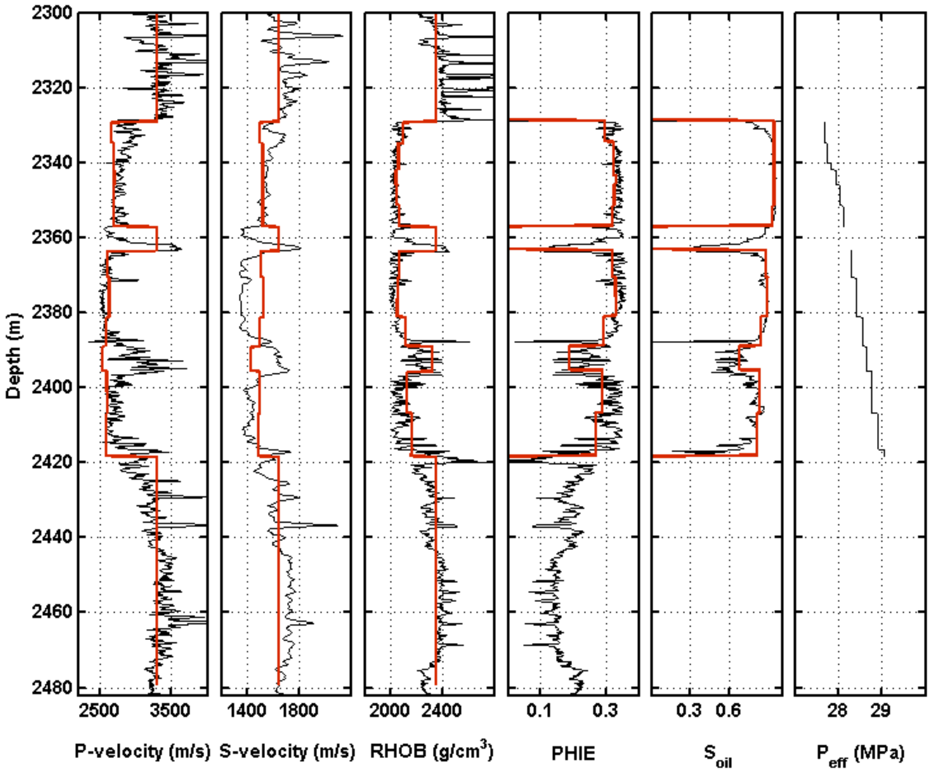

Figure 3.11 *The PEM prediction after calibration. The blocky red lines in the first three tracks are the resultant predictions for P-velocity, S-velocity and density. The blocky red lines are the effective porosity and oil saturation panels are the initial values in the reservoir model. The*

effective pressure in the Fangst group is between 28 MPa and 29 MPa, given a pressure gradient equal to 1.01.

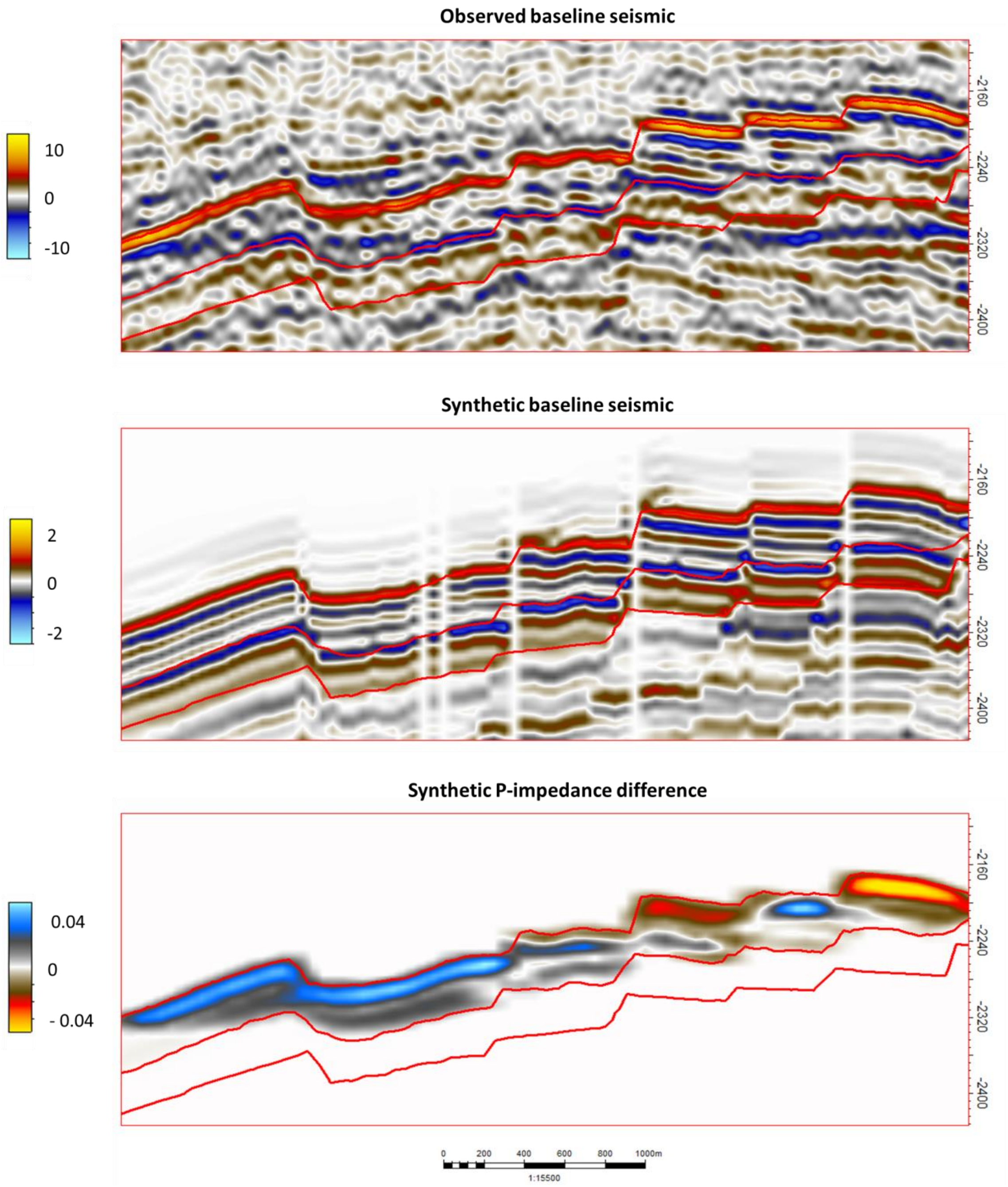
Observed baseline seismic

Synthetic baseline seismic

Synthetic P-impedance difference

Figure 3.12 *The synthetic 3D seismic amplitude intersection (middle) and the predicted 4D P-impedance changes (bottom) from the calibrated PEM. The seismic events are consistent with the observed interpretation, while the 4D predicts a 5% impedance change due to the water flood (blue) and gas cap (red).*

represented by a distinctive peak and the bottom by a trough. This leads to the conclusion that the interval velocity from the PEM prediction is consistent with the seismic, otherwise these seismic horizons would shift away from the corresponding interpretations.

3.4 Seis2sim application to the Heidrun 4D data

With the PEM predictions, the proposed EC seis2sim workflow is applied to invert the selected pair of time lapse vintages. The objective is to make inferences about the reservoir elastic properties in both 3D and 4D, which are to be used to update the reservoir model in the next chapter. The baseline and monitor surveys are coupled during the seis2sim, to ensure the time-domain consistency in the posterior solutions. From a statistical perspective, the solution of the proposed seis2sim approach is not limited to a single set of predicted parameters, but is represented by a probability density function (pdf) in model space. The task of seis2sim is not only to find a best-fitting set of model parameters, but also to characterize the uncertainty in the inversion results. The Bayesian setting is a natural choice to combine the PEM predictions with the information contained in the measured 3D and 4D data (Tarantola and Valette, 1982; Tarantola, 2005).

3.4.1 Baseline seis2sim

As discussed before, the top reservoir is characterized by a decrease in P-impedance from the shale to the reservoir sand. The base reservoir is clearly delineated on the seismic by the strong contrast between the sand and shale, as well. The specification of the prior model is the controversial part of the Bayesian inversion. Often the available prior information is not sufficient to define a unique parametric prior distribution.

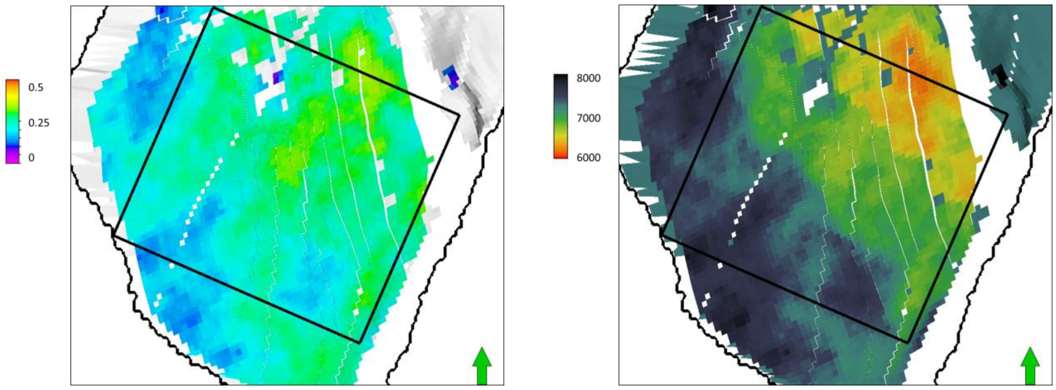

Figure 3.13 *The initial PORO model (left) and the PEM prediction of the P-impedance (right) on the reservoir model grid, which is used as a prior expectation for the baseline seismic inversion.*

Indeed, when the PEM prediction is introduced, a pragmatic approach is to select a parametric distribution with expectations equal to the sim2seis results. However, the most obvious pitfall with this approach is that the prediction is deterministic and it cannot provide the seis2sim with realistic estimations about the variances. Although the variances can be estimated by looking at the statistics from Figure 3.5, it is rather risky to use information from this single well to represent the entire area. Therefore, fairly big variances are given to the prior estimates, to ensure the inversion covers the full solution space. The estimated standard deviation for the overburden and underburden shales is $2*\sigma_{shale} = 3200$ m/s*g/cm^3 (), while for the the reservoir sand it is $2*\sigma_{sand} = 2700$ m/s*g/cm^3. The seis2sim solution for P-impedance is *a priori* assumed to be Gaussian. This assumption can be graphically evaluated in the well statistics by a Gaussian probability fit, shown in Figure 3.5.

The temporal correlation function of impedance is estimated for certain time lags from the well logs (see Figure 3.14). This function is modelled by an analytic correlation function,

$$\gamma(t;a,b) = \frac{1}{2}\cdot e^{-\left(\frac{t}{a}\right)^2} + \frac{1}{2}\cdot\left(1-\frac{2t^2}{b^2}\right)\cdot e^{-\left(\frac{t}{b}\right)^2}, \tag{3.6}$$

defined by the sum of an exponential correlation function, with a range a = 1.8 ms, and a second order term with b = 9 ms. The fit to the estimated correlation function is considered to be good for the purpose of stabilising the seis2sim solution.

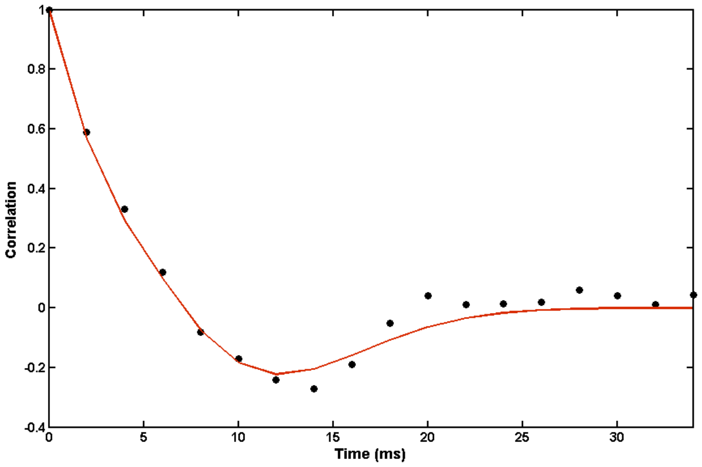

Figure 3.14 *Correlation function estimated from well logs (dots), and an analytical correlation function (red line) derived from a second order exponential correlation function.*

The solution of equation (2.3) is obtained by the adaptive Markov chain Monte Carlo (MCMC) simulation proposed in Chapter 2. One trace for the seis2sim inversion at the well location is displayed in Figure 3.15, showing the matches to the observed seismic trace and the posterior realisations of P-impedance traces. The P-impedance is well determined, as the prediction intervals are reduced by up to 95%. The Fangst reservoir is between 2180 to 2244 ms in TWT, inside which the "soft" sand is successfully delineated. Figure 3.16 displays the convergence of the MCMC process. The Markov chain begins to converge after the first 1500 iterations which is usually referred to as the "burn in" stage, after which the "detail balance" of the MCMC is achieved and the samples are representing the posterior probability distribution.

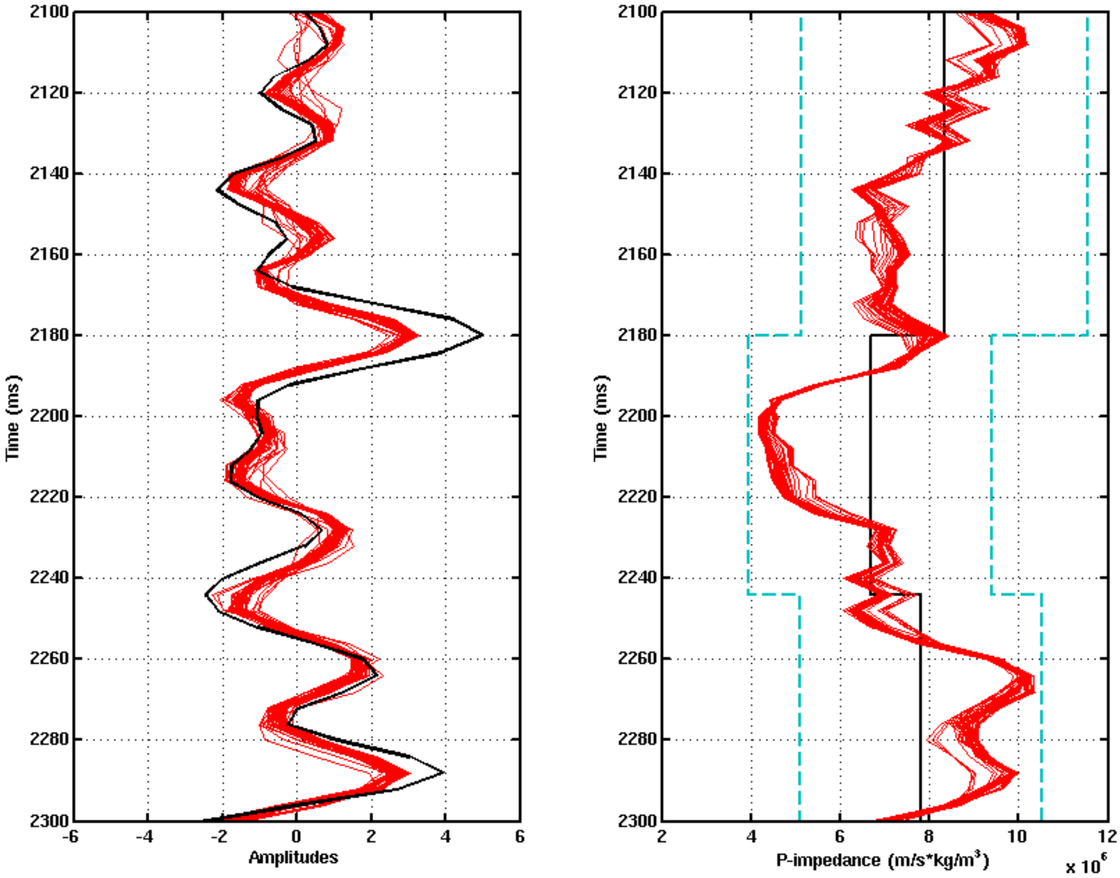

Figure 3.15 *The posterior inversion results for 1D baseline seis2sim inversion. The red traces are the realisations of seismic traces (left) and the corresponding P-impedances (right), where the black trace in the left diagram is the observation. The light blue dashed lines on the right are the prior prediction interval, while the blue and the black is the prior expectation. The range that is covered by the realisations reflects to the posterior uncertainty after inversion.*

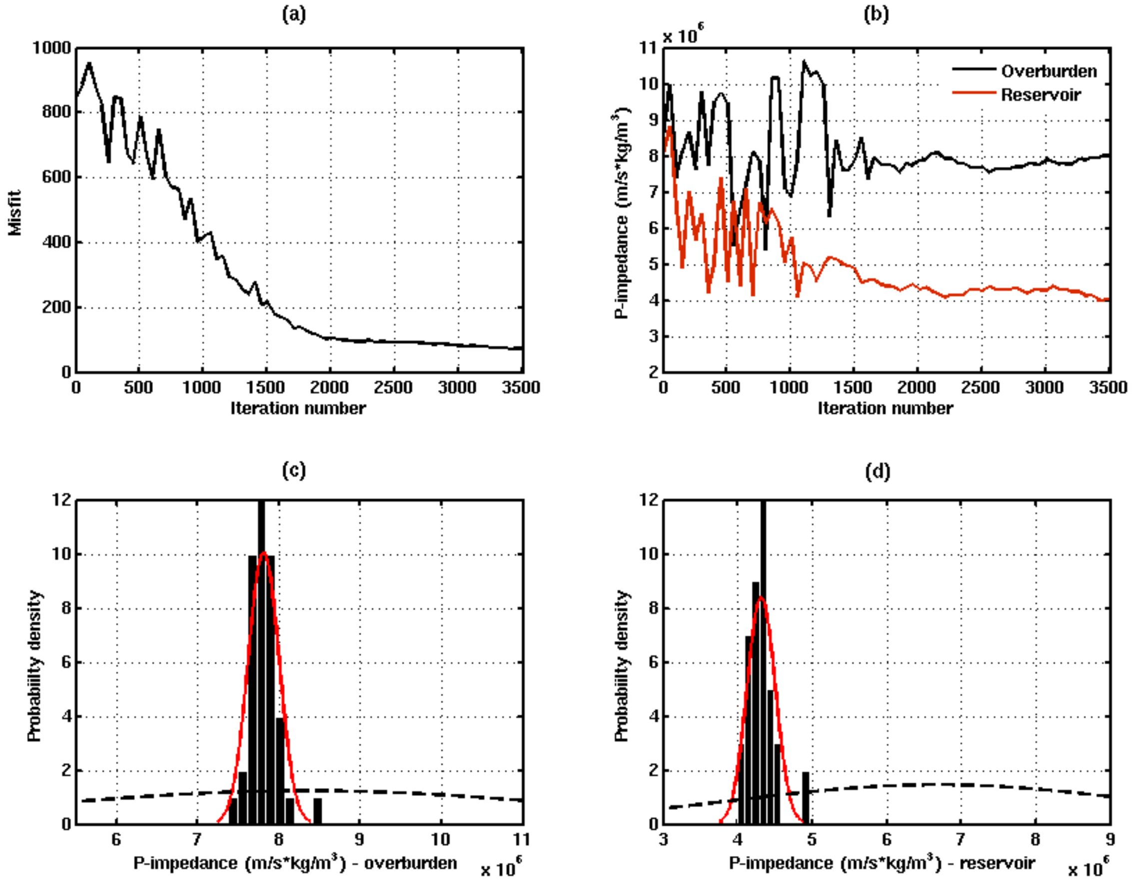

***Figure 3.16** The MCMC convergence process for the 1D example in Figure 3.15. (a) the overall misfit evolution with iterations; (b) the evolution of P-impedance of two samples from the overburden (black) and the reservoir (red); (c) the histogram of the posterior realisations of the overburden sample; (d) the histogram of the posterior realisations of the reservoir sample.*

In Figure 3.16 (b) there are two different examples from the overburden and the reservoir, with different converging paths. The inversion for the reservoir interval has a shorter "burn-in" period compared to the overburden, which starts to converge from 1500 iterations. After seis2sim inversion, the overburden sample has a mean of 7940 m/s*g/cm^3, associated with a standard deviation of 341 m/s*g/cm^3 (the prior estimation of the standard deviation is 1600 m/s*g/cm^3), while the sample from the reservoir interval has a mean of 4372 m/s*g/cm^3, associated with a standard deviation of 230 m/s*g/cm^3 (the prior estimation of the standard deviation is 1350 m/s*g/cm^3).

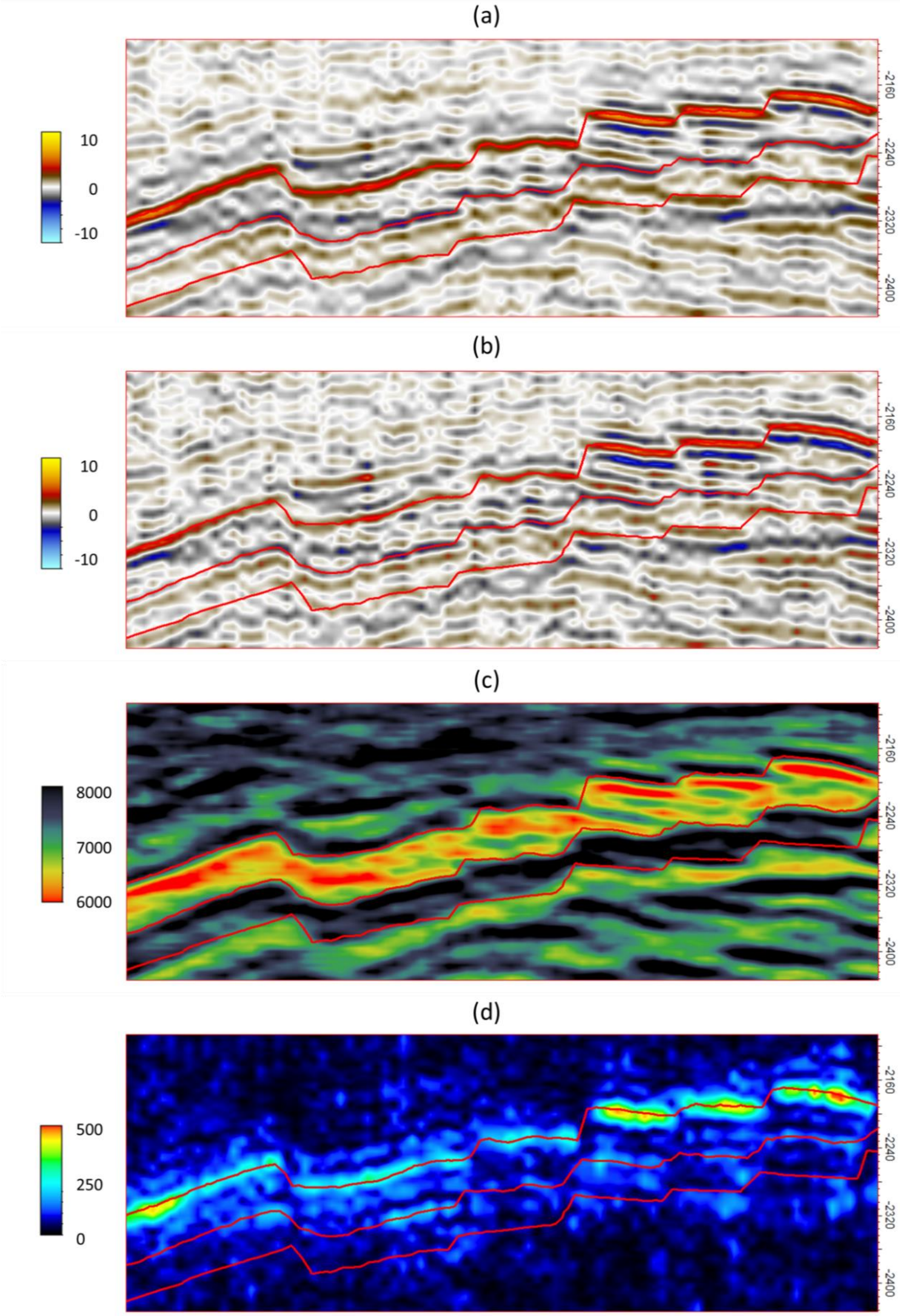

Figure 3.17 *The various baseline seis2sim results. (a) observed baseline seismic; (b) synthetic baseline generated by the posterior mean of the P-impedance; (c) posterior mean of the P-impedance from seis2sim; (d) the posterior standard deviation after inversion.*

The maximum posterior solution for the P-impedance is equal to the posterior expectations which are displayed in Figure 3.17. This maximum *a posteriori* solution is generally smoother than a single realization in Figure 3.15. A single realization, however, will be a possible solution with the full variability defined mainly from the prior distribution. Figures 3.17 (a) and (b) show the contrast between the observed baseline seismic and the synthetic, from the posterior mean P-impedance volume. The largest mismatch is found along the top reservoir, where the sand to shale contrast lies. Indeed, the details inside the reservoir show a reasonably good match. Figures 3.17 (c) and (d) show the intersections of the posterior mean and the standard deviation of the P-impedance, in which the reservoir sand distribution is better imaged. The biggest

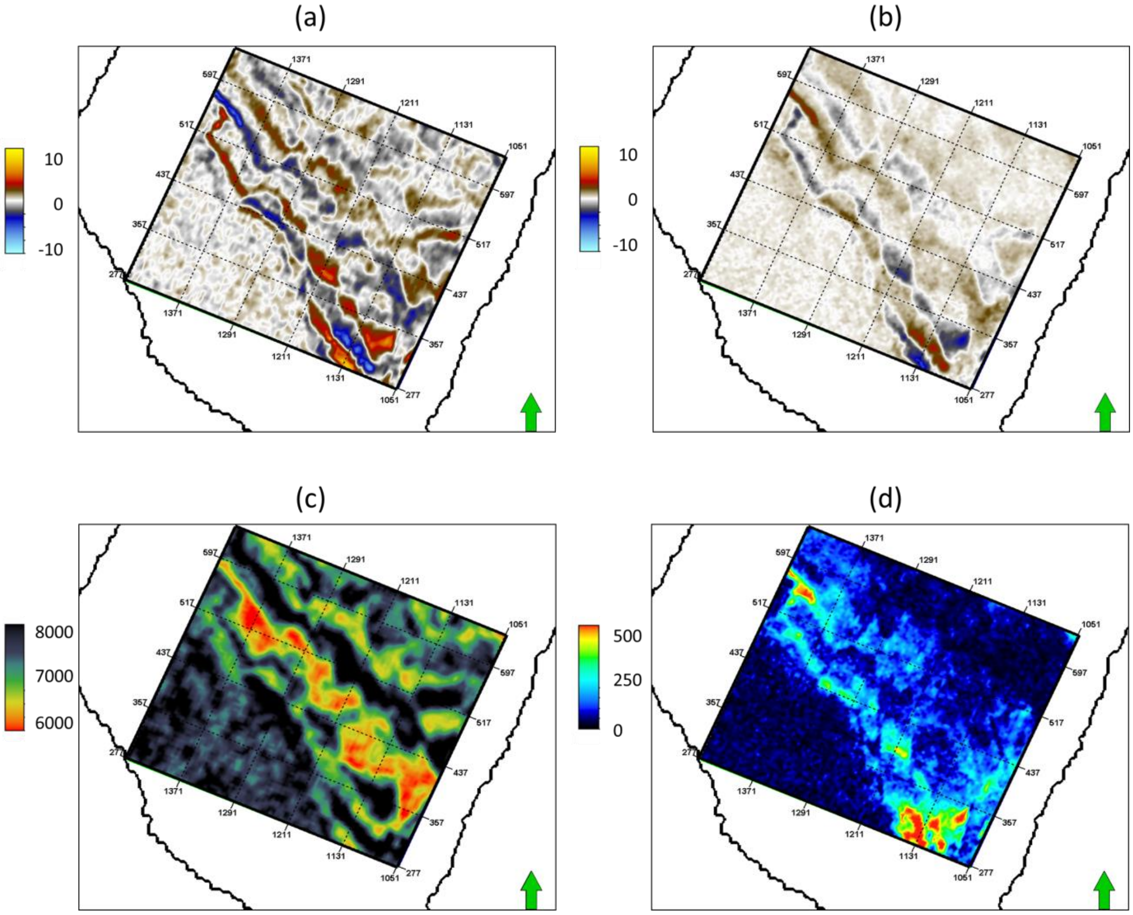

Figure 3.18 *Time slices of the baseline seis2sim results. (a) the observed baseline seismic; (b) the residual error of the synthetic baseline from the inversion; (c) the posterior mean of P-impedance from seis2sim; (d) the posterior standard deviation.*

uncertainties are found along the top reservoir, which could be caused by the default constant models of the overburden. Figure 3.18 shows the time slices of the inverted volumes, where the posterior standard deviation shows a consistent pattern with the residual misfits. This misfit volume will be propagated into the 4D seis2sim, as an additional uncertainty term formulated in the inversion.

3.4.2 The EC 4D seis2sim

The proposed EC 4D seis2sim scheme is applied to the selected time-lapse seismic vintages of the 1991 baseline and 2008 monitor. The aim is to estimate the changes of the elastic properties in the Fangst group caused by the production activities, including the uncertainty bounds on these estimates. The seis2sim operates indirectly on the seismic amplitude difference between the baseline and monitor survey: this is because the inverted baseline P-impedance, together with its uncertainty, is referred as the prior condition of the reservoir. This static estimate will be altered to generate the desired 4D amplitude observation during the 4D seis2sim, in a coupled scheme.

The observed 4D seismic amplitude difference is obtained by subtracting the 1991 baseline and the 2008 monitor. From the difference data, an estimate of the data uncertainty can be extracted from the overburden lying immediately above the Fangst group, where it was not affected by production. Figure 3.19 displays the current information prior to the inversion. The reservoir simulation predicts a zone of water flood in the south, as shown in Figure 3.19(a), where there is a 2 to 3 percent decrease in P-impedance. In contrast, P-impedance increases of 4 to 5 percent are found to the north of the water flood zone, as a result of gas injection. This *a priori* prediction is employed as a reservoir engineering consistent (EC) constraint for the 4D seis2sim to honour. In practice, an expectation and covariance matrix are calculated to formulate the prior model at each trace location. based on the sim2seis prediction. The expectation vector is composed of zero elements, which are not affected by the production in the overburden and underburden, and non-zero elements, corresponding to sim2seis predictions inside the Fangst group. The diagonal elements of the covariance matrix are the variances of P-impedance changes for each seismic sample, while the off-diagonal elements are the correlations for samples at different TWT depths which reflect the vertical reservoir connectivity. Apart from the this prior information, an estimate of data noise is also shown in Figure 3.19 (b), which maps the standard deviations of the 4D seismic amplitude difference, using a 40 ms time window, over the top horizon of the Fangst group. In contrast, the 4D signal strength can be represented by the standard deviations of the 4D amplitudes inside the reservoir interval, as shown in Figure 3.19(c). There is a consistent signal pattern compared to the noise-free sim2seis predictions in Figure 3.19(a). The quotient of the two maps is considered as an indication of the confidence level of the observed 4D difference data, which is converted into a covariance matrix in the likelihood function during inversion. The covariance matrix, which represents the non-repeatability of the time-lapse data outside the reservoir zone, is set stationary at each seismic trace location of the 4D data but varies laterally.

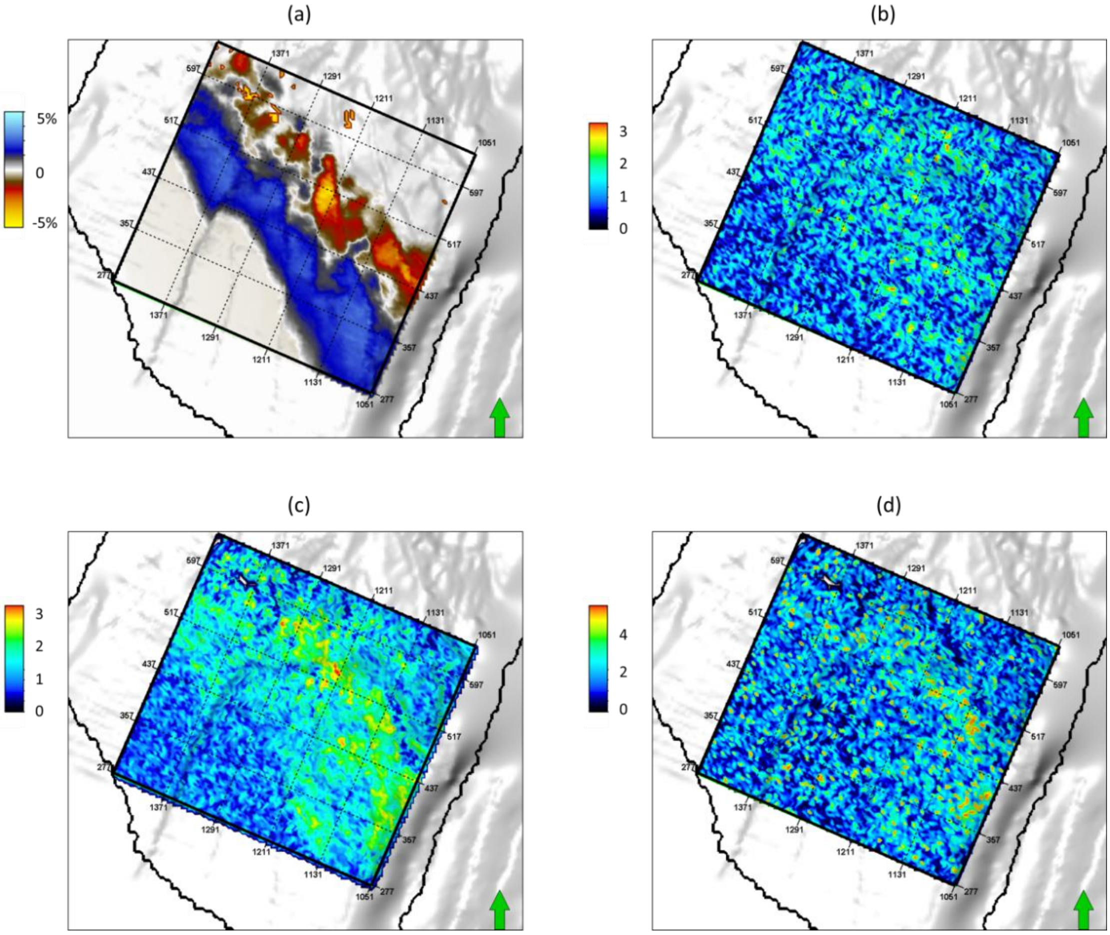

Figure 3.19 *The a priori information for EC 4D inversion. (a) the reservoir engineering prediction of the 4D P-impedance changes under production; (b) the noise map estimated from the overburden area; (c) the 4D signal map estimated from the Fangst reservoir interval; (d) the quotient of the signal and noise.*

The Bayesian posterior distribution of the changes in P-impedance is estimated with the MCMC approach similar to the baseline seis2sim, as discussed in Chapter 2. Two inversion tests are done with and without the *a priori* information, to highlight the impact of the proposed EC constraints. Figure 3.20 shows the 4D seis2sim results without any engineering predictions or deliberate consideration for the non-repeatability noise. In other words, it is supposed to conduct a free search in the posterior solution space in which the observed 4D seismic amplitude is the only criterion metric to be assessed. Figure 3.20(a) plots the observed 1991 baseline trace (black line) and the 2008 monitor (red line) in time. The Fangst reservoir lies between the largest peak reflection, at about 2180ms, and the largest trough, at around 2244ms. It is noticed that the monitor trace shows a smaller lithology variation in the overburden area, as the amplitude changes are smoother. Given the fact that the monitor seismic was better processed, the 2008 data is more reliable and the relatively large amplitude oscillations in the baseline would be a primary source of data noise in the 4D amplitude difference for seis2sim. Indeed, the standard deviation of the 4D amplitude in the overburden is 0.46 (noise) in contrast to 0.51 of that in the reservoir interval (signal strength), resulting in a signal-to-noise ratio fairly close to unity. Therefore, the inverted impedance changes tend to present a large posterior uncertainty in the results. Consequently, most of the realisations are hard to interpret in the overburden and underburden areas, where no impedance changes are expected to happen. Statistically, the confidence region is on average reduced by 47% in the overburden and 65% in the reservoir interval throughout the inversion.

In contrast, Figure 3.21 shows the EC 4D seis2sim results. Firstly, a larger data uncertainty is given to the likelihood assessment, which reflects the uncertainty introduced by the residual misfit of baseline inversion, the estimated 4D noise, and signal strength. Outside the Fangst group reservoir, the data uncertainty is characterized in the covariance matrix as the diagonal elements which sum up the variances of the baseline residual error and the noisy amplitudes from the overburden. This scheme results in a wider confidence interval outside the production zones, as seen in Figure 3.21 (b) while statistically respecting the amplitude changes inside the Fangst formation. The sim2seis prediction of P-impedance change is employed in the Bayesian prior model as *a priori* expectation (see Figure 3.21 c). The prior model is assumed to

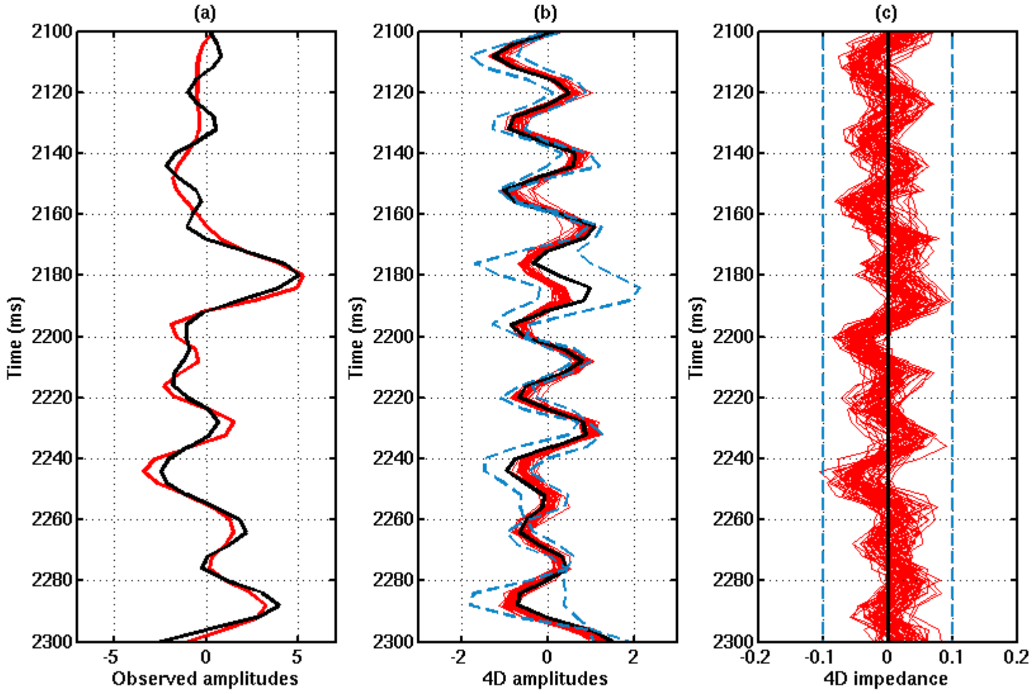

Figure 3.20 *1D example for the difference inversion without constraints. The reservoir lies between 2180ms and 2244ms. (a) the observed baseline trace (black) and the monitor (red); (b) 40 posterior realisations of the synthetic 4D seismic trace (red) and the observed 4D difference trace (black) obtained by subtracting the baseline and monitor traces in (a). The blue dashed lines show the uncertainty associated with the observed data, which are caused by the residual misfit from the baseline synthetic shown in Figure 3.15; (c) the calculated realisations of impedance differences associated with the prior expectation (thick black line) and the 0.95 prediction interval (blue dashed lines).*

be multi-Gaussian, in which the sim2seis predictions are the diagonal elements. The off diagonal elements are the cross-correlations featuring the vertical reservoir connectivity.

After 4D seis2sim inversion, the amplitude realisations show a relatively poorer match to the observed data, due to the larger data uncertainty. However, the match inside the Fangst group is fairly close. The resultant 4D P-impedances suggest a more consistent trend over the realisations in Figure 3.21 (c). The unexpected changes outside the reservoir zone are suppressed by the designed EC constraints and the revealed decreases in P-impedance are meaningful under the gas flooding scenario. Comparing the performances of the unconstrained approach with the constrained in Figure 3.22 (a), it is noticed that both of them start to converge after 2000 iterations. Although the EC constrained inversion shows a 10 percent higher residual error in the likelihood than the

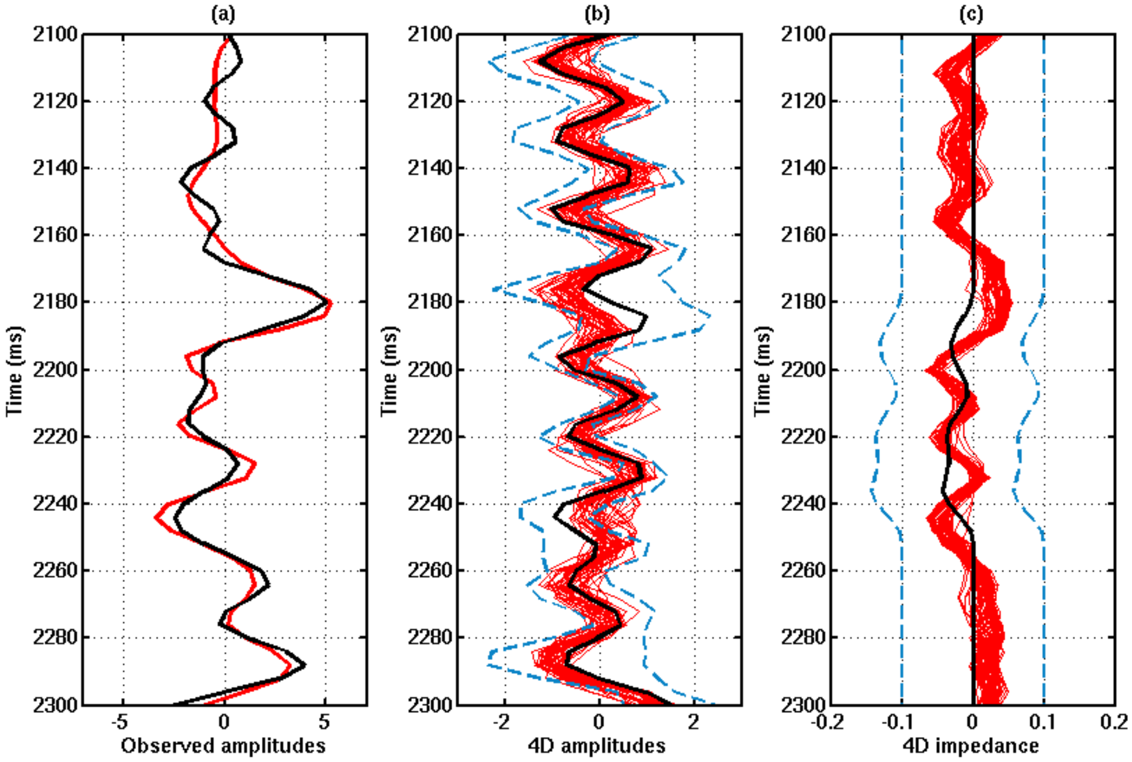

Figure 3.21 *EC constrained inversion. (a) the observed baseline trace (black) and the monitor (red); (b) 40 posterior realisations of the synthetic (red) and observed 4D difference trace (black). The blue dashed lines show the 0.95 confidence interval associated with the observed data, which are determined communally by the baseline residual misfit and the data noise estimated from the overburden; (c) the constrained inversion results (red), associated with the prior PEM expectation (thick black line) and the 0.95 prediction interval (blue dashed lines).*

unconstrained one, it could be argued that the unconstrained inversion might have over-matched the noisy data. By comparing the convergence processes of a same seismic sample at the gas cap location, in Figure 3.22 (b), the EC result converges to a more stable solution at around -0.07 while the other does not. This indicates that the unconstrained inversion, though matching the data well, is not as stable as the constrained. Figure 3.22 (c) and Figure 3.22 (d) show the statistics of the realisations for the gas cap sample, as discussed before. The *a priori* expectation of the unconstrained inversion is zero, with a standard deviation of 10%, and after inversion the changes are found to be around 2%, associated with a standard deviation of 5.5%. The constrained case is better determined, as the posterior realisations have converged to -6% with a smaller standard deviation of 1.7%.

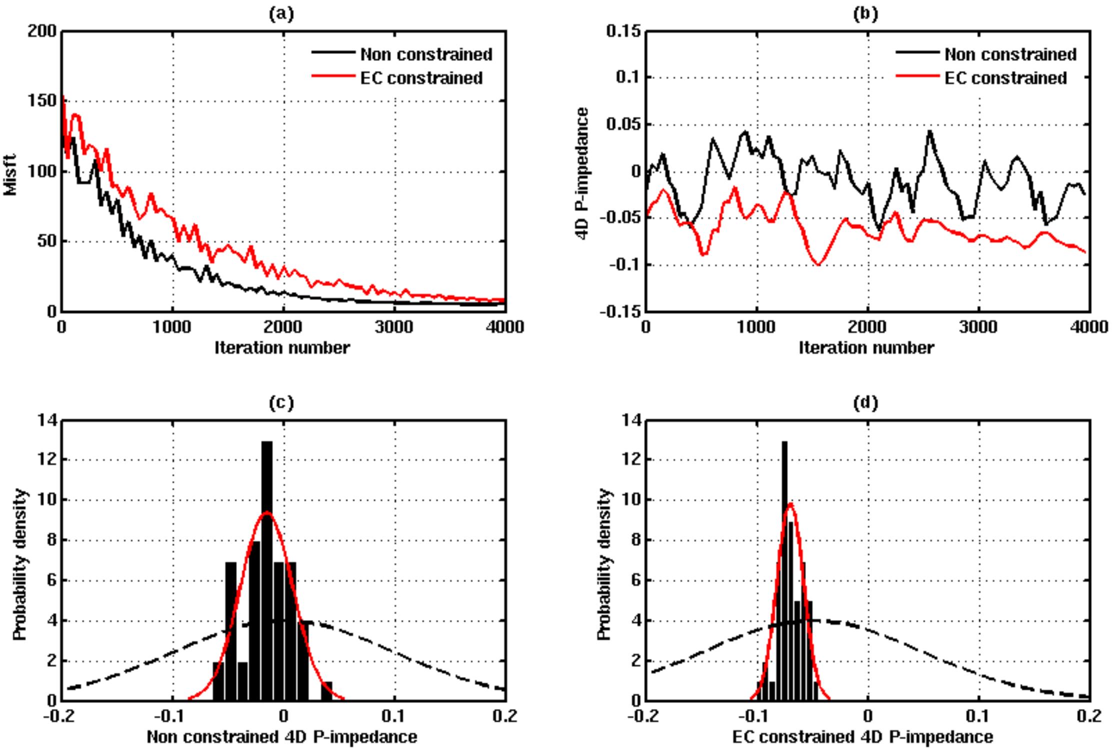

Figure 3.22 *Convergence for the unconstrained and EC constrained seis2sim approaches. (a) the evolution of residual misfits for the unconstrained (black) and EC constrained (red) inversion recorded in the amplitude likelihood function with iterations; (b) the evolution of P-impedance changes of two samples from the gas cap horizon. The unconstrained method (black) fails to converge while the EC constrained (red) converges to a 0.07 decrease; (c) the histogram of the posterior realisations of the unconstrained 4D inversion; (d) the histogram of the posterior realisations of EC 4D inversion. The black dashed lines show the prior distribution.*

The posterior mean solution of the EC 4D seis2sim is shown in Figure 3.23. The top and bottom of the Fangst group are plotted as the first two red lines, and the area bounded by the second and the third red horizons represents the underburden shale in the Not formation. The original 4D amplitude changes in Figure 3.23 (a) are very noisy, so that the signal could barely stand out. Figure 3.23 (b) and Figure 3.23 (c) show the inverted P-impedance difference and the associated uncertainty. The extensive impedance decrease on the right is related to the gas injection. The consequent gas cap which accumulates in these shallow compartments led to a 5 to 10% decrease in P-impedance, which is associated with a standard deviation of up to 6%. The large uncertainty here could be a consequence of the combination of the noise and a fault panel, where the processing is more difficult. Additionally a 3 to 7% impedance

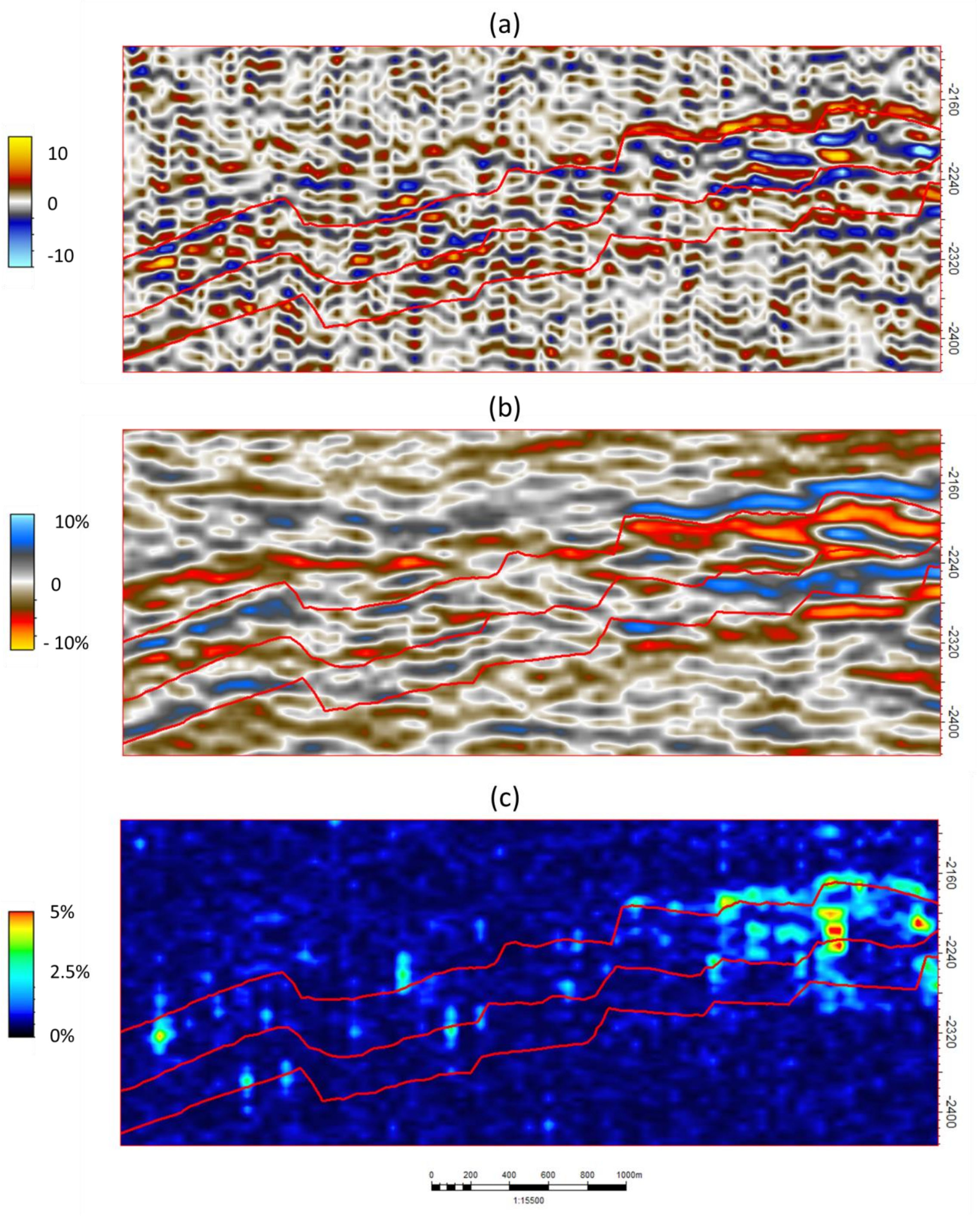

Figure 3.23 *The posterior mean solution of the EC 4D seis2sim. The top Fangst, bottom Fangst and the bottom Not shales are represented by the three red lines. (a) the observed 4D seismic amplitude; (b) the EC 4D P-impedance solution; (c) the associated standard deviation of the EC 4D solution.*

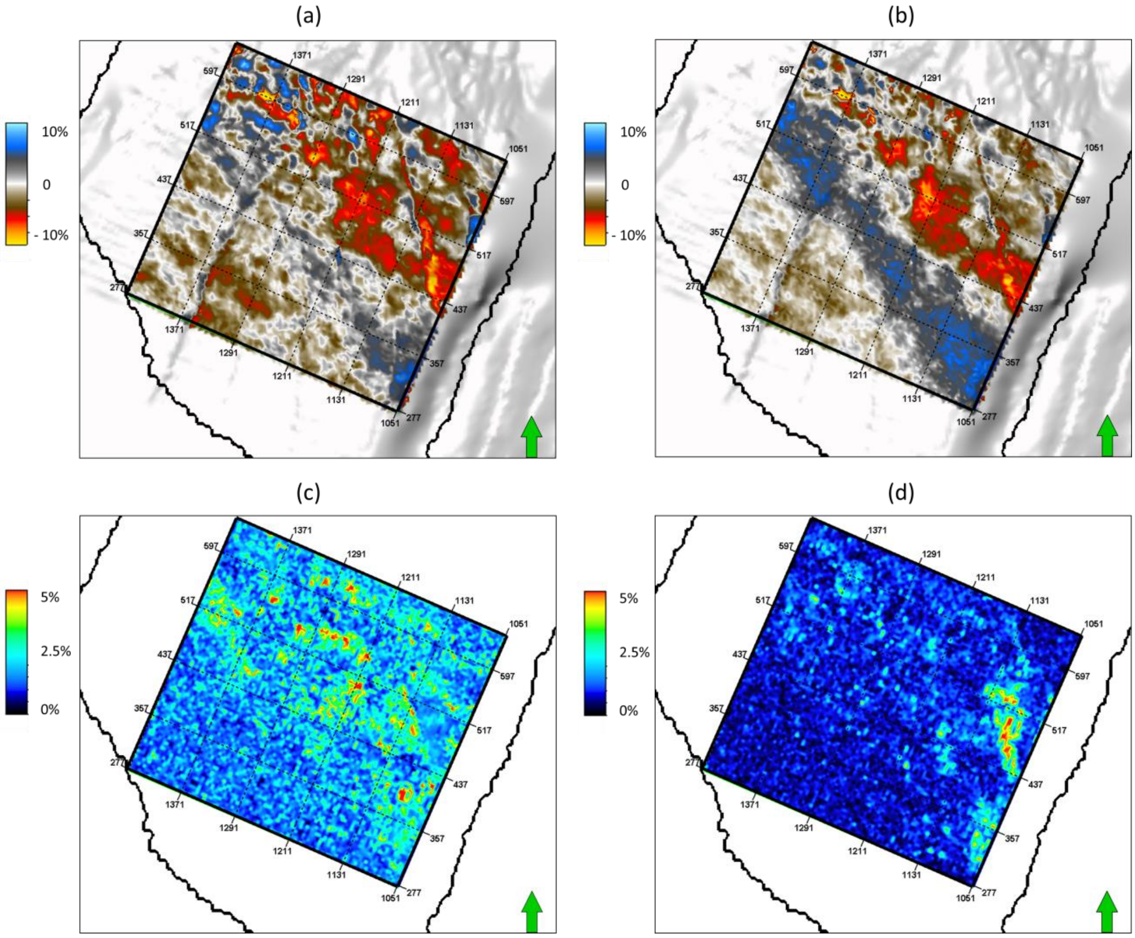

Figure 3.24 *The average maps of the EC 4D seis2sim in the area of interest. (a) the average 4D P-impedance over the Fangst group by the unconstrained inversion; (b) the average 4D P-impedance map by the EC 4D inversion; (c) the average map of the standard deviation by the unconstrained inversion; (d) the average standard deviation map by the EC 4D inversion.*

increase is observed on the left where the water injection takes place. These results are averaged over the Fangst group to generate the maps shown in Figure 3.24. Visually, the unconstrained and the EC 4D seis2sim show a similar pattern of P-impedance change. In both cases, the gas cap is represented by 7 to 10% impedance "softening" in the central north of the of interest, while the water-flooded area is represented by impedance "hardening" above the original oil-water contact (Figure 3.24 (a) and (b)). However, the unconstrained inversion could not determine the solution in the water flooding zones, as the posterior solution has mean values close to zero, with large standard deviations. The EC 4D seis2sim shows a more accurate map overall, and the fluid pattern of the water flood in the south is better imaged. The uncertainty is primarily found to the west of a major fault, due to the potential problem of the horizon pick.

3.5 Summary

Application of the proposed seis2sim approach to the Heidrun dataset reveals a clearer and more meaningful solution, according to the static reservoir characterisation and dynamic flow simulation. The petro-physical study of the well log data, and the geological framework are integrated into the seis2sim workflow as *a priori* information. The inverted baseline P-impedance shows a clear image of the distribution of Fangst sands, which is honoured by the 4D seis2sim as an initial reference to generate a consistent 4D impedance attribute. The EC 4D seis2sim approach is more stable than the unconstrained (non-EC) inversion, and the associated uncertainty is smaller, according to the reservoir simulation predictions. The results provide higher confidence for a subsequent cross-domain comparison, which is considered as the key to performing the closing-the-loop exercise, which is to be discussed in the next chapter.

Chapter 4

Closing-the-loop with seis2sim for the Heidrun field

“The softest thing in the world dashes against and overcomes the hardest.”
「天下之至柔，馳騁天下之至堅。」

Lao Tze, *Chapter. 28, Tao Teh Ching, 400 BC to 700 BC*

“Nature is pleased with simplicity.” - Isaac Newton

“Everything should be made as simple as possible, but not simpler.” - Albert Einstein

A two-stage workflow is designed to close the static and dynamic loops of the Heidrun dataset, in which the seis2sim results are used as the key drivers. The reservoir model is initially matched to the production data only while its static and dynamic seismic responses do not replicate the observations. Closing the 3D and 4D seismic loops according to this discrepancy leads to an improved model reliability in both the geophysical and reservoir engineering domains.

The Heidrun dataset primarily consists of well log measurements, the reservoir simulation model, and the 3D and 4D seismic vintages. To make sense of the seis2sim results and update the reservoir model, a workflow to close the loops between them is needed, which is expected to be as simple and robust as possible.

4.1 Closing-the-loop workflow for the Heidrun field

Fürre et al. (2003) extracted 4D amplitude maps for the main production units by subtracting the corresponding vintage maps. The maps show the pattern of water flooding and the movement of the fluid contacts. A visual comparison between the seismic-derived maps and the fluid-flow simulation highlighted the fault compartments, in which the seismic and reservoir model show disparities (Fürre et al., 2004 and 2006). In spite of the fact that the comparison was visual and qualitative, the integration of well log, reservoir simulator, 3D and 4D seismic has proven its value in updating the reservoir model. However, in order to quantitatively close the loops among the available datasets, efforts are not only required in the extraction of a robust attribute with which to perform the cross-domain comparison, but also in rationalizing the workflow to update the key parameters according to their impact. This leads us to a workflow that is designed to quantitatively close the static and dynamic loops by updating different

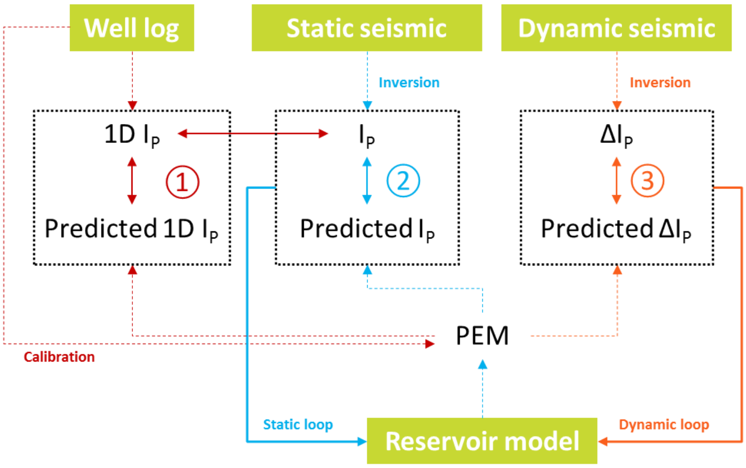

Figure 4.1 *The workflow to close the loops. Dashed lines indicate the processes that have been performed during the seis2sim workflow discussed in the previous chapter. The two-way arrows show where the comparisons take place in order to feed back to the reservoir model.*

aspects of the reservoir model in a fast-track manner (Figure 4.1). The impedance domain is selected to close the loops, as it is believed to be an adequate attribute which represents the entire reservoir volume in the exercise (MacBeth et al., 2006). The first loop is closed at the well log domain in which the PEM model is calibrated prior to the seis2sim (see Chapter 3). This loop is closed only if the P-impedance log predicted by the reservoir model, the seismic derived P-impedance log and the wire-line logged P-impedance agree with each other. Closing this loop gives confidence in the calibrated sim2seis predictions, as well as the consistency between the wireline log's measurements and the static reservoir model. It is also crucial for the quality check of the seis2sim results at the well location. A second loop to be closed is the static loop, as labelled in blue in Figure 4.1. This ensures that the static reservoir model synthetic 3D seismic response matches with the observed response. Updating the porosity distribution in the reservoir model is considered to be the primary objective in closing the static loop, as the sand fraction in the Fangst group is almost unity. Additionally, the net-to-gross (NTG) values in the reservoir model are set to unity inside the Fangst zones and retained during the workflow. The 4D seismic and its inverted impedance changes are used to close the dynamic loop by comparing them with the corresponding model predictions. The primary uncertainty that dominates the dynamic model behaviour is the presence of fault connections between different compartments (Benguigui, 2010), which will be updated according to the discrepancy highlighted in the dynamic loop. The production match is of continuous concern during the workflow, as it indicates adherence to reservoir engineering laws.

4.2 Reservoir characterisation and development scheme

The Fangst group reservoir is complex in structure. It consists of several fault blocks with partial pressure and fluid flow communication. As discussed before, the Fangst group was subject to partial erosion during the Cretaceous uplift, which is underlying the later Cretaceous sand deposits. These Cretaceous sands cannot be mapped seismically with great confidence (Fürre et al., 2006), because of the lack of seismic contrast between them. However, these laterally extensive sands serve as local paths for fluid flow across different fault segments, resulting in additional uncertainty in the flow simulation. Apart from the difficulty in modelling the distribution of these highly porous (up to 35%) sands, the primary challenges for the dynamic field management is the compartmentalisation caused by the fault connectivity between different reservoir segments.

4.2.1 Static reservoir description

In the flow equations used in the reservoir simulation, porosity appears to be one of the parameters that scales the volume of fluids present in the reservoir at any time. During production, this volume is depleted, and reservoir pressure drops. The higher the reservoir porosity is, the less this pressure decline will be over the production time. Figure 4.2 shows the average pore volume map over the Fangst group cells for the

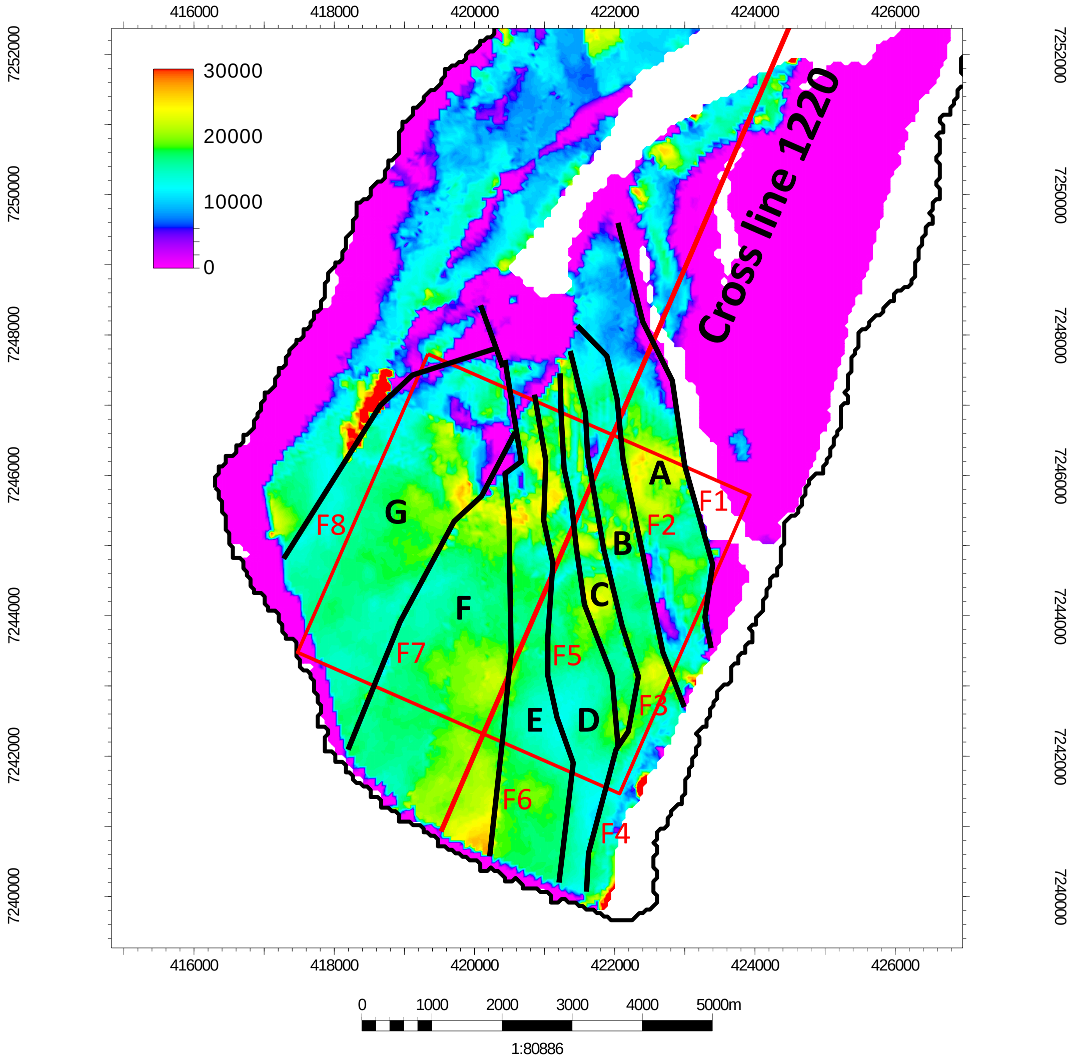

Figure 4.2 *Map of average pore volume over the Fangst group. The major faults that are modelled for simulation are shown in solid black lines which divide the reservoir into seven segments.*

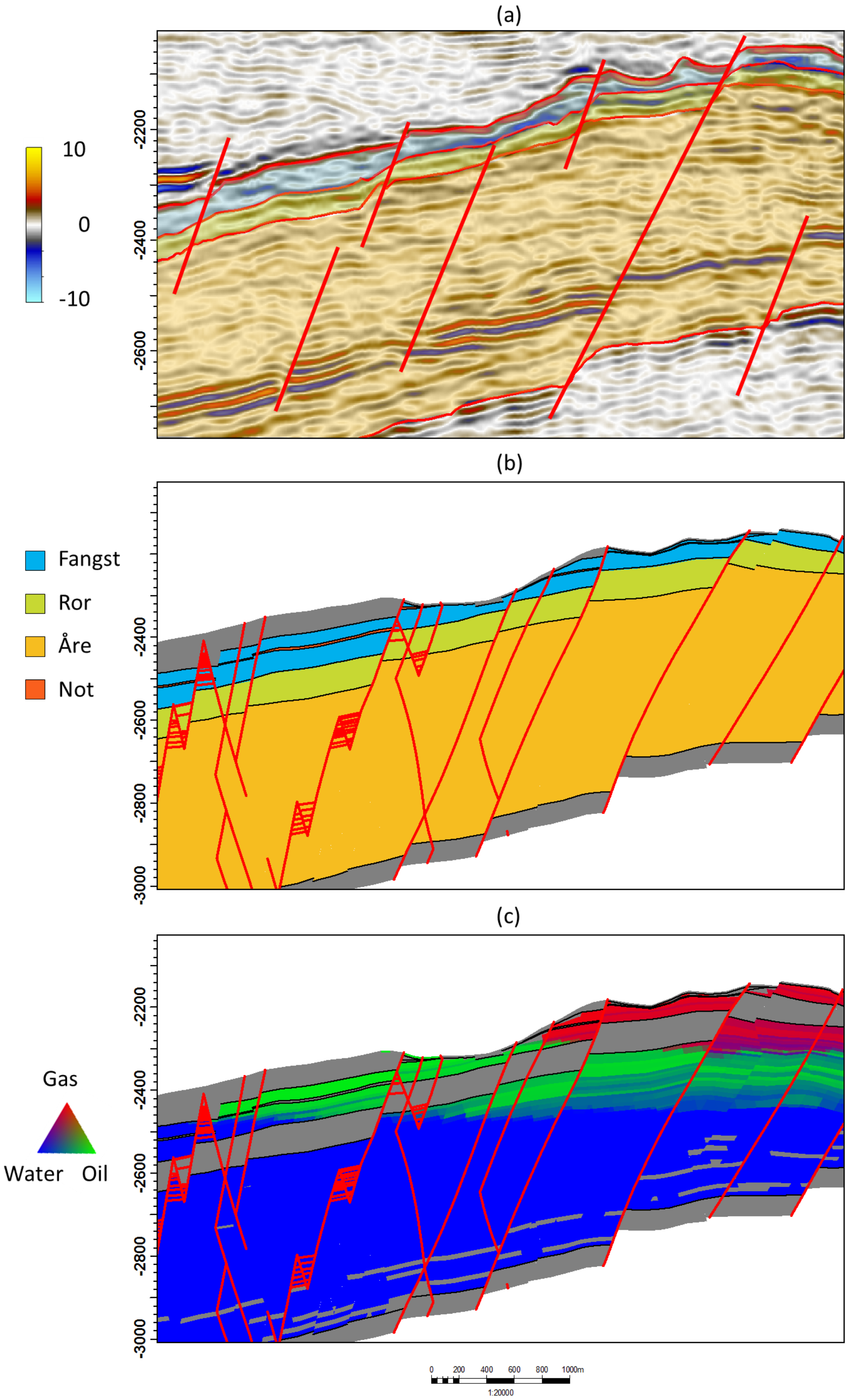

Figure 4.3 *A vertical view of the Fangst reservoir through cross line 1220. (a) the baseline seismic and the interpreted reservoir zones; (b) the corresponding depth zonation in the reservoir simulation model; (c) the initial fluid contacts in the reservoir model.*

initial reservoir model. The eight major faults that are modelled in the south flank (labelled from F1 to F8) have divided the reservoir into seven reservoir segments (labelled from A to G). The pore volume has a mean of 16000 rm^3 (reservoir cubic metres) and the distribution of the highly porous sands does not show any distinctive sedimentary features due to down-cutting and erosion from the overlying fluvial sediment. A seismic cross-section through Cross line 1220 is selected to understand the reservoir vertically (Figure 4.3). The Fangst group has an average seismic thickness of 50 ms at a sample interval of 4 ms. These 10 to 12 seismic samples are modelled by 10 layers of model cells in the reservoir model, with an average height of 10 m. These lead to an identical number of variables vertically for the seismic inversion and reservoir modelling. In other words, the seismic and the reservoir model share similar resolutions, which is the the key to performing the time-to-depth conversion based on a mapping technique (Thore, 2011). The initial oil-water contact is at a depth of approximately 2490 m, with an initial gas cap lying 100 m above. The Not shale separates the Fangst from the underlying Åre group, and its properties are retained during the CtL workflow.

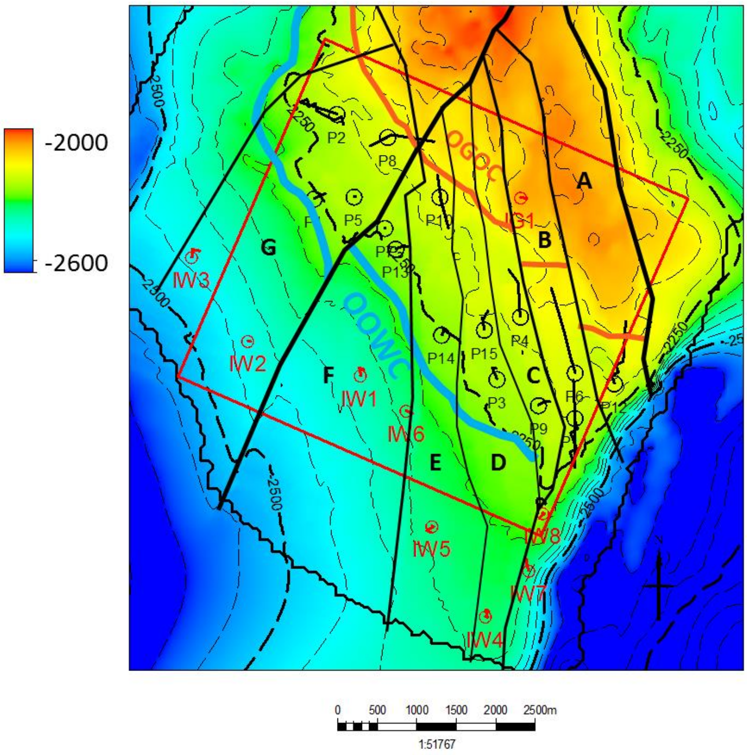

Figure 4.4 *Well pattern modelled for the Fangst group. The water injectors are labelled from IW1 to IW8, together with the gas injector IG1 in the initial gas cap.*

4.2.2 Production history

The primary drainage strategy of the Fangst reservoir in the south flank was a row of producers drilled in the porous part of the oil column in each segment, with pressure supported by the down-flank water injectors. Re-injection of gas into the initial gas cap at the top of the structure also provides pressure support. Fifty-five wells and side tracks have been drilled during the field development, while fifteen of them are active during selected study period (Figure 4.4). Seven water injectors are placed in the southern aquifer to drive the oil up to the northern producers while IG-1 injects gas into the gas cap to maintain the pressure in the top reservoir. The simulation model incorporates the production history from 1995 to 2011, during which most of the producers were watered out around 2004. Figure 4.4 (a) and (b) show the initial and post-production maps of the fluid distribution, according to the simulation. The oil has been produced in

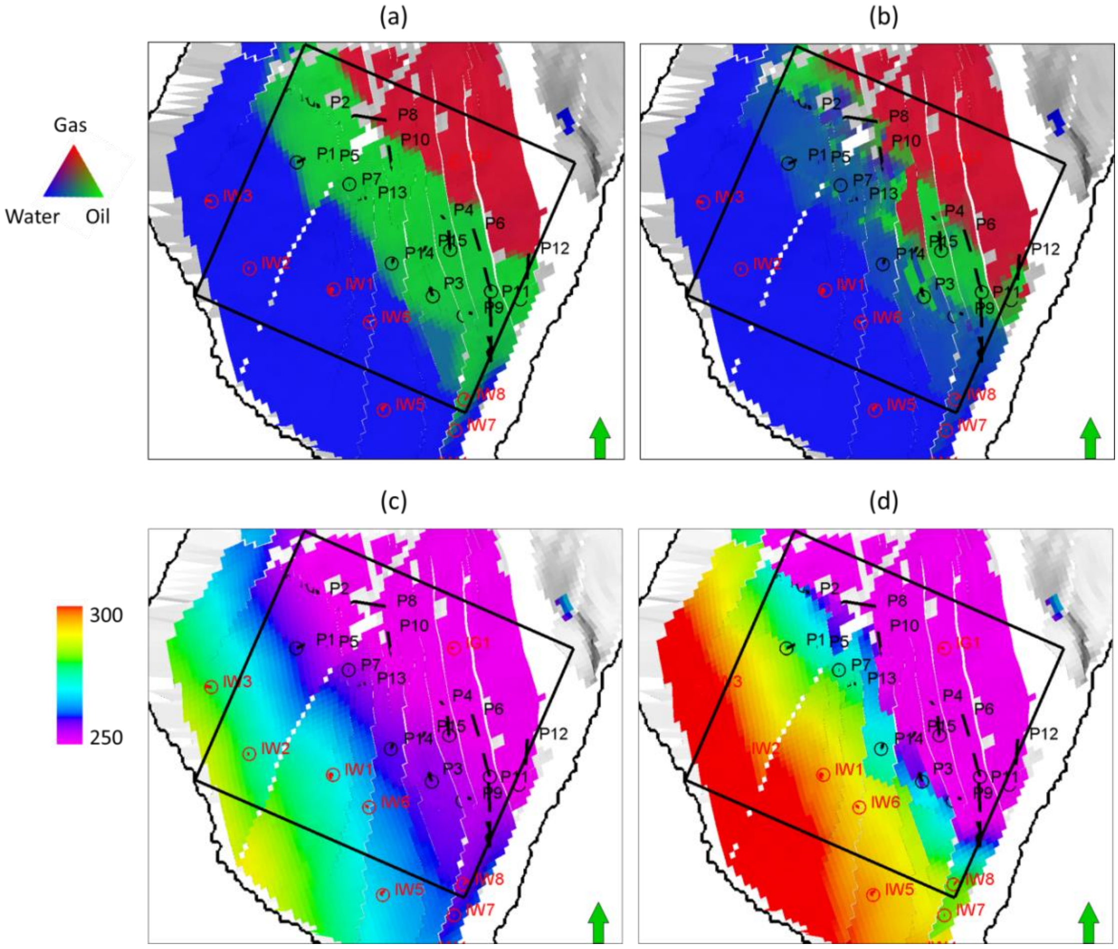

__Figure 4.5__ (a) The initial fluid distribution at 1995; (b) the prediction of fluid distribution after 13 years of production; (c) the initial pressure field in the Fangst group; (d) the post-production pressure field prediction by the simulator.

most of the segments, resulting in a rise of the oil-water contact. The water saturation change between the original oil-water contact and the new oil-water contact is up to 85%, which is considered as the primary source of signal for the 4D seismic in this area. Pressure changes of up to 10 bars of are predicted in the aquifer area, where above the original oil-water contact the pressure changes can be as high as 25 bars. The initial reservoir model is matched to the production history. According to Figure 4.6 (a), the selected 4D seismic pair (baseline 1995 and monitor 2008) are expected to detect an average change of 25 bars in pressure. However, according to Fürre et al. (2003), the pressure signals are considered negligible compared to the saturation changes. The field scale gas-oil ratio and water cut profiles are considered as two first order parameters for history matching, in addition to the overall material balance. According to Figure 4.6 (b), history matching with the initial model is able to replicate the overall production, and the volumetrics are reasonably close to reality.

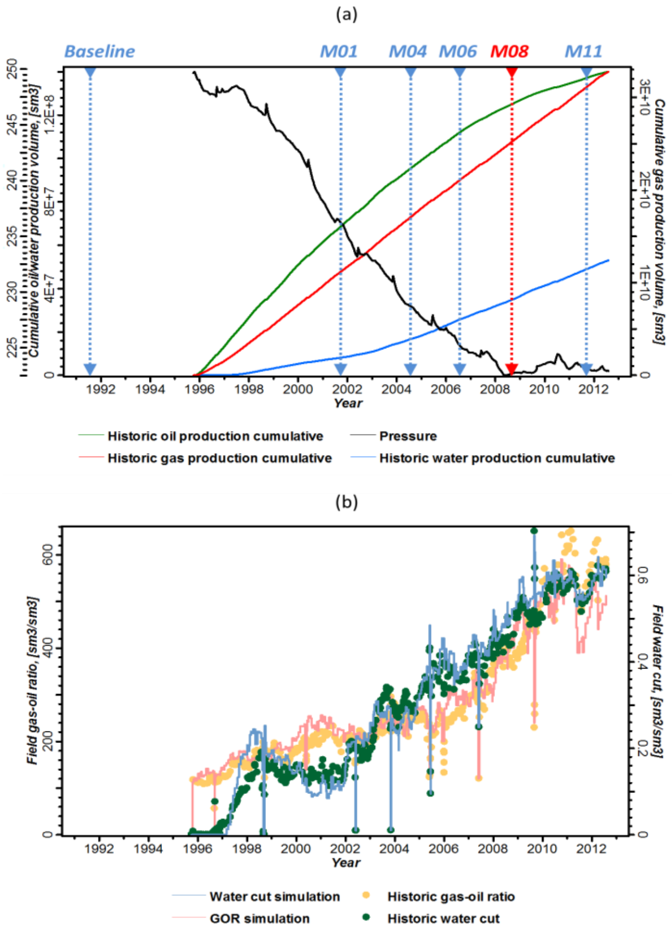

Figure 4.6 *Field scale history matching: (a) the cumulative production volumes of the oil, gas and water, together with the field scale pressure profile; (b) the simulated and historic gas-oil ratio and water cut, which are the first order parameters for the material balance check.*

4.3 Closing the static loop with 3D seis2sim results

It is common practice for the framework and property distributions of a geological or reservoir property to be defined by the integration of 3D seismic and geostatistics. However, the practice is rarely performed in a consistent way, due to operational reasons. Therefore, the primary objective of closing the static loop is to ensure the reservoir model has the ability to replicate the observed static seismic. In the sim2seis calculation, the porosity and NTG (net-to-gross) sand fraction are the two controlling parameters which effectively determine the resultant velocity model. Indeed, the NTG is assumed to be unity, as the Fangst group consists only of clean sands. Therefore the populated porosity distribution needs to depict the reservoir as an alternative representation of the 3D heterogeneity observed by the baseline seismic.

The static loop needs to be closed in both the wireline logs and the reservoir model domain. Practically, a petro-physical model has been validated at the seis2sim stage (see Chapter 3), with which the synthetic P-impedance model can be predicted in order to compare with the wireline measurement and inversion result. The process of this model-derived P-impedance is referred to as a forward modelling and the result is compared with the other two "hard" observations – the seis2sim inverted P-impedance log and the wireline log – where the loop is closed. However, the seismic does not directly measure the petrophysics, therefore a valid rock-physic model is needed to estimate the porosity,

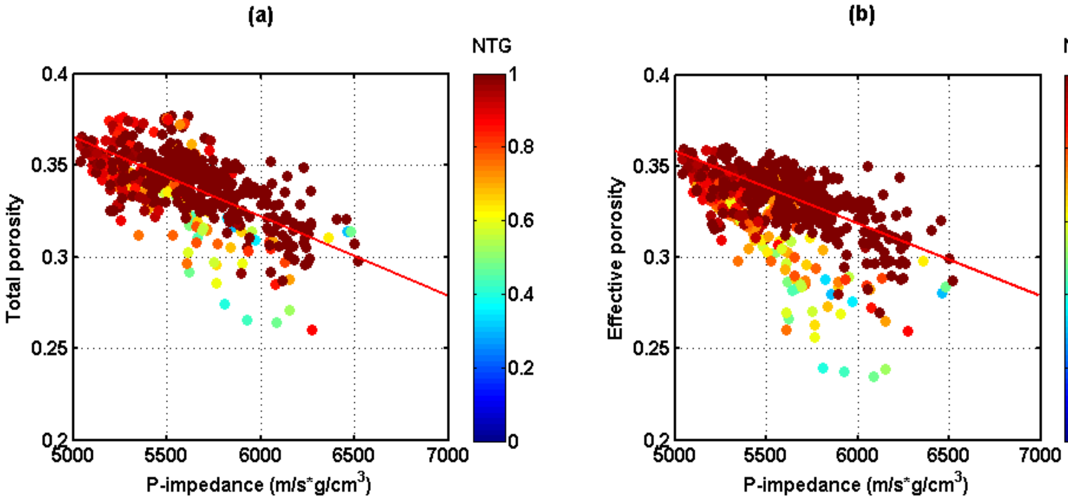

Figure 4.7 *The empirical calibration between (a) P-impedance and total porosity and (b) P-impedance and effective porosity.*

This rock-physics model can be theoretical, empirical or heuristic (Avseth, Mukerji and Mavko, 2005). In our workflow, a hybrid model including both the theoretical and empirical approaches is chosen to keep the updates simple and robust. An empirical linear relationship (Han, 2001; Avseth et al., 2005) between the P-impedance and porosity is assumed and the log data of the Fangst group is used to calibrate and determine the empirical gradient and intercept by linear regression (Figure 4.7). Little difference is observed in the regressions of total and effective porosity to P-impedance; it was therefore decided to make no distinction between them, while directly correlating P-impedance to the effective porosity, for the ease of reservoir simulation. With the calibrated rock-physics model, the multi-disciplinary comparison can be performed by assessing the impedance and porosity attributes in the log domain. Figure 4.8 (a) seeks the match in P-impedance among the wireline log, the seis2sim and the forward

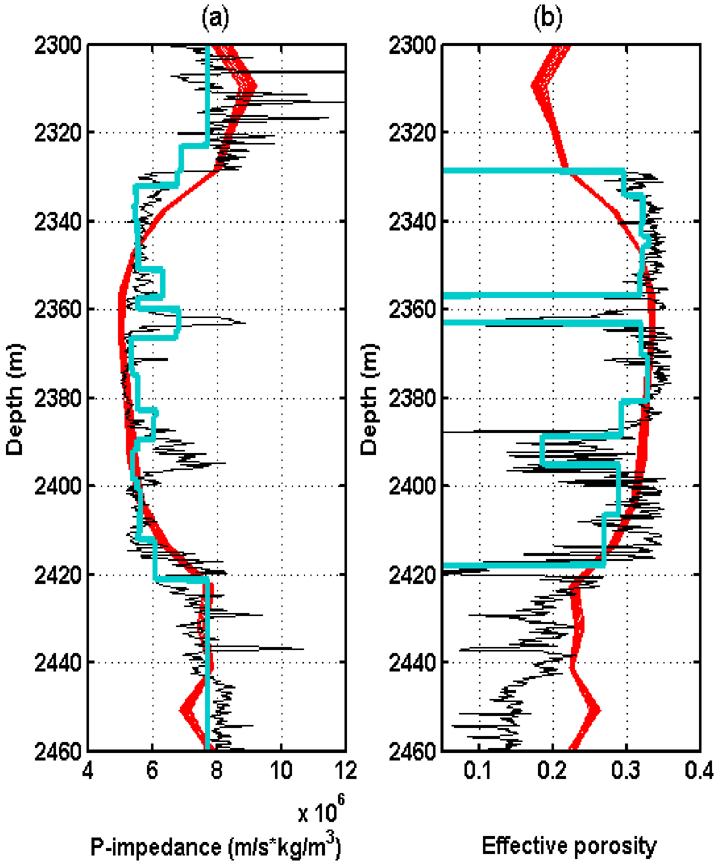

Figure 4.8 *Closing the static loop in 1D: (a) The match in P-impedance among the wireline log measurement (black), the synthetic from the reservoir model based on the initial porosity (blue) and the 40 realisations from seismic inversion (red); (b) the match in effective porosity among the wireline log measurement (black), the initial values from the reservoir model (blue) and the 40 realisations converted from the seismic inverted impedance (red).*

modelling by sim2seis. Generally they agree with each other, while the seis2sim results tend to be smoother than the other two, due to the original resolution of the seismic. Therefore, the ability of the seismic to detect vertical heterogeneity of the Fangst reservoir is poor, while the simulation cells could potentially model details at a resolution of 4-5 metres, limited by the cell heights. Nevertheless, the seismic prediction of effective porosity also features the general trend of the wireline log measurement inside the Fangst group. In contrast, the predicted seismic porosity deviates from the log data in the underburden shale, where the calibrated rock-physics model is not valid (Figure 4.8 (b)). In summary, the match in the log domain presents the very first loop that is closed by the success of the petrophysical calibration and conversion, which provides the workflow with the fundamental reliability in the static reservoir characterisation.

After closing the 1D loop, a seismic consistent effective porosity model is derived from the seis2sim P-impedance volume and assigned to the 3D reservoir model. The aim is to redistribute this porosity model to enable the model to replicate the observed 3D seismic - in other words, to close the static seismic loop. As a parameter closer to the reservoir engineering domain, the reservoir pore volume (PV) is the product of the gross volume of a cell, the NTG and the effective porosity, which directly reflects the volumetric capacity of the reservoir and affects the seismic response of the reservoir model. Since the NTG value is held constant for the Fangst group, the PV is adequate to highlight the distribution of reservoir quality. Figure 4.9 (a) and (b) show the PV distribution before and after the porosity update, where Figure 4.9 (c) shows the percentage difference between them. It is found that the seismic solution visually shows a similar pattern with the reservoir model, in which the porosity model is initially populated by the conditioned geostatistics. The fact that the percentage change of PV is continuous instead of being scattered proves that the EC inversion has honoured the initial geology concepts employed by the modeller. Figure 4.9 (d) shows the difference of the predicted reservoir pressures at the same monitor time. In segment E, up to 2 bars of pressure increase is found, which is correlated to a 10% decrease in PV. In Segments C and D, the correlation is not straightforward, but clear barriers are noticed at the faults. Figure 4.9 (e) displays the water saturation map before and after the porosity update.

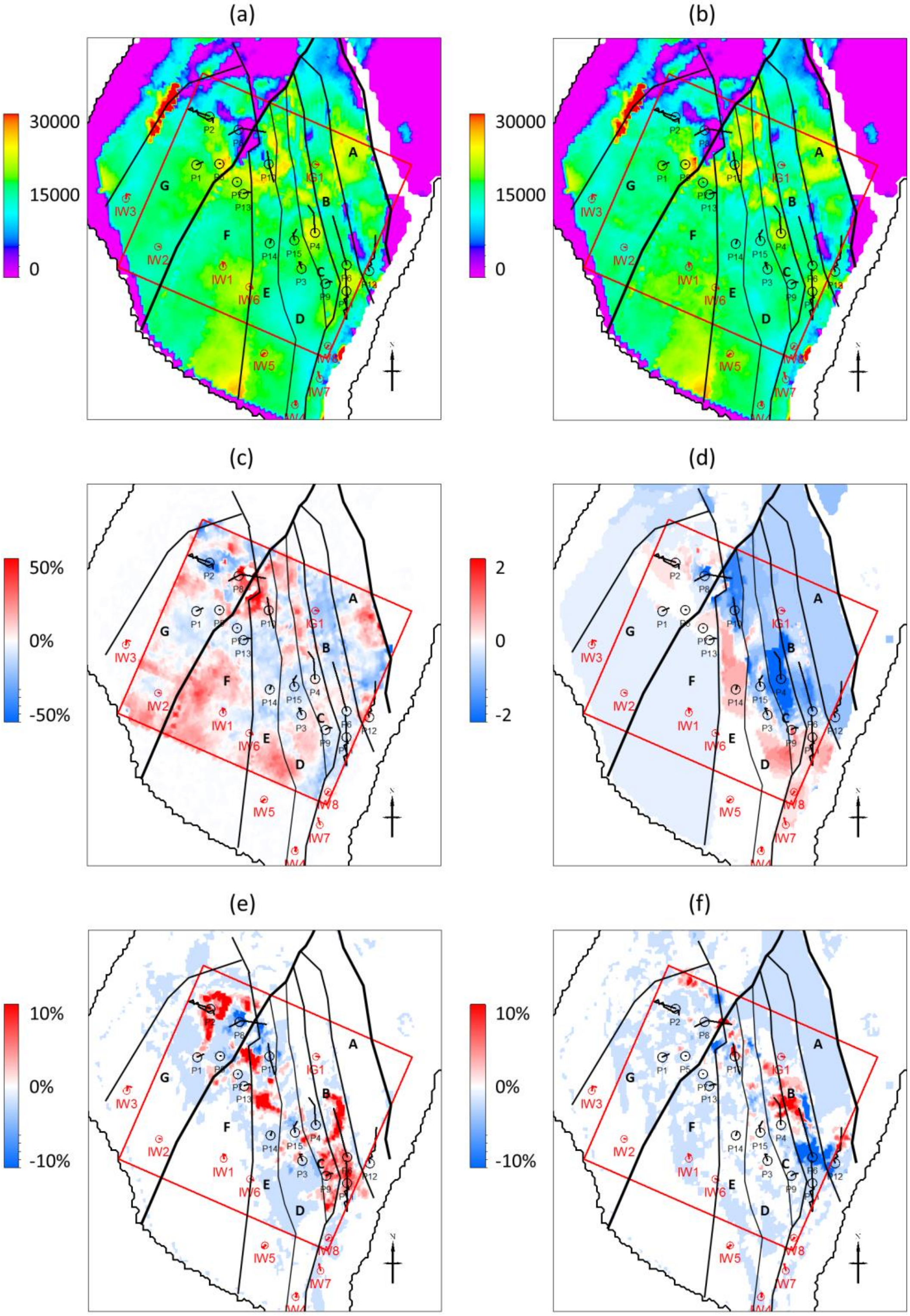

__Figure 4.9__ (a) The initial PV map in standard cubic metres; (b) the updated PV map in standard cubic metres; (c) the percentage difference between (a) and (b); (d) the difference of the predicted pressure map at the 2008 monitor time; (e) the difference of the predicted water saturation map at the monitor time; (f) the difference of the predicted GOR map at the monitor time.

Remarkable patches of water saturation increase are found in Segments B, C, E, F, and G, all of which are associated with PV decreases. This indicates a speed-up in the water flood due to the reduction in available flooding volume. Significant gas presence is found in Segments B and C, where the PV decreases and the GOR increases. In fact, these areas correspond to the secondary gas cap and the change in PV could alter the gas saturation predictions.

A number of local wells are chosen in these segments to evaluate the corresponding impact of the porosity update. The GOR profiles of P-4 and P-6 are plotted in Figure 4.10 (a) and (b). P-4 is sited in Segment C, next to the area which has more gas presence

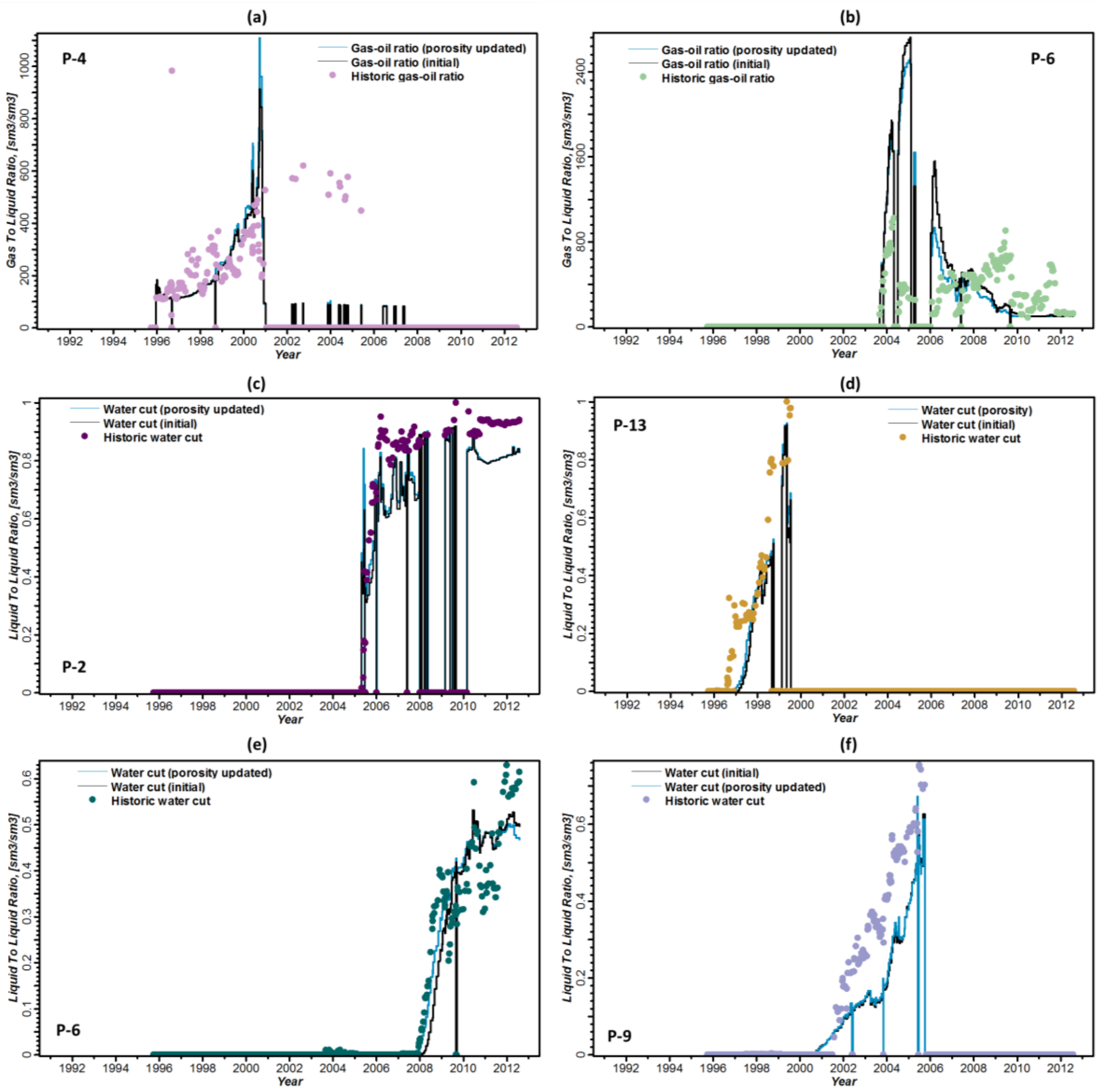

Figure 4.10 *The production profiles from 6 local wells.*

in Figure 4.9 (f). Compared to the historic GOR record, the updated model tends to predict more gas than it does before the porosity update. P-6 is in Segment B, where its perforation lies in an area of reduced gas saturation. According to the simulation, the updated model gives a lower GOR profile compared to the initial one, which is closer to the historic observation. P-2, P-6, P-9 and P-13 are chosen to evaluate the impact on the water saturation prediction, as their perforations are carried out in the areas where the major changes take place. All of them show positive changes in terms of water cut, according to the updated simulation model, with minor improvements. Nevertheless, the updated model tends to give more accurate predictions based on the new PV model. In addition, the field scale match in both GOR and water cut are retained to a similar level; it can be thus concluded that the new model has honoured the material balance (Figure 4.11).

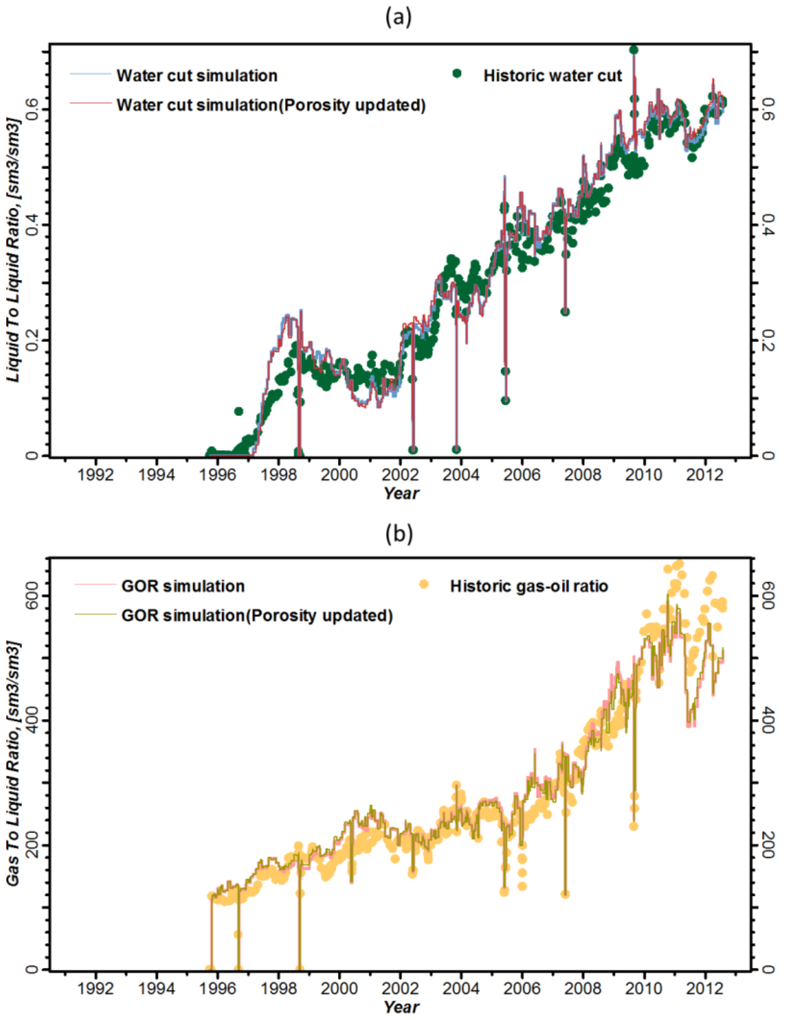

Figure 4.11 *(a) The field-scale profiles of water cut before and after the PV update. (b) The field scale profiles of the GOR before and after the PV update.*

As discussed previously, the primary aim of the porosity update is to capture the realistic lateral heterogeneities that are featured by the 3D seismic. In order to assess this,a synthetic 3D seismic cube is generated based on the new porosity model, from which the RMS amplitude map is calculated using a 20ms window sitting on the top of the Fangst group. The strength of the resultant RMS amplitude reflects the lithological contrast between the overburden shale and the underlying Fangst sands, and therefore the distribution of the reservoir quality. This map is subsequently compared with the maps without the porosity update and which were directly obtained from the observed seismic (see Figure 4.12). Generally, the lateral resolutions of the model-generated maps are lower than the ones from observed seismic. This is due to the fact that the model cells are of an average width of 100m while the seismic was acquired at bin size of 12.5m by 12.5m. A major change is found in the southern aquifer area, where the model was almost homogenous before the porosity update. With the new PV distribution, the reservoir model now honours the disposition of the fault compartments that are captured in the observed seismic, as well as the reservoir distribution in between the faults. The updated map resembles the observed one, and this indicates that the static loop is sufficiently closed between the reservoir model, the observed 3D seismic and the production data. Thus realistic PV model also alters the flow behaviour in the dynamic simulation, forming a new framework in which the production takes place.

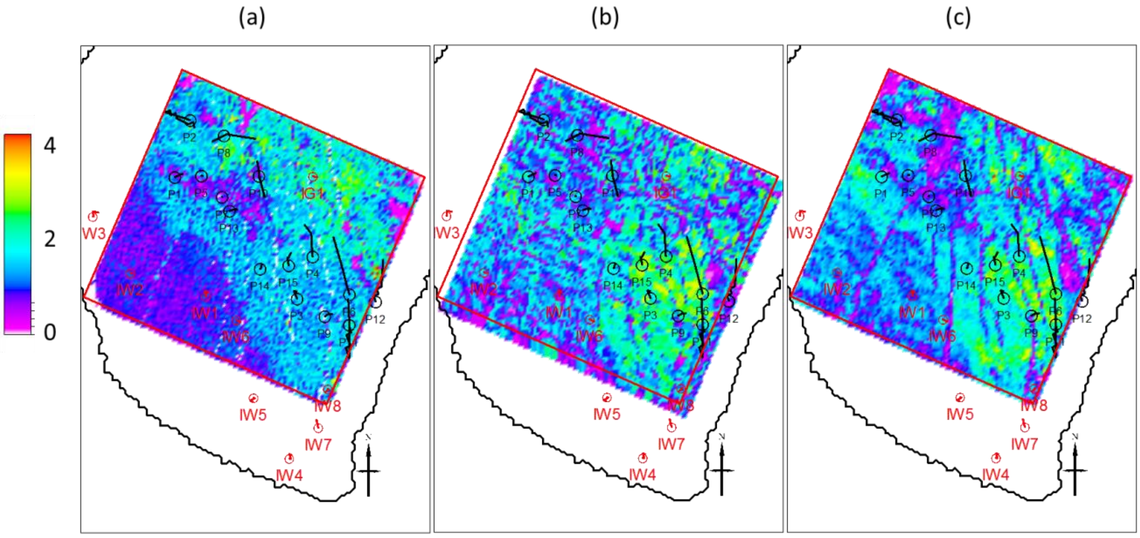

Figure 4.12 *The RMS seismic amplitude maps generated with a 20ms window on top of the Fangst group. (a) The map generated by the initial reservoir model; (b) the map generated after the porosity update; (c) the map generated from the observed seismic.*

4.4 Closing the dynamic loop by updating the fault connectivity

After closing the static loop by updating the PV distribution, the areal distribution of the modelled Fangst group is now reshaped to honour the observed baseline seismic data. However, as reported by Fürre et al. (2003), it is the connectivity between the different fault compartments that effectively dominates the dynamic fluid behaviour. Therefore, the fault transmissibility is of direct impact on the synthetic pattern of the 4D signal. Indeed, the comparison between this predicted and observed 4D constitutes the key step in closing the dynamic loop, leading to a consequent revision of the communication system over the faults.

4.4.1 Fault modelling

There are over 200 faults modelled in the reservoir simulation model, most of which are of negligible displacements. Therefore, conventionally defined transmissibility is adequate to determine the pressure propagation and fluid evolution across them. However, the major faults plotted in Figure 4.4 have at least 3 metres vertical displacement along the fault panel. Given an average cellular height of 3 to 5 metres, cells along the fault lines that are continuous in terms of indices may not have direct contact to each other, based on this proportionally populated model grid. With a positive defined transmissibility value along the faulting panel, the fluid flow will be led along an unphysical path, as indicated in Figure 4.13 (a). So, in order to correctly simulate, the

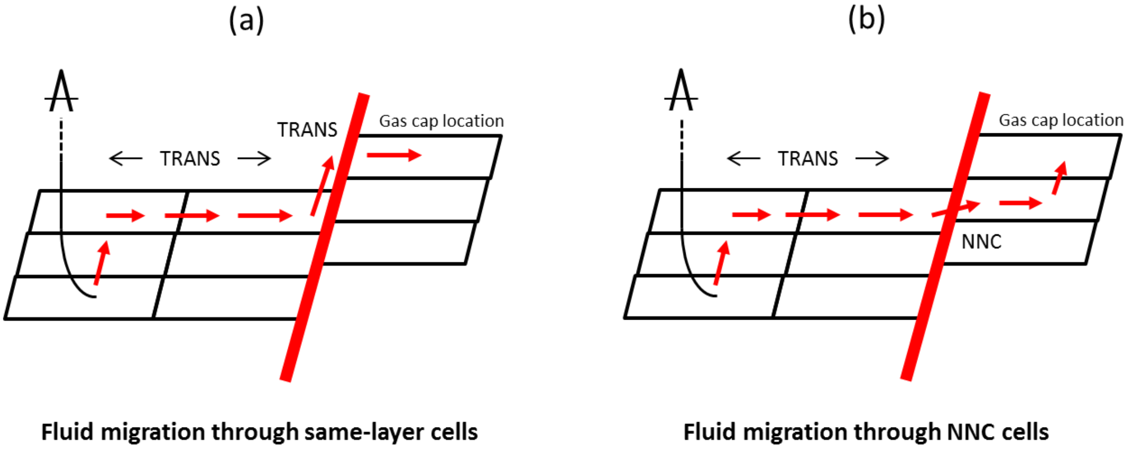

Figure 4.13 *Schematic paths for fluid migration through the fault displacement. (a) Fluid migration path through cells with positive defined transmissibility values; (b) Fluid migration path across the fault plane by non-neighbour connection (NNC) cells.*

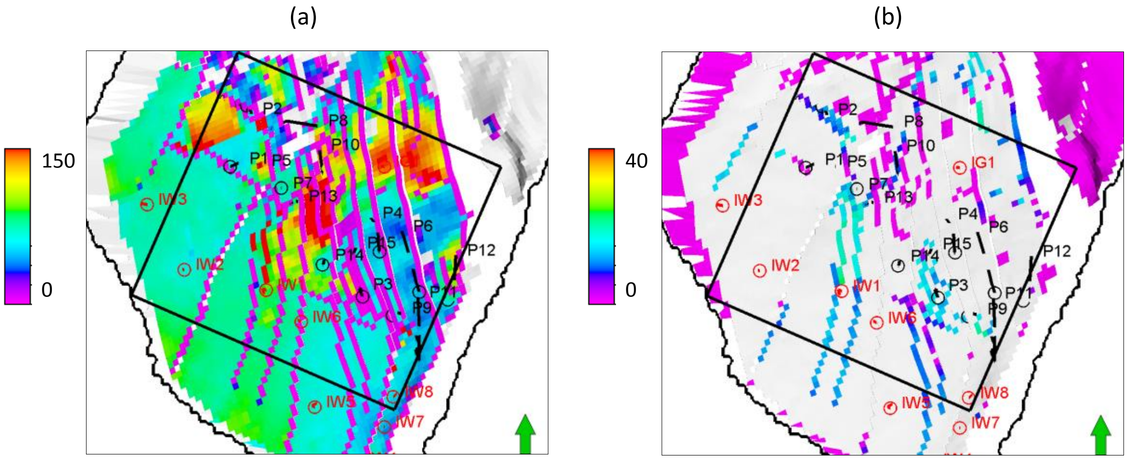

Figure 4.14 (a) The TRANX value initially defined in the reservoir model, indicating the transverse transmissibility between the major faults. (b) The NNC values initially defined in the reservoir model, indicating transverse transmissibility across the fault complexes.

NNC (non-neighbour connection) value is introduced which allows realistic leakage between the hanging wall and footwall. Figure 4.13 (b) sketches the gas flow behaviour through a fault with a zero transmissibility and positively defined NNC values; such a fault modelling scheme is utilised over the entire model to control the communication between compartments. Figure 4.14 (a) and (b) are the initial transmissibility and NNC values that populate the model in order to history match the production data. It has been noticed that some minor faults are assigned to low (5-20) NNC values, while the major faults that separate compartments B, C, D and E either lack definition or have zero NNC values. This initial set-up assumes very little cross-fault communication and that the segments are isolated from each other by faults.

4.4.2 Cross-domain comparison and fault update

A reservoir simulation is launched and the predicted fluid saturation and pressure fields are converted into elastic parameters by the calibrated PEM and sim2seis calculation. By subtracting the predicted P-impedance with the one at the baseline time, the 4D P-impedance is revealed, from which a map is averaged over the Fangst group layers and plotted in Figure 3.15 (a). In the area of interest, the OOWC moves to the north, and the water flooded area is represented by the impedance “hardening” (water replacing oil) zone. In contrast, re-injection of gas from the crescent has pushed the OGOC towards south, resulting in individual lanes of impedance “softening”. The gas signals are well

(a)

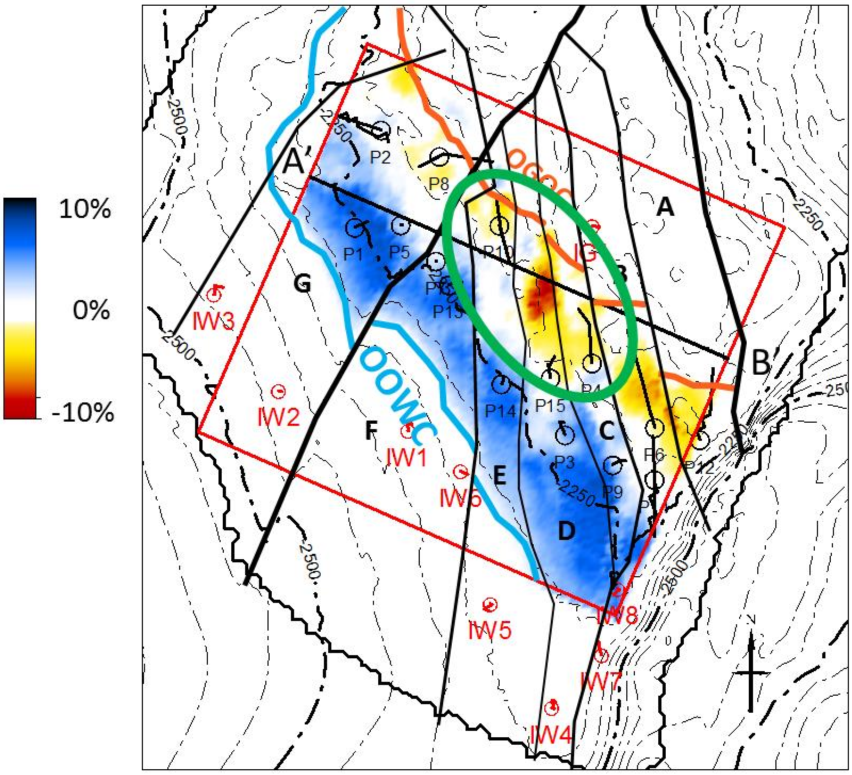
10%
0%
-10%
A'
B'
A
B
C
D
E
F
G
OOWC
OGOC
IG
P1
P2
P3
P4
P5
P6
P8
P9
P12
P13
P14
P15
IW1
IW2
IW3
IW4
IW5
IW6
IW7
IW8
2250
2500

(b)

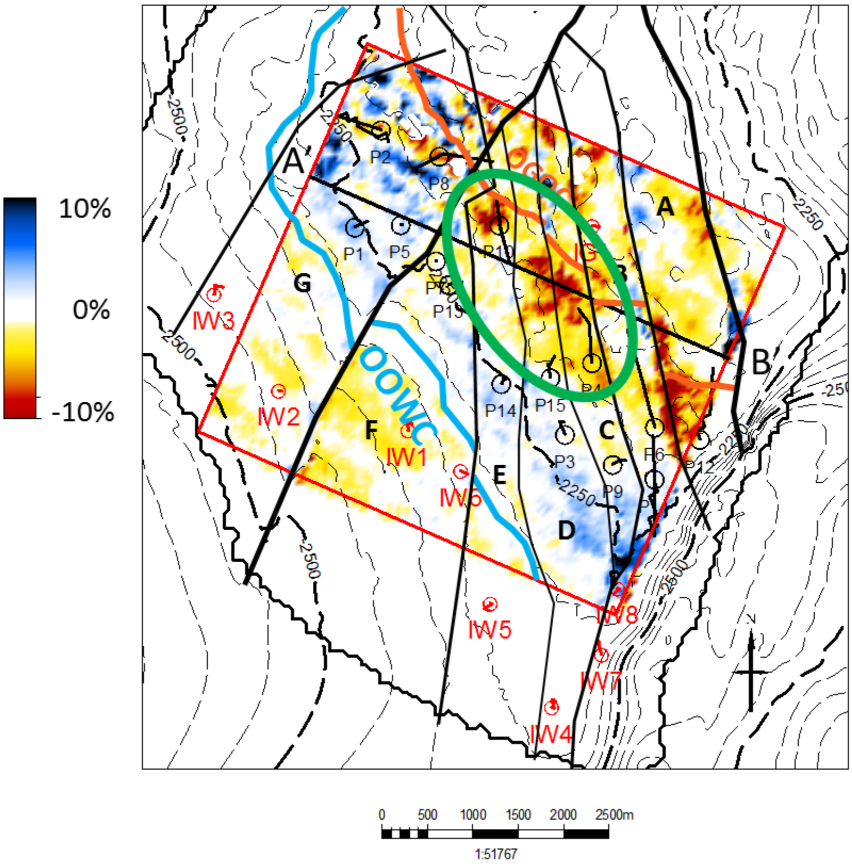
10%
0%
-10%
A'
B'
A
B
C
D
E
F
G
OOWC
OGOC
IG
P1
P2
P3
P4
P5
P6
P8
P9
P12
P13
P14
P15
IW1
IW2
IW3
IW4
IW5
IW6
IW7
IW8
2250
2500
0
500
1000
1500
2000
2500m
1:51767

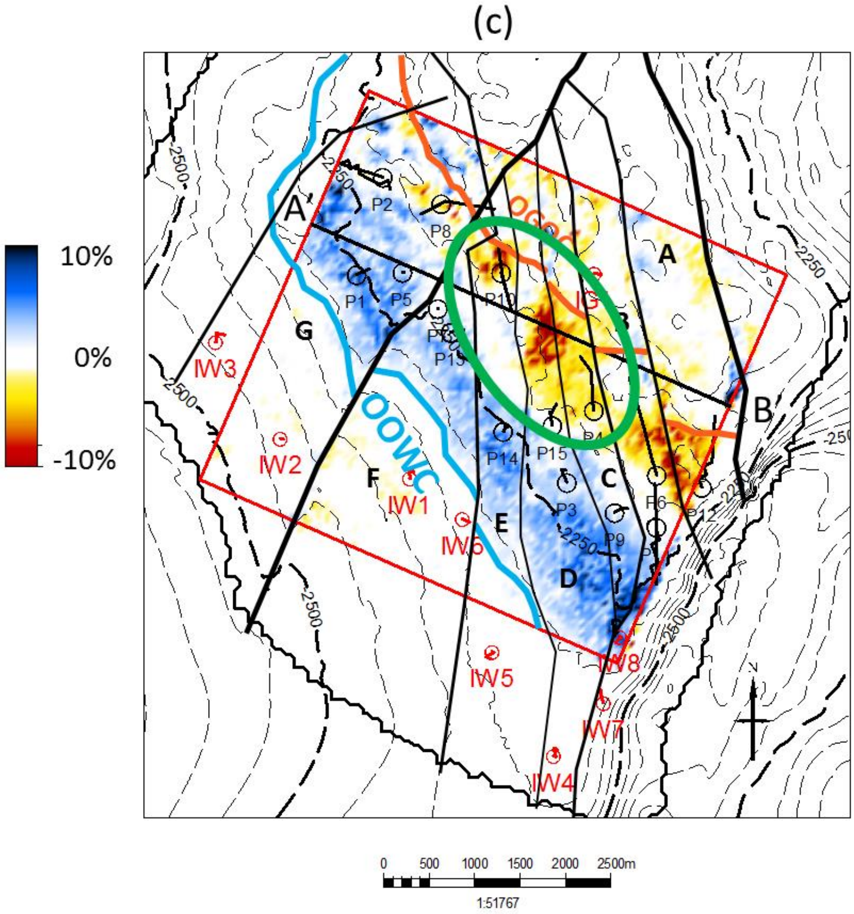

Figure 4.15 *(a) The 4D P-impedance map averaged over the Fangst group layers from the reservoir model; (b) The inversion derived map of 4D P-impedance. The gas cap is highlighted. (c) The constrained inversion results, in which the gas cap extends over the C and D Segments.*

confined in the B, C and D Segments, which reflects the initial set-ups of the transmissibility and NNC values. Figure 4.15 (b) and (c) compare the 4D seis2sim results with and without sim2seis constraints. The fundamental difference between them has been discussed in the previous chapter, but it is still worth pointing out that the constrained seis2sim indicates the leakage of gas between Segments B and C in the south, in addition to Segments C and D in the north. However, the lateral extension of the gas signal from the model prediction does not replicate this observation. In order to update the model, it is vital to have insight into the 4D volumes to figure out where the leakage exactly takes place. To assess this, a vertical cross-section through the problematic segments is created. Figure 4.16 (a) and (b) show the comparison between

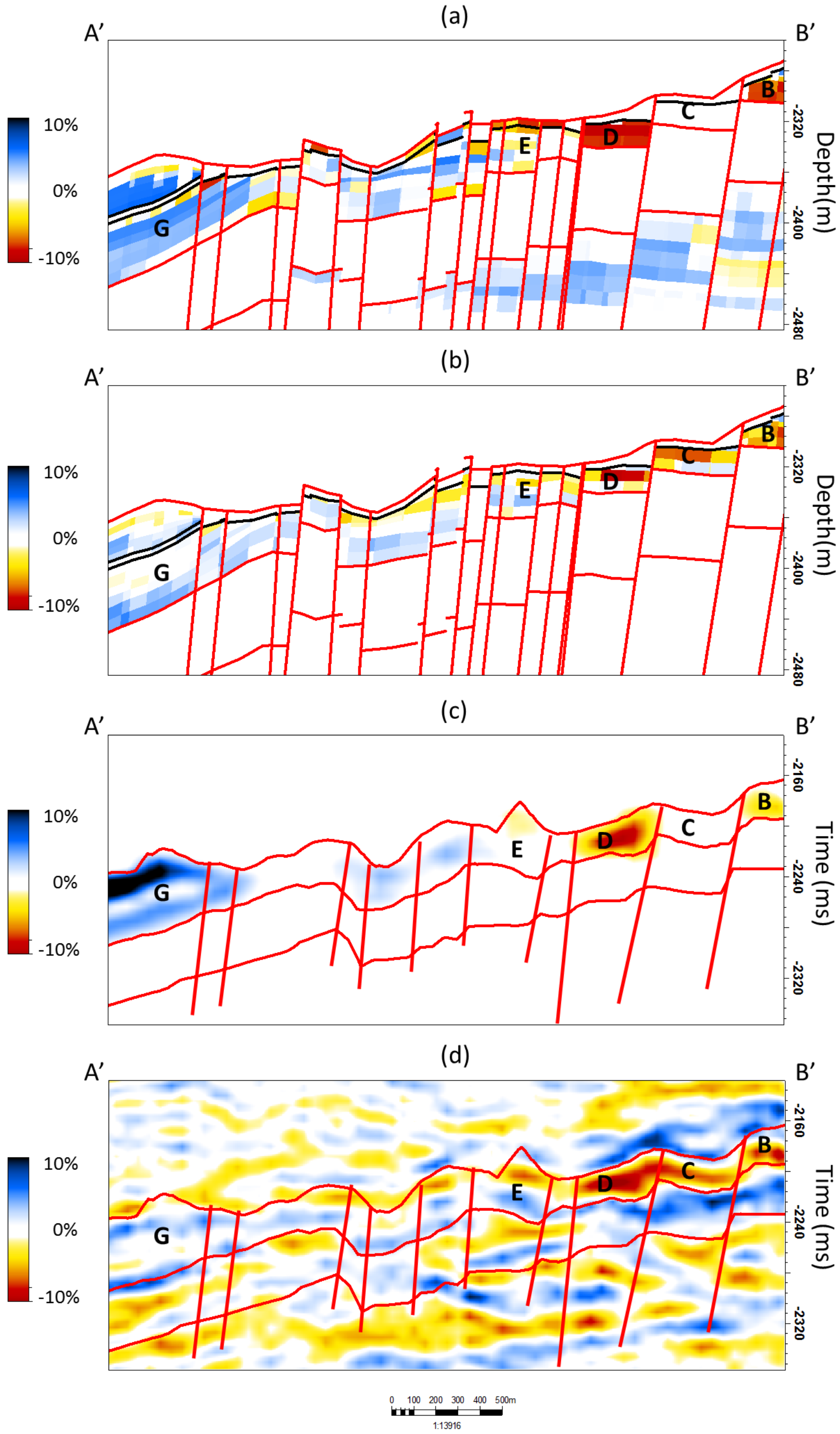

Figure 4.16 *(a) The 4D P-impedance from the sim2seis prediction on the model grid; (b) The seis2sim inverted 4D P-impedance on the model grid; (c) 4D P-impedance prediction in TWT; (d) Inverted 4D P-impedance in TWT.*

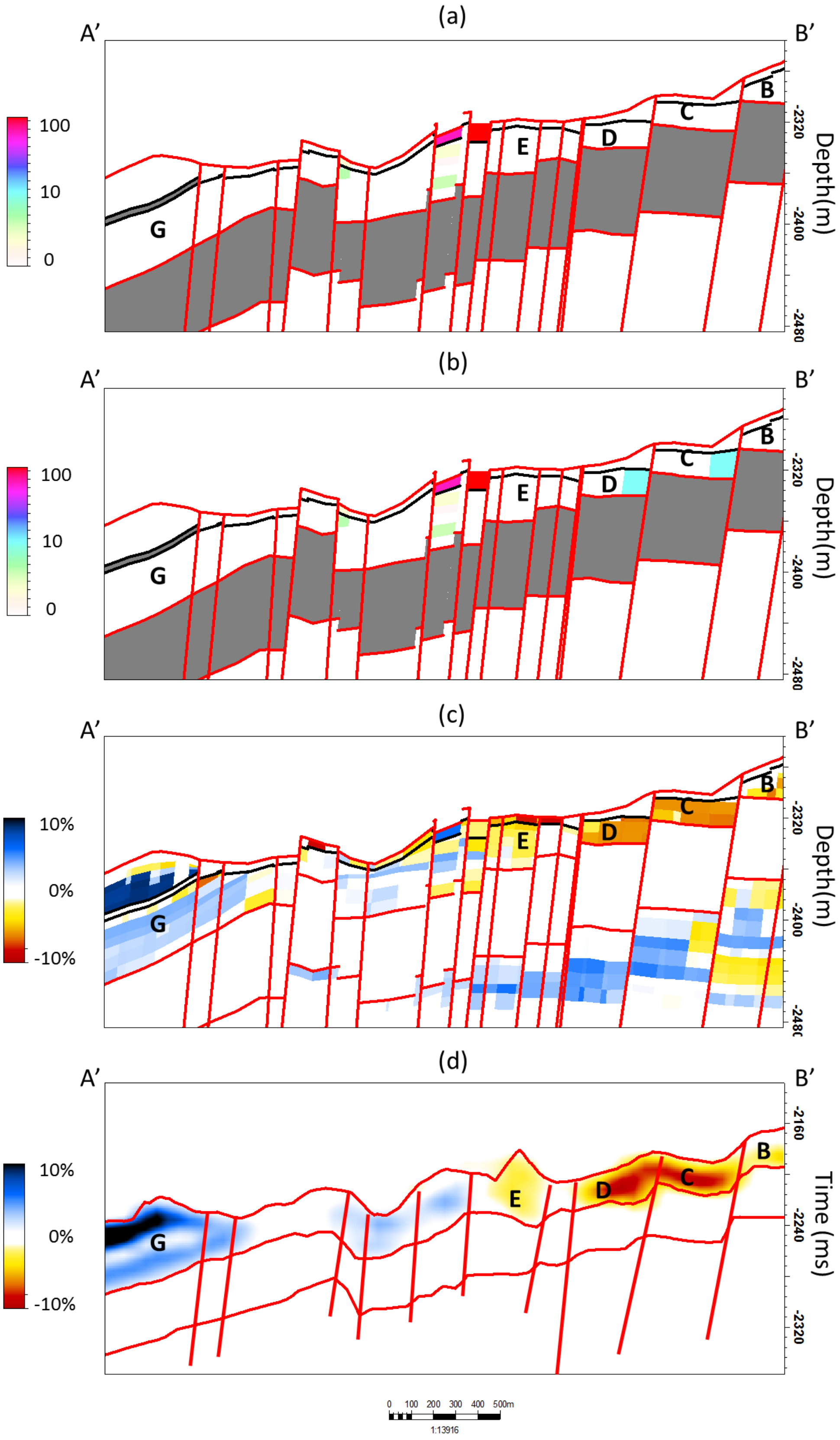

Figure 4.17 *(a) The initial NNC values at the fault locations; (b) The updated NNC values, which opened Segments B,C and D; (c) Updated 4D P-impedance prediction in the reservoir model; (d) Updated 4D P-impedance prediction in TWT.*

the prediction and inversion results on the reservoir model grid, in which the black lines indicate the NOT shale layer. In the G Segment, the water flood is represented by a 4-6% impedance “hardening”, and there are locally some “softening” signals, indicating the gas presence, particularly in the compartments B, C and D. By comparing the sim2seis prediction with the seis2sim inversion result, a prominent discrepancy is found in Segment C, where seis2sim suggests continuous extension of a gas cap over the B, C and D segments, while the prediction isolates the C Segment from its neighbours. Such a disagreement exists, too, in the time domain when converting the model prediction to TWT, as shown in Figure 4.16 (c) and (d). The time-domain comparison shows a visually similar behaviour in both the model and the 4D seis2sim, except for the presence of gas in the C Segment. This sharp contrast reflects the non-permeable fault defined initially in the model, which needs an update. The initial NNC model is shown in Figure 4.17 (a), in which the cells beside the faults have zero NNC definitions. According to the seis2sim results, it is decided to open the barriers between the B, C and D Segments by adding non-zero NNC values, as shown in Figure 4.17 (b). Therefore, the fluids are now capable of migrating through the faults at these particular points. The prediction of the 4D P-impedance of the updated model is shown in

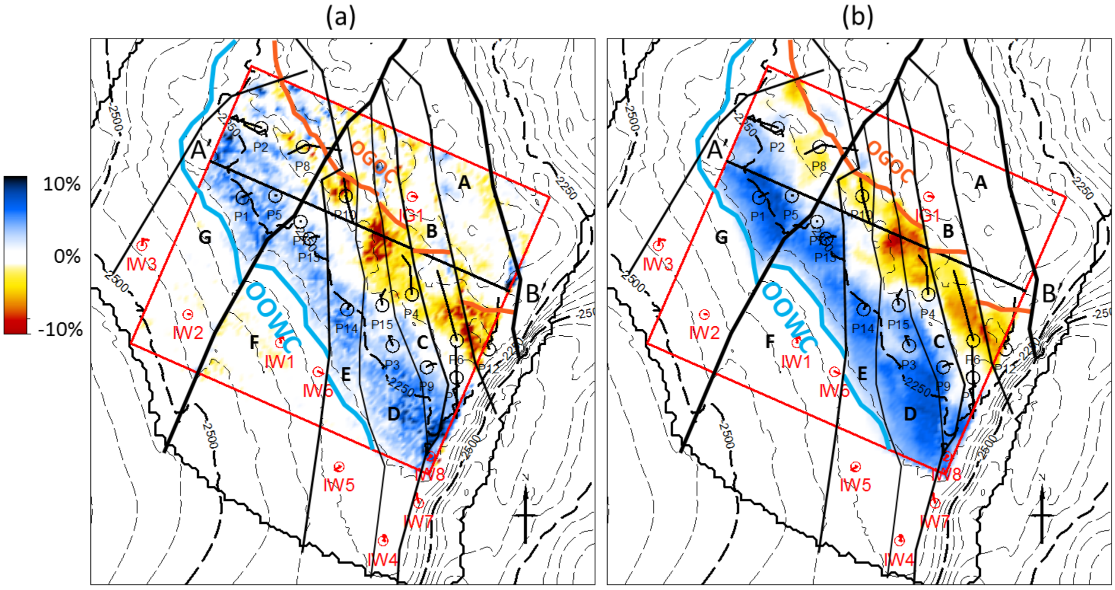

Figure 4.18 *(a) The average map of the 4D P-impedance; (b) The average map of the 4D P-impedance prediction from the updated reservoir model, in which the missing gas in Segment C has appeared.*

Figure 4.17 (c) and (d). The previous discrepancy has been improved, as the expected gas signal in Segment C appears, being represented by a consistent increase in the P-impedance with the inversion result.

Laterally, the updated model shows a consistent dynamic behaviour with the seis2sim results, as shown in Figure 4.18 (a) and (b), which is now capable of predicting the correct gas cap extension over the B, C and D Segments in the centre crescent. Thus an improvement leads to a closed dynamic loop in matching the seismic behaviour of the reservoir model to the observed in the P-impedance domain. However, since the gas signal is the main driver in this update, Well P-4 in Segment C and Well P-6 in Segment B are chosen to test the local impact of the NCC values introduced into the history match loop. The predicted GOR ratios shown in Figure 4.19 (a) and (b) suggest additional improvements in both wells, whose magnitudes are greater than those introduced during the static loop. This proves that the model updating is more sensitive for the Heidrun field in terms fault communication. Moreover, the reduced GOR

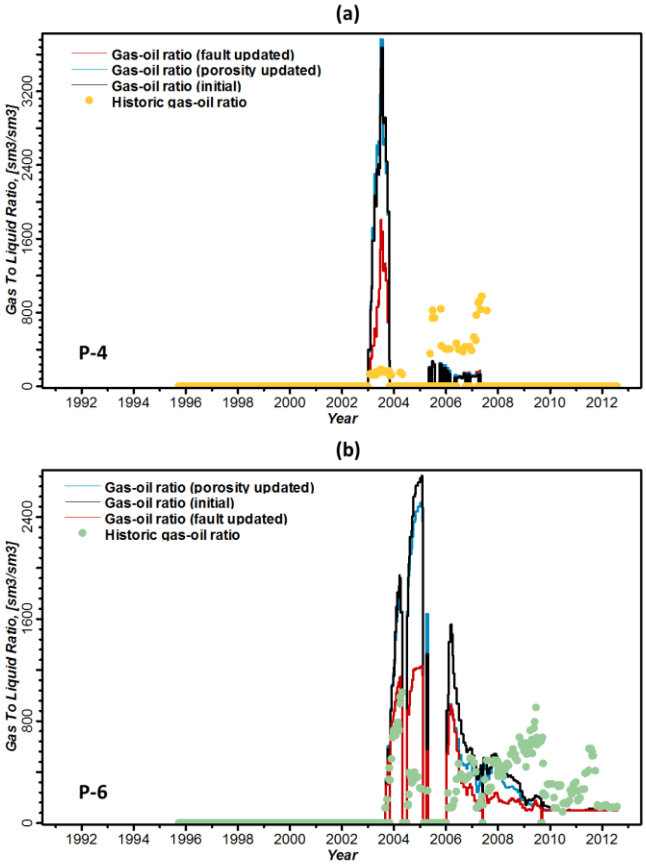

Figure 4.19 *(a) The simulated GOR profiles of well P-04 before and after closing the dynamic loop; (b) The simulated GOR profiles of well P-06 before and after closing the dynamic loop.*

at the wells is caused by the opening of new reservoir volume that was closed by the faults. The fault updating strategy here is relatively straightforward according to the 4D observation, in contrast to any other form of artificial revision required by the numerical optimisation. With only the dynamic insight into the 4D seismic, such an engineering consistent update can be obtained. Further improvement can be possibly achieved by looking at other areas of the field.

4.5 Summary

Regardless of what history matching techniques have been applied to the Heidrun reservoir model, its original mismatch to the observed 3D and 4D seismic data indicates the potential problem it contained. To improve its reliability, the reservoir model has to be updated to simultaneously to honour the observation of time-lapse seismic and the engineering production histories. The proposed workflow to close the static and dynamic loops becomes applicable by the virtue of its attempts to update the model according to the mismatches between the sim2seis predictions and seis2sim observations. The seis2sim-derived 3D and 4D P-impedance, are considered as “hard” data in the model updating practice. It is also noticed that the static parameter, effective porosity, dominates the calculation of effective reservoir volume, but is less efficient in altering the production loop. However, its impact on the static seismic response is vital. This implies a situation where the initial reservoir model has reached the material balance by utilising an unrealistic porosity distribution. By closing the static loop, the reservoir model turns out to retain the history match, while reproducing the observed 3D seismic.

However, due to the uncertainty in the seis2sim prediction, especially the lack of dynamic calibration, the comparison between the predictions and observations is limited to a qualitative or visual level for the Heidrun field. Despite this, the comparison is still powerful in detecting the field-scale patterns of production changes by analysing the seis2sim inversion results in a map-based approach. Moreover, because of the volumetric representation of the 4D changes, decisions could be made to open the faults by adding positive NNC cells in specified locations. This is effective because the 4D impedance represents passages of fluid migration. Overall, the allocation of different tasks to different stages seems to be a successful approach in addressing the static and dynamic problems of the given Heidrun model.

Chapter 5

Application of 4D EC seis2sim to the Girassol Field

> “That which has no (substantial) existence enters where there is no crevice. I know hereby what advantage belongs to doing nothing (with a purpose). ”
>
> 「無有入無間，吾是以知無為之有益。」
>
> Lao Tzu, *Chapter 43, Tao Te Ching, 700 BC. - 400 BC.*

This chapter provides the application of the EC seis2sim method to the Girassol dataset. The heterogeneous nature of a turbidite sand raises greater challenges to seis2sim with multi-offset 4D seismic stacks. Additionally, unlike the Heidrun example, the seismic data are of higher SNR and repeatability, which means the Girassol data does not require as many constraints from the sim2seis predictions as Heidrun. Therefore, the balance between “doing something” and “doing nothing” is the art in this case.

In order to assess the performance and limits of the proposed seis2sim CtL workflow, the technique is applied to a dataset from the Girassol field. This West African dataset, unlike the Heidrun example, will challenge the seis2sim approach with pre-stack information, higher resolution and higher 4D repeatability. The main focus of this particular chapter is to understand to what extent the reservoir engineering information needs to assist the seis2sim when the time-lapse signal is sound. As the quote introducing this chapter implies, the balance across the domains must be established to deliver only benefits to the integration.

5.1 Introduction to the Girassol field

The Girassol field, together with the adjacent Jasmim and Dalia fields, are located in the Girassol Development Area of Block 17 within the Congo Basin, offshore of Angola (Figure 5.1). Girassol was discovered in 1996, followed by the discovery of the neighbouring Jasmim field in 2000. Geologically, the reservoir developed in the Upper Oligocene Malembo Formation, which was deposited after the Cretaceous rifting (Lerat et al., 2007). The supply of sediments to this area increased tremendously, due to

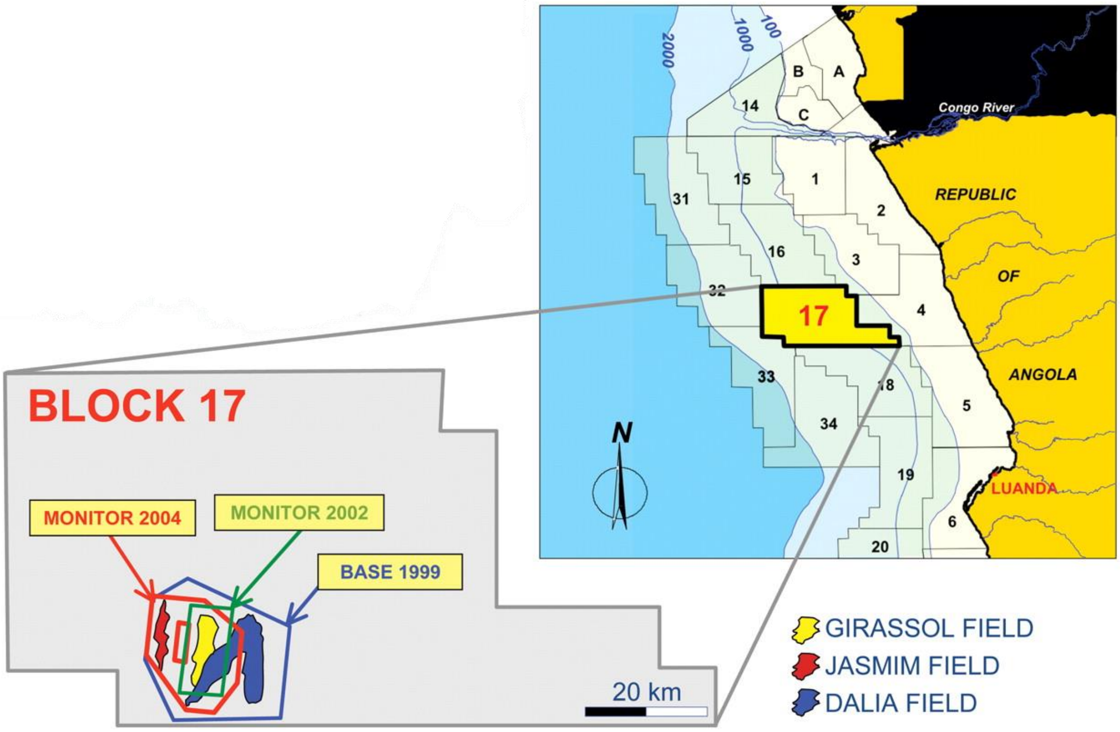

Figure 5.1 *Location and geological neighbours of the Girassol field.*

the uplift of the African craton, sea level drop and river drainage in the Oligocene times, which formed the westward-prograding Congo fan in the Tertiary. The sediment influx consists of clastic sources and was accommodated with growth faults and salt withdrawal. Later, the deltaic deposition was remobilized as turbidites during the sea level drops, forming a downslope-southwest trending area of paleo-turbidic sediments. Structurally, Block 17 lies in a transition zone between the updip extensional and downdip compressional domains of the Angolan margin (Lerat et al., 2007). Generally, the field is developed in a turtle-back shaped salt withdrawal anticline, with a NW-SE orientation. The salt deformation caused the structural faulting after the reservoir was deposited.

5.1.1 The heterogeneous turbidite reservoir

The reservoir of Girassol is composed of several stacks of turbidic channel complexes and channel-levee complexes and sand sheets, extending widely over 18 km. Based on the core data and high resolution (HR) baseline seismic, the reservoir has been classified into 16 detailed sedimentary facies (Navarre et al., 2002), that are correlated to interpreted seismic attributes to map the individual elements of the reservoir architecture. The highly amalgamated channel complexes are the main units of the reservoir, inside which there have developed multiple scales of lithofacies heterogeneity and potential flow barriers. For example, the shaly or silty facies are deposited and preserved in variable proportions in the reservoir sands, which introduces large uncertainty in estimating the porosity and NTG values. Nevertheless, the lateral migration of these meandering channels may form collapsed margins. Once preserved locally, these will form a lateral reservoir barrier. The abandoned channels are usually associated with high shale and silt contents, which can have thicknesses up to 10 metres and be hundred metres wide between the channel storeys. However, due to the erosion caused by channel plugs, they may not always serve as vertical flow barriers. These channel plugs have very small thickness, but are laterally extensive. They usually correspond to highly sinuous, narrow channel elements filled with uncertain shaly sediments, which may contribute to the reservoir connectivity. Apart from these, the channel levees in this depositional system may have potential reservoir properties. The levees are usually developed in association with the channel complex

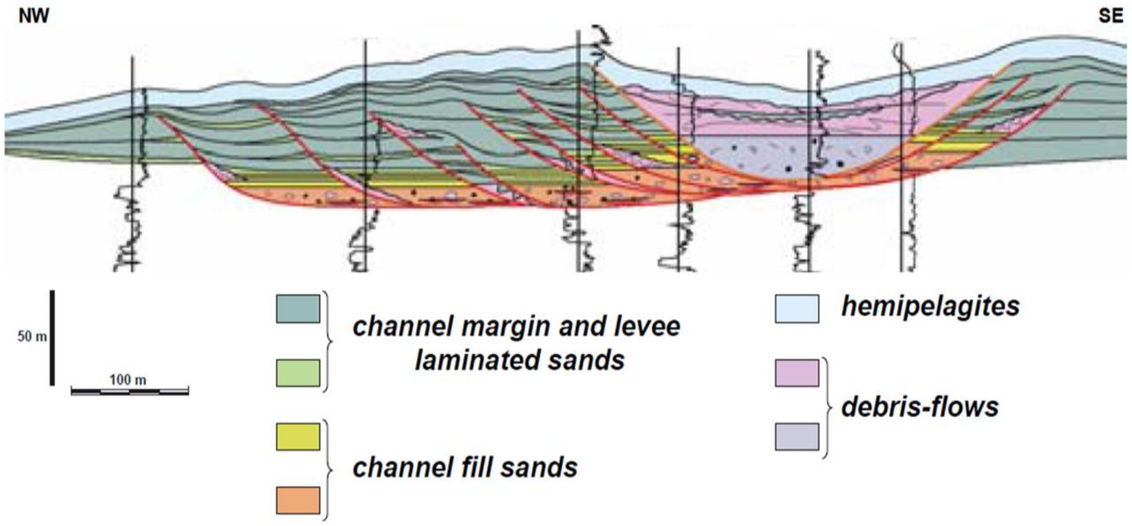

Figure 5.2 *A NW-SE cross-section within the upper channel storey of the Girassol channel complexes. The channel aggradation/migration ratio is associated with the distribution of fine-scale heterogeneities such as channel margin collapses, shaly debris-flows and constructive levees (from Navarre et al, 2002).*

with extensively sandy to shaly wedeges. The Net-to-Gross of the sand contents vary from a proximal sand-rich facies area flanking the main channels, to a distal shale-rich area (Navarre, 2002). The proximal levees may be sand-rich, serving as part of the reservoir. However, the transition from possible reservoir quality to non-reservoirs can be very smooth, resulting in ambiguous determination of the reservoir distribution. This raises an issue in estimating the reservoir volume, as well as modelling the consequent 3D and 4D seismic responses.

5.1.2 The seismic interpretations of the channel complex

A high resolution baseline seismic was acquired in 1999 with the aim of understanding the detailed reservoir architecture (Navarre et al, 2002). According to the interpretation, the main turbidite channels correspond to 200 metre thick intervals bounded by two regional seismic markers: B490 and B550, which are hemipelagic horizons at the maximum flooding surfaces during the sea-level changes (Figure 5.3). From the seismic sequence stratigraphy point of view, Broucke et al. (2004) classified the turbidite

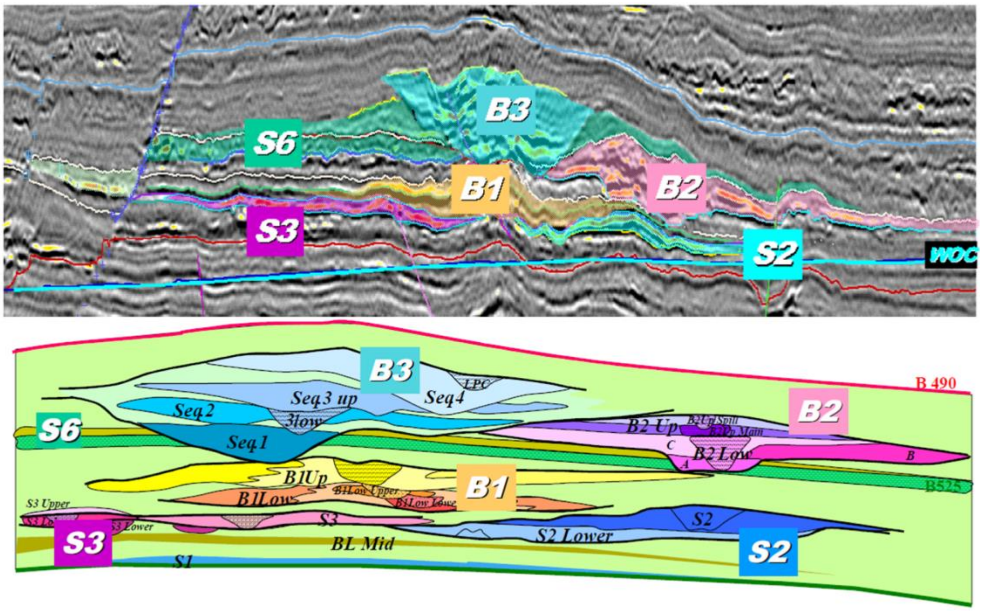

Figure 5.3 *A cross-section of the turbidic channel sequences. The main reservoir lies between B490 and B550. Three channel sub-sequences are defined as B1, B2 and B3 (Bouchet et al. 2004).*

channels inside the third-order sequence boundaries into two main types: the lobate sand sheets that are thin in thickness (5 to 10 metres) but wide in extension (several kilometres) and thick channel complexes. Among the channel complexes, three fourth order subsequences were defined as B1, B2 and B3. Each of them can consist of up to 4 sub-channel storeys (30 to 40 metres thick). Vertically, the channel storeys have successions that fine and thin upwards. The shale content also increases vertically, which reflects the depositional process during the turbidite flux.

5.2 Calibration for EC 4D seis2sim

5.2.1 Data acquisitions

Generally, the Girassol dataset was acquired and refreshed over a period of time (Bouchet et al., 2004). As depicted in Figure 5.4, the baseline seismic surveys were acquired in 1996 and 1999 with aims for discovery and detailed reservoir characterisation. Later time-lapse monitors were acquired at the end of 2002 and 2004. Reservoir modelling of the Girassol and its adjacent fields has been an on-going process, driven by the integration of cross-domain information into a single reservoir model. Interference tests, MDT, downhole measurements, PLT and tracer injection were all applied to the field at the appraisal stage to understand the reservoir connectivity by the operator. Consequently, a series of reservoir models have been built at different stages of the field life (Figure 5.4).

Reservoir Models 1 to 3 incorporated the information from exploration wells and the 1996 baseline seismic, whereas Reservoir Model 4 picked up the 1999 3DHR seismic and its successive processing results. Reservoir Model 4 better describes the interpreted seismic stratigraphy and the reservoir architectural elements. In addition, eight development wells were integrated into this version, according to which the inter-reservoir communication was a big uncertainty in the development of the field. Reservoir Model 5 started to match the 2 years production history. However, a seismic inversion was conducted to constrain this model, with a specific aim to improve the static channel elements. Reservoir Model 6, including the Girassol and Jasmin reservoirs, was built in order to incorporate the acquired 4D seismic data. It includes all the previous knowledge and the newer time-lapse information to monitor the gas injection. A second 4D monitor was acquired in 2004, which was planned to help to understand the water flood (Bouchet et al. 2004).

The reservoir model used for my study is the Reservoir Model 6. My main interest is to assess the mismatch between the model prediction and the 4D seismic observation, in order to improve the quantitative predictability of this model. Figure 5.5 displays the 7 fluid equilibrium regions defined in the reservoir model, which correspond to different reservoirs. It is assumed that Regions 1 to 3 are used to model the Jasmim field,

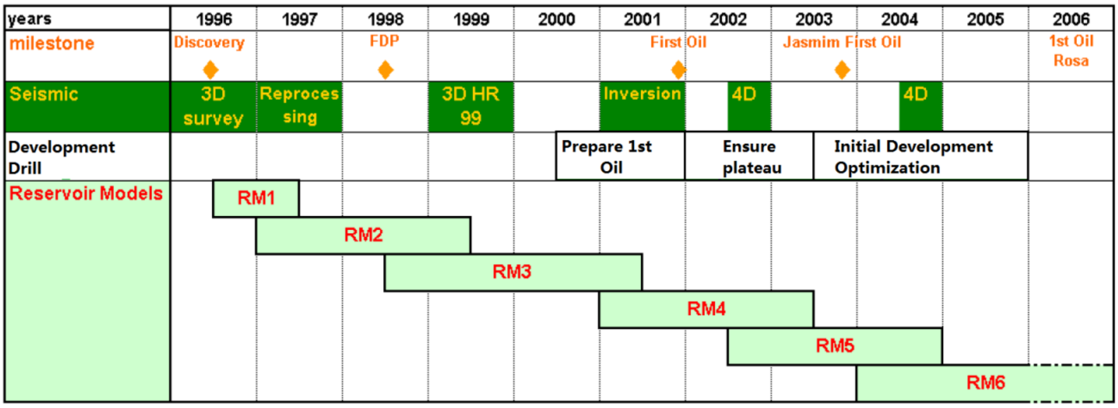

Figure 5.4 *The seismic data acquisition and reservoir modelling history of the Girassol field (modified from Bouchet et al. 2004).*

whereas the others are jointly used to simulate the Girassol and the Dalia fields. The Girassol channel complexes are mainly in Regions 4, 5 and 7, which correspond to the B3, B2 and B1 sequences respectively. In addition, each of the regions has a unique set of identical parameters for the PVT relationship and capillary pressures.

In order to replicate the geological concepts, eight different rock facies are defined in the model. This is different from the earlier Heidrun example discussed above, which has only one unique type of rock facies. As shown in Figure 5.6, the distributions of these facies follow specific geological patterns. According to the data vendor, these facies are derived from analysis of the seismic sand probability, and wireline log data.

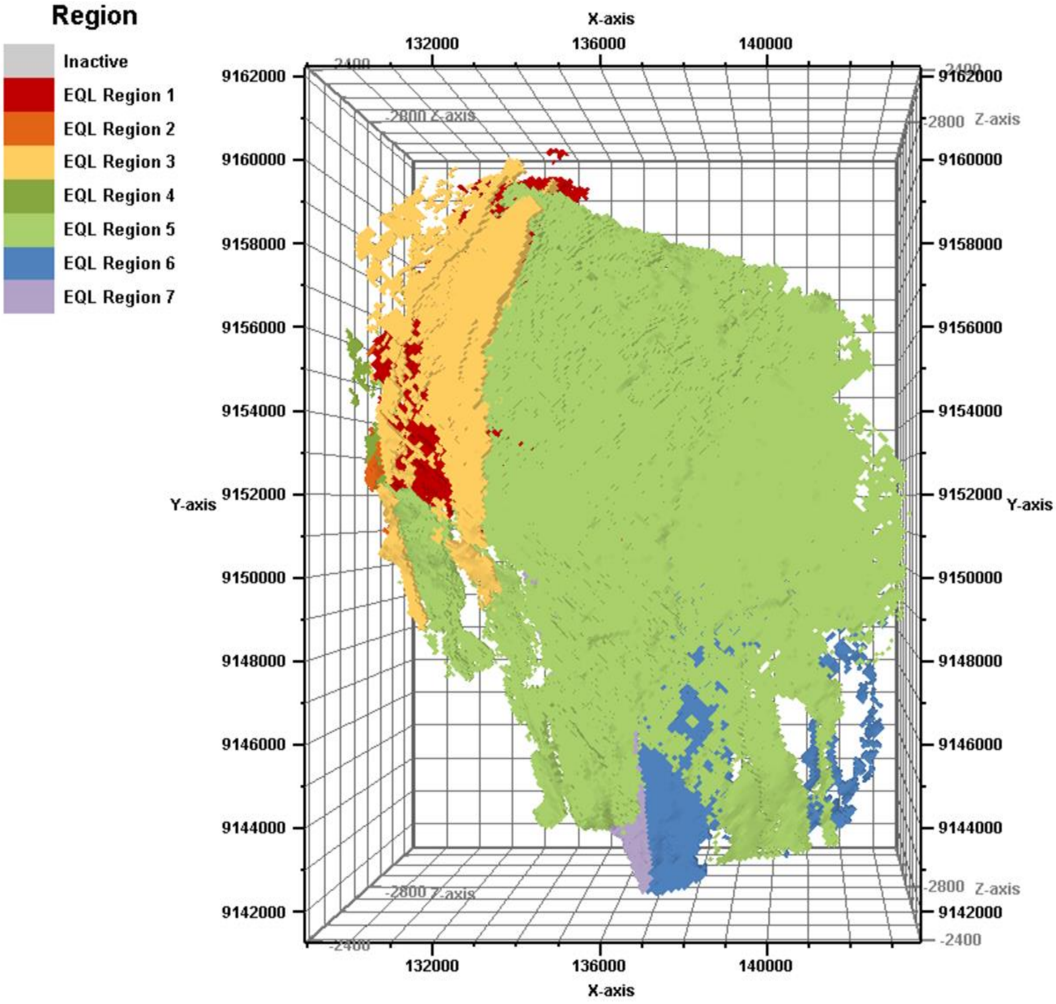

Figure 5.5 *The regions define the reservoir model. It is assumed that Regions 1 to 3 model the Jasmim field whereas the rest are jointly used to simulate the Girassol channels and the Dalia field.*

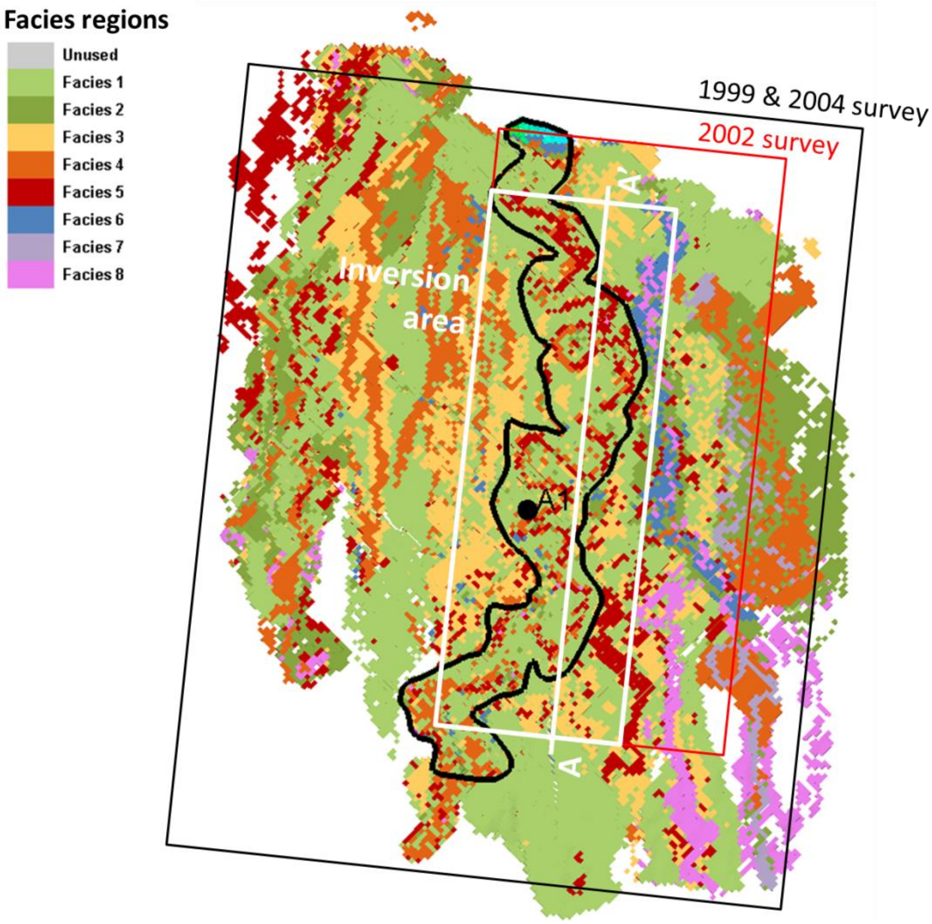

Figure 5.6 *The facies model defined in the target reservoir model. Facies 4 and 5 are assumed to be the porous sand channels.*

In particular, Facies 4, 5 and 6 feature the most porous parts of the turbidite channels whereas Facies 1 to 3 correspond to the sandy levees or shaly part of the reservoir.

As discussed before, one HR seismic baseline and two seismic monitor surveys are available. The coverage of these surveys is not identical at year 2002. For the application of the seis2sim and CtL workflows, the area of interest chosen is within the white rectangle, which covers most of the B1 and B3 sequences. The B2 sequence lies to the right of the area of interest, and therefore is not considered. The time lapse seismic data are stacked at different offsets (near, mid and far), so the seis2sim workflow needs to cope with pre-stack information, which was not present in the Heidrun example. The repeatability of the time lapse seismic between the baseline and 2002 monitor is evaluated as NRMS, in Figure 5.7, at various offsets. The NRMS were

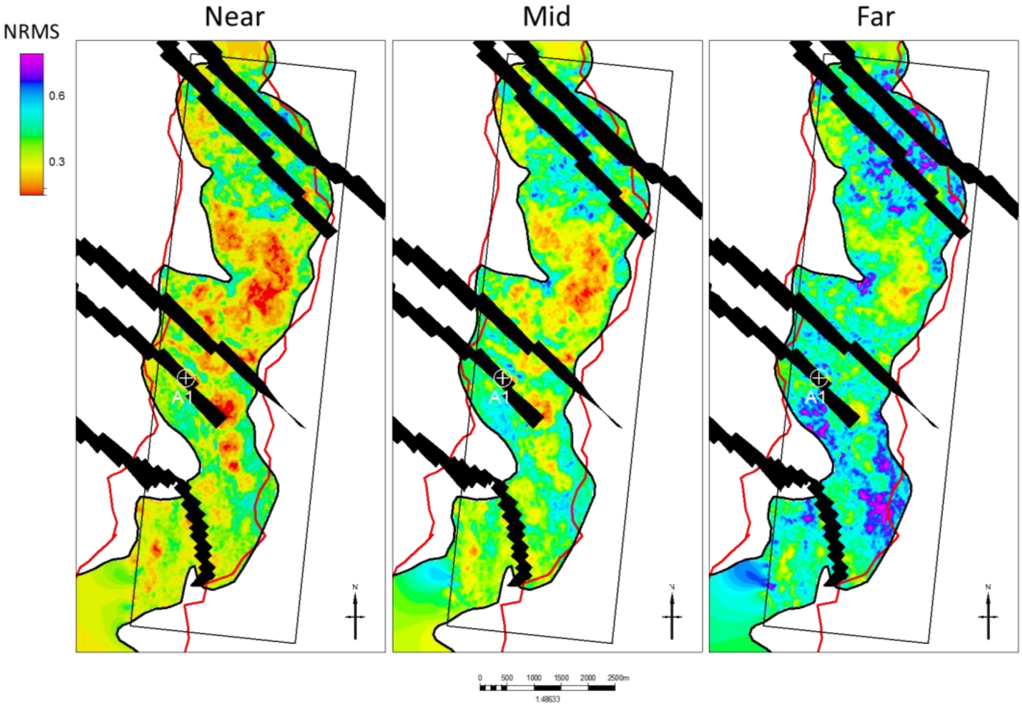

Figure 5.7 *The NRMS maps of the time lapse seismic surveys at near, mid and far offsets.*

calculated using a 100ms window defined at the top of the B3 sequence, which includes part of the shale layers below B490 and the overburden above. In general, the repeatability varies across the offsets. The near offset has the highest repeatability (mostly less than 0.25) whereas the mid and far offsets are worse. Locally, the far offset has NRMS values above 0.6, which is not very encouraging in terms of data quality.

5.2.2 The rock physics of the Girassol field

The wireline log data is analysed first, to understand the elastic properties of the rocks. The full set of acoustic logs is only available from the appraisal well A1 (see Figure 5.7). The well is not perfectly vertical but the deviation is negligible. Therefore, a pseudo log is extracted by its trajectory for the SATNUM values defined in the reservoir model. The SATNUM represents the modelled facies and is used for sim2seis calculation. In order to make sense of these SATNUM facies, they are correlated to the elastic and petro-physical logs in Figure 5.8. As discussed in the previous session, it is assumed that SATNUM 3, 4 and 6 are used to model the most porous sand packages, whereas SATNUM 1 and 2 are used for the shaly parts of the reservoir. This assumption is reinforced in the vertical direction according to the zonation superposed on the

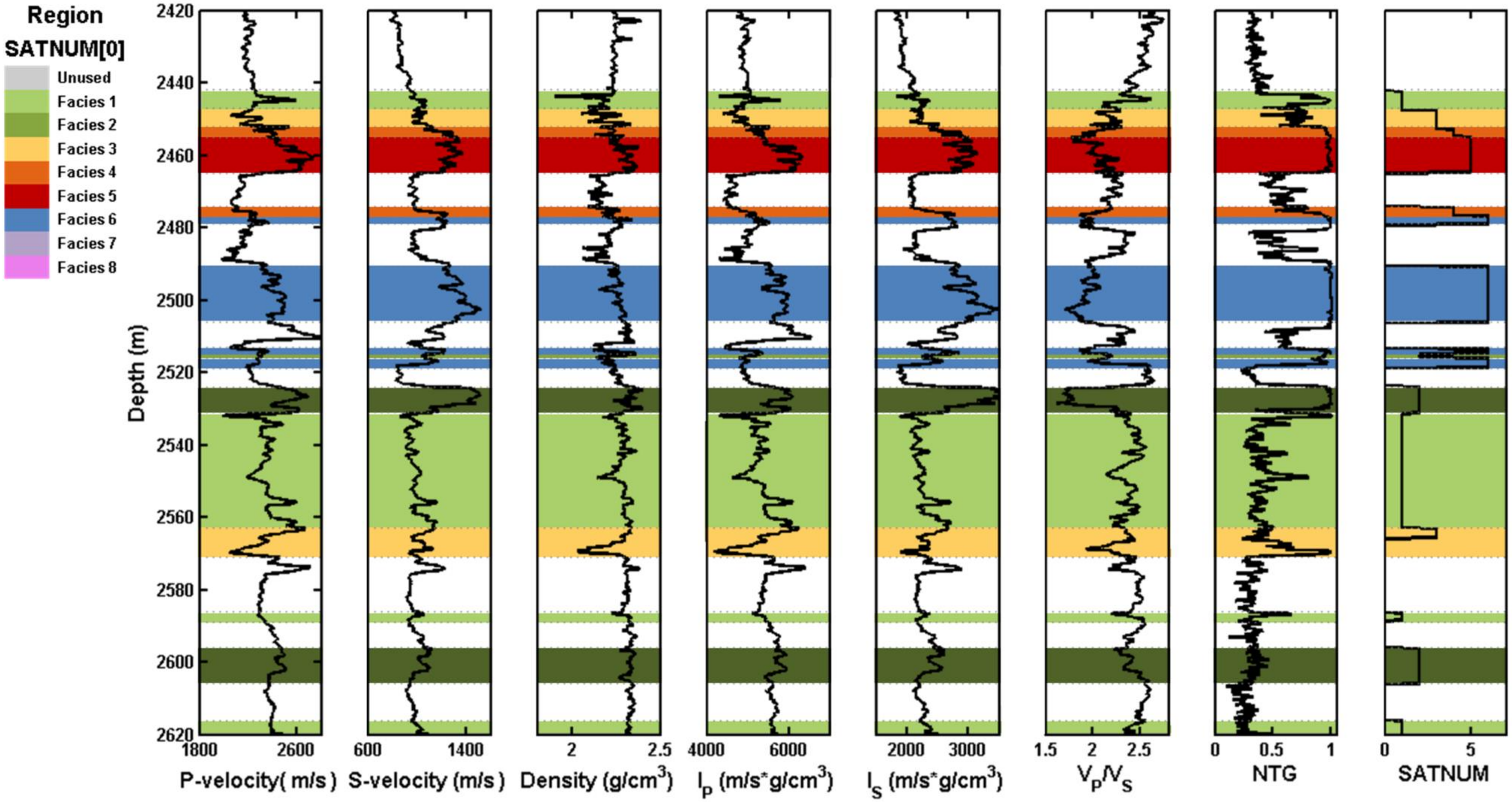

Figure 5.8 *The elastic logs from the appraisal well A1. The SATNUM log is extracted through its trajectory from the reservoir model to group the facies.*

porosity and NTG logs. These multi-facies models require various sets of PEM models in order to sense this diversity, which is important in the quantitative prediction of their static and dynamic elastic changes during the sim2seis modelling and CtL comparison.

5.2.3 Sim2seis for the Girassol field

The elastic contrasts between the sand and shale in B3 and B1 are very different. As shown in the cross-plots of Figure 5.9 (a) and (b), the shale impedance is very distinct from those of the sand in the B3 sequence, because both the P and S impedances of the shale are much smaller than those of the sand. However, this contrast is blurred in the lower B1 sequence, where the sand and shale properties are in the same range. This similarity results in the ambiguity of reservoir identification from the elastic domain. Therefore, the seis2sim will be challenged unless tailored, *a priori* information is applied during the inversion. Moreover, calibrating the parameter sets for the multiple facies is also required. According to the facies zonations highlighted in Figure 5.8, samples from the wireline logs are statistically grouped to represent each of the facies. The resolution of the wireline data is fine enough (1.2 metres per sample) to provide a sufficient population of samples that can be used to estimate the statistical distributions of each facies. Practically, the calibration of the PEM parameters is carried out in a similar manner to the Heidrun exercise except for this multi-model assumption. In general, the dry bulk modulus and the shear modulus of each facies are backed out, according to the inverse Gassmann calculation (see Equation 3.2).

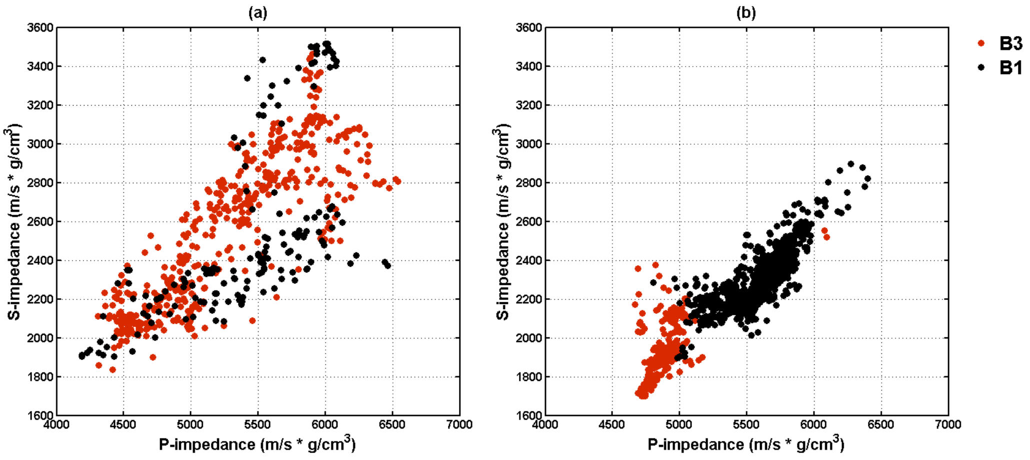

Figure 5.9 *Cross-plots of P and S impedance of the sand (a) and the shale (b) in B3 (red dots) and B1(black dots) sequences. The contrast between the sand and shale is less obvious in the lower B1 sequence.*

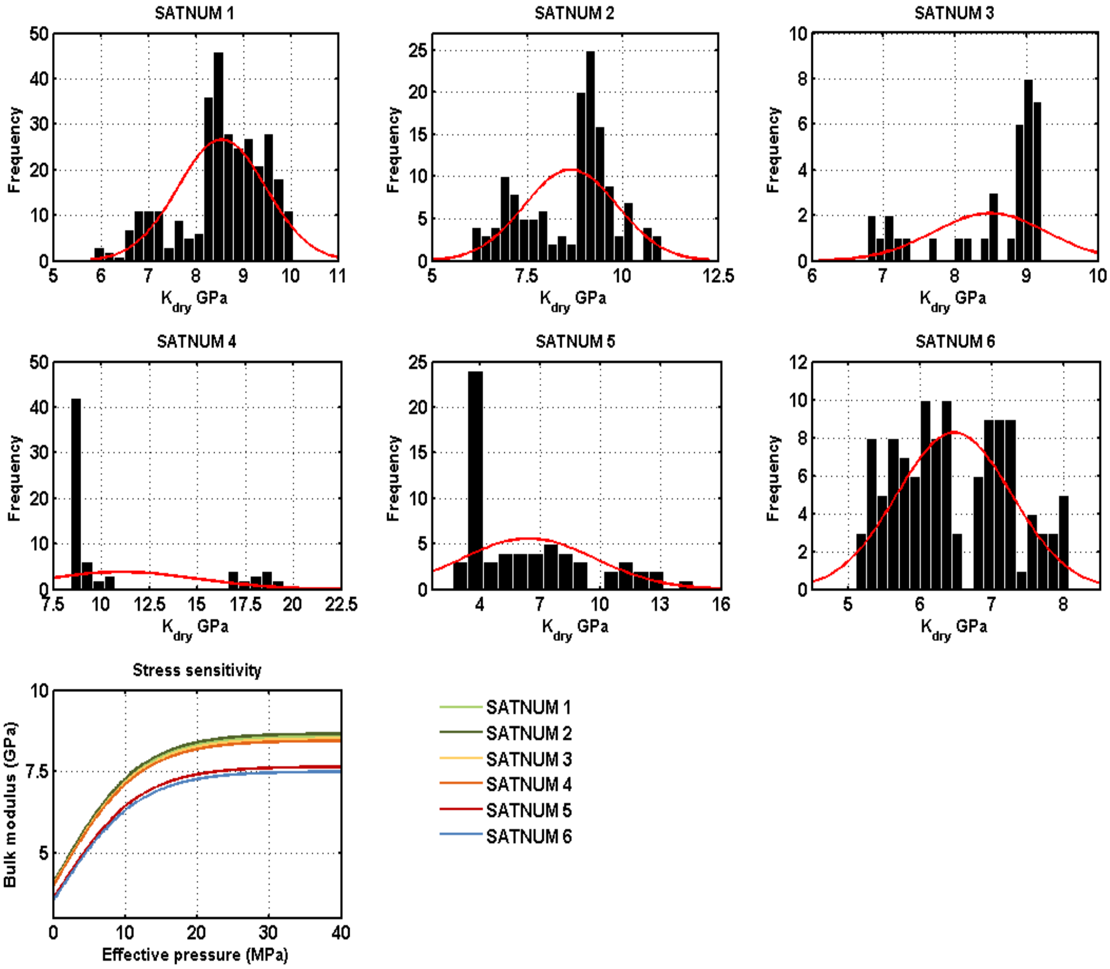

Figure 5.10 *The calibrated dry bulk modulus for the 6 facies presenting at A1. The associative stress sensitivity curves are also plotted.*

The stress sensitivity curves are also estimated by a similar approach to that describe in Chapter 3 (see Equations 3.4 and 3.5). The resultant dry bulk modulus and the stress curves are shown in Figure 5.10. Facies 4 does not show a distinctively centred distribution, therefore the arithmetic average mean is used in the sim2seis prediction. Facies 5 and 6 have lower bulk modulus under high effective pressure, which reflects their high porosities. Generally, the k_{inf} values decrease from Facies 1 to Facies 6, as shown in Table 5.1. Noticeably, Facies 7 and 8 are not present at the A1 location because they are mainly defined in the Dalia part of the model. In practice, they are assumed to have similar PEM parameters to Facies 5 and 6, during the sim2seis calculation.

Facies	K_{dry}	K_{inf}	μ_{dry}	μ_inf
SATNUM 1	**8.38**	**8.77**	**4.36**	**6.84**
SATNUM 2	**8.24**	**8.64**	**4.61**	**6.97**
SATNUM 3	**8.04**	**8.57**	**4.13**	**6.41**
SATNUM 4	**7.59**	**8.52**	**3.95**	**6.23**
SATNUM 5	**6.67**	**7.61**	**2.77**	**5.51**
SATNUM 6	**6.58**	**7.51**	**2.94**	**5.76**
SATNUM 7	**6.50**	**7.50**	**3.00**	**5.80**
SATNUM 8	**6.50**	**7.50**	**3.00**	**5.80**

Table 5.1 *Calibrated stress sensitivity parameters for the eight facies in the reservoir model.*

After calibration, the PEM is used to predict the P-velocity, S-velocity and density, based on the initial reservoir model at the A1 location, as a quality check (Figure 5.11). The last two tracks show the initial porosity and NTG values of the reservoir model as red blocky curves, in contrast to the well log data (black logs). The zero porosity and NTG are inactive cells in the reservoir model, where constant P-velocity, S-velocity and density are assigned by the PEM. Generally the reservoir model tends to overestimate the porosity whilst underestimating the NTG in the lower B1 sequence below 2520 metres (see Figure 5.11). This results in a mismatch in the prediction of the elastic parameters when mixing sand with shale, because the NTG weights them wrongly when calculating the overall bulk modulus. In the upper B3, the predictions of P and S velocities show similar trends to the log data. However, one potential uncertainty of the calibration is that the absence of gas in the well log in the first place. Because the initial pressure in Girassol is very close the bubble point, the later depletion will cause gas to be liberated from solution and this is not considered in the calibration.

5.3 EC 4D seis2sim application

Prior to the seis2sim inversion, quick 4D RMS amplitude maps were generated to understand the reservoir changes. These are displayed in Figure 5.12, three 4D RMS

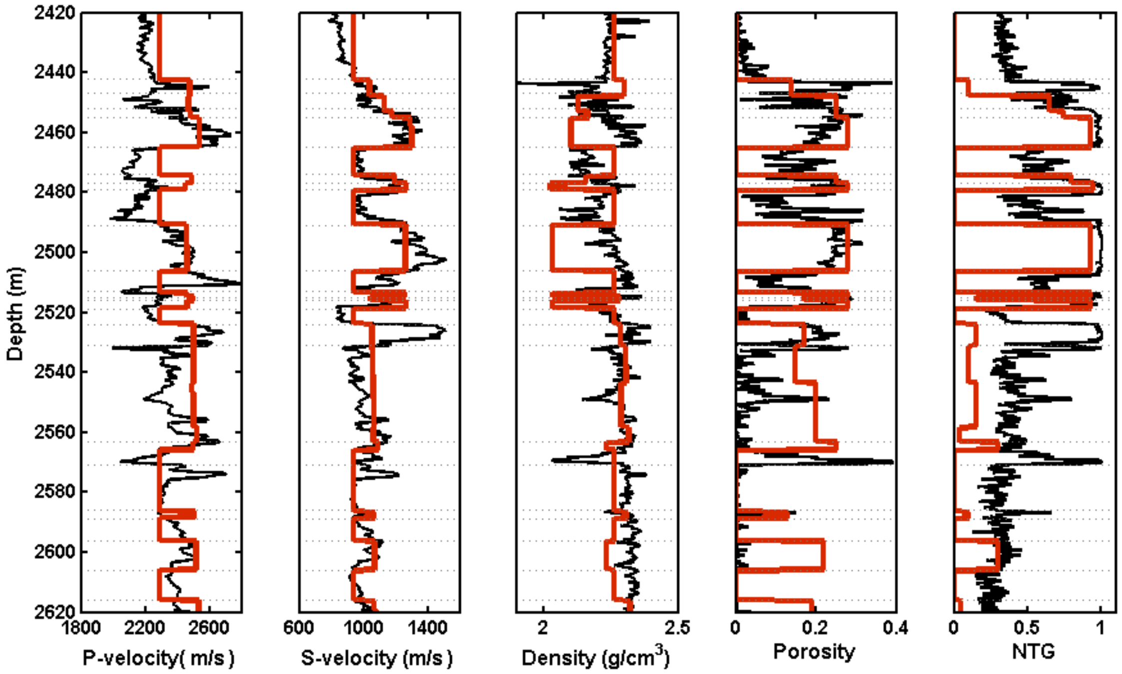

Figure 5.11 *Sim2seis predictions at A1 after the discussed PEM calibration. The red blocky curves are the predictions of the P and S velocities, the density and the initial porosity and NTG in the reservoir model. The black logs are the wireline data.*

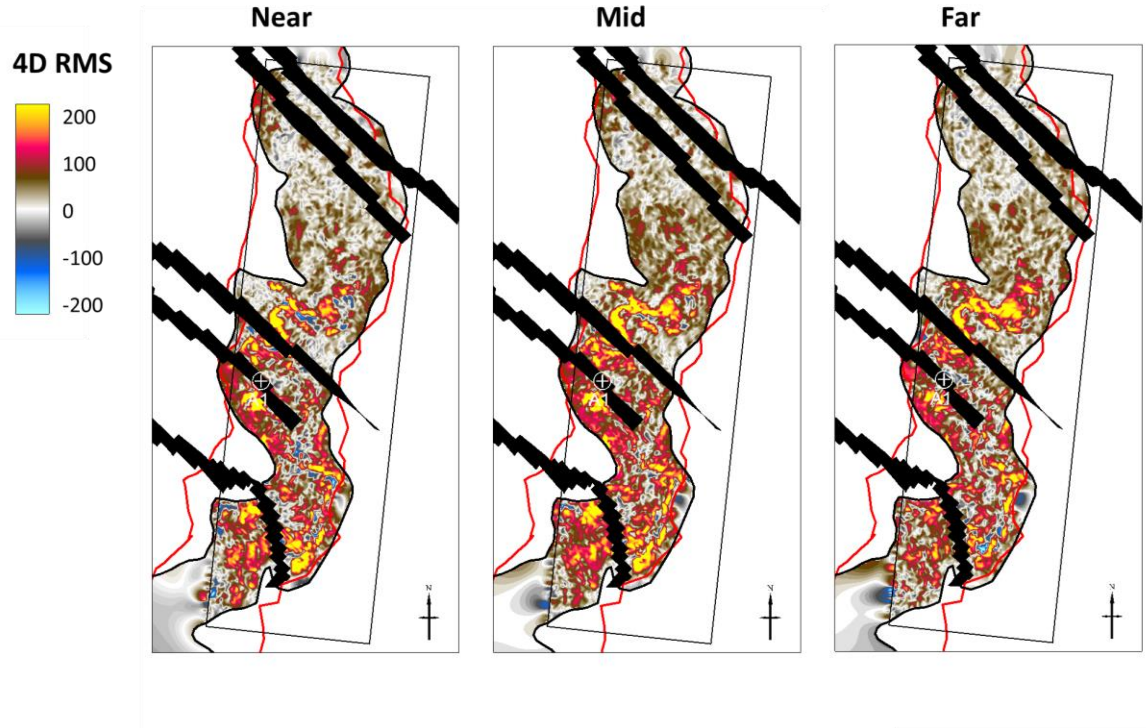

Figure 5.12 *4D RMS maps at near, mid and far offsets between the baseline 1999 and monitor 2002.*

maps are generated at the near, mid and far offsets. The window used in this calculation includes the entire B3 and B1 sequences. In the central area, the amplitude increases can be correlated to the gas presence. However, the 4D maps do not make sense in the remaining areas of interest. This is essentially caused by the loss of information in the vertical direction when generating maps for thick reservoirs. The HR seismic data has so much information in the seismic amplitude cycles that it is difficult to understand unless it is converted into volumetric information by seis2sim.

5.3.1 The baseline inversion

Sim2seis is run to yield elastic models of P-velocity, S-velocity and density, stored for the reservoir grid in a cell by cell form. It is then the seis2sim's role to update this initial prediction. Practically, the entire calculation follows the progression below:

- Full PEM calibration for each facies.
- Forward predict the baseline P-velocity, S-velocity and density on the reservoir grids.
- Extract *a priori* information (bounds, ranges ad standard deviations of elastic properties) from the log plots and sim2seis predictions (initial model).
- Select a seismic trace and extract the elastic values in the corresponding cells along the trace trajectory, vertically, to form the initial input models for seis2sim.
- Repeat
    1. Chose a random cell from the initial model.
    2. Perturb the P-velocity, S-velocity and density values of the selected cell.
    3. Calculate the reflection coefficients by the Zoeppritz Equation (Equation 2.5) at each cell intersection depth for every incident angle.
    4. Stack the reflection coefficients at near, mid and far offsets.
    5. Convert the stacked coefficients to TWT, according to the current P-velocity values.
    6. Calculate the synthetic seismic for different offsets.
    7. Calculate the transition probability according to the prior term and likelihood of the perturbed model (see Equations 2.5 to 2.8) and the original model.
    8. Conduct Metropolis-Hastings (M-H) sampling and convergence diagnostic.
- Analyse the statistics of the posterior realisations.

When converting the coefficients from the depth domain to time, an alignment exercise is performed. During alignment, the reflection coefficient of the first layer of the reservoir model is shifted to the corresponding TWT depth picked by the seismic interpreter. This time shift is also applied to successive reflection coefficients. In addition, wavelets were extracted for the near, mid and far offsets prior to the inversion by performing well ties. The wavelets are convolved with the reflectivity series to generate synthetic seismic traces.

Before applying the workflow to the entire reservoir volume, an inversion test was firstly performed at the A1 location. The posterior results are shown in Figure 5.13. The likelihood function assesses the mismatch within the B3 and B1 sequences only, which is the reason for the poor match underneath the reservoir. In practice, an extra cell is padded to the input vector to generate the base reservoir reflection. This pseudo cell is not in the original reservoir model and the reflection here is hard to model. Nevertheless, the amplitude match is good at the near offset, whereas the far offset shows a relatively loose match. This is caused by the decreasing robustness of the signal with offsets. Larger uncertainty is thus given to the far offset data (see Equation 2.6). The σ_{e_b}values at the near, mid and far offsets are set to 1.1, 1.3 and 1.5 respectively. The simultaneously inverted P and S wave velocity show good agreement with the log data. The posterior uncertainty ranges in the upper B3 sequence are actually smaller than the ones of the lower B1, because of the sand to shale contrast, as mentioned before. The inverted density is not as close to the wireline data as the other two, and additionally the uncertainty range is greater. The spike in the uncertainty between depths 2560 m and 2580 m is caused by 13 pinch-out cells, which have negligible thicknesses. Similarly, the thin cells at 2520 m present themselves with higher resolution than the other parts of the model. This is distinctive from a conventional time-domain inversion, in which the sample interval is uniform.

After the test, the seis2sim workflow is applied to the entire reservoir model in a parallel scheme (see Figure 2.16). The results are shown in Figures 5.14 to 5.16. Figure 5.14 shows the near, mid and far offsets data at the baseline time associated with the interpreted horizons. The residual amplitudes that are not matched after seis2sim, are displayed in Figure 5.15. It is noticed that the residual amplitudes have a lower frequency than the original HR seismic, and in most places, the residuals are smooth from top to bottom, except for the strong channel reflections to the right.

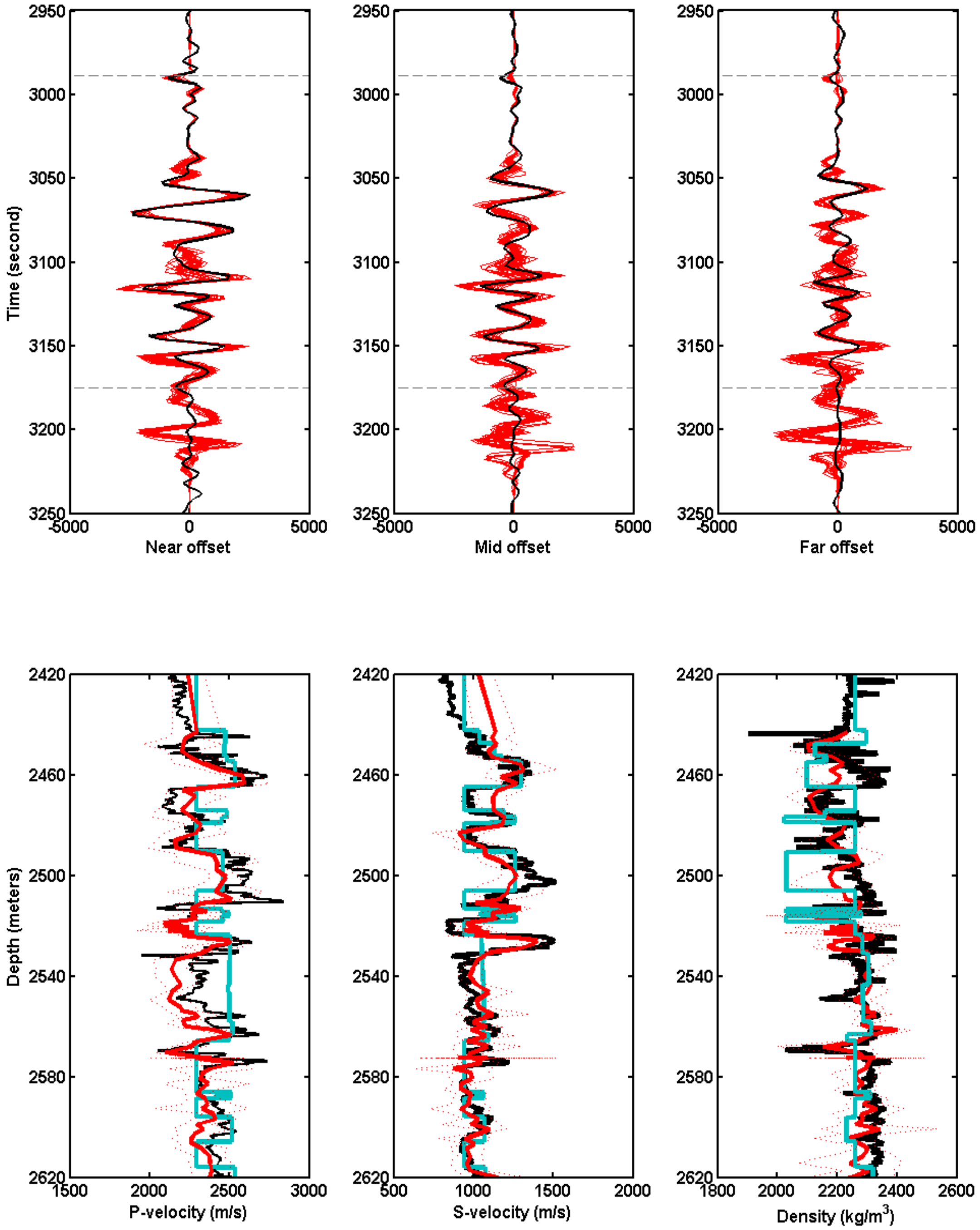

Figure 5.13 *A 1D test run at the A1 location. The black traces in the upper three diagrams are the observed baseline seismic at near, mid and far offsets, where the red are the posterior realisations of the synthetic seismic amplitudes. The lower three show the posterior means (thick red curves), the 0.95 uncertainty ranges (dashed lines), the sim2seis predictions (light blue lines) and the wireline log data of the P-velocity, S-velocity and density.*

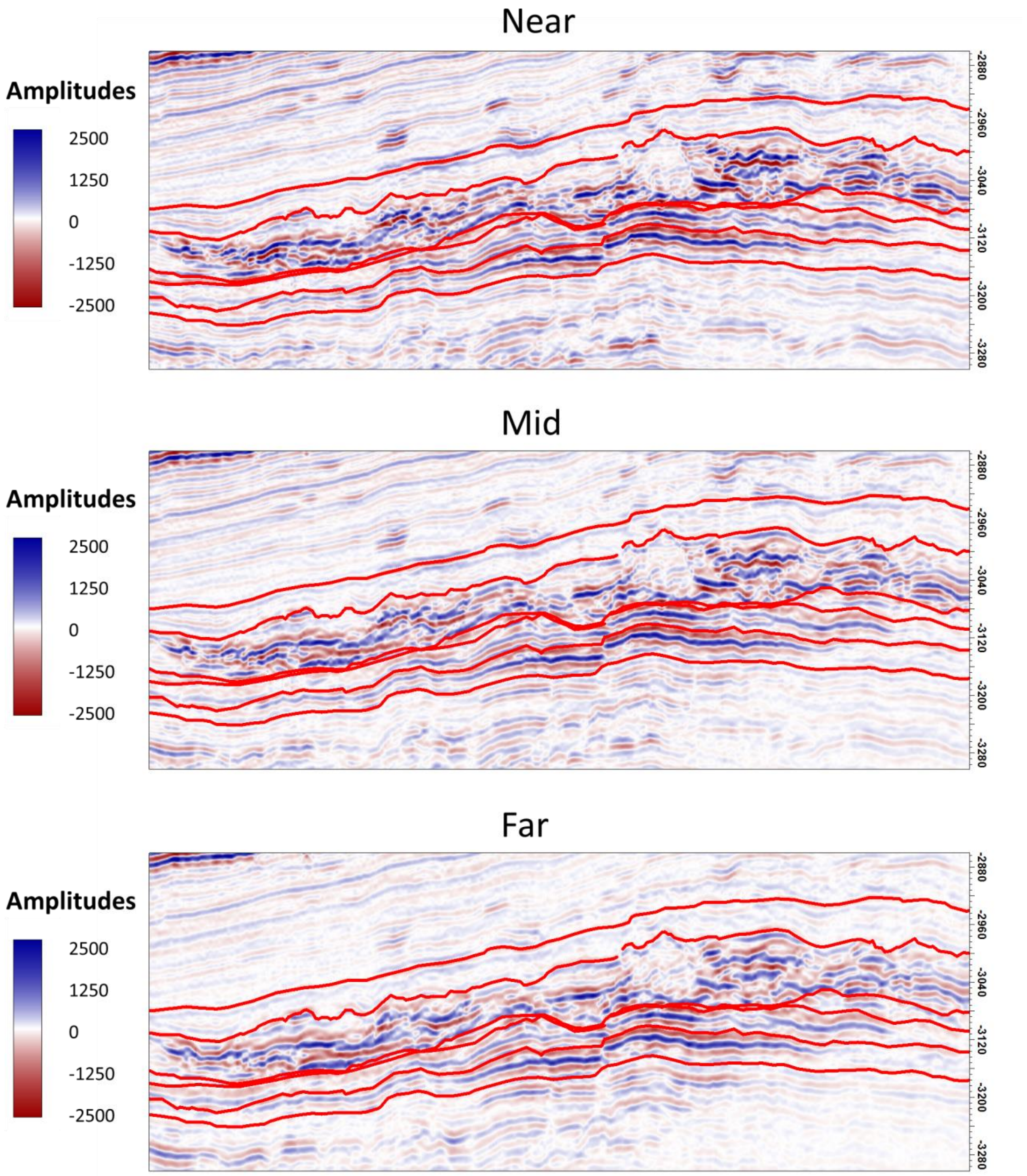

Figure 5.14 *The baseline HR seismic at near, mid and far offsets. The red lines from top to bottom are the seismic horizon picks at B490, top B3, bottom B3, top B1, bottom B1 and B550. There are no reports available to specify the gridding scheme in the model, but it is decided to correlate them to Layers 1, 2, 48, 52, 77 and 103 in the provided reservoir model, according to the geometric similarity.*

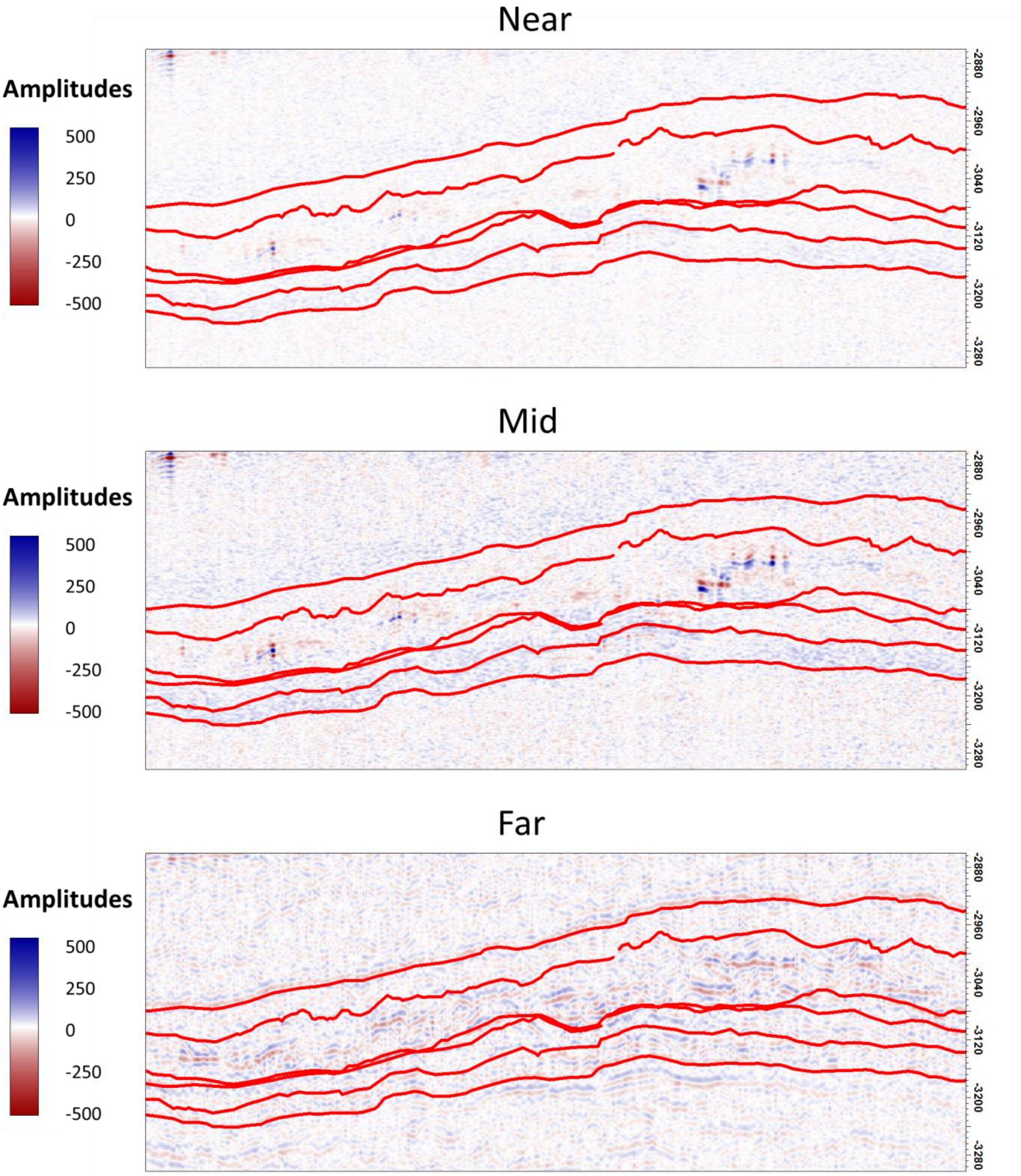

Near

Mid

Far

Figure 5.15 *The residual amplitudes after seis2sim at the near, mid and far offsets. Note that the scales of the coloured bars are one fifth of those in Figure 5.14. The residuals are generally smooth over all the traces.*

These small residual errors are then taken into account during the 4D seis2sim, as part of the data uncertainties (see Equation 2.9). The inverted P-velocity, S-velocity and density are combined together as P-impedance, S-impedance and V_p/V_s, and shown on the reservoir grids in Figure 5.16. The P-impedance shows the distinctive contrast

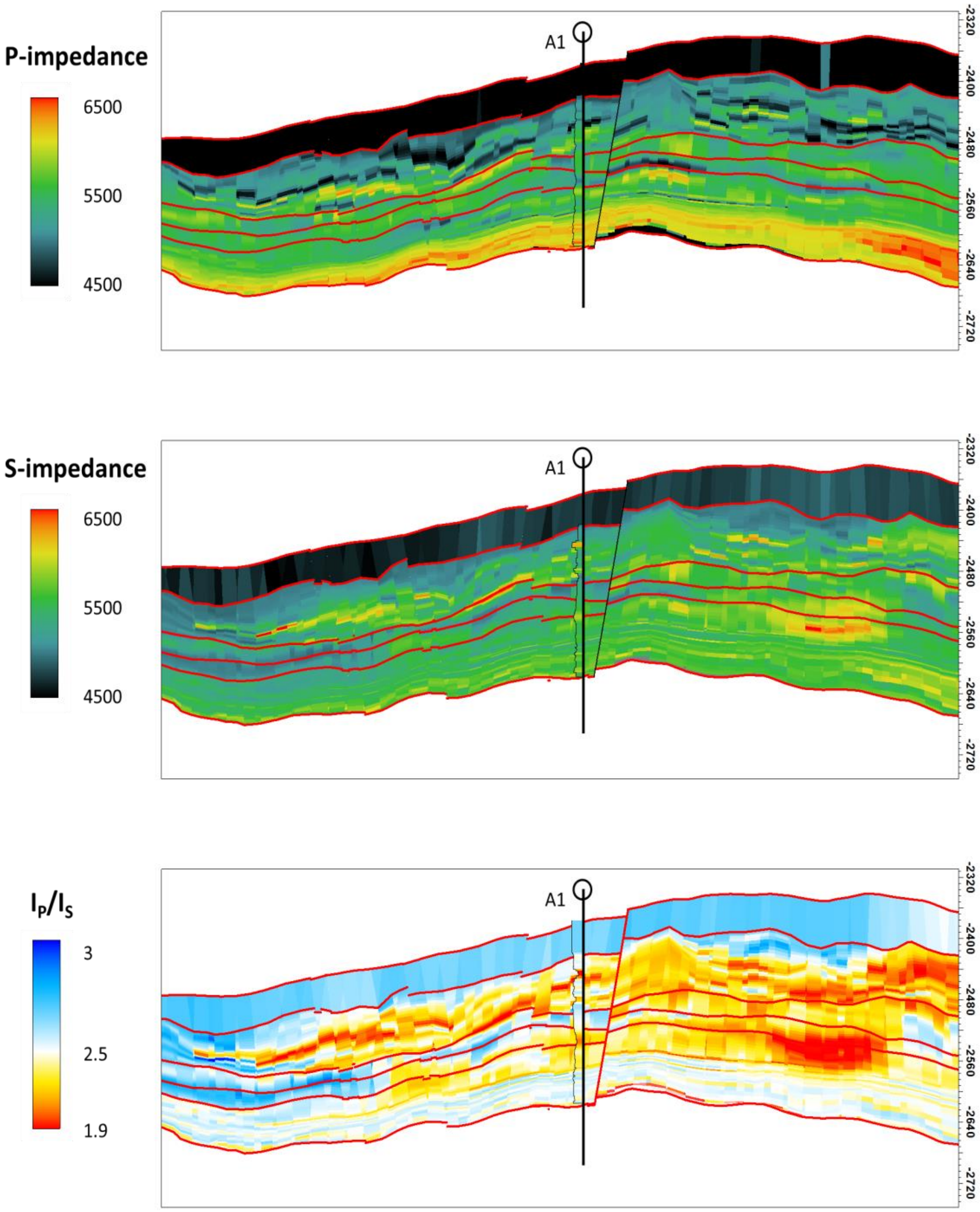

Figure 5.16 *The seis2sim P-impedance, S-impedance, and* V_p/V_s *on the reservoir engineering grid. The log data from A1 is superposed on it to check the accuracy at the well location.*

between the sand and shale in the upper B3 part of the reservoir. However, for the lower B1, this is not as prominent. The coloured bar of the V_p/V_s attribute is white at 2.45, which is derived from the wireline log data, as a loose threshold for sand and shale separation.

5.3.2 The 4D inversion

The signal to noise ratio (SNR) plays an important role in the 4D seis2sim workflow. It balances the trust between the seismic data and the *a priori* predictions. In Figure 5.17, three SNR maps are displayed at the near, mid and far offsets for the time lapse seismic pair between 1999 and 2002. The SNR is calculated as the ratio between the standard deviation of the 4D amplitudes inside the reservoir and in the overburden. To highlight the outstanding signals, areas where the SNR is below unity (namely the signal is weaker than the noise) are coloured in white. In general, the signal strength decreases from the near offset to the far offset, whilst the signal patterns vary as well. This difference is usually understood to be due to the differing sensitivity of the 4D AVO data to the pressure and saturation changes. However, the average SNR here is between 4 and 6, in contrast to 1 to 3 in the Heidrun example, which means the data has a higher reliability and the inversion need not struggle against the noise.

Although it seems that fewer assistance are needed from the reservoir engineering predictions in this dataset, the engineering constraints can indeed help the 4D seis2sim in other ways. For example, the Girassol time lapse seismics are time-aligned at the top of B490, which provides the dataset with very clean 4D signals in the overburden. However, the velocity changes induced by production cause changes in both reflections and time shift. Because of the high resolution (essentially, the dominant frequency is up to 65 Hz compared with 25 Hz in the Heidrun dataset), a small amount of time shift will

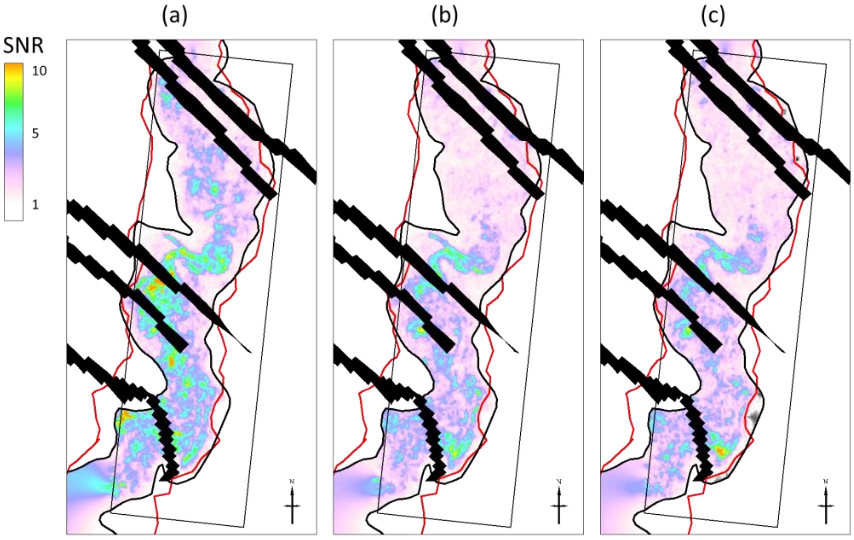

Figure 5.17 *4D SNR maps at the (a) near, (b) mid and (c) far offsets between the surveys of 1999 and 2002.*

cause large amplitude change. This phenomenon is demonstrated in Figure 5.18, where the time lapse seismic traces and the differences are shown at the location of appraisal well A1. The visual comparison between the baseline and monitor traces clearly indicates the subtle change in reflectivity, while the difference between them shows remarkable amplitude differences. According to the reservoir engineering, A1 is situated next to the main turbidite channels but the reservoir here is not heavily affected by gas injection and production. If 4D seis2sim inverts this difference data without this prior knowledge, the anticipated results would create an artefact.

In the examples discussed in Chapter 2 and 3, the Bayesian prior and likelihood terms are jointly used to incorporate the reservoir engineering predictions. They help balance the inversion between model prediction and noisy data, in order to converge the algorithm at meaningful answers. In contrast, the Girassol 4D data by itself has a stronger SNR, therefore the residual errors of 3D inversion become the primary uncertainty source in the likelihood term. Nevertheless, seis2sim needs to honour the *a priori* information, such as the stratigraphy and geological connection under the heterogeneous turbidite context. This information emerges in the prior term of the

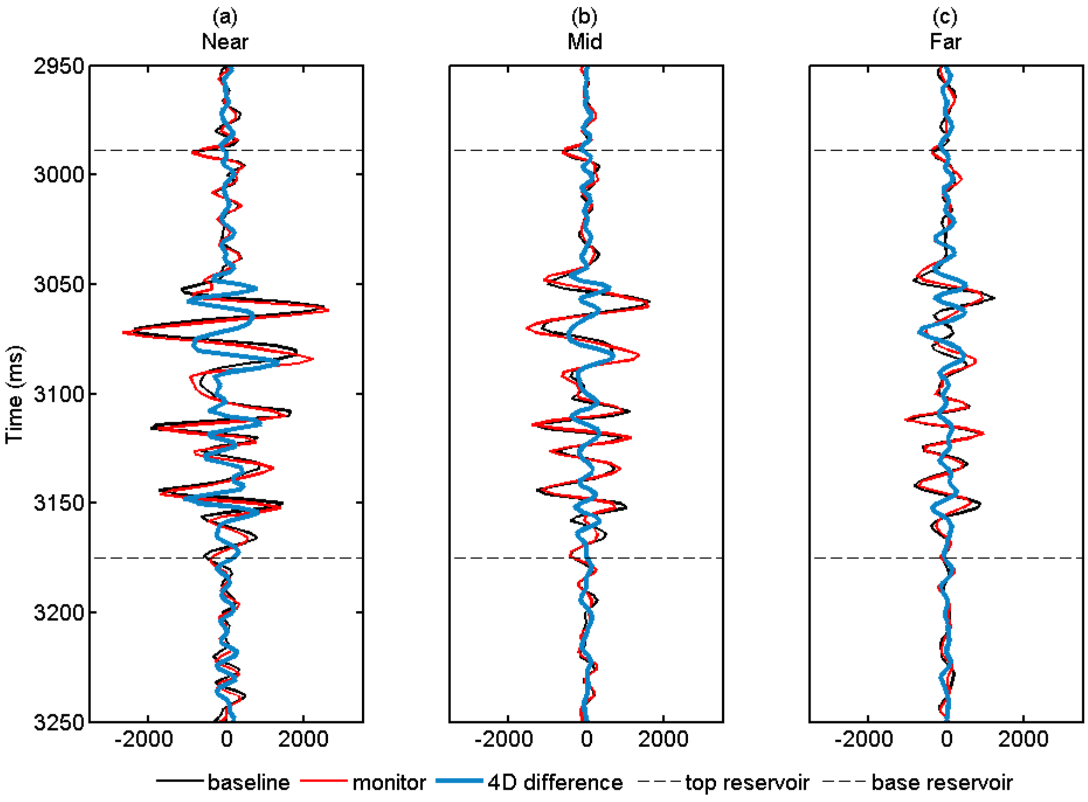

Figure 5.18 *The (a) near, (b) mid and (c) far offset data of the baseline (black), monitor (red) and the difference (blue) traces at well A1.*

Bayesian theorem. Figures 5.19 to 5.21 explain the procedure of constructing this prior knowledge in the 4D seis2sim. Firstly, the 4D sim2seis predictions of the reservoir's elastic properties are generated at the baseline (2001), monitor 1 (end of 2002), monitor 2 (end of 2003) and monitor 3 (end of 2004) times. In fact, time-lapse seismic data is acquired only at the time of monitor 1 and 3, but sim2seis is capable of filling the "time gap" according to the simulation. As shown in Figure 5.19, because of gas injection into the B3 sequence, the upper part of the reservoir (layers 2 to 48) is "softened' in P-impedance, while S-impedance increases slightly. The later water injection in 2003 and 2004 causes "hardening" in both P and S impedance but the changes are still very subtle. These small elastic changes are consistent with the minor changes in time lapse traces, as discussed.

These changes are rearranged by subtracting one from the other in all possible combinations of sequences, to form vectors of changes which are later plotted along a common time axis as shown in Figure 5.20. This technique originated from Huang and

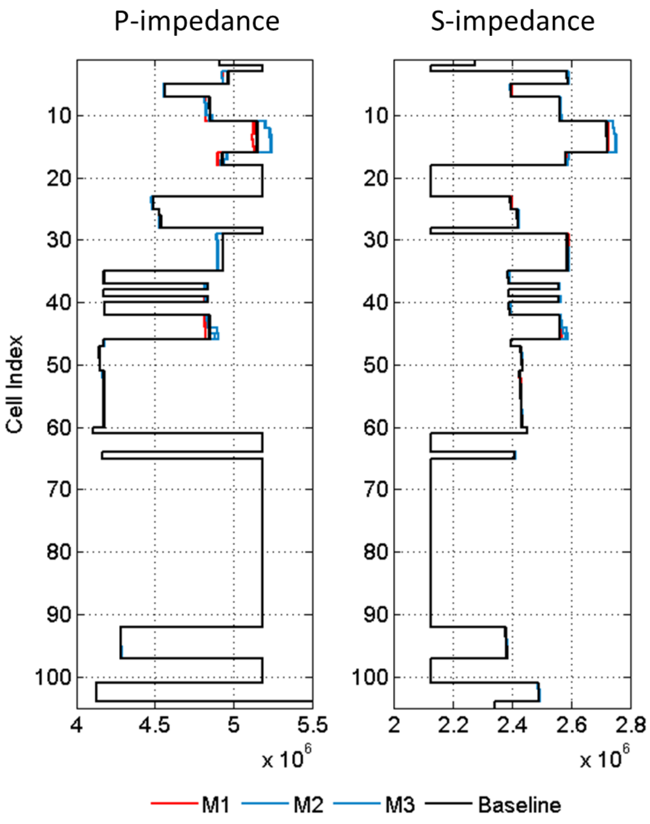

Figure 5.19 *The sim2seis predictions of P and S impedance profiles at baseline, monitor 1, monitor 2 and monitor 3. The vertical axis is the layer index of the reservoir model.*

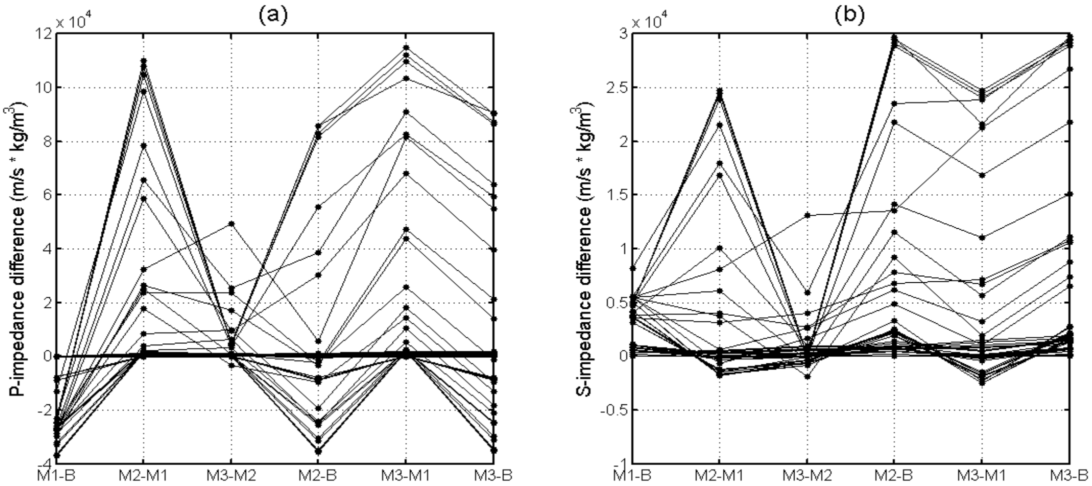

Figure 5.20 *The time series of P and S impedance changes of all the cells shown in Figure 5.19. Cells of no or small changes stay close to the zero level.*

MacBeth (2011, 2012). The covariance and correlation coefficient matrices over all these time series are then calculated and displayed in Figure 5.21. The purpose of this exercise is to extract the connectivity for different parts of the reservoir, according to their time lapse responses. As shown in Figure 5.21 (c) and (d), the correlation matrices for both P- and S-impedance changes firstly identify the active part of the reservoir. In this case, layers of small changes are shown as white gaps. Secondly, the correlation coefficients are high when two layers present a similar pattern of changes, and they are thus assumed to have higher connectivity to each other. High correlations could be found not only in neighbouring cells, but also in the non-contact cells, representing connected geological formations. The S-impedance correlation coefficients are more uniform, while the P-impedance correlation coefficients show different polarities above and below cell 52. This boundary agrees with the model zonation where the transition from B3 to B1 takes place. The coefficient matrices are merely the normalised covariance matrices, which are easier to interpret and explain in this thesis. But essentially, it is the covariance matrices that are inserted into the Bayesian prior term to ensure the posterior realisations honour this piece of reservoir engineering knowledge.

With this engineering *a priori* knowledge, the 3D residual misfits and the SNR, seis2sim is applied to the example in Figure 5.18. The anticipation is to remove the

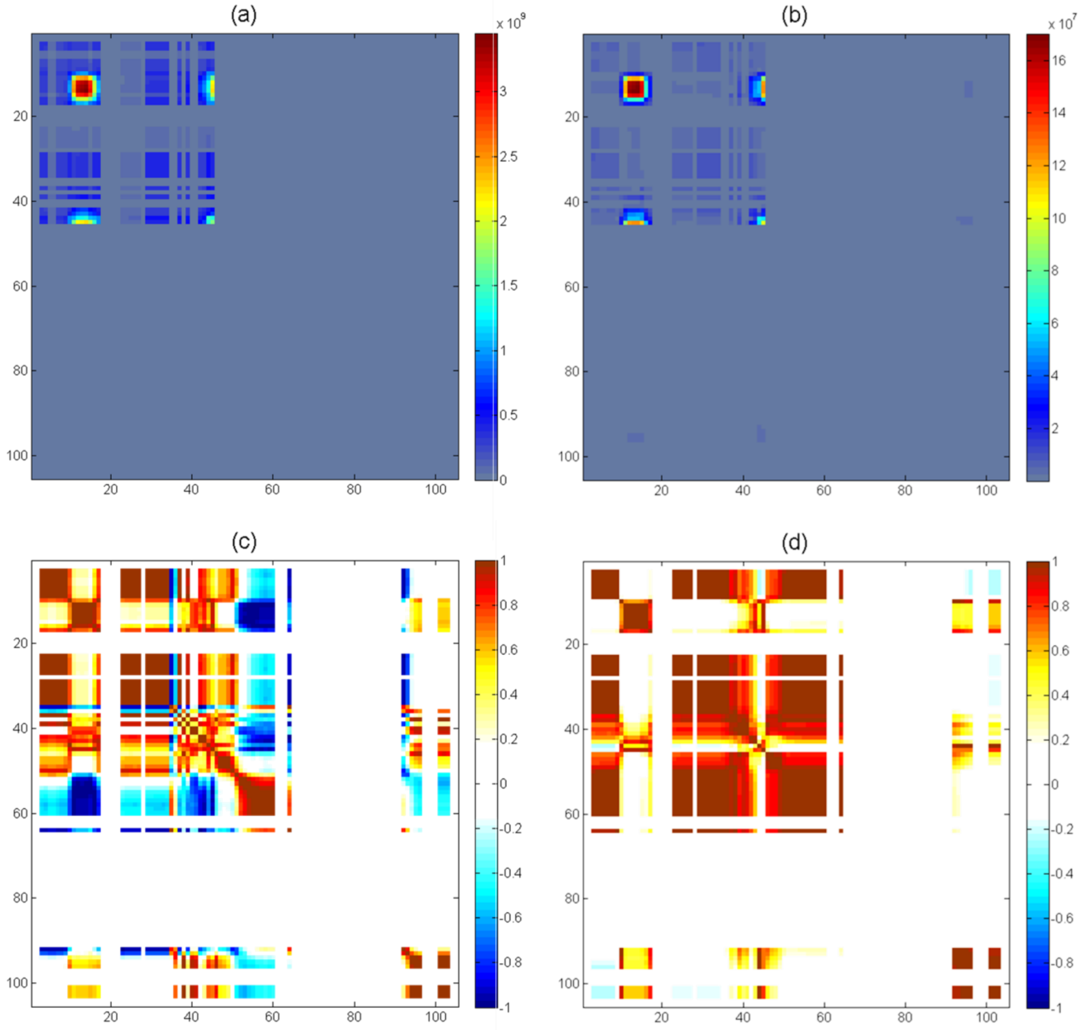

Figure 5.21 *The covariance matrices of (a) the P-impedance changes and (b) the S-impedance changes. The corresponding correlation coefficient matrices are shown in (c) and (d).*

artefacts introduced by the residual time shifts and place the subtle velocity changes at the correct location. The results of unconstrained and constrained seis2sim are shown in Figure 5.22 and Figure 5.23 respectively. In general, the constrained match to the observed 4D amplitude is not as strict as the unconstrained at all offsets. This is primarily because the 3D residual errors do not propagate to the 4D inversion in the unconstrained settings. It can be seen that the matches to the far offsets are in general worse than those to the near and mid offsets, which suggests the 4D AVO modelling has some inherent uncertainty. However, the unconstrained seis2sim gives less stable solutions than the constrained. In the unconstrained results, 4D P-velocity, S-velocity and density changes are found at all depths. The means of the posterior realisations show distinctive seismic imprints.

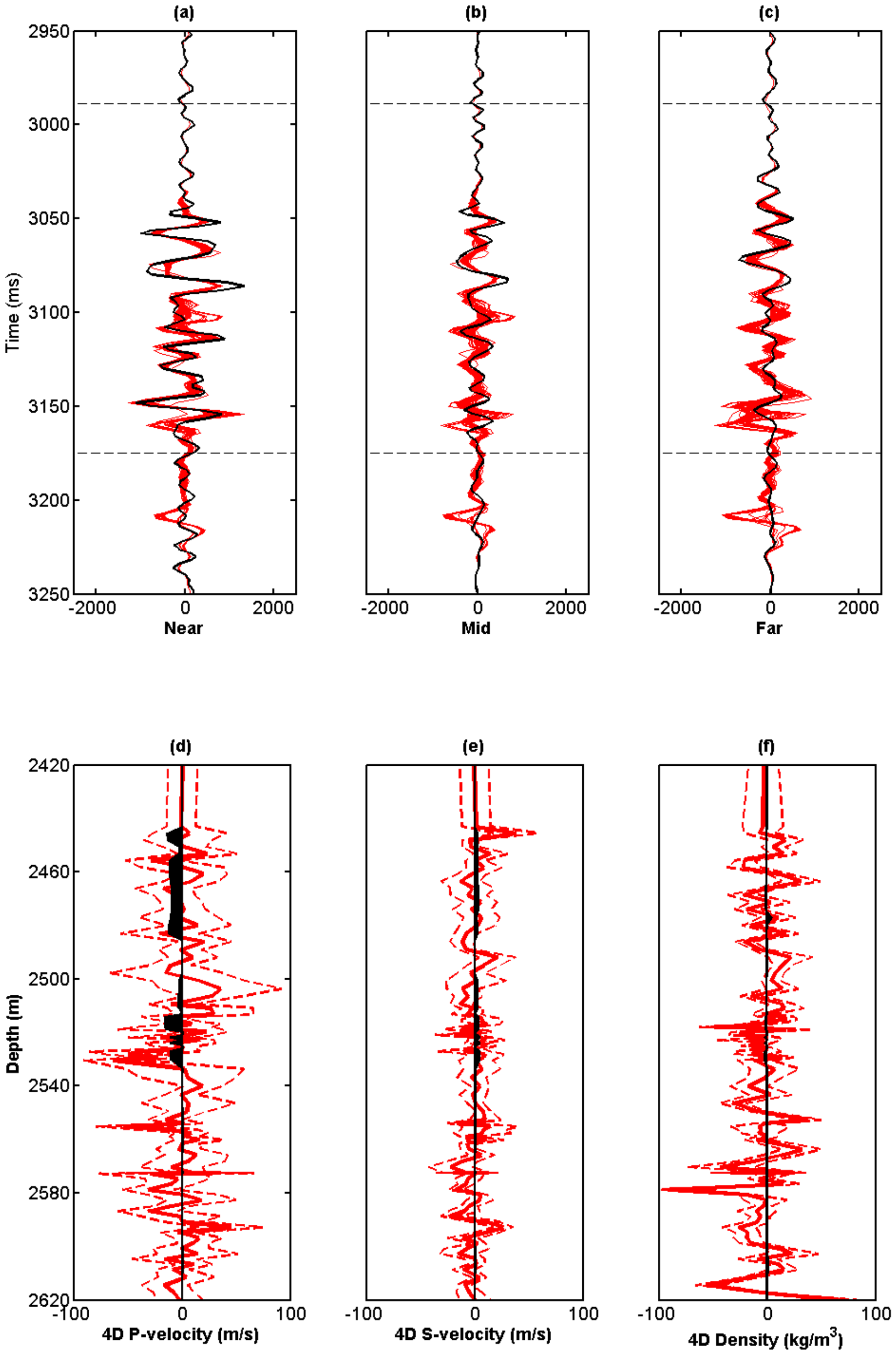

Figure 5.22 *Unconstrained 4D seis2sim results. The observed 4D traces (black) and the posterior realisations (red) are plotted at the (a) near, (b) mid and (c) far offsets. The posterior mean (thick red line), 0.95 uncertainty ranges (dashed lines) and the sim2seis predictions (black) for the 4D (d) P-velocity, (e) S-velocity and (f) density changes are plotted below.*

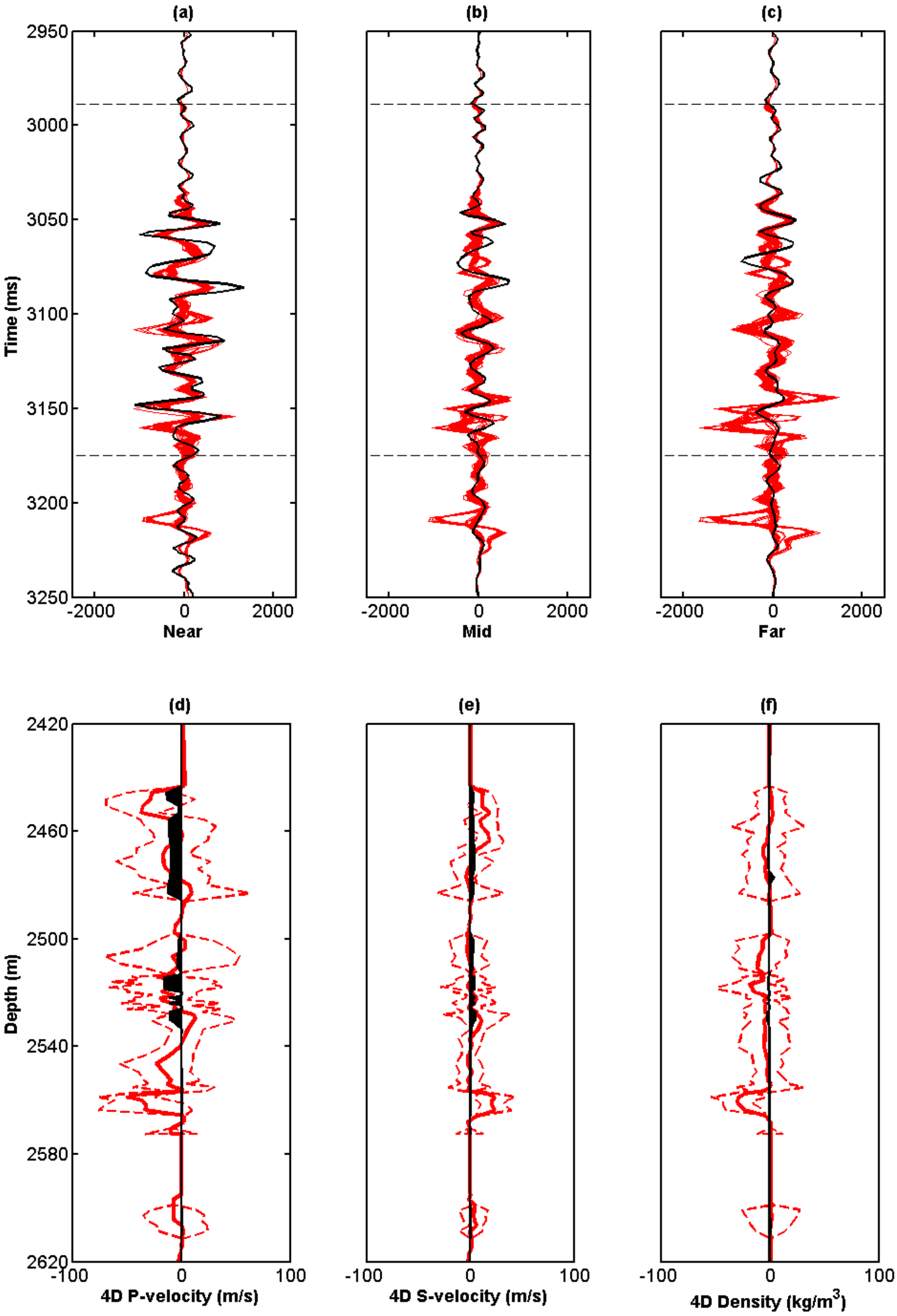

Figure 5.23 *Constrained 4D seis2sim results. The observed 4D traces (black) and the posterior realisations (red) are plotted for the (a) near, (b) mid and (c) far offsets. The posterior mean (thick red line), 0.95 uncertainty ranges (dashed lines) and the sim2seis predictions (black) for the 4D (d) P-velocity, (e) S-velocity and (f) density changes are plotted below.*

In addition, the uncertainty ranges for the unconstrained results are slightly tighter than for the constrained. This indicates the algorithm converged better, but in unrealistic directions. The constrained solutions show smoother means, which are more compatible with the sim2seis predictions. The inactive parts of the reservoir show only small changes, which means the inversion honours the geological background. In short, given the displayed degree of match to the data, the constrained seis2sim delivers more confident solutions for the later CtL workflow.

The same benchmark work is also done in a volumetric way. Figure 5.24 shows the examples from the same cross-section of Figure 5.14 and Figure 5.15, with the observed 4D data, and 4D seis2sim residuals for the near and far offsets. The far offset data shows a lower frequency than the near, but after seis2sim, the residuals, both the unconstrained and constrained, are of similar character. The biggest mismatches are found in common – where the gas is injected and accumulates as the gas cap is formed. The possible reason for this is the inappropriate modelling for 4D tuning, which will be discussed further in Chapter 7. The resultant 4D P-impedance and 4D S-impedance are shown in Figure 5.25. In both cases, the 4D P-impedance shows better images than the 4D S-impedance. The 4D S-impedance images are more scattered and sometimes confusing in terms of the polarity in 4D changes, e.g. gas is represented by S-impedance increase. The constrained seis2sim results show much cleaner images than the unconstrained, because of the geological background defined from the engineering constraints. Moreover, the signal patterns are different in the northern part, also. Generally, the impedance decreases are caused by the gas injection and exsolution, which gives very bright 4D signals. The only criteria to judge the discrepancies between the unconstrained and constrained results is the production data, which will be discussed in detail in the next chapter.

5.4 Summary

The seis2sim technique has been fully applied to the Girassol HR 4D seismic dataset and the results are now available with the sim2seis predictions in both TWT and reservoir grid domains (Figure 5.26). The comparison between them is the key driver for the next chapter. Unlike the Heidrun example, the 4D seismic data are present in angle stacks and at higher resolutions. The geology of the turbidite reservoir is by itself

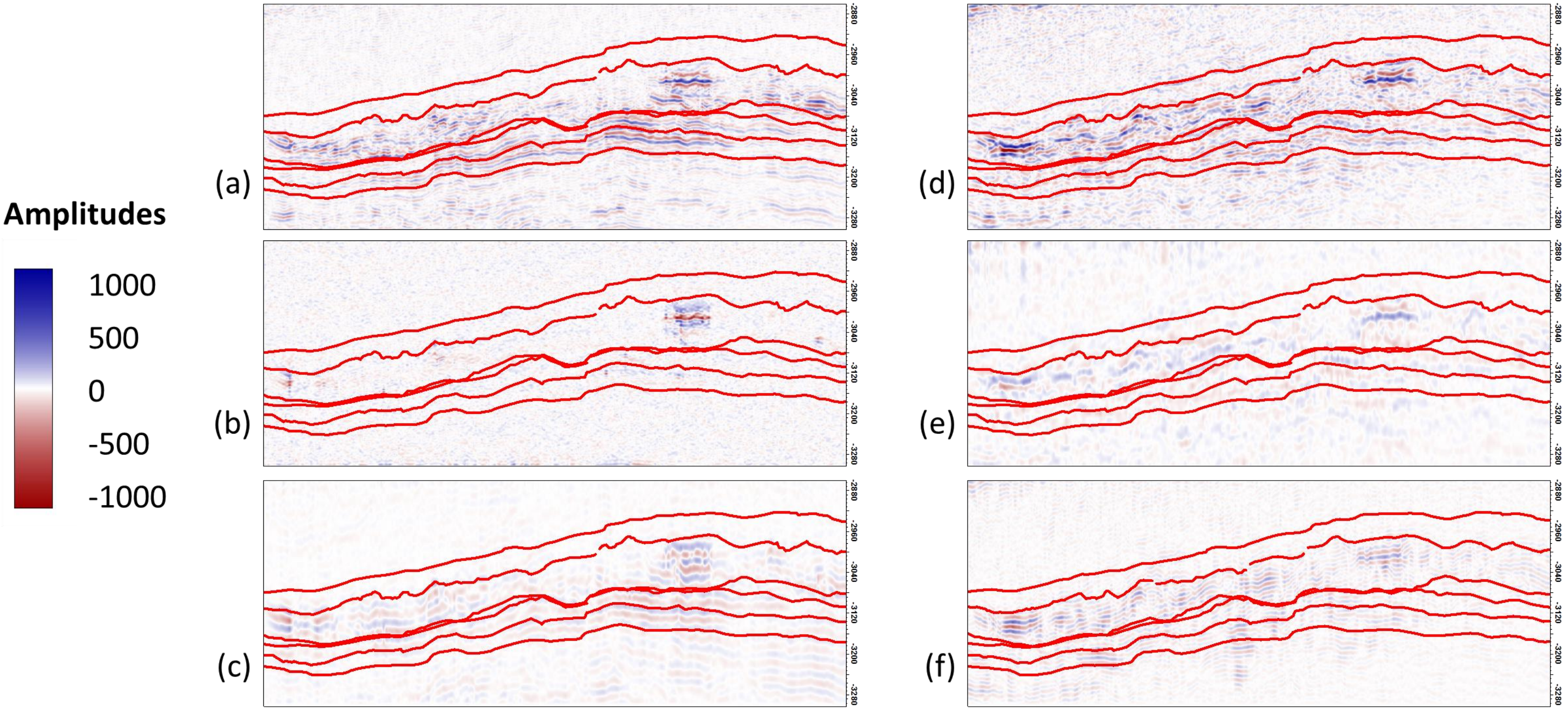

Figure 5.24 *(a) The observed 4D seismic at near offset, and the residual amplitudes after (b) unconstrained 4D seis2sim and (c) constrained 4D seis2sim; (d) the observed 4D seismic at far offset, and the residual amplitudes after (b) unconstrained 4D seis2sim and (c) constrained 4D seis2sim;*

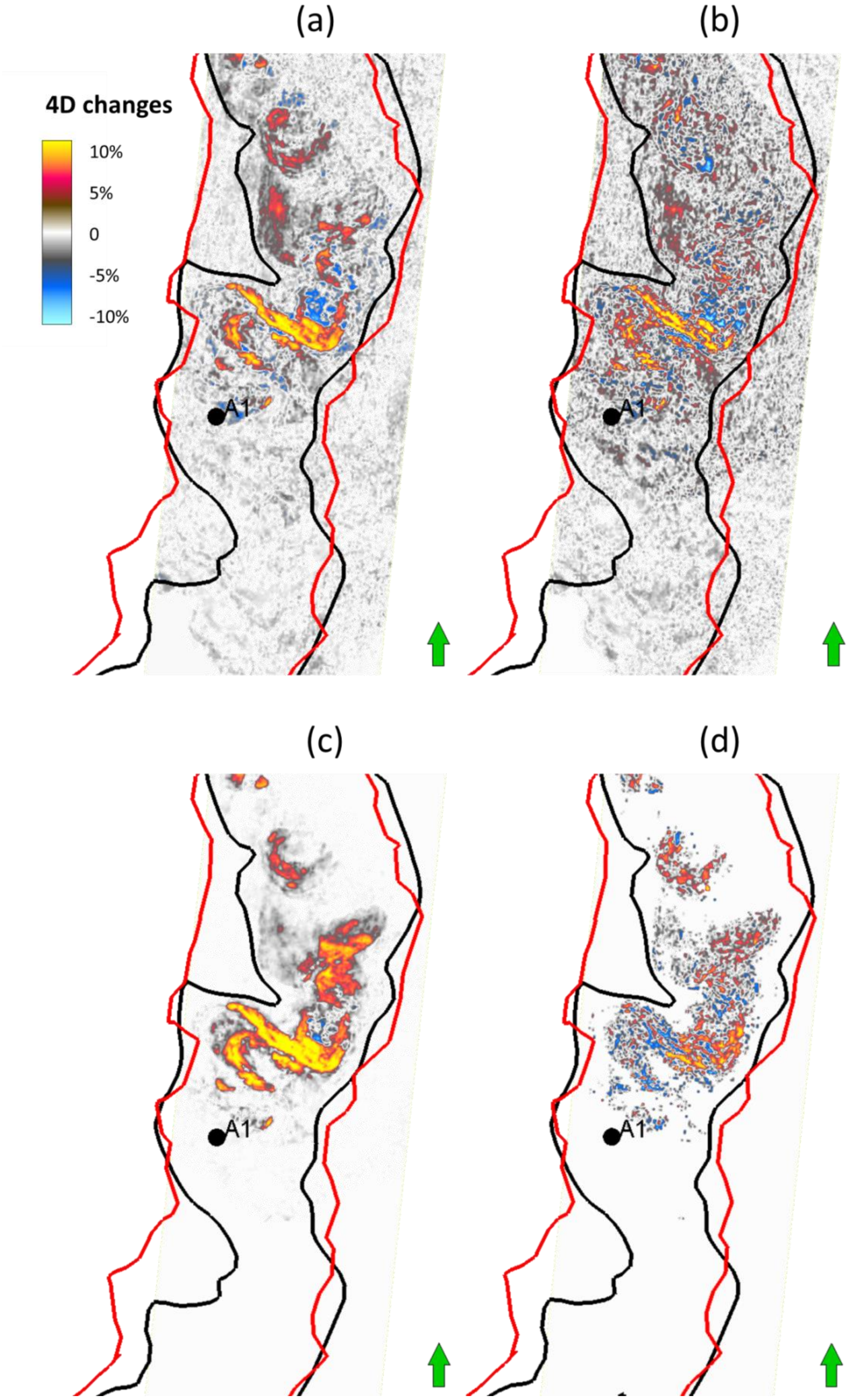

Figure 5.25 *Time slices of (a) 4D P-impedance and (b) 4D S-impedance at the gas injection depth of the unconstrained 4D seis2sim results.(c) and (d) are the corresponding results for the constrained 4D seis2sim.*

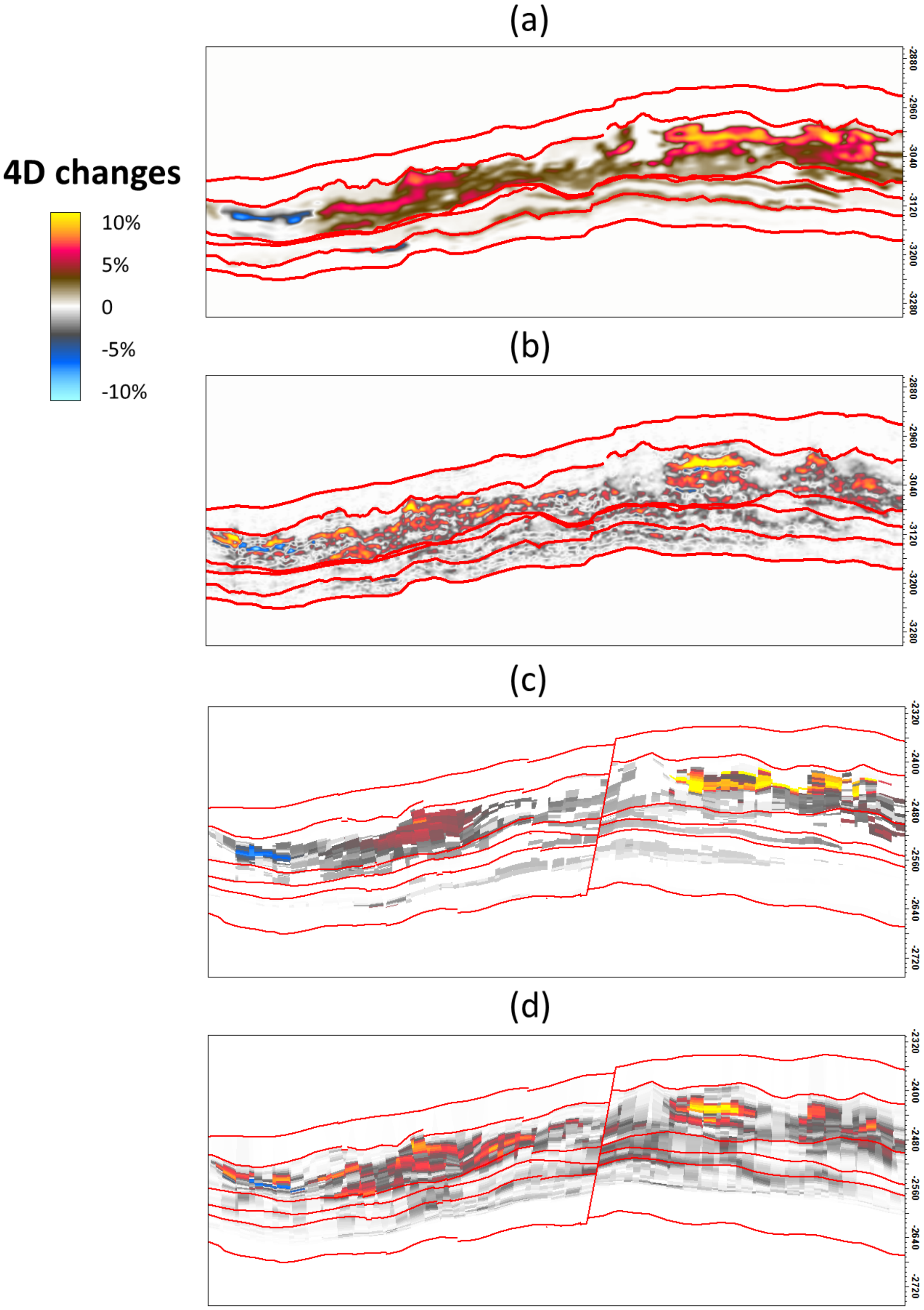

Figure 5.26 *(a) Sim2seis and (b) seis2sim 4D P-impedance in the TWT domain. (c) and (d) are the corresponding results on the reservoir grid.*

much more complicated than the Heidrun fluvial channels, and this, together with the HR seismic data, has raised a higher challenge to the seis2sim technique. The coupled scheme of the proposed 4D seis2sim not only gives static and dynamic seismic characterisation for the reservoir, but also helps to resolve the artefact of amplitudes caused by residual time shifts. The sim2seis-derived constraints play an important role in guiding the 4D seis2sim search, which provides the algorithm with engineering consistent *a priori* information regarding geology and production changes.

The discrepancy between the constrained and unconstrained seis2sim results is debatable at this stage. But for the interests of CtL, more compatible seismic solutions are welcomed. Nevertheless, any 4D seismic must make sense in terms of reservoir engineering, because the latter is the essential cause. This dispute will be discussed in the next chapter, during the presentation of the CtL workflow.

Chapter 6

Closing-the-loop using EC 4D inversion for the Girassol field

“Is the action of nature not unlike drawing a bow? What is higher is pulled down, and what is lower is raised up; what is taller is shortened, and what is thinner is broadened; nature’s motion decreases those who have more than they need and increases those who need more than they have.”

「天之道，其猶張弓欤？高者抑之，下者舉之，有余者損之，不足者補之。天之道，損有余而補不足。」

Lao Tze, *Chapter. 77, Tao Teh Ching, 400 BC to 700 BC*

“You can't make an omelette without breaking eggs.”

In this chapter, an approach similar to that of Chapter 4 for integrating engineering and 4D seismic data into a dynamic reservoir characterisation workflow is applied to the Girassol dataset. An attempt is made to update the reservoir geometry by analysing the consistency between the 3D, 4D data and the static reservoir model. This aims to update the fluid flow simulation model whilst simultaneously honouring all data sources from the engineering, seismic and geological domains.

The starting point is in the reservoir engineering domain, where the process of history matching has been used in updating procedures for a number of decades. This approach attempts to mathematically adjust the fluid flow simulation model and/or the geological model, until the predicted and observed historical well production are in agreement (for example, Oliver et al., 2008). This workflow may be regarded as closure of a small inner loop (Figure 1), and does not involve the seismic. For the past two decades, 4D seismic has also been included in history matching as it is known to supply important information on the dynamic behaviour of the reservoir, with which to constrain the non-unique process of history matching (Landa and Horne, 1997, Stephen and MacBeth, 2008). Many approaches are possible for implementing this constraint. One is to simply match the production data and the 4D seismic simultaneously in a joint objective function, as an extension of the history match. However, the degree of fit is known to depend on the initial geological model created, in turn, by the 3D seismic. Thus, another approach is to build the geological model using both the 3D and/or 4D seismic data, and then production history match (Castro et al., 2006). More recently, many more possibilities for closing the loops between the 3D and 4D seismic data, production data, and the simulation/geological model have become possible, with the advent of techniques to determine 4D impedance changes (El-Quair et al., 2005, Toinet et al., 2011) and pressure and saturation changes (Landrø et al., 2001, Tura et al., 1999, MacBeth et al., 2006).

Figure 6.1 illustrates the various options available for CtL in the Girassol dataset, labelled as the reservoir, static, dynamic and history matching loops. The reservoir loop attempts to preserve the match to defined boundaries of the reservoir, defined from the 3D seismic interpretation but also the 4D seismic. It is common practice for the structural framework and property distributions of the reservoir to be defined by the 3D seismic only. However, this does not guarantee a fit to the 4D seismic. Mismatch between the presence/absence of a reservoir sand detected from 3D seismic and the observed 4D seismic response would not allow the loop to be closed between the predicted and observed 4D seismic. Staples et al. (2006) reinforce this point with an example from the Gannet-C field, in which joint reinterpretation of the 3D/4D seismic prompted the revision of the extent of a reservoir sand volume. In the dynamic loop, pressure and saturation changes estimated from 4D seismic are rarely used to match the

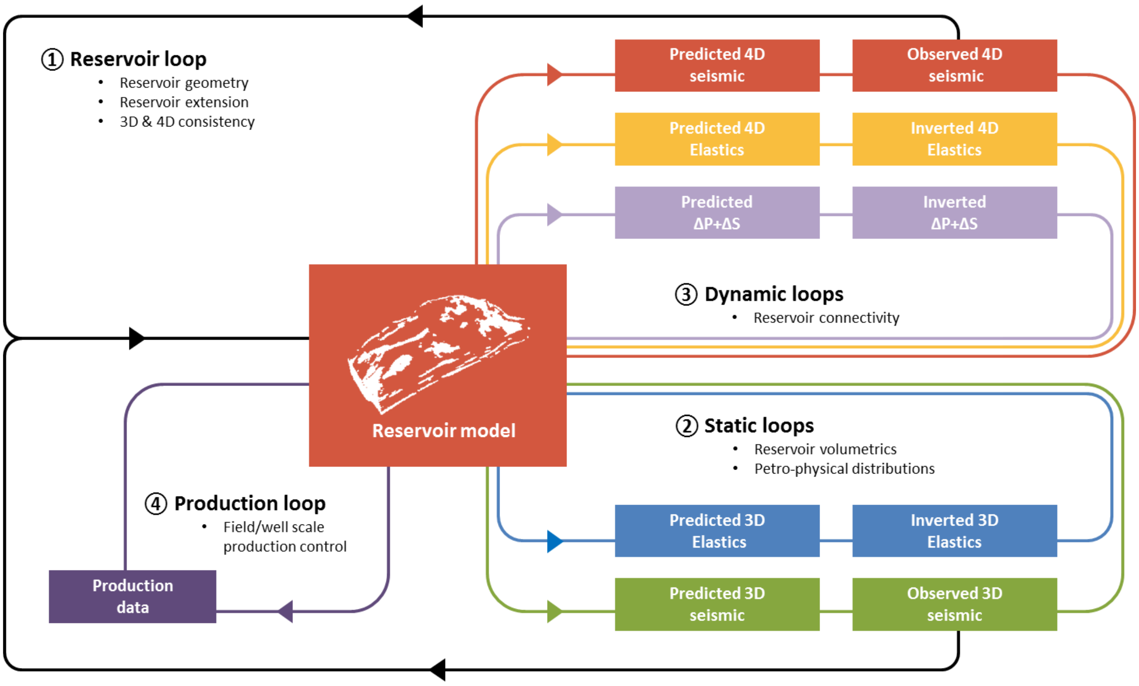

Figure 6.1 *The various loops to close for the Girassol example. The reservoir loop takes into account both the 3D and 4D seismic data, while the predictions (sim2seis) and inversion (seis2sim) of 3D and 4D attributes are compared in the static and dynamic loops, correspondingly.*

predictions of the simulator, due to difficulties in achieving a satisfactory inversion and the nature of the simulation model (Huang et al. 2010). Matching in the impedance domain offers a good balance between computation time and robustness. It is relatively easy to model a volume of impedance changes from the simulation model, and furthermore, techniques for inverting for 4D changes are now readily available. Examples of this approach include Guderian et al. (2003) in the Draugen field, and Roggero et al. (2007) in the Girassol field, all with a reasonable degree of success.

6.1 An inversion-driven workflow for closing the loops

Whilst there are many individual examples of model updating using one of the above approaches, there is a need for a more satisfactory workflow that attempts to honour all the loops shown in Figure 6.1. To address this challenge, here I propose a practical sequential workflow and apply it to a West African field. The scheme incorporates several benefits which help make the workflow tractable. In the first, the inevitable non-uniqueness associated with the 4D inversion is reduced by imposing a constraint from the reservoir engineering domain, as discussed in the previous chapter. The second is exploitation of a consistent grid for the inversion and the simulation, to avoid re-scaling issues. The focus of this workflow is to accomplish a comprehensive update in a sensible sequence of closing-the-loop exercises.

In this workflow, the loops described above are closed in a series of three stages that focus on reservoir geometry, then volumetrics and finally reservoir connectivity updating. In Stage I, the 3D and 4D signals are combined to capture a common reservoir. This solves the problem of observing a valid reservoir signal in the 3D seismic but no 4D seismic signal, as shown by Staples et al. (2006) in the Garnet-C field, which may indicate either a by-passed reservoir zone or an isolated reservoir segment. Alternatively, a 4D seismic signal but no 3D seismic signal indicates a need for a closer look at the 3D interpretation. This idea is further explained in Figure 6.2. According to the signal strength in 3D and 4D, the reservoir volume could split into four of the discussed conceptual areas. The grey area stands for the inactive reservoir, since there are neither 3D nor 4D seismic signals. The green area stands for the active reservoir, since it is detected as reservoir in both 3D and 4D. The blue area represents reservoir has only 3D recognition, whilst the red area means reservoir volume that is not seen by 3D but later revealed by 4D interpretation. Indeed, the threshold is usually difficult to define, as there is often an uncertainty in separating the signal from noise by a single value.

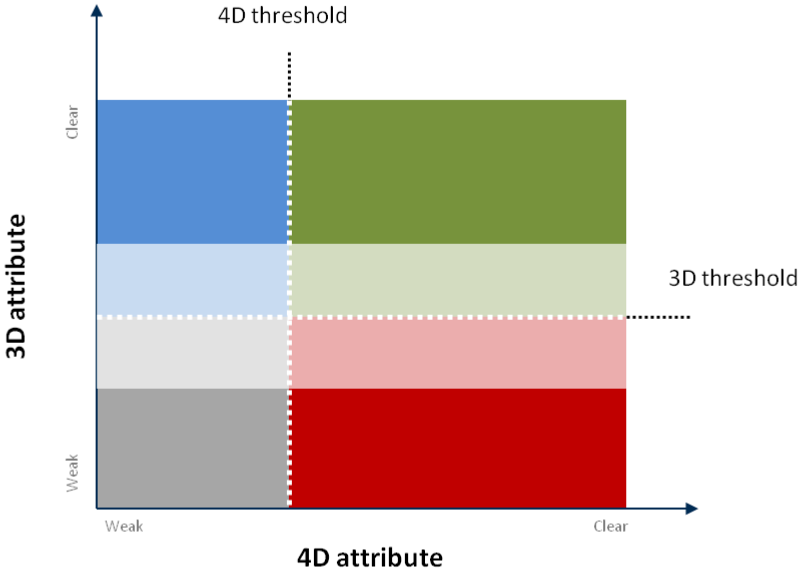

Figure 6.2 *Four conceptual scenarios may appear in the reservoir loop. The white box indicates the uncertainty introduced by the 3D data as a result of lithological ambiguity.*

After refining the reservoir layout according to 3D and 4D data, Stage II focusses on the inversion of the baseline (pre-production) 3D seismic into volumes of impedance and $V_P/V_{S,}$ using an initial background solution calculated from the simulation model. These results are then converted into porosity and net-to-gross values using the wireline logs. This closes the static loop in which the synthetic 3D seismic from the reservoir model now matches with the observed data. After the new porosity and net-to-gross values are in place, in the next stage, impedance change predictions from the simulation model can now be compared directly to the inverted 4D seismic impedance changes. The latter are inverted in a coupled inversion scheme according to an engineering constraint fed back from the simulation domain, which encourages solutions that tend to converge to those that make sense in both domains. Finally, transmissibility multipliers in the simulation model are adjusted until the match for the dynamic and history matching loop is improved.

6.2 Application to the Girassol field

The above updating workflow was tested on the Girassol field. As introduced in the previous chapter, this particular field has stacked unconsolidated turbiditic sands of several cycles. Reservoir characteristics were carefully studied from the rich FEWD and wireline logging data acquired from the early stage development wells. It has been reported by Retail et al. (2002) that the grain size of the turbiditic sequences ranges from fine to medium which are generally well sorted with very good porosity (30-40%) and good permeability (1 to 5 D). The medium to coarse sands have good porosity (20-30%) and very good permeability (3 to 10 D), while the very coarse sands and conglomerates have fair porosity (15 to 20%) and fair permeability (100 mD to 1 D). Therefore, it is concluded that the geological nature has a direct impact on the reservoir quality, which requires static modelling of the reservoir to take the depositional facies into consideration. Particularly, the large porosity range suggests a high uncertainty in predicting the effective reservoir volumes, therefore, closing the static loop by updating the initial porosity and NTG values in the reservoir model is of great importance.

A regional structural fault pattern was established on all the Girassol structure (Retail et al., 2002). The faulting scheme found through the Girassol structure is primarily of compensation normal faults caused by progressive folding during the Tertiary inversion. The faults in the B3 complex present mostly as post depositional normal faults with a

NW to SE direction in the north and N-S direction in the south (Figure 6.3). The B3 complex structure is twisted, dipping toward the northeast in the northern part and toward the southwest in the southern part. The throws along the faults are generally 10-30m. A well interference test was conducted by Retail et al. (2002) before the first oil, in which the fault throw, the clay smearing, the segmentation of the faults and the sand gouge material were studied by investigating numerous 3DHR seismic attributes as well as the down-hole gauge pressure interference. They found the faults are generally communicating, although the pressure passages are potentially via some individual sub-sequence inside the main turbiditic channels. This draws attention to the important role of the transmissibility field update in closing the dynamic loop.

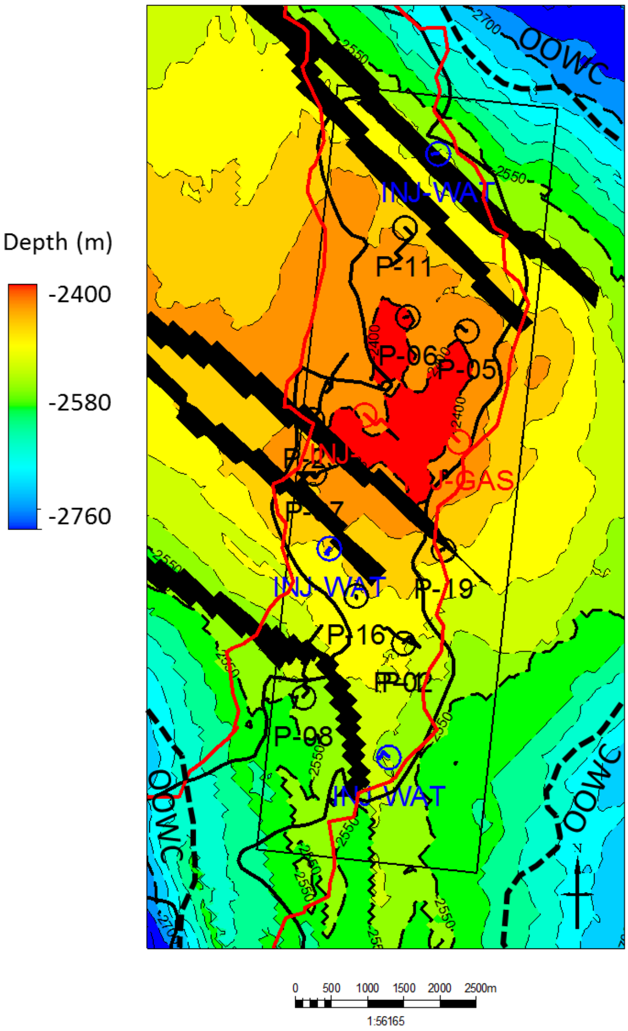

Figure 6.3 *The subsurface topography of the B3 channel complex modelled for simulation. The black polygons indicate the fault panels, while the rectangle shows the seismic inversion coverage. The sinuous black lines indicate the top layout of the channels while the red ones indicate the bottom.*

In addition, high solution gas to oil ratio and a reservoir pressure near bubble-point are reported at the exploration stage, resulting in a large amount of exsolved gas after early production. Figure 6.4 shows the predictions of these 4D phenomena by the initial reservoir model, which had been initially production history matched.

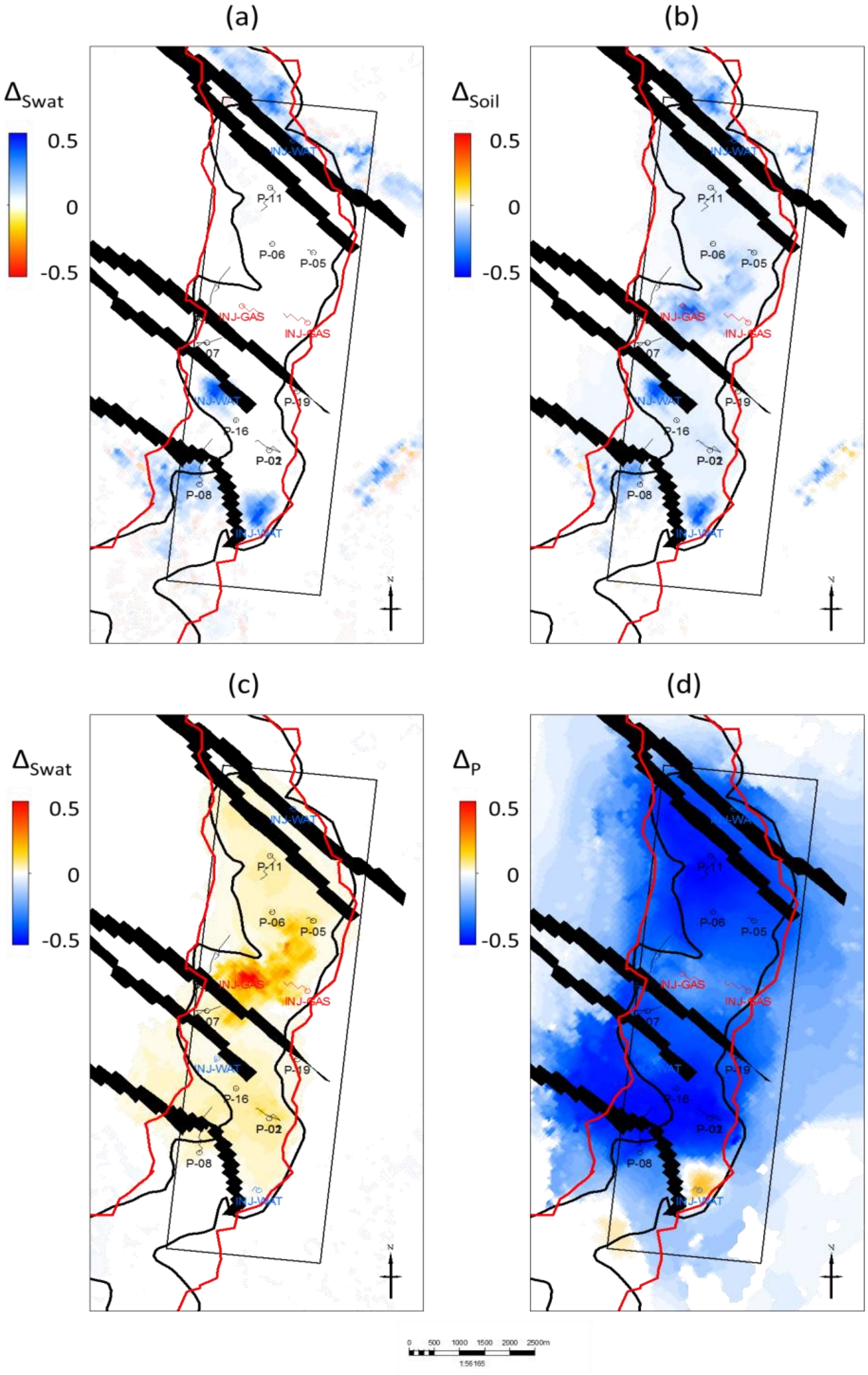

Figure 6.4 *(a) The prediction of water saturation difference between baseline 2001 and monitor 2002; (b) the prediction of oil saturation change for the same period; (c) the prediction of gas distribution as a result of gas reinjection and exsolution; (d) the predicted pressure difference.*

As introduced before, high resolution time-lapse seismics were acquired two years prior to the first oil in December 2001, and then subsequently in 2002 and 2004. In my study, the 2001 and 2002 time-lapse seismic pair has been inverted, leaving the 2002 to 2004 period as a predictability test. The area of interest is also shown in Figure 6.4, inside which the seismic data is inverted, and the reservoir model updated.

6.2.1 Closing the reservoir loop

The primary objective of closing the reservoir loop is to examine the model in terms of geometric consistency with the observed 3D and 4D seismic data, as the layout of the reservoir model depends on the interpretation of these data. The top and the base of the initial model follow the geometry of the seismic horizons picked at the B490 and B550 events, inside which the B1, B2 and B3 sequences constitute the main production units (Figure 6.5). There is no clear evidence to precisely relate any of the seismic domain horizons to the gridded model layers, which may suggest a level of inconsistency between reservoir model and seismic data. Consequently, the mapping technique employed in Chapter 4 is not applicable here. The alternative is to use the inverted

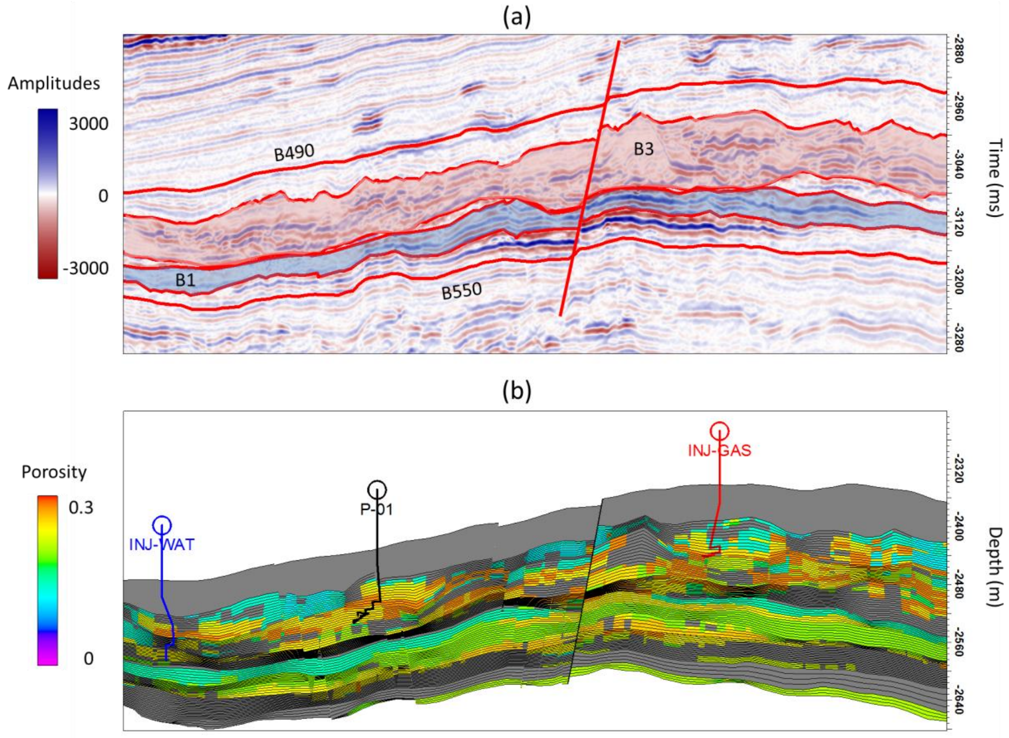

Figure 6.5 *The seismic stratigraphy (a) and the model zonation (b). The model grid is locally refined therefore there is no uniform correspondence between the seismic horizons and model layers.*

baseline velocity model to perform the time to depth conversion, while having the B490 aligned up with the first layer of the reservoir model.

The active part of the initial reservoir model is defined according to a 3D seismic derived sand probability attribute. This sand probability is identical to the NTG concept, according to an internal reference - a NTG value higher than a preset threshold indicates the presence of reservoir. However, a geological uncertainty is reported, in that the threshold is hard to define and there is no clear cut distinction between the reservoir sand and non-reservoir shale, due to overlapping elastic properties. Therefore, it is vital to review the definition of the active cells of the initial model, in order to include all possible reservoir volumes detected by both 3D and 4D and close the reservoir loop - otherwise, the static and dynamic loops may be never be closed because of this fundamental mismatch.

In order to depict the reservoir layout, representative seismic attributes are needed from both the 3D and 4D seismic data. During the Stage I update, the V_P/V_S ratio is derived from the baseline seismic by inversion and higher quality reservoir sands are identified. Petrophysical analysis of the well log data suggests that a NTG cut-off of 0.4 separates reservoir sands from the surrounding non-reservoir shales. V_P/V_S is found to have only a scattered relationship with the NTG, so this suggests that 3D interpretation of the reservoir activity by this route may be uncertain (Figure 6.6). In contrast, the acquired 4D seismic has a very good repeatability, with an average normalized root-mean-square (NRMS) value below 0.1, and a signal-to-noise ratio of up to 6. So it is decided to

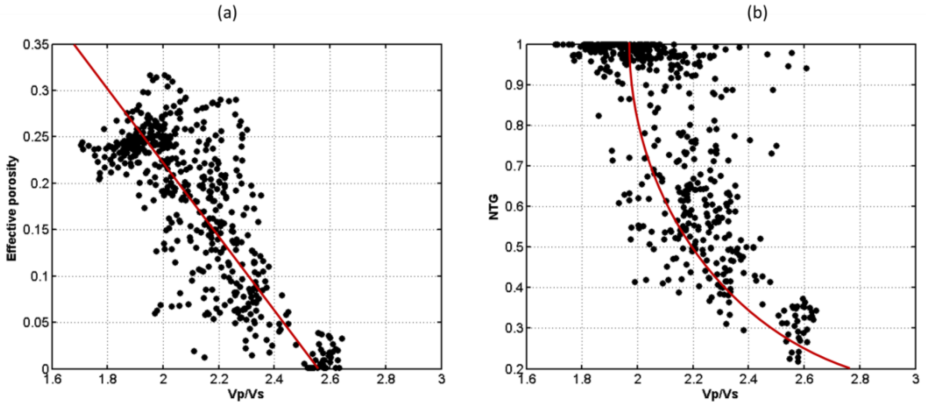

Figure 6.6 *(a) The cross plot between effective porosity and VP/VS, (b) the quadratic relationship between NTG and VP/VS.*

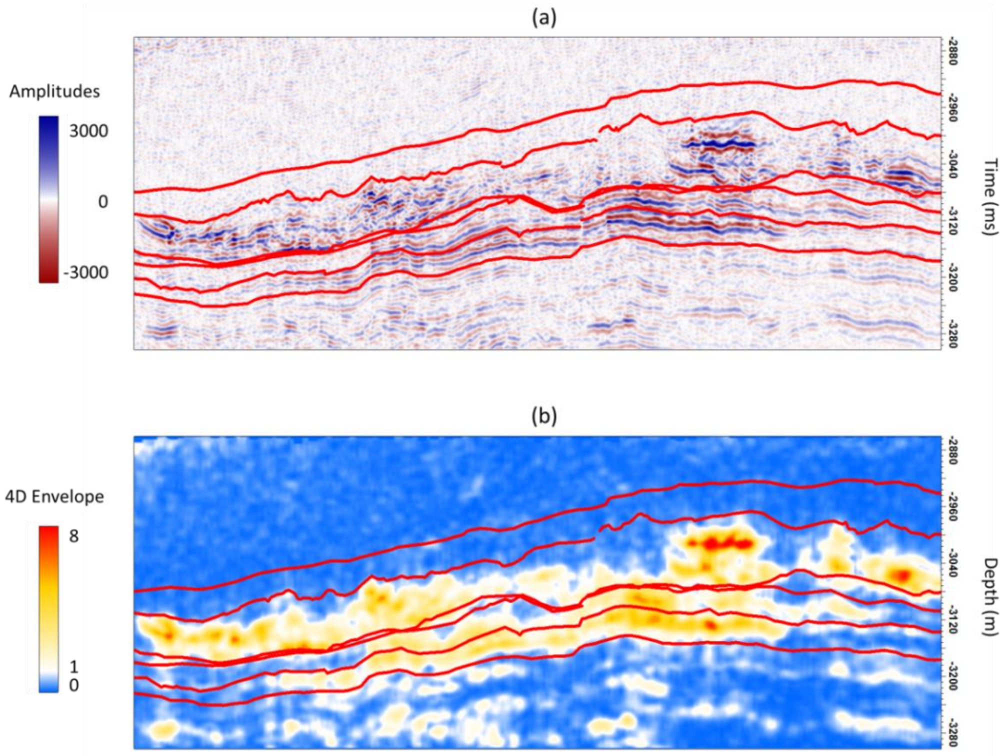

Figure 6.7 *(a) The observed 4D seismic amplitude; (b) the thresholded envelopes of the 4D amplitudes, where the threshold is set to unity, according to the signal-to-noise ratio at each seismic trace location.*

incorporate the 4D seismic signature to assist the determination of the active reservoir. Because of the high seismic resolution (dominant frequency of 65 Hz), reservoir changes inside a single sand channel are presented as a number of distinct cycles. Therefore the magnitude (modulus) of the 4D difference trace is calculated using the Hilbert transform to enclose the changes as an envelope attribute. The thresholded envelope of the 4D seismic amplitudes is regarded as active representation of the reservoir and used to identify the major sand packages undergoing dynamic change (Figure 6.7). The example in Figure 6.8 shows a time slice at the gas injection depth of the inverted baseline results. The V_p/V_s threshold is set to 2.3, below which the volume is coloured in red and yellow, indicating the sand presence. It can be seen that neither the seis2sim inverted P-impedance nor the V_p/V_s has the ability to clearly separate the reservoir sands from the surrounding shale along the main channel. Geologically this ambiguity can be argued as a turbidic flood plain. However, it is found, in a similar exercise to that of Kumar and Landa (2008), that the 4D envelope clearly indicates the genuine active pattern of production-related changes, from which this part of the

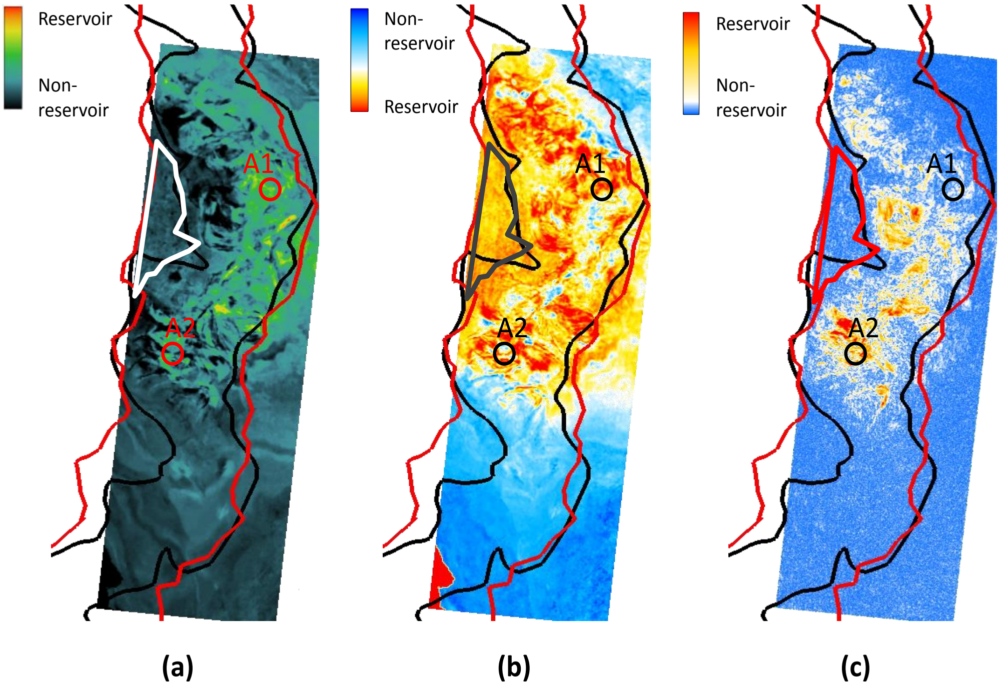

Figure 6.8 *Inverted (a) P-impedance, and (b) VP/VS, together with the 4D envelope (c) used to define the presence of reservoir in this field example.*

reservoir is excluded as inactive. This proves the value of combining the 3D and 4D seismic together in order to enhance the confidence in determining the reservoir when the 3D interpretation is difficult alone.

The next step is to condition the reservoir model to the interpreted 3D and 4D data on the model grid. The inverted P-impedance and V_p/V_s cubes are converted to depth using the inverted baseline velocity, before being re-sampled into the corresponding cells. If multiple seismic samples lie in the same cell, their values are averaged. The same comparison is done again in the depth domain, in order to define the seismic consistent layout. This reservoir architecture is then compared directly with the active reservoir cells in the initial simulation model (Figure 6.9). The common cells are retained, whilst the missing cells are added to the initial model in order to cover all the observed 3D and 4D seismic signals (Figure 6.10). An extra 4% of cells are added, which in turn creates a 10% increase in the overall gross pore volume of the field. The new cells are mainly found to lie along the edges of the original channel complex, rather than floating in an isolated fashion (which would indicate a low probability of being correct). These additional cells are then given the rock permeability and fluid property values of their neighbours, so as to create a natural expansion of the reservoir. Due to the addition of the new cells, the model is now capable of matching both the observed 3D and 4D data.

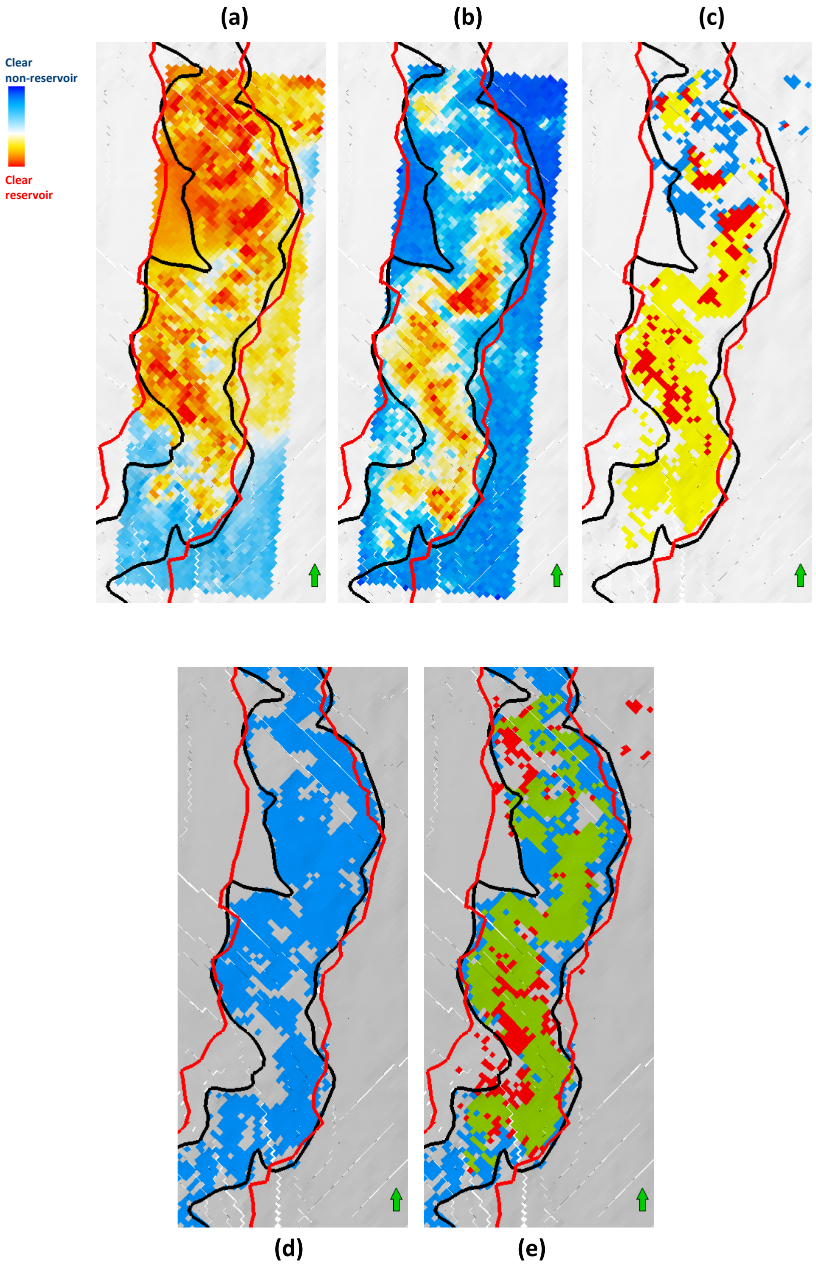

Figure 6.9 *(a) The inverted VP/VS, (b) 4D amplitude envelope, upscaled to the reservoir grid. (c) Cells of the reservoir model, defined by the overlap of the 3D and 4D data. Yellow cells represent active reservoir cells classified by the 4D envelope, red cells represent agreement between 3D and 4D, whilst blue indicates cells that the 3D alone classifies as reservoir. (d) Original distribution of reservoir cells in the model prior to update. (e) Updated distribution of reservoir cells. Red indicates the new cells which have been added to the model; green represents those in common between the model and the yellow cells in (c), and blue indicates the initial model, unclassified by the 3D and 4D data.*

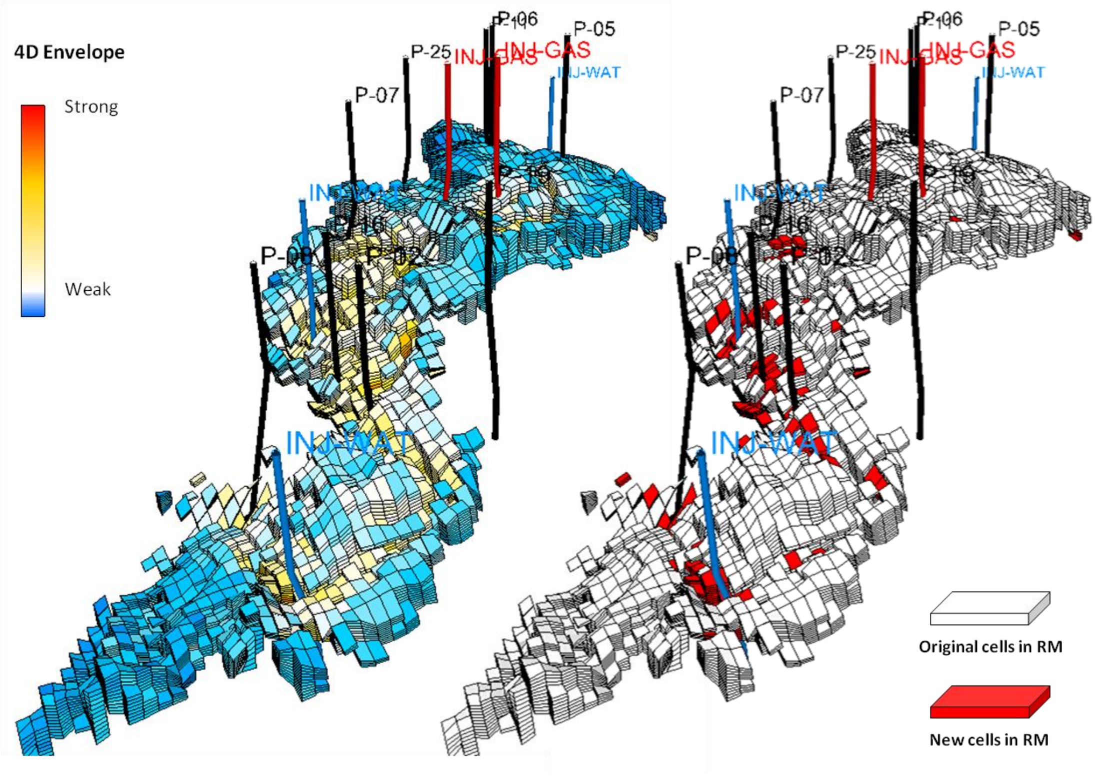

(a) (b)

Figure 6.10 *(a) The converted 4D envelope, and (b) the added new cells along the channel complex. Visually the new cells are primarily determined by the 4D signals.*

6.2.2 Closing the static loop

In closing the static loop, the original NTG and effective porosity values of the reservoir model are re-scaled, according to the inverted V_p/V_s, by utilizing the petrophysical relationship extracted from the well log data (Figure 6.4). In my example it is found that the resultant channel sand distribution is subject to a reduction of pore volume and this, in fact, compensates for the pore volume increase from the new cells inserted during the Stage I update (Figure 6.11). However the porosity and-net to-gross from Stage II better constructs the lateral heterogeneity in the reservoir. Because the lateral variations are inputted into the model from the observed 3D seismic, the synthetic 3D seismic response immediately matches the observed one, which closes the static loop. However, a small degree of mismatch still exists due to the loss of details during the forward seismic modelling process, as the reservoir model scale is coarser than that of the seismic (see Figure 6.12).

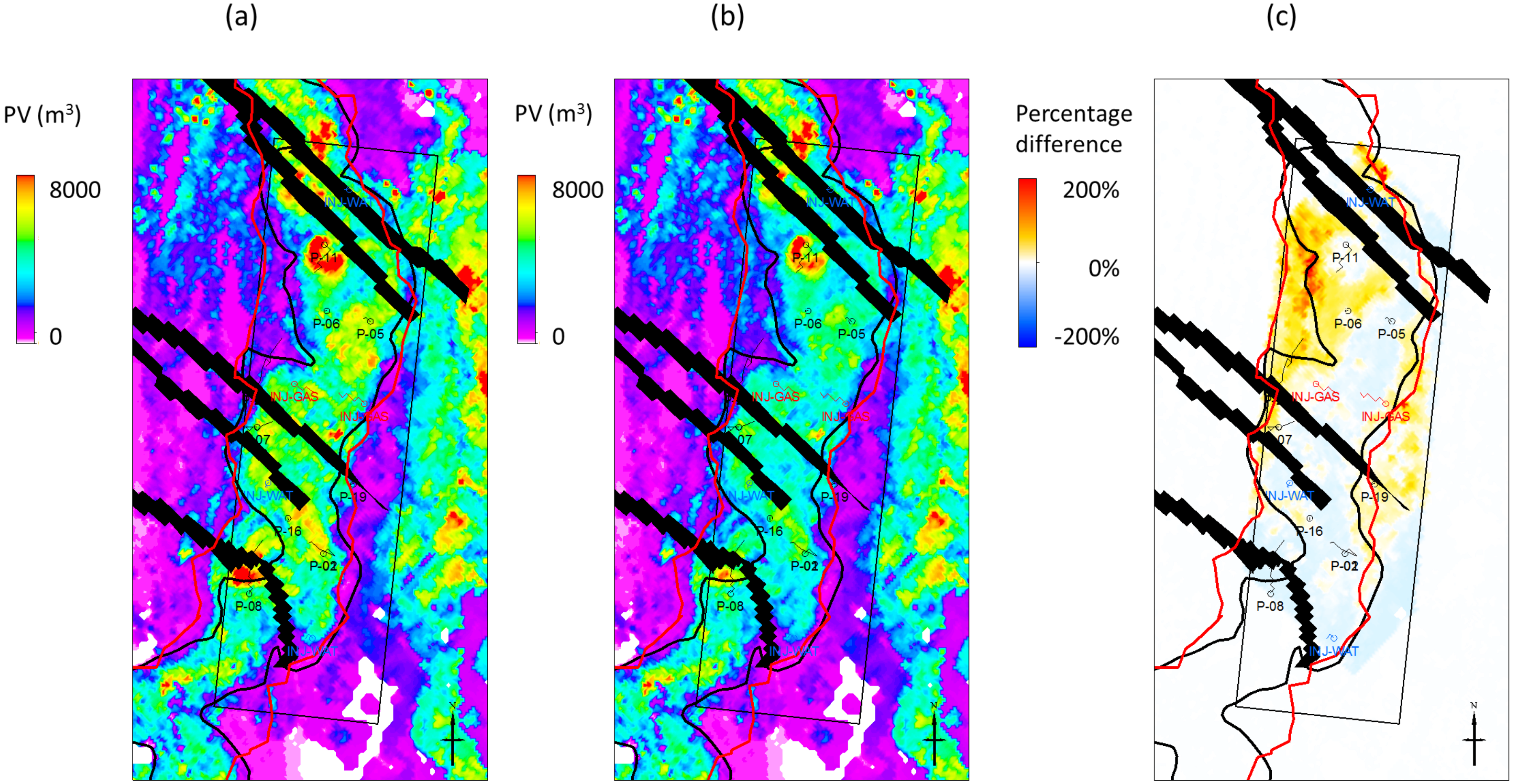

Figure 6.11 *(a) The original PV map averaged in the B3 sequence; (b) the updated PV map generated; and (c) the percentage difference in PV.*

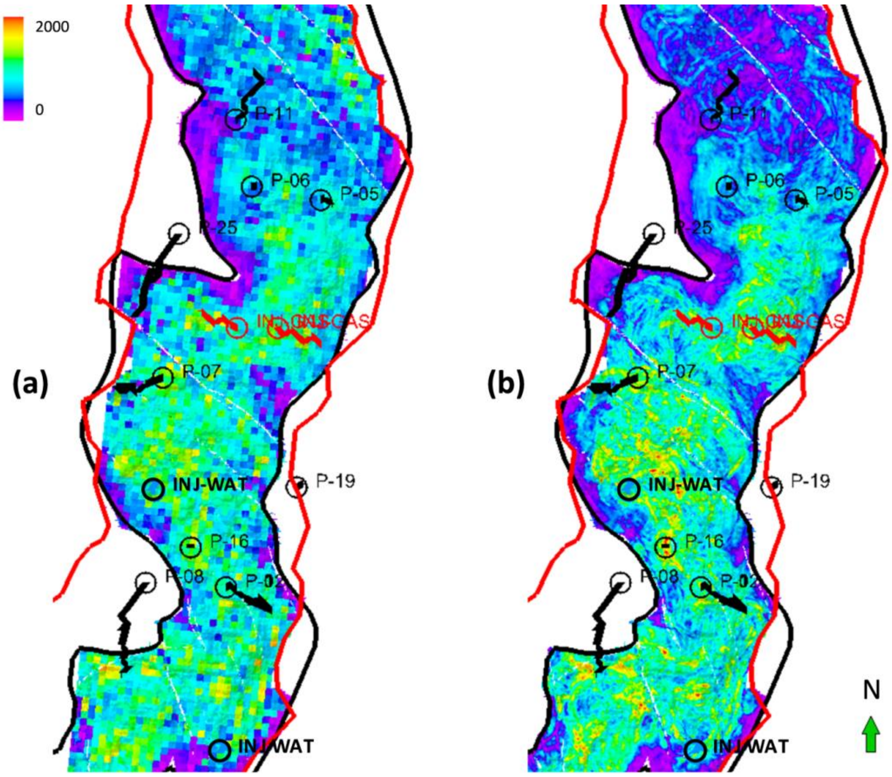

Figure 6.12 *(a) Predicted 3D RMS seismic amplitude map from the simulator to seismic calculation, at the reservoir model scale and (b) the corresponding map from the 3D data.*

As a result of the Stage I and II updates in the reservoir geometry and volumetrics, the matches to the production histories are also changed. Although these impacts are temporal and dynamic, it is important to check the resultant material balance by looking at some key parameters. This has to be done before moving to the later dynamic loop, since it cannot alter the fundamental volumetrics. Figure 6.13 (a) shows the oil-in-place during Stage I and II updates, which reflect the volumetric updates. The pressure profiles plotted in Figure 6.13 (b) show little difference with the variant updates. However, the field scale GOR and water cut suggest the overall failure of material balance with the additional cells, resulting in a significant drift of predictions from the observed records. However, after re-scaling the PV of the reservoir model, the balance is established and the GOR prediction shows a subtle improvement after the first seismic monitoring time. The water break-through turns up at a closer time to the observed history after updating, however, a large mismatch starts to appear from the beginning of 2003.

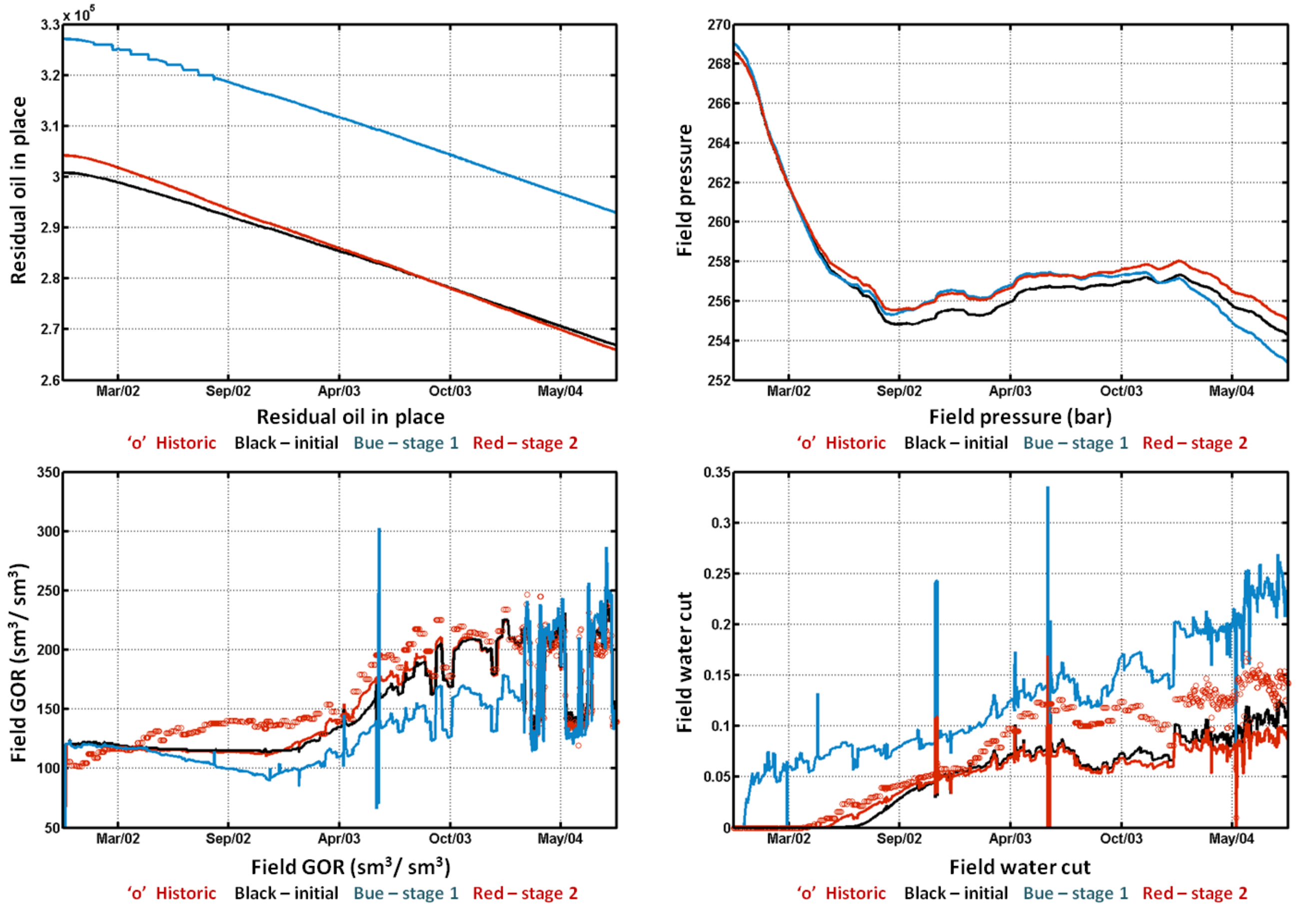

Figure 6.13 *The model prediction of (a) the OIP; (b) the field pressure; (c) the field GOR (gas-to-oil ratio) and (d) the field water cut in the original situation (black line), Stage I (blue) and Stage II (red).*

6.2.3 Closing the dynamic loop

In order to close the dynamic loop in Stage III, the reservoir impedance differences are now calculated by inverting the 2001 and 2002 seismic surveys in my engineering consistent scheme. It is found that predictions from the new simulation model determined after Stages I and II, and the inverted impedance differences, show a good degree of similarity. Features such as a general impedance decrease due to gas injection can be observed in the upper B3 formation of the reservoir (Figure 6.14 (a)). However, visual discrepancy is found at the northern producer P-06, which is one of the two representative wells supported by the gas injectors INJ-GAS (see Figure 6.14 (c)) situated in the centre of the field. The reservoir model predicts that the re-injected gas is directly connected to wells P-05 and P-06, while my work suggests very little presence of gas signal around P-06. By checking the historic gas oil ratio (GOR) data at well P-06, it turns out that my solution appears more consistent with the production history, as the model prediction of GOR exceeds the historic data. In addition, a time-slice from the deeper part of the reservoir shows that there is a reasonably good match between the model and my inversion for the southern water injector INJ-WAT (see Figure 6(a)). Generally, the water sweep in the south resulted in a 5% impedance increase, while the unflooded reservoir is subject to a 5 to 10% impedance increase caused by the gas exsolution during depletion.

Since saturation changes are the primary causes of 4D signals in the Girassol example, the transmissibility of the reservoir is considered to be the dominant factor in updating the dynamic loop, as it determines the total amount of fluid exchange arising from the well injection and production rates. The 4D inversion results are superimposed onto the reservoir grid and quantitatively compared with the model predictions. A discrepancy cube is then obtained by subtracting the sim2seis predictions from the inversion results. This difference is used as guidance to manually adjust the fluid flow predictions by fine-tuning the transmissibility field predictions to the observations. This procedure reveals that transmissibility in the northern area of the field should be reduced by 60%, whilst in the south it should be increased by 30% (see Figure 6.15). Following from this Stage III update we observe that the production match remains fairly good and does not significantly change, whilst the predicted 4D seismic improves throughout (see Figure 6.16), and the dynamic loop is closed progressively.

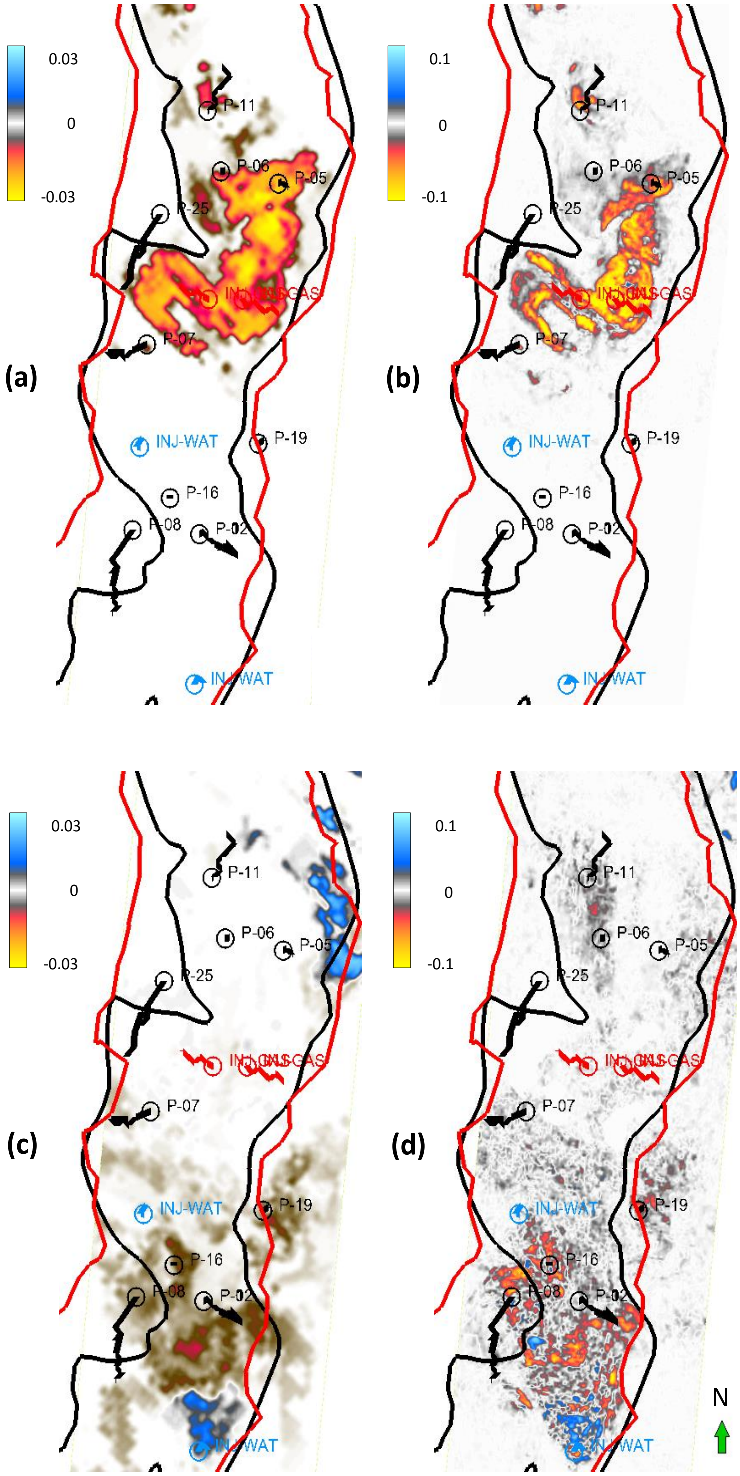

***Figure 6.14** Examples of the comparison between (a) model predictions of impedance change and (b)the engineering-consistent 4D inversion results, showing a time slice at the level of the gas injection. (c) time slice at the water flood level of impedance changes from the model; (d) the corresponding changes from the 4D seismic. The injector wells for which the wireline log data are used in the cross-plot of Figure 2 are also shown.*

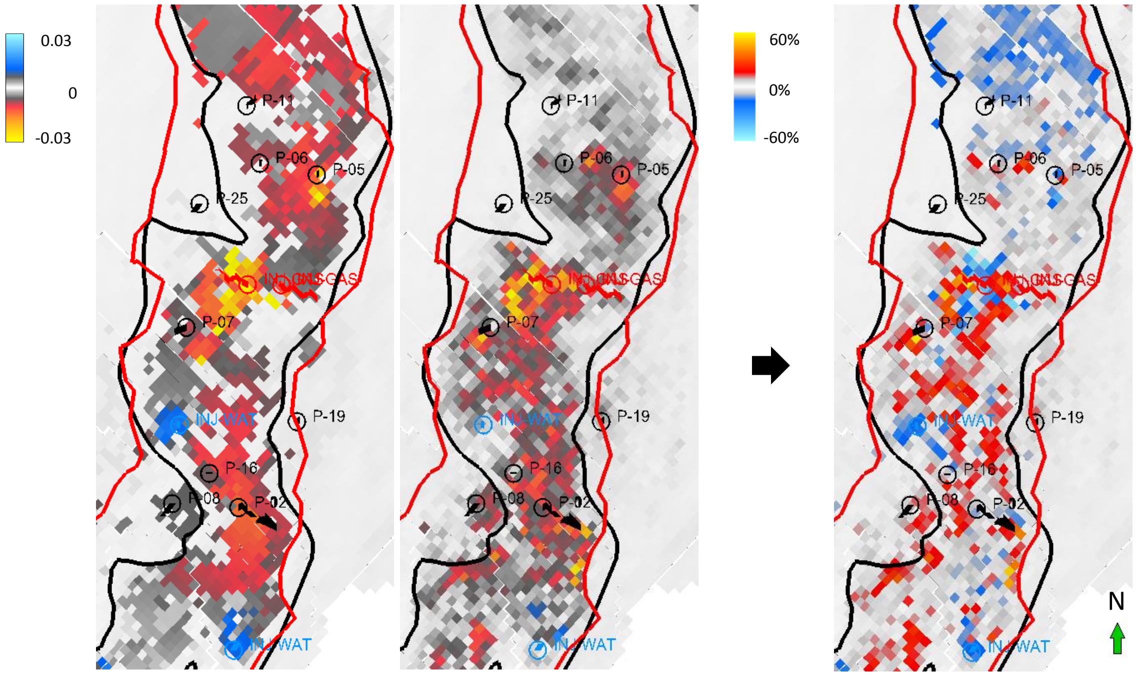

(a) (b) (c)

Figure 6.15 Values from a single layer of the misfit cube generated by comparing model prediction and data inversion results. (a) predicted changes in impedance; (b) impedance changes from the 4D seismic; (c) the percentage difference between (a) and (b).

Figure 6.17 summarises the evolution of the production profiles through the three update stages. With the new cells, the overall reservoir volume is increased by 10% and then reduced after re-calibration of the porosity and NTG values. Thus, the pressure profiles remain similar in all of the loops. The solution gas-oil ratio and water cut, two important parameters in the history matching process, diverge initially from the recorded history before improving again with the static and dynamic loops. The southern producer P-02 has the most significant improvement in its prediction of water breakthrough, where the initial prediction is one year later than the observed, until the volumetric and transmissibility revision is applied. In Figure 6.18, the degree of match is displayed for different stages of the workflow, obtained by calculating the normalized cross-correlations among the RMS maps and one minus the normalized sum of production misfit. In summary, the synthetic and observed 3D and 4D seismic maps start with a moderate fit. With the addition of new cells, the production match is initially degraded before Stage II, in which the volumetrics are updated. By incorporating the realistic reservoir heterogeneities in the model, the match to 3D seismic and the production data is improved immediately, with a consequent improvement in the 4D match. In Stage III, the manual adjustments were iterated three times, during which the resultant misfit cubes showed consistent patterns. This represents the convergence between the model prediction and inversion, with a third decrease of transmissibility in the north by about 25% (60% for the first iteration) and an increase in the south of about 10% (30% for the first iteration). As the quantitative 4D difference between prediction and inversion reduces in the impedance domain, the match to 3D seismic and production history stays more or less the same, while the 4D seismic match gets better and better. However, the northern RMS signals still show a remarkable difference around P-11, which is situated on the edge of the updating area (see Figure 6.16 (f) and (g)), which suggests the potential for further adjustments.

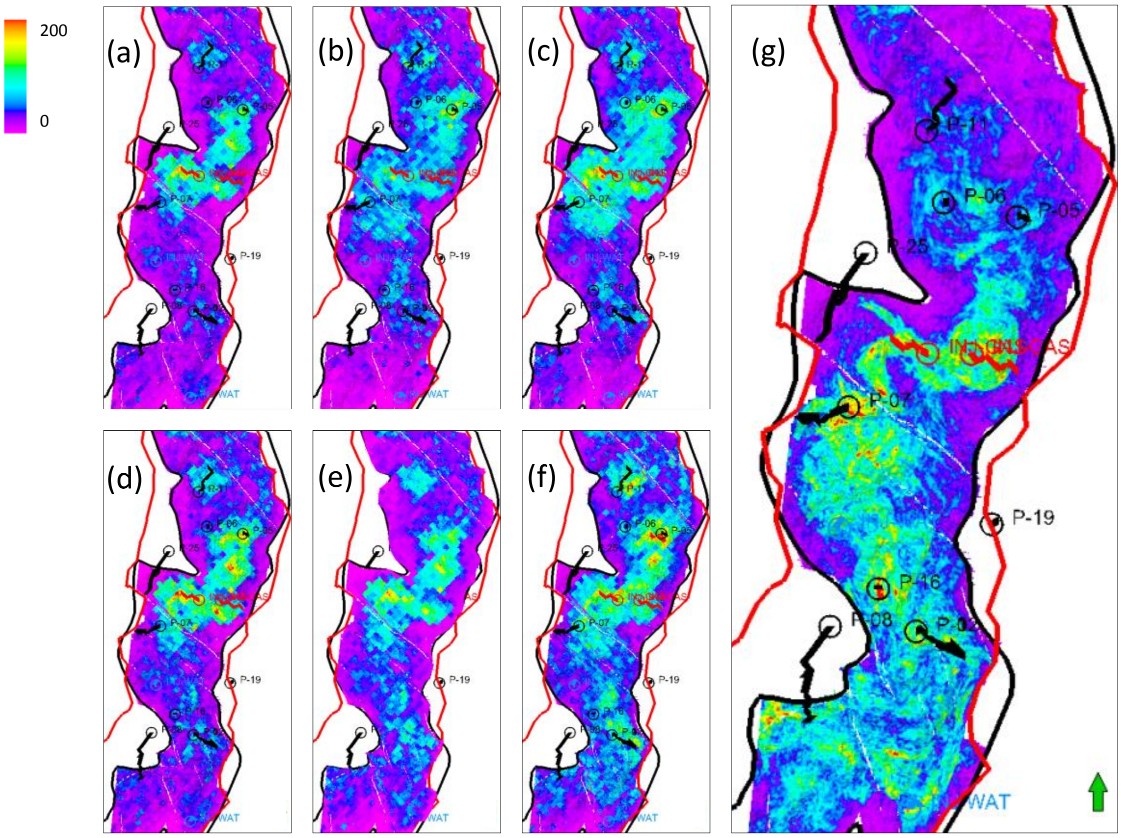

Figure 6.16 *A display of the evolution of the predicted 4D seismic signals throughout my workflow. In (a) the 4D RMS, amplitudes from the base case model show a decrease in the south, whereas in (b) they begin to appear after the Stage I update of the model. (c) shows the result after the Stage II update during which the volumetrics are enhanced. (d) to (f) show the signal being influenced by the transmissibility during three iterative Stage III updates. All these should be compared with the observed 4D RMS map in (g).*

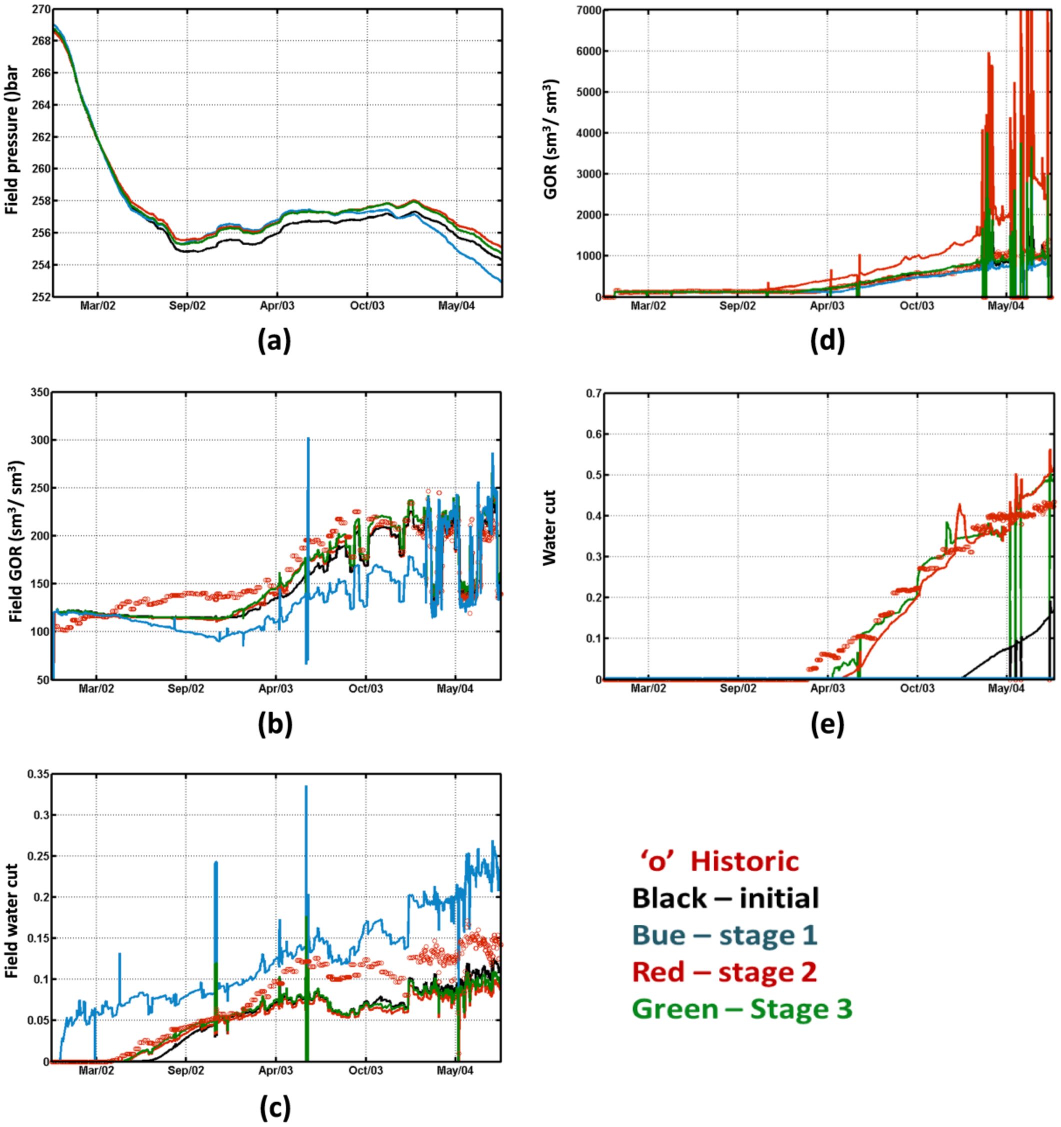

Figure 6.17 *(a) to (c) show the production history matches throughout the different stages of the updating, for the field average pressure, gas-oil-ratio (GOR) and water cut respectively. (d) shows the solution gas-oil ratio for the northern producer P-06, supported by gas injection and (e) is the water-cut for the southern producer P-02, supported by water injection. Open red circles represent the historical well data, whilst the blue lines correspond to the results after the Stage I update, a red line for the Stage II update, and finally the green line represents the final iterative update of Stage III.*

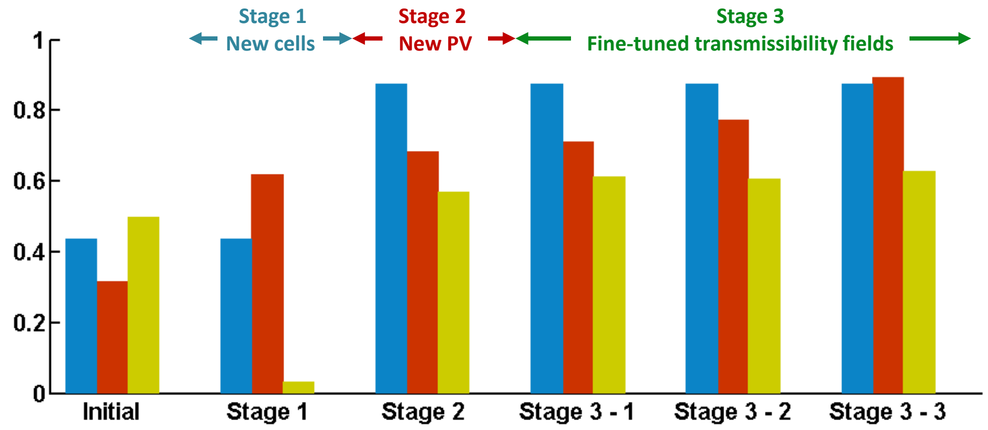

Figure 6.18 *The evolution of the fit between predictions and observed data at different stages of the workflow. The blue bars are cross-correlation values between the synthetic and observed 3D RMS seismic maps, and the red indicates the match to the observed 4D RMS amplitudes. The light green bars are the cumulative fit to the well production history and field data, normalized between 0 and 1.*

6.3 Conclusions

A workflow had been designed and applied to reconcile 3D and 4D seismic data, together with the simulation model and historical production data. At the heart of this procedure is an engineering-consistent 4D inversion which uses prior constraints from the simulation model to influence the seismic inversion. Several stages of closing the loop have been proposed, and the successful implementation of the geometric, volumetric and dynamic updates has been addressed in a sequential workflow.

Closing the reservoir loop revealed a setback to the production match in the Girassol example initially, but it was an important necessity, as it paved the way for the Stage III dynamic update. In particular, when the geological foundation of a given reservoir model is inconsistent with the observed 4D, it is this reservoir loop that is capable of fixing it. From the actions taken to update the static model, it can be concluded that the volumetrics are the most sensitive parameters for altering the dynamic predictions of the reservoir model. In other words, a reasonable estimation of the overall material balance is the first thing to ensure closing of the dynamic loops. The derivations of effective porosity and NTG from the seismic inversion utilise a conventional approach by virtue of its simplicity. However, there is potential to incorporate the geology at this stage, as the depositional facies has a strong correlation to the reservoir quality. In terms of 4D, the signals are predominantly saturation driven, but arguments exist that it is actually the pressure drop that resulted in the exsolved gas that was detected by the 4D. Indeed, the timing and rate of the pressure drops below the bubble point pressure are mainly determined by the overall reservoir volume, which did not vary significantly in the Stage I and II updates (see Figure 6.17 (a)). Therefore, the consequent updates are aimed only at the transmissibility field. The comparisons in closing the dynamic loop are indeed subject to much uncertainty. For instance, the velocity model employed may vary from the one used to build the model initially, which requires a lot of effort in the quality control of the interpretation. In particular, it is believed that this workflow is efficient in bringing the reservoir model to the starting point with sensible matches to all the available data, before proceeding to the conventional SHM for more sophisticated optimisation.

Chapter 7

Facts, improvements and conjectures

“To know and yet (think) we do not know is the highest (attainment); not to know (and yet think) we do know is a disease.

It is simply by being pained at (the thought of) having this disease that we are preserved from it. The sage has not the disease. He knows the pain that would be inseparable from it, and therefore he does not have it.”

「知不知，尚矣；不知知，病也。

聖人不病，以其病病。夫唯病病，是以不病。」

Lao Tzu, *Chapter 71, Tao Te Ching, 700 BC. - 400 BC.*

This chapter summarises the lessons learned during the development and implementation of the 4D seis2sim and CtL workflows. The detailed obstacles confronted are discussed on three levels – the inversion of 4D data, the assimilation with sim2seis and the ultimate CtL – in relation with which some possible research threads are suggested from a practitioner’s view.

After displaying the brighter sides of the examples discussed, it is also constructive to look over the less significant facts and pitfalls revealed during this practice. The lessons learned during the development and implementation of the CtL idea are of equal, or more, importance than the results themselves. As quoted in a chapter from *Tao Te Ching* : to make sense of the "illnesses" - uncertainties, errors and any other type of unknowns - instead of ignoring them, is ultimately beneficial.

7.1 Facts in EC 4D Inversion

The inversion is by itself non-unique, therefore a large number of subjective decisions have to be made according to one's experience and knowledge of the dataset. The issues involved can include the modelling and inversion of the seismic data, additional constraints to stabilise the seis2sim and the possible cooperation with other disciplines.

7.1.1 The modelling and inversion of seismic data

Forward modelling of the seismic response was the very first issue during the development of the EC inversion algorithm. The convolution-based seismic modelling approach, in contrast to the other approaches that are based on full wave equation and finite difference simulation (Carcione et al., 2002; Domes et al., 2012), has been widely used and qualified by many authors in the context of 4D (Thore, 2006; Arts et al., 2007; Marvillet et al., 2007; Shahin et al., 2012; Amini, 2014). Inversion by this approach relies on the approximation of the Zoeppritz equation (Shuey, 1985) which takes the AVO effect into account. For instance, the Girassol seismic dataset consists of partial stacks for the near, mid and far offsets. In theory, inversion of such data requires concurrent modelling of as many pre-stack gathers as possible. However, with regard to the computational cost, it was pragmatic to model some of the reflectivity traces at selected angles/offsets to replicate the desired stacks. Such a trade-off between efficiency and accuracy is always problematic. The practical solution carried out in the Girassol example was to model the reflection coefficients with fifteen calculations for stacks between 0° and 30° in a single iteration of the inversion. However, investigating the sensitivity of this trade-off would be worthwhile.

Additionally, it is impossible to monitor the computational process for the entire volume. Hence, 1D inversion tests are usually run at the well locations to determine the "globally applied" parameters for the Seis2Sm task. For instance, the determination of weights set in the Bayesian likelihood (see Equation 2.6 and 2.20) of the Girassol example was such a case. In the equation, measured errors between synthetic and observed are summed equally from the near, mid and far offsets, forming an overall misfit number. The contributions to this misfit sum from different offsets reflects their sensitivity to the MCMC process. It is noticed that the mid and far offset data have weaker amplitudes than the near offset, therefore the seismic match to these is less important, unless dedicated weights are assigned to them. After a few trials at the well location, it was decided to give weights of 1.03 and 1.045 to the mid and far offsets respectively, in order to have them reasonably matched. An adequate match will prove a determination of the S-wave velocity, according to the AVO theory; however, the inversion for S-impedance, in both 3D and 4D, is always more difficult and less stable than that of the P-impedance. Figure 7.1 gives an insight into the inversion results for the P and S wave impedance. Generally, they reveal similar stories, where the gas injection was interpreted in the central area, with some exceptions where the 4D S-impedance is more scattered than the 4D P-impedance, and, locally, the 4D S-impedance shows confusing increases at the gas cap position. Therefore, the 4D AVO effect needs to be investigated further for better inversion methods.

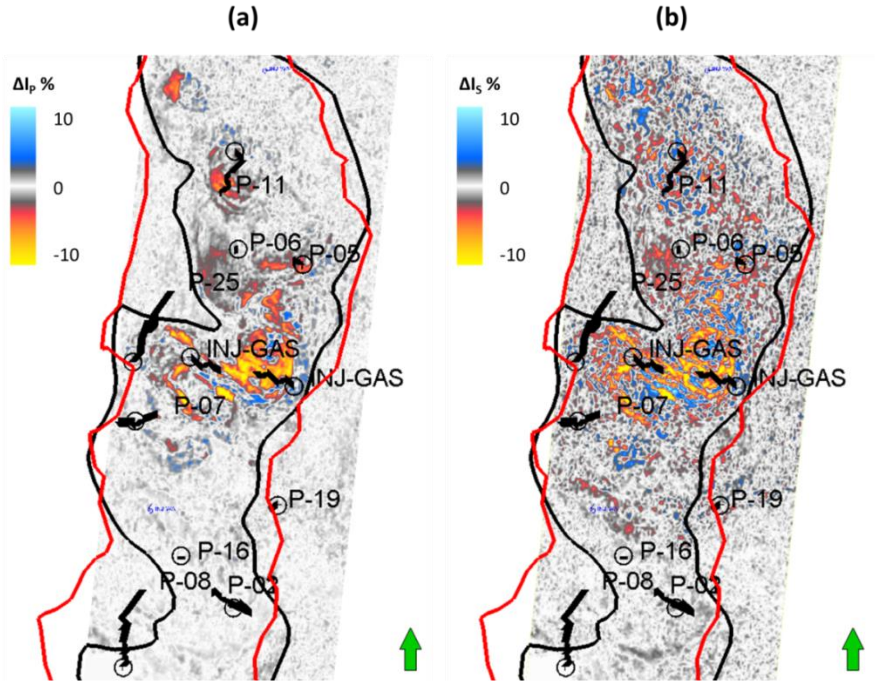

Figure 7.1 *Time slices at the gas cap location of (a) inverted 4D P-impedance volume and (b) inverted 4D S-impedance volume.*

Another issue is about the stability of the inverted solutions. As discussed in Chapter 1, a number of authors introduce sparseness constraints or linearise the input parameters to stabilise the inversion process (Zhang, 2005; Bulland et al., 2003; Bulland and El Ouair, 2006). This is not necessarily needed in my inversion, as the reservoir model grid is used to parameterise the earth. The grid itself will work as a sparse constraint, as it has discretised the earth into cells. Thore (2011) has discussed the coupling of the reservoir model grid in the inversion with the benefit of consistent seismic solutions directly stored onto the reservoir engineering grid. Nevertheless, the Bayesian MCMC approach is by its nature stochastic and able to solve this high dimensional and multimodal inverse problem (Ye, 2011), without linearisation of the input parameters. The initial model suggested by a sim2seis prediction can give a full bandwidth background model to perturb for the posterior solutions by MCMC.

However, one limitation of the current inversion method is caused by the inactive shale layers defined in the reservoir model. Figure 7.2 demonstrates the impact of inactive shales from one column of cells in the Girassol example. Figure 7.2 (a) is the sand probability cube derived from the 3D seismic data and is thresholded at 0.45, to separate reservoir sands and shale. The later geomodelling workflow discards the shale according to the cut-off values, leaving them as inactive layers. Inside these inactive volumes, neither fluid exchange nor the pressure diffusion would take place. Consequently, the sim2seis modelling would not predict any elastic changes inside these cells, as shown in Figure 7.2 (d). According to the methodology proposed earlier, the engineering-consistent constraints are therefore derived expecting no changes inside these cells. However, a number of authors have proved the sensitivity and importance of the shale activity while undergoing the production and development. Since the 4D signal is usually subtle, the impact of shale could well be critical for quantitative estimation of the reservoir changes. Particularly, in geomechanically sensitive reservoirs, the simulation of the shale physics may actually become a common routine for dedicated 4D analysis. The adaptation of the current EC constraint to a shale sensitive mode is not too different from what it is doing now. However, opening the inactive cells to the inversion will make the non-uniqueness problem more severe, therefore dedicated constraints for shale should also be considered.

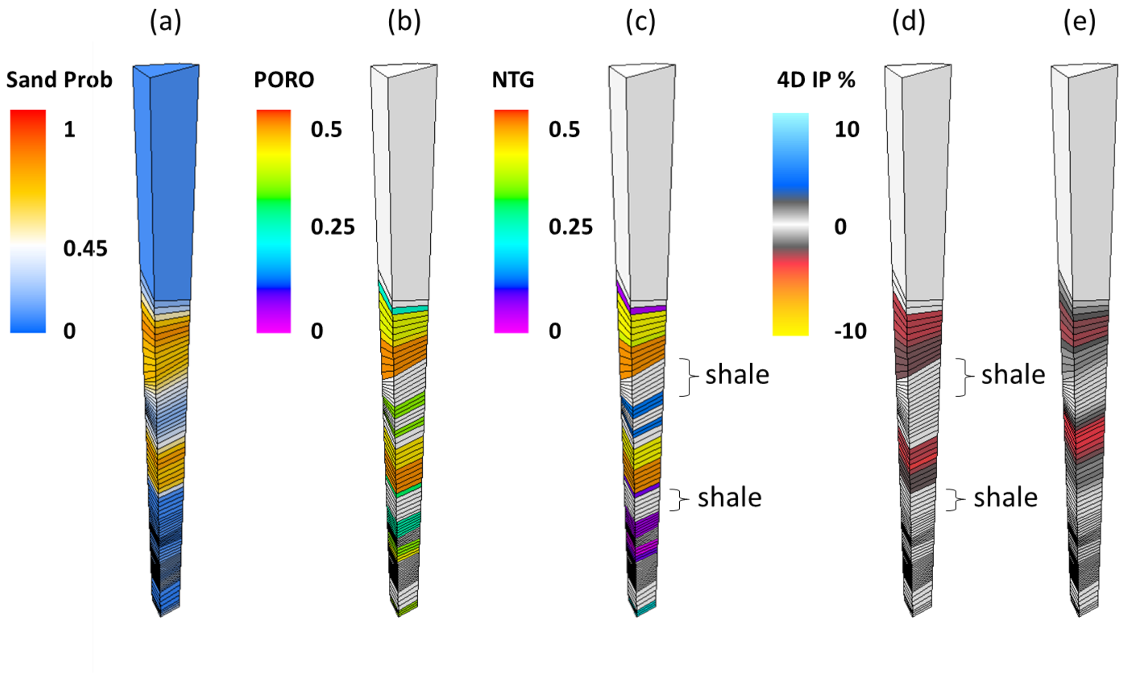

Figure 7.2 *One column of cells in the Girassol field that are intersected by a seismic trace. They are used as the input parameters for the inversion. (a) The sand probability attributed derived by 3D seismic; (b) the porosity values and (c) the NTG values assigned to the initial model, where the grey cells are inactive, to model the shale; (d) is the sim2seis prediction of 4D P-impedance while (e) is the seis2sim results.*

7.1.2 Issues related to the 4D resolution

One overwhelming benefit of conducting seismic inversion mentioned by many 3D inversion practitioners, is the enhancement in imaging resolution. Indeed, the trick inversion plays is the removal of the wavelet effect. Seismic tuning, which is primarily caused by the wavelet resolution, had been previously well-studied in 3D. Under the context of 4D, it has also extended itself into 4D scenarios. For example, Figure 7.3 (a) assumes a pre-production reservoir, the top and base of which are initially far enough apart to be detected by the seismic. Seismic tuning will not occur even between the top and the OOWC. However, after production, the reservoir has been gradually flooded, and the OOWC raises to the position at POWC, and a gas cap is formed at the top of reservoir. The gas cap "softens" the oil-bearing reservoir significantly, and a strong reflection results. Usually, a gas cap has a time thickness that is much thinner than the oil-bearing reservoir itself; therefore the "4D tuning" effect may actually lead to an exaggeration of the reflection. Inverting these stronger 4D amplitudes may be

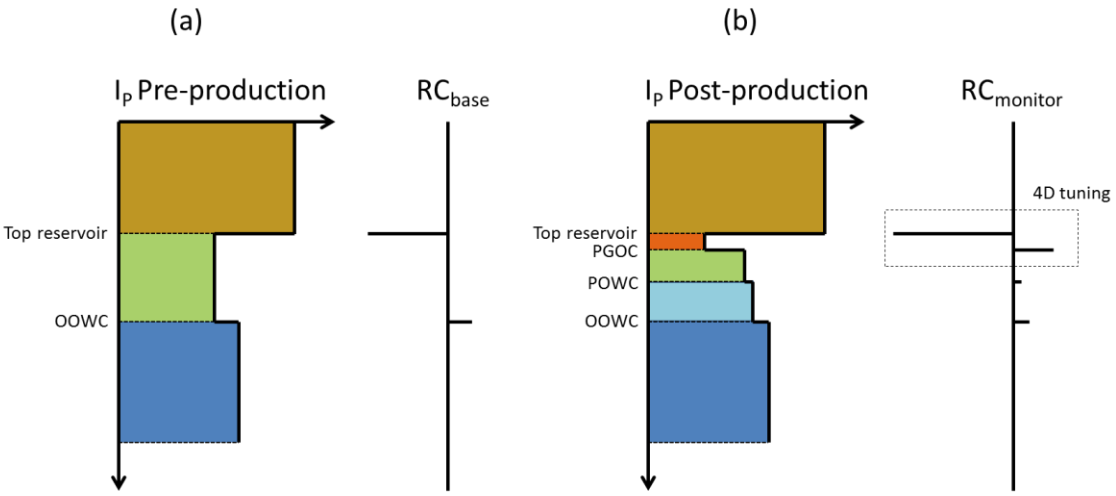

Figure 7.3 *Schematic 4D tuning scenarios. (a) pre-production reservoir impedance profile; (b) post-production impedance profile. A gas cap is formed after production, the thickness of which falls below the tuning thickness.*

misleading, unless the estimation of the wavelets for baseline and monitor surveys is accurate enough. Nevertheless, the resolution of the parameterisation scheme – e.g. the reservoir grid thickness – needs to be fine enough to capture such thin layers as well. One possible case of this kind is found in the Girassol example, where gas is injected into the turbidic channels to maintain the reservoir pressure. As shown in Figure 7.4 (a), the 4D seismic amplitudes at the gas cap location are almost 60% of the baseline seismic. Although the gas saturation change can be as large as 90% (fully flooded by gas injection), shown in Figure 7.4 (b), the sim2seis prediction of the change in P-impedance is only 4-5% (d), in contrast to the 10% by inversion (c). The seismic resolution here is between 6 and 10 metres, while the cell thicknesses are, on average, 1.5 metres. In theory, it is possible to detect the true position and thickness of gas cap in terms of impedance change but the 4D tuning effect makes the inversion extremely difficult. For example, Figure 7.4 (c) reveals a different character to Figure 7.4 (a), in terms of reservoir cycles, although they are both derived from the seismic. The seis2sim inversion results tend to interpret these cycles as two sets of turbidite sand, because the 4D seismic alternations from red to blue in 4D do not imply a geological switch from sand to shale.

One other impact of the various seismic resolutions is the influence of data repeatability. The current development of seismic technology tends to broaden the

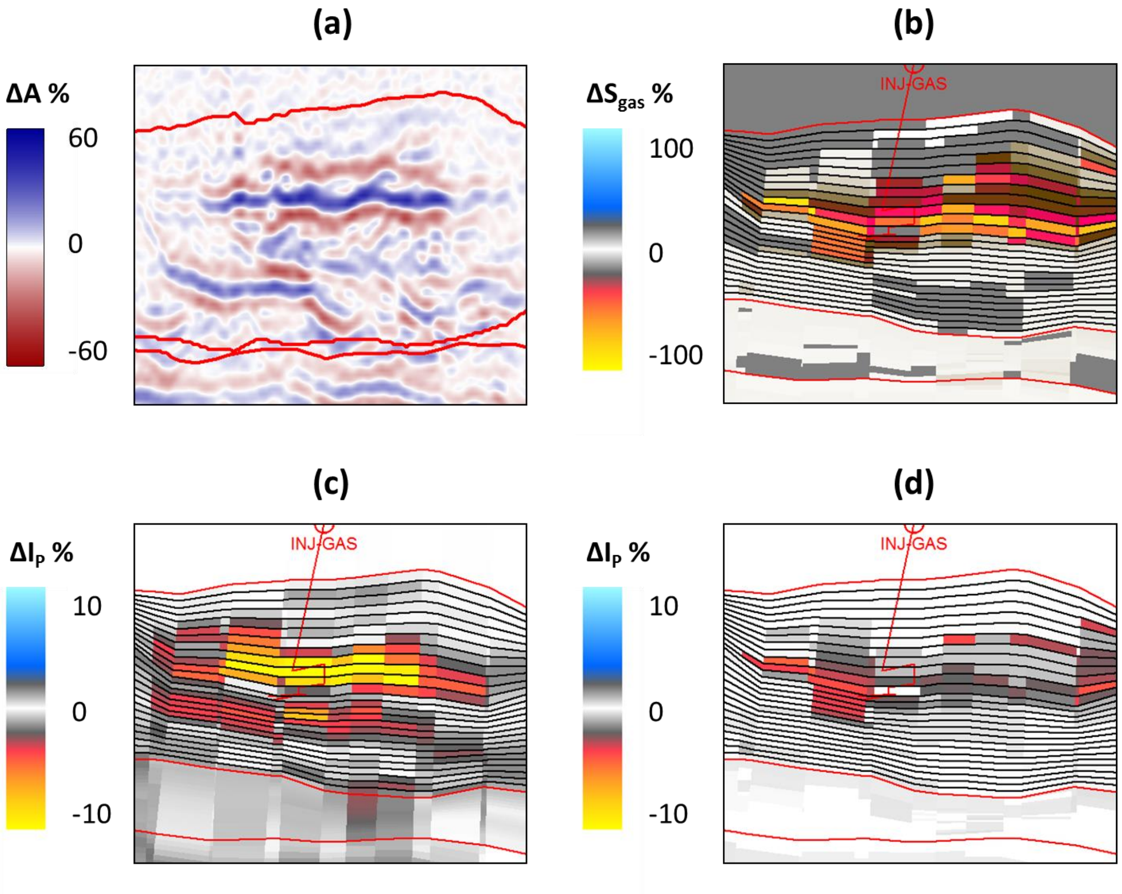

Figure 7.4 *One possible 4D tuning example from the Girassol dataset. (a) shows the observed 4D amplitude differences, using a colour template that is 60% of the one used for baseline seismic, to highlight the strength of reflections at the gas cap location; (b)is the simulation prediction of gas saturation changes on the model grid; (c) shows the seis2sim results and (d) is the sim2seis prediction of P-impedance changes.*

bandwidth of the acquired data, as well as improving its resolution. Higher resolution, of course, provides more details to the interpreter, which could be extremely useful in describing the internal heterogeneities of thick reservoirs. However, a reservoir is considered as “seismically thick” only if the amplitude differences consist of multiple cycles, under the context of 4D. The examples discussed in the Heidrun field and Girassol field are considered as thin and thick respectively in 4D. The reservoir changes in the Fangst group of the Heidrun field are represented by a single cycle of amplitude change while the turbidic channels of Girassol show multiple cycles (see Figure 7.5). In practice, it tends to be easier to invert the single cycle data, because it does not require too much prior information to stabilize the results. In contrast, the high resolution data needs to be carefully constrained in order to deliver less seismic-looking answers.

The key to removing this seismic input from the impedance volumes is again the estimation of a representative seismic wavelet. The phase, frequency and amplitude of the estimated wavelet must be able to deconvolve the observed seismic data itself, in order to recover the true geology. However, higher resolution requires more accuracy from the wavelet extraction. The example shown in Figure 7.5 tries to simulate such errors and compare the 4D sensitivities of the Heidrun and Girassol dataset for incorrect estimation of seismic phase. In the example, the baseline data of the two fields are both applied with phase shifts of three degrees, before subtracting each with the initial amplitudes. The contrast of the seismic resolution can be found in Figure 7.5 (a) and (c), while (b) and (d) are the consequent error at same level of phase errors. If (b) and (d) are assumed as errors introduced by inaccurate wavelets, the NRMS value of the Heidrun, in such a case, is only 3%, whilst for Girassol it is as high as 8%. In general, the higher the dominant frequency of the seismic, the more sensitive the time-lapse signals are to all possible errors, such as time-shift, phase shift, amplitude equalisations and so on.

When the time lapse data sets are time warped or top-aligned, any reservoir changes inside the reservoir would prompt residual time shifts downwards. These time shifts are cumulative and could easily affect the imaging of the underburden. In particular, when the resolution of the seismic is high, any subtle time shifts could become significant in the lower part of reservoir and most severe in the underburden. Figure 7.6 uses the Girassol dataset to illustrate such a phenomenon. Figure 7.6 (a) shows the static seismic (baseline) including the overburden and underburden areas. It is clear to see some geological features above and below the reservoir intervals bounded by the red interpretations. Figure 7.6 (b) shows the 4D difference after production. It is evident that the overburden merely consists of random background noise, because of the alignment performed at the top reservoir by the data provider. In contrast, some clear geological features are present in the underburden, with a reversed polarity to what they were at the baseline time. The presence of these residuals varies laterally in space, but the strength of them is coincident with the changes inside the reservoir. As mentioned before, the reservoir is injected with gas, which could significantly slow down the reservoir and causes prominent time shifts beneath the gas cap. Therefore, inverting with the time shifts requires a better understanding of the location of the true changes, which has been designed as part of the constraints discussed in both Chapters 2 and 5. However, it could potentially be better to remove such shifts before inversion, as the constraints derived from the model definition may not be actually certain.

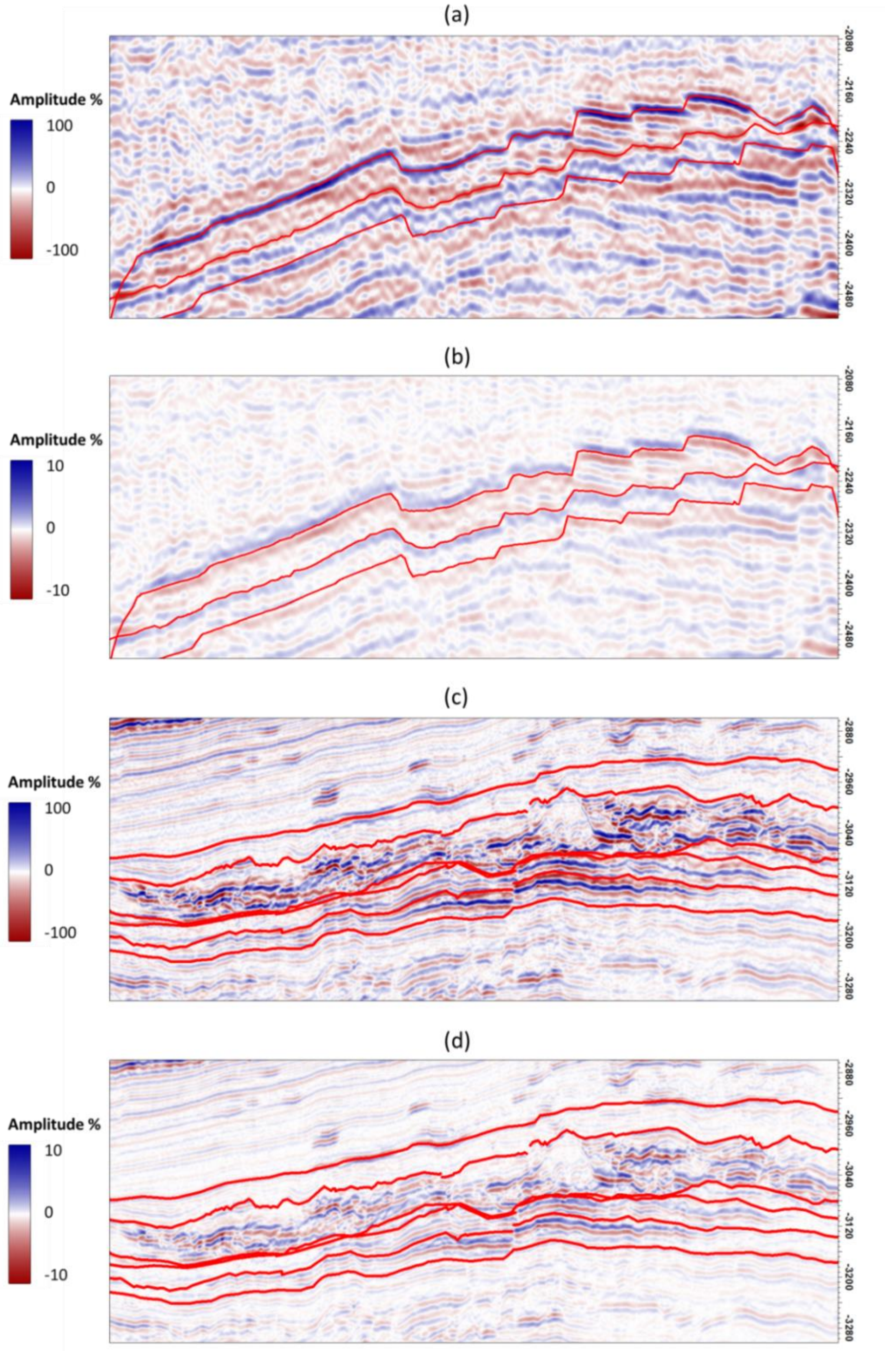

Figure 7.5 *Sensitivities to wavelet errors of low and high resolution 4D. (a) the baseline seismic of Heidrun; (b) the difference between the baseline and itself after a 3° phaseshift of (a); (c) the baseline seismic of Girassol; (d) the difference between the baseline and itself after a 3° phase shift of (c).*

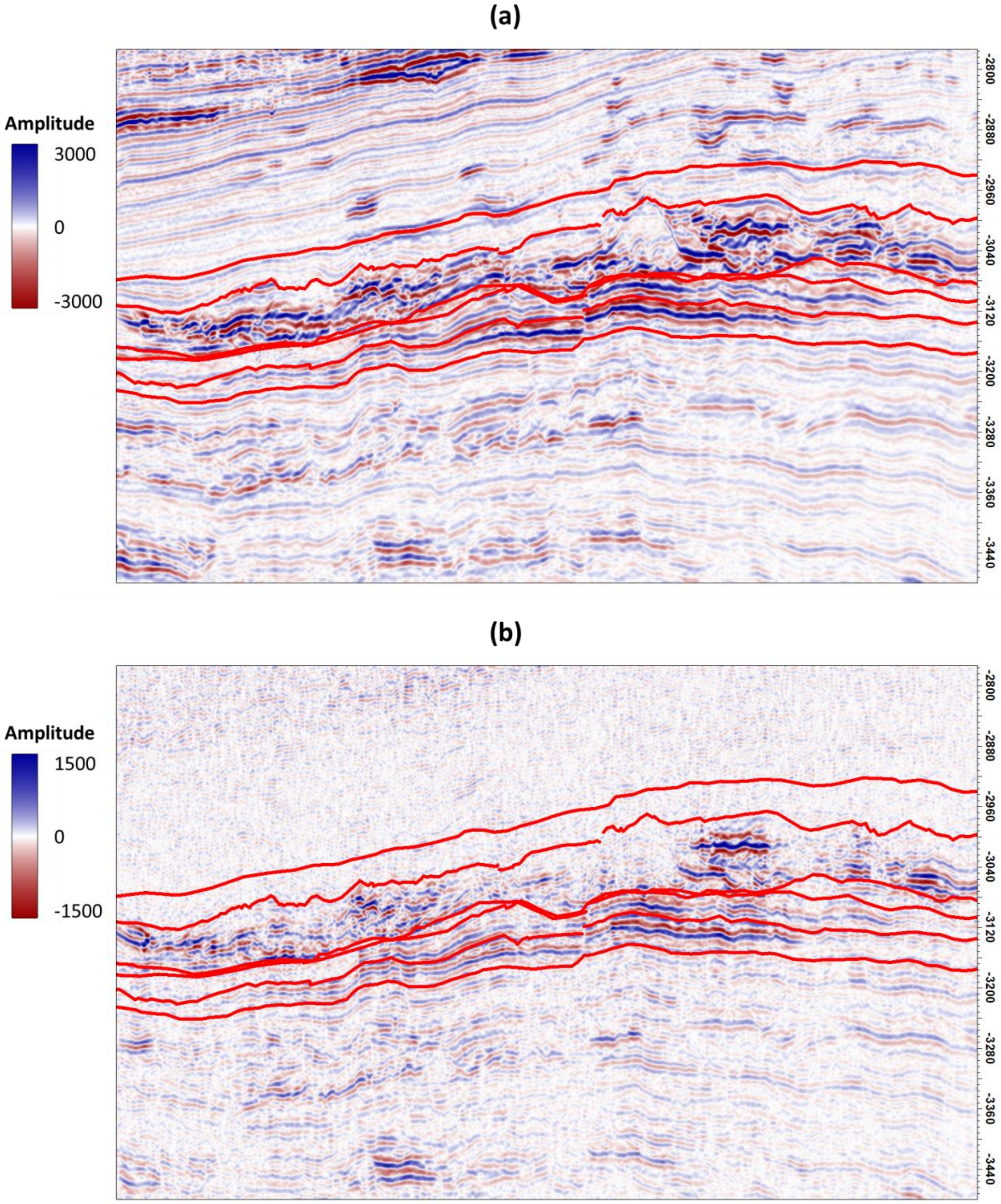

Figure 7.6 *Example of residual time shifts. (a) The baseline seismic of the Girassol data; (b) the 4D amplitude difference with the overburden and underburdens.*

Nonetheless, these time shifts could also be informative, as they are implicitly connected to the reservoir changes. Especially, the underburden time shifts can include almost all the reservoir changes sitting above. Figure 7.7 shows the comparisons of 4D RMS maps generated from the Girassol field. Figure 7.7 (a) is the observed 4D RMS map calculated from the B3 sequence (equal to the zone between the second and third red line in Figure 7.6), where the primary production takes place. Figure 7.7 (b) shows

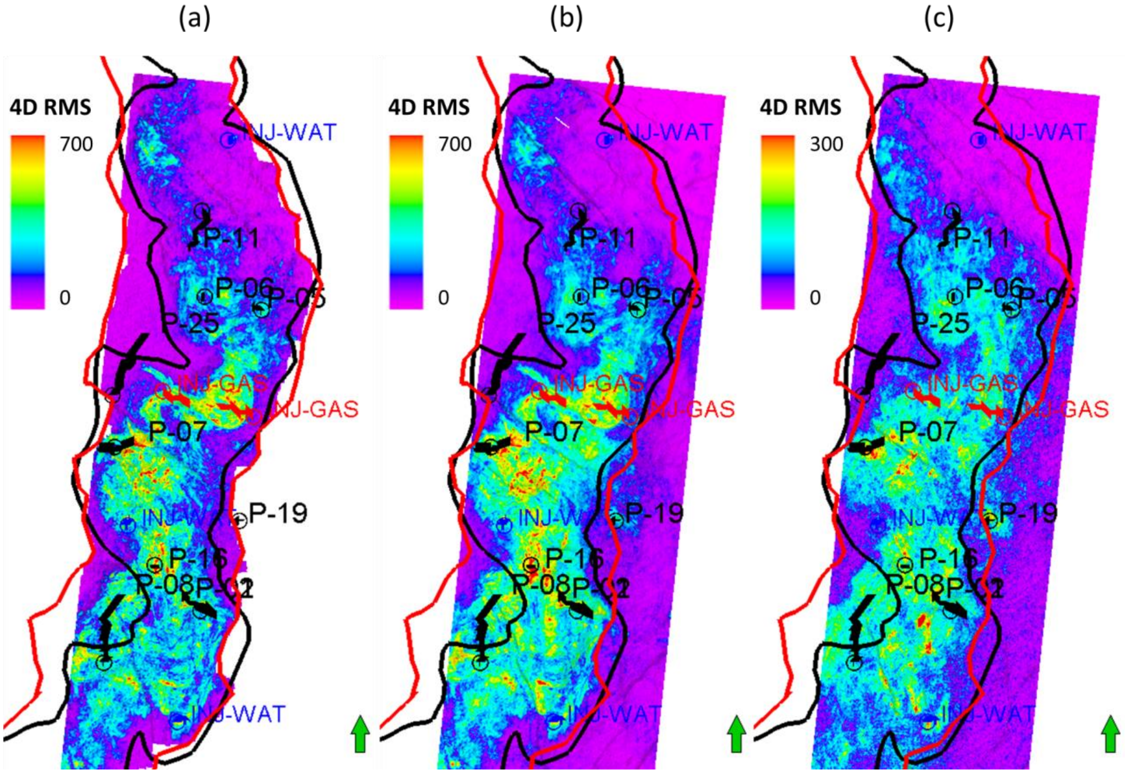

Figure 7.7 *(a) The 4D RMS map estimated in the B3 sequence of the Girassol field; (b) the 4D RMS map generated from the entire reservoir volume, including B1, B2 and B3; (c) the 4D RMS map calculated from the underburden, using a 100ms window, which has a weaker amplitude.*

the 4D RMS map calculated from the entire reservoir interval, including B1, B2 and B3 sequences. Spatially, the 4D RMS map from the entire reservoir is far closer to the one generated from the underburden,as shown in Figure 7.7 (c), using a 100ms window beneath the base of the reservoir zones. Therefore, a joint inversion scheme could be designed in the future to take account of the underburden time shifts. The benefit of honouring such data is a better control over the velocity changes from the top-aligned data.

Currently, the seis2sim inversion is implemented in a trace by trace manner. The constraints it has been using are primarily useful in detecting the vertical variations at individual trace locations. The benefit of such a scheme is the ease of parallel computation. However, the changes inside the reservoir are in fact correlated laterally, as the pressure and saturation fields evolve progressively in space. Such correlation therefore needs to be honoured by the inversion. Thore (2011) uses a propagation system, which detects the sequence of inversion by calculating the necessary changes next to an inverted location. It helps the inversion to converge to smoother solutions but the order is determined by the similarity of seismic data rather than reservoir engineering information. In contrast, the Well2Seis technique developed by Huang and MacBeth (2011) tends to correlate the 4D seismic signal to the production and injection wells by calculating the normalized correlation coefficients (NCC). Zhen et al. (2014) extended the NCC calculation in 3D to estimate volumetric correlations. The NCC volume gives a unique engineering understanding of the spatial extent of the 4D signal and is extremely useful to help seis2sim in a lateral direction. Practically, the trace by trace inversion can perturb only the cell that is are intersected by a seismic trace. This limits the constraint to be designed only in the vertical direction. In order to incorporate lateral information such as NCC volumes as *a priori* information, the trace by trace system can be adapted into a layer by layer approach (see Figure 7.8). Therefore, instead of randomly picking one single cell from one trace location, the new

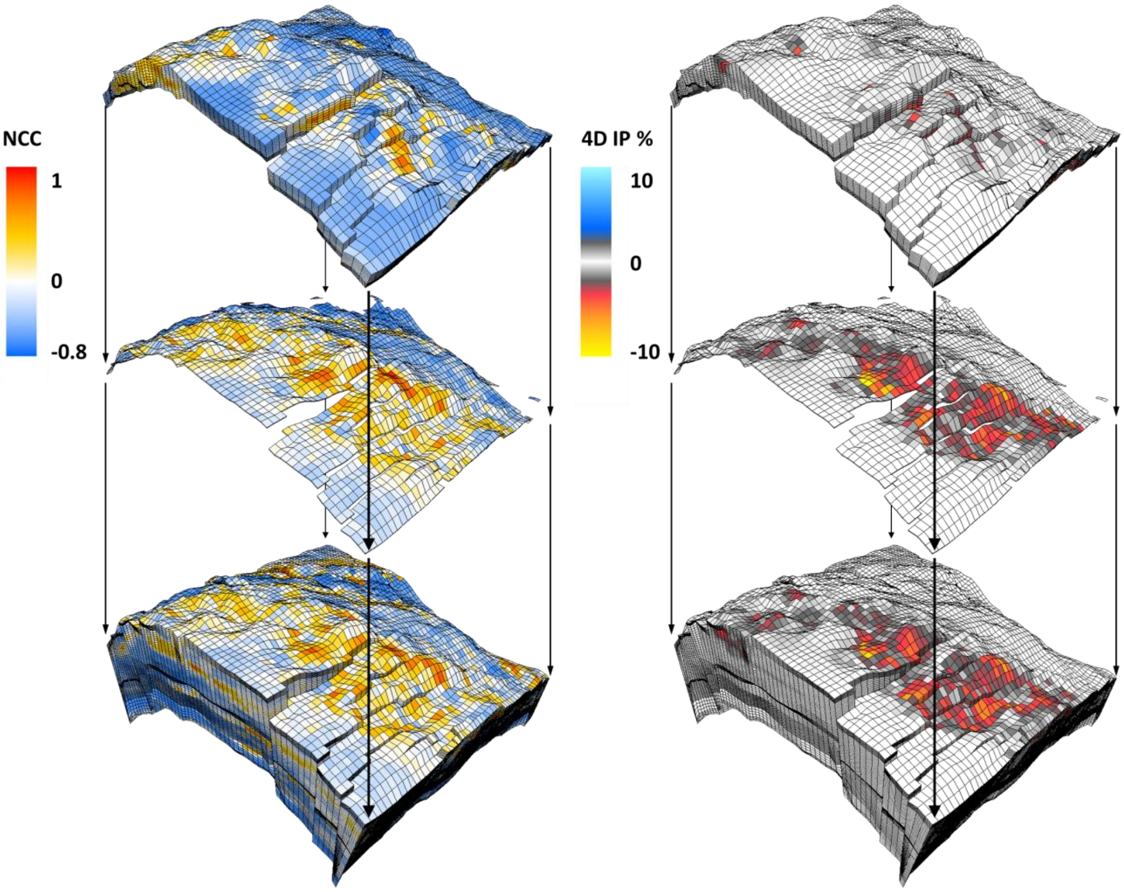

Figure 7.8 *Schematic illustration of possible adaptation for incorporating Well2Seis results into the inversion scheme. Left, the NCC volume derived from Well2Seis; right, the seis2sim inverted impedance volume. The perturbation can be performed in a layer by layer manner instead of the traditional trace by trace one, as depicted in the middle slice.*

system is capable of perturbing an entire layer of the reservoir model, before calculating the synthetic 3D and 4D seismic. The perturbation applied to the old model needs to honour the spatial correlations suggested by the *a priori* NCC volume. Although the adaptation needs to handle a large volume of data concurrently and iteratively, modern computers should be able to tackle this, according to practical experience.

Time-lapse seismic inversion is unique to 3D inversion because of its continuity over time. In this time dimension, unique constraints are also needed. However, very few authors have paid enough attention to this when multiple vintages are processed concurrently. For instance, Figure 7.9 assumes a situation where N time-lapse vintages are subject to inversion (noted as Seismic 1 to Seismic N). In addition, there are N earth models corresponding to the N seismic data and N-1 consecutive 4D differences between the 4D pairs. By performing the coupled inversion, it is possible to work out $\Delta_{1,2}$, $\Delta_{2,3}$,…, $\Delta_{n-1,n}$ one by one. However, because of the lack of constraints in time, the sum of $\Delta_{1,2}$, $\Delta_{2,3}$,…, $\Delta_{n-1,n}$ may not be equal to the coupled solution $\Delta_{1,n}$, because of the loss of time continuity. Although the "global" or "simultaneous" 4D inversion has the capacity to process these volumes at same time, the consistency and non-uniqueness over time is still debatable. One possible solution is to introduce the Well2Seis or Seis2Seis concepts to stabilize and constrain the seis2sim inversion in the time-lapse domain.

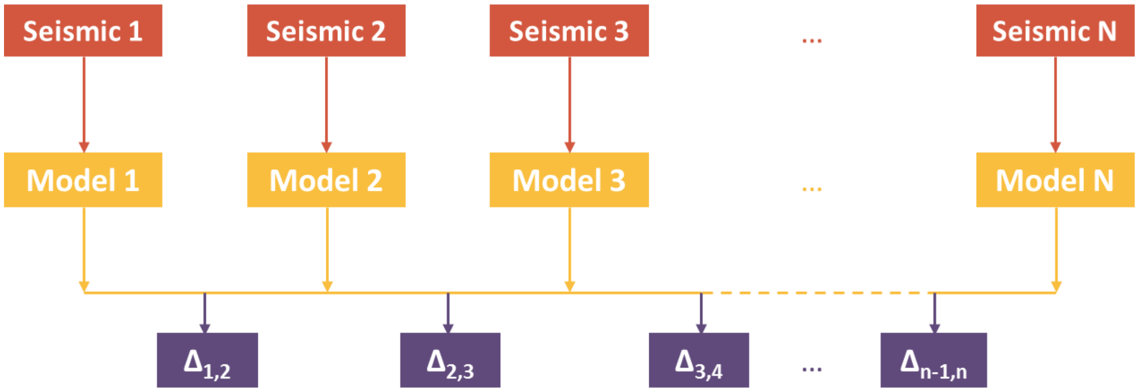

Figure 7.9 *The constraints for the inversion of multiple time-lapse vintages are needed, ensuring the sum of the consecutive difference pairs is consistent with the coupled inversion of the first and last vintages.*

7.2 Improvements for 4D seis2sim

Driven by the EC inversion, the seis2sim workflow needs to convert the seismic solutions into parameters that can be employed by the reservoir model. Among the “engineering wishes” listed in Figure 1.6, the ones that are more sensitive to seismic data than the others have been selected and summarised in Table 7.1. From a forward modelling point of view, these parameters include the model frameworks, porosity, NTG and transmissibility. The frame, or skeleton, is usually constructed according to the interpretations of seismic horizons. It determines the layout of the reservoir, which is difficult to update after gridding into layers of cells. Additionally, the distributions of porosity and NTG reflect the understandings of the effective geometry of the reservoir extension in space. This product jointly determines the effective pore volume that is used by the simulator for the calculation of material balance and simulation of fluid and pressure evolutions. Therefore, the distribution can significantly affect the static and dynamic responses of the 3D and 4D seismic, as well as simulation of historic production and the future predictions. In fact, the inactive part of a reservoir model is usually defined according to a pore volume threshold which exclude shale parts.

Aspect	Parameter	Comments	Impact
Model frame	Geology concepts	Horizons	Static& Dynamic
	Model grid	Resolution/Structure	
Active volume	Porosity	Reservoir volume for fluid exchange	Static& Dynamic
	NTG	Reservoir volume and Transmissibility	
Inactive volume	Elastic properties	Seismic modeling	
Transmission	Faults	Reservoir compartments	Dynamic
	PERM/Transmissibility	Ability to transmit fluid flow	

Table 7.1 *Some selected milestones of the seismic technology and the reservoir engineering practices from the 1940’s to recent times.*

The excluded cells are switched to be inactive during the simulation for reservoir engineering; however, they are equally important in modelling the static and dynamic seismic responses. The transmission group includes the characterisation of the reservoir conductivities in the rock and in between the compartments. Unlike the previous category, they have only a dynamic impact on the 4D seismic and production. Based on the table, the updating sequence in the CtL workflow in the previous chapters and examples is rationalised and designed as the reservoir loop, static loop and dynamic loop. Indeed, the volumetrics of a reservoir may vary under particular circumstances, such as geomechanically sensitive chalk reservoirs, where the porosity will change during the production-prompted pressure changes. Therefore, a new CtL scheme is needed when confronting these problems.

On the inverse side, the seis2sim could potentially deliver these parameters with confident petro-elastic models, such as the examples brought by Floricich et al. (2010, 2011). However, confidence in the PEM is difficult to build up because of the lack of in-situ data for calibration. The PEM calibrations shown in Chapters 3 and 5 are limited to the wireline logs acquired prior to the production start-up, which is not repeated at monitoring times to constrain the dynamic sensitivities. Indeed, even the effective pressure estimated at the baseline time is not verified by any “hard data”, due to the lack of data availability – in fact, such data are very rare and would be of great value when available. Hence, the inversion stops at the elastic level, instead of incorporating the uncertain PEM into the seis2sim process. Instead, the empirical cross-plots between the petrophysical parameters and the elastic parameters are used to derive these parameters. The cross-plots are straightforward but the regression usually results in a smoother resolution. As a result, the synthetic seismic cannot replicate the one matched by inversion (see Figure 6.12). Therefore, to strictly close the loops back and forth, the PEM used by the sim2seis and seis2sim needs to be identical and compatible (Figure 7.10). The best effort made in this thesis to ensure this consistency is the Heidrun example, shown in Figure 4.8, where the wireline log, seis2sim and sim2seis, although obtained through different PEMs, show a good agreement. Hence, developing a petro-physically sensible PEM could be a key advancement for seis2sim and the CtL exercise in the future.

Domain conversion is another key issue. Firstly, the wireline logs should be converted to the model domain, to quality control the match of the 1D log and 3D model. The

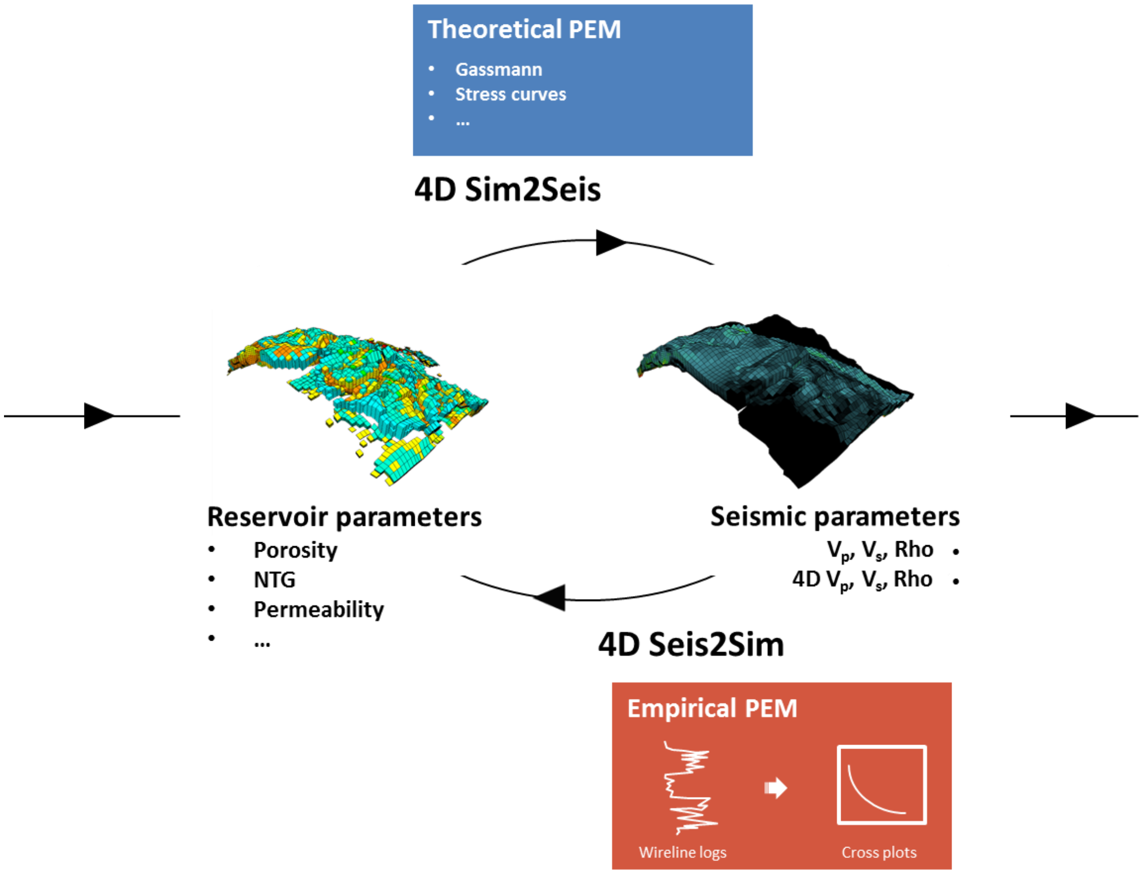

Figure 7.10 *Some selected milestones of the seismic technology and the reservoir engineering practices from the 1940's to recent times.*

wireline logs are typically recorded at measured depth (MD), where the reservoir model is built in TVDSS. The difference between them is not only the KB (Kelly Bushing), because the reservoir model was originally built with the time domain seismic interpretation. This data triangle puzzle can be solved only if the velocity model used by the model builder becomes available. However, it is very unlikely that such a velocity model remains accessible for the later updates, and the quality of it might be questionable due to the early stage uncertainty. To address this, a common platform needs to be chosen to perform the cross-domain comparison. In this thesis, the reservoir model is selected because of its central location in our study. In the example of Heidrun, the well logs were initially in consistency with the reservoir in depth, therefore the Fangst group model could be well tied to the logs. The inverted results were mapped to the reservoir instead of being converted by the seismic derived velocity, because of the difficulty in aligning up the pinch-out structure of the model to the interpreted seismic. In contrast, the Girassol inversion gives relatively good velocity estimation. With reliable alignment between the reservoir model and seismic horizons, the seismic properties were converted to the model grid directly during seis2sim. Neither the mapping nor the seismic velocity method is industry standardized, but they are “the best of a bad bunch”.

When comparing the 4D sim2seis and seis2sim, it is a common exercise to map the changes to a surface in order to assess the lateral consistency. However, interpreting the mapped attributes is subject to more uncertainties when low angle faults are present. For example, in Figure 7.11 (a) and (b), because of the mapping, it becomes difficult to decide where the true 4D changes terminate, and it can be very misleading when assessing the connectivity of a fault. Figure 7.11 (c) maps the 4D RMS attribute to the top surface of the Fangst group, in which the interpretation of the fault transmissibility can be ambiguous at the fault displacements. Hence, choosing the reservoir engineering grid as a platform can make the comparison sharper in 3D, as the information in the vertical dimension is retained by seis2sim.

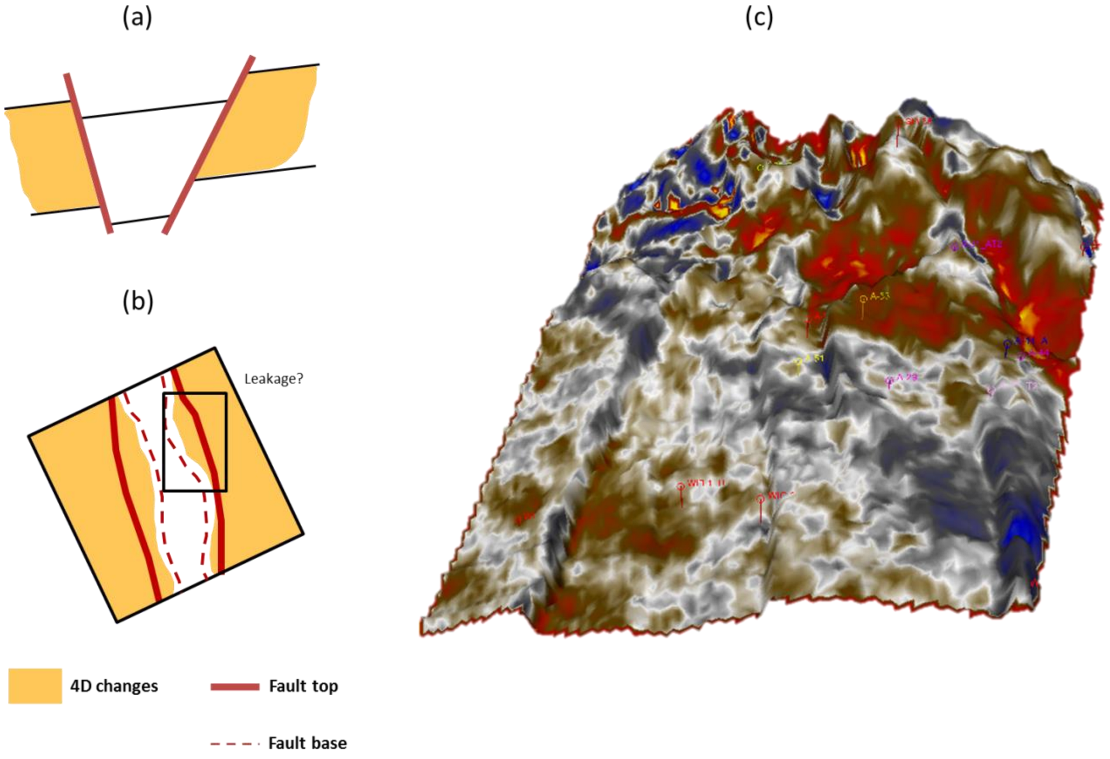

Figure 7.11 *Figure 7.11 (a) A vertical view of a schematic 4D example with tilted faults; (b) a map view of the same changes with fault lines; (c) the observed 4D RMS of the Heidrun field, mapped to the top surface, where the interpretation of fault connectivity is ambiguous.*

7.3 Conjectures for future CtL

Apart from the technical challenges, getting to grips with the big picture of the CtL workflow – in terms of its limit and potentials – gives some hints to its possible development. Currently the CtL workflow intends to update an existing reservoir model instead of building a new one. It is developed in such a way because of the availability and accessibility of data in academia. However, there is no harm in imagining what might happen if the entire workflow started from scratch. Figure 7.12 depicts the reservoir modelling and updating workflow from Skjervheim et al. (2012), as an industry example of seis2sim and CtL. The workflow is sequential, in which the model revision, simulation, and production match have been more or less tackled in a similar way as in my CtL workflows. However, the first three stages of seismic data processing, interpretation, domain conversion and geo-modelling are not primarily taken into account in the seis2sim workflow. Indeed, there are also loops to close in these domains. For instance, the consistency between various seismic responses, say the 3D elastics, 4D changes and time shifts effects is one of them. Theoretically, the elastic changes are supposed to show consistent behaviour with the time shifts or any other geomechanics related attributes. However, the literature has widely reported observations of

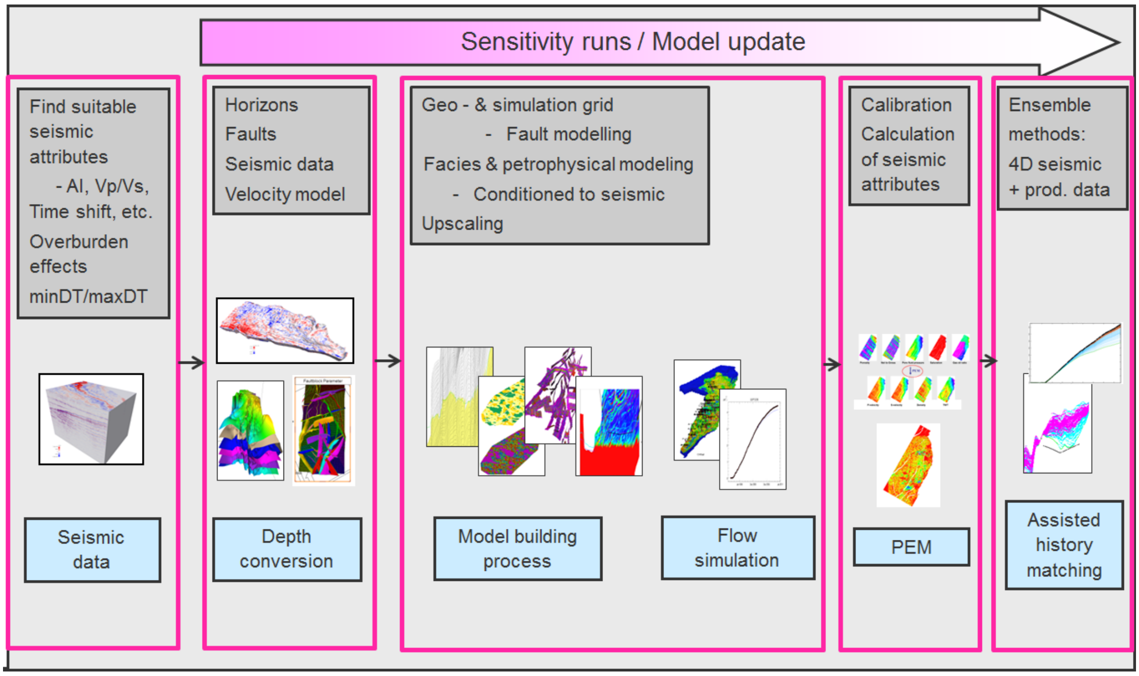

__Figure 7.12__ The reservoir modelling and updating workflow from an industry research group (used by permission).

disagreement without understanding the causes fully. Figure 7.7 (b) and (c) give an example of a “closed loop” between amplitudes and the time shifts. This reveals the possibility of unifying the intra-reservoir changes and the underburden time-shift signals. Closing this geomechanical loop may benefit certain types of reservoirs where the pressure-induced strains are not trivial.

The exercise of domain conversion in Figure 7.12 emphasises the localisation of horizons and faults from time domain to the model domain. The velocity model required in such conversion needs to cover the entire subsurface from seabed, if offshore, to the reservoir. The origin of this velocity model could be the seismic migration velocity, which can be potentially improved with the advances of FWI (full waveform inversion). It is recommended to use this consistent velocity model to perform all the necessary conversions once the reservoir model has been built. In addition, the interpretation of modelling of the seismic stratigraphy and faults are subject to uncertainties. Multiple realisations may be the ultimate tool in assessing these uncertainties, as the deterministic calculation of them is not well established yet. Such consistency in domain conversion is in fact the key and premise to the success of multi-disciplinary integration.

Apart from closing more loops, one other aspect that has not been covered in Chapter 4 and 6 is the need for quantitative evaluation of the accuracy that is needed after CtL. In SHM, objective functions are used to assess the errors, whereas the improvement by comparing the sim2seis and seis2sim is not quantified. In practice, the reservoir loop determines the presence or non-presence of the reservoir, which is actually a binary question. Therefore, the mismatch can be integrated in space in a binary system. The static loop and dynamic loop measure the misfits in seismic or impedance, and are similar to the cost measurements in the seismic inversions. These errors are shown as fixed values because the most of the updates do not need to be repeated, except for the transmissibility updates in Chapter 6. The revision of transmissibility is actually based on the quantitative assessment of 4D impedance discrepancy, in a cell-by-cell manner. Moreover, the mismatches of production data have different orders of magnitude, and therefore the quantified mismatch values need normalisation and the balance between seismic and engineering errors can be sensitive, depending on the preferences of the practitioners. The seis2sim CtL focuses on improving the reservoir model by primarily matching the performance to historic data. Thus improvement in assimilating the history is obvious; however, the ultimate usage of a reservoir is its predictability. Assessing the CtL impact on future predictions should also be taken into account when judging the influence of an update, which is rarely done at the same time, during the update. Similar exercises can be found in many history matching literature, which can be referred to when developing the CtL in the future.

Overall, the seis2sim update is predominantly driven by a series of data interpretations, while the SHM relies more on the optimisation algorithms, as illustrated in the charts in Figure 7.13, where it is observed that most of the effort is spent on searching for historically matched models by the SHM model and little on the other three aspects. Alternatively, the sei2sim and CtL workflows tend to focus more on the reservoir distribution, static and dynamic aspects, to improve its simulation of reality. However, if the two approaches could be combined into one single workflow, as shown in Figure 7.14 (a), their advantages could be jointly retained. In this ideal workflow, the seis2sim CtL would regulate the behaviour of the reservoir model effectively by conditioning the geometry, volumetrics and transmissibility to the observed 4D

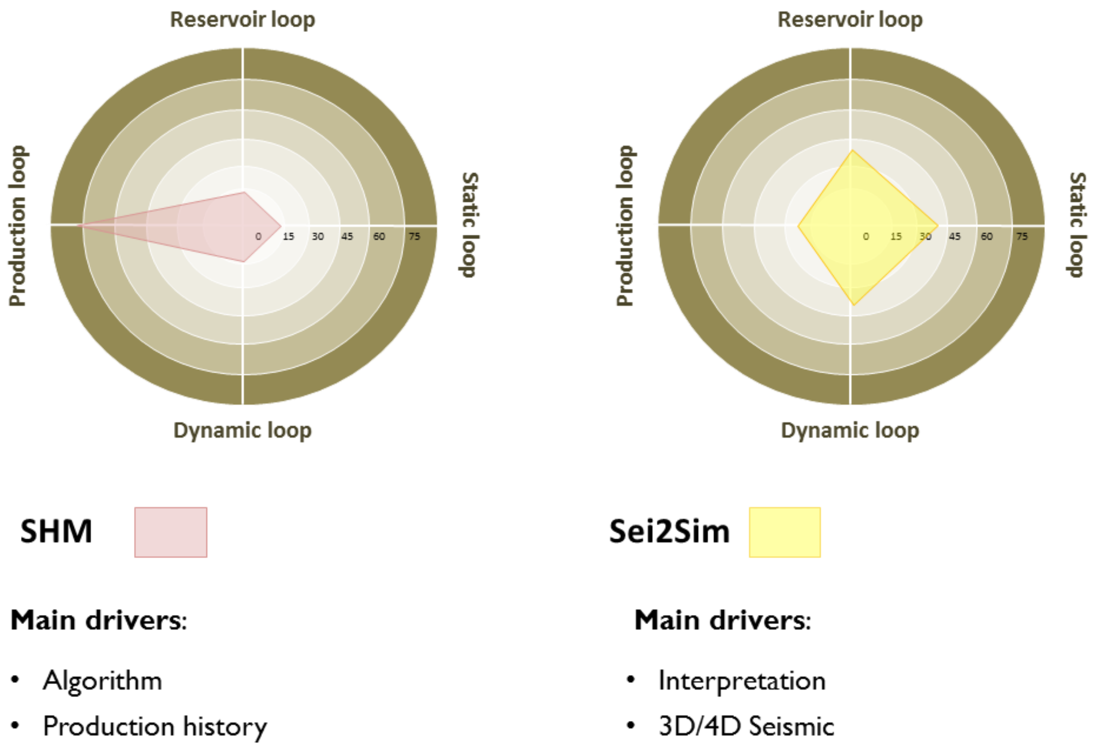

Figure 7.13 *The schematic demonstration of effort spent on different aspects between the SHM and seis2sim CtL approaches.*

observations. The consequent model is thus more mature and is free of any fundamental mistakes arising from the automation of history matching. It can also avoid incomplete parameterisation of the known unknowns, which are very likely preventing the optimisation from converging to sensible model settings, as illustrated in Figure 7.14 (b). Such a union will scope out the joint solution space of reservoir engineering and geophysics, returning with the consistent reservoir models that are needed in the time-lapse seismic practice.

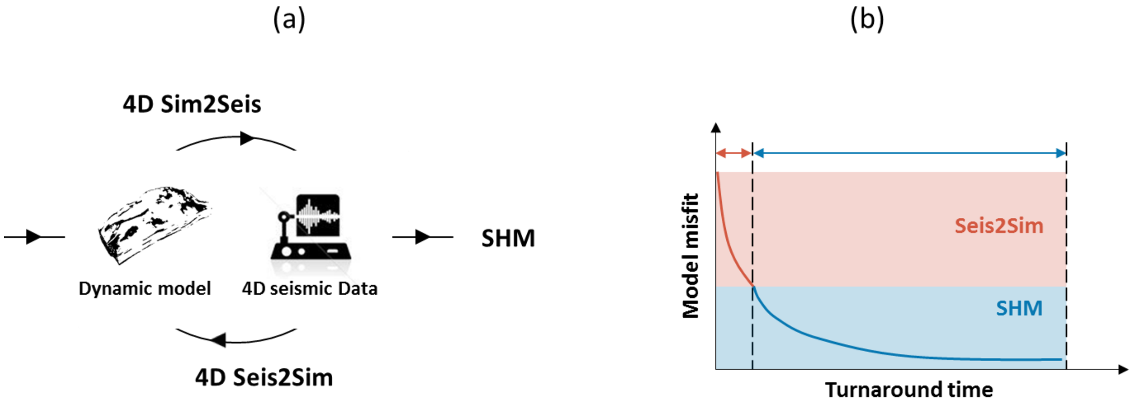

Figure 7.14 *(a) a joint workflow of seis2sim CtL and SHM; (b) the corresponding elimination of the seis2sim and SHM in terms of model misfits.*

Appendix 1

Bayesian inference by MCMC

As discussed in Chapter 2, to make inferences about the statistics of elastic parameters, Bayesians need to integrate over the probability distributions of these parameters. However, analytical evaluation of Equations 2.3 and 2.4 are difficult. An alternative is to draw samples from these target distributions directly, and evaluate their representative statistical features. This appendix briefly introduces the theory of the MCMC sampling approach and relative issues in the implementation.

A1.1 Monte Carlo methods

To demonstrate the idea of Monte Carlo in a Bayesian-free flavour, the posterior expectations of Equations 2.3 and 2.4 are re-written as

$$E[f(m)|d)] = \frac{\int f(m)p(m)L(d|m)dm}{\int p(m)L(d|m)d(m)}, \qquad \text{(A1.1)}$$

where m is the model to be inverted and d is the observed seismic data. It can be further generalized as

$$E[f(X)] = \frac{\int f(x)\pi(x)dx}{\int \pi(x)dx}, \qquad \text{(A1.2)}$$

by comprising m and d as X. Therefore, the Monte Carlo approach approximates the population mean of $f(X)$ as the mean of the drawn samples $\{X_t, t = 1, \dots, n\}$ from $\pi(\cdot)$ as

$$E[f(X)] \approx \frac{1}{n}\sum_{t=1}^{n} f(X_t). \qquad \text{(A1.3)}$$

If the randomly drawn samples are assumed independent, the law of large numbers ensures an accurate approximation when $n \rightarrow \infty$. However, $\pi(\cdot)$ in the seismic inversion problem is always hard to express, therefore a Markov chain can be used to draw a number of posterior samples directly from the unknown $\pi(\cdot)$, which is assumed to be the invariant target distribution.

A1.2 Markov chains

A Markov chain consists of a sequence of random variables $\{X_t, t = 1, \ldots, n\}$ from a target distribution, e.g. $\pi(\cdot)$ in our case. The Markov chain process is memory-less and random, which means the next state of X_{t+1} at $t + 1$ totally depends on the current state of X_t, and is independent from the previous samples $\{X_0, X_1, \ldots, X_{t-1}\}$ as

$$Pr(X_{t+1} = x | X_1 = x_1, X_2 = x_2, \ldots, X_n = x_n) = Pr(X_{t+1} = x | X_n = x_n). \quad \text{(A1.4)}$$

Therefore the determination of a new state, X_{t+1}, requires only a transition probability $Pr(X_{t+1}|X_t)$, assuming the Markov chain is time homogeneous, - $p(X_{t+1}|X_t)$ is independent of time t. The evolution of a Markov chain in a solution space $\Omega \subset \mathfrak{R}$ is controlled by a *transition kernel*, which is

$$P(x, A) = Pr(X_{t+1} \in A | X_t = x), x \in \Omega, A \subset \Omega, \quad \text{(A1.5)}$$

which contains continuous and discrete components (Robert and Casella, 1999). The use of the *transition kernel* is to construct a sequence of samples that converge to the invariant distribution $\pi(A)$.

$$\pi(A) = \int P(x, A) \pi^*(x) dx, \quad \text{(A1.6)}$$

where $\pi^*(x)$ is the density of π with respect to the Lebesgue measure (Ye, 2011). Suppose that P has a density, denoted as $q(x, y)$,

$$P(x, A) = \int_A \; q(x, y) dy: \quad \text{(A1.7)}$$

the sufficient condition for π to be the **invariant** distribution for P is the *detailed balance,* as

$$\pi(x) q(x, y) = \pi(y) q(y, x). \quad \textit{(A1.8)}$$

Satisfying this means the Markov chain is **reversible**. Additionally, a Markov chain is said to be π-**irreducible** if, for every $x \in \Omega$,

$$\pi(A) > 0 \; \Rightarrow P(X_t \in A | X_0 = x_0) > 0, A \subset \Omega, \quad \text{(A1.9)}$$

and **aperiodic** if there is no partition of $\Omega = (D_0, D_1, \dots, D_m)$ for some $m > 2$ such that, for $\forall t$,

$$P\left(X_t \in D_{(t)} \middle| X_0 \in D_0\right) = 1. \tag{A1.10}$$

These properties are necessary to link the Markov chain to the Markov chain Monte Carlo method.

Suppose $\{X_t, t = 1, \dots, n\}$ is a π-irreducible Markov chain with transition kernel P and invariant distribution π, then π is the unique invariant distribution of P and for all π-integrable real-valued functions h,

$$\tfrac{1}{M}\textstyle\sum_{t=1}^{M} h(X_t) \rightarrow \int h(y)\pi(dy) \text{ as } M \rightarrow \infty, \tag{A1.11}$$

which guarantees the convergence of the Markov chain to the unique target distribution, irrespective of t or X_0. After a sufficient transient period (burn-in) from the given initial state, the members of the chain can be used to estimate Equation A1.3, provided the samples in the transient period are discarded.

A1.3 Markov chain Monte Carlo

In order to construct a Markov chain for the seis2sim inversion, the Metropolis-Hastings (M-H) algorithm is employed (Metropolis et al., 1953; Ye, 2011). The M-H sampling method includes two parts: a proposal and an acceptance of the proposal. The proposal suggests a next state of the Markov chain to the algorithm, while the acceptance decides whether to accept it, according to the transition probability. The workflow can be summarised as:

- Initialize x_0 and set $t = 0$
- Repeat:
    1. Sample x' from $q(\cdot, x_t)$
    2. Sample u from a uniform distribution $U(0,1)$
    3. If $u \leq a(x_t, x')$, accept x' and set $x_{t+1} = x'$; otherwise set $x_{t+1} = x_t$

The acceptance probability, $a(x_t, x')$, is discussed by Chib and Greenberg (1995). However, it is difficult to specify and sample from the *transition kernel* explicitly during calculation. For this reason, an arbitrary proposal function $q(\cdot,\cdot)$, for example, a standard distribution with mean equal to x_t, is introduced to the system. Nevertheless, q may not be reversible for π, which means $\pi(x_t)q(x_t, x') \neq \pi(x')q(x', x_t)$. To compensate and balance this non-stationarity, an unknown transition function $0 \leq a(x, x') \leq 1\}$ is introduced, provided the Markov chain has converged to the invariant target distribution,

$$\pi(x_t)q(x_t, x')a(x_t, x') = \pi(x')q(x', x_t) \tag{A1.12}$$

and the final expression of $a(x_t, x')$ is

$$a(x_t, x') = \min\{1, \frac{\pi(x')q(x', x_t)}{\pi(x_t)q(x_t, x')}\}, \tag{A1.13}$$

which is, in practice, written as Equations 2.8 and 2.22. The transition probability is the ratio between the Bayesian posterior probability of x_t and x', where the complex marginal density terms are cancelled.

A1.4 Convergence assessment

With infinite length and a properly designed sampler, a Markov chain should theoretically reach the convergent state, which represents the invariant target distribution. However, only a finite number of samples are generated in reality, which raises the issue of convergence assessment. Ye (2011) summarised the popular convergence diagnostic methods, as listed in Table A1.1 according to different criteria. The interested reader could refer to her thesis for further details.

The Gelman and Rubin (1992) method is employed. The method is based on the analysis of the variances in the invariant distribution of $\theta(x)$. It requires simulation of m chains of $2n$ samples in each sequence. The idea is, given a variance σ^2 of $\theta(x)$ at the invariant distribution, $\frac{1}{\sigma^2}$ can be used to understand the statistical representation of $\theta(x)$. Secondly, an empirical variance $\hat{V}$ is calculated from the generated samples, and the *potential scale reduction factor* (PSRF) $\hat{R} = \frac{\hat{V}}{\sigma^2}$ can be formed as a diagnostic factor.

Method	**Theory**	**U/M distribution**	**S/M chains**	**Burn-in detection**	**Convergence diagnostic**	$\boldsymbol{x}, \overline{\boldsymbol{x}}, \boldsymbol{q}$	**Mixing**	**Accuracy evaluation**	**Ease of use**
Gelman and Rubin	Variance	U	M	No	Yes	x	No	No	a
Raftery and Lewis	2-state Markov	U	S	No	No	q	Yes	Yes	a
Geweke	Compare	U	S	No	Yes	$\bar{x}$	Yes	Yes	a
Schruben, Singh	Brownian bridge	U	S	No	Yes	x	No	No	a
Heidelberger and	Procedure design	U	S	Yes	Yes	x	Yes	Yes	a
Yu and Mykland	CUSUM path plots	U	S	No	Yes	x	No	No	a
Subsampling	Subsampling	M	S	Yes	Yes	x, q	Yes	Yes	b
Zeller and Min	Conditional	M	S	No	Yes	x	No	No	c
Riemann Sums	Riemann Sums	U	S	No	Yes	x	No	No	c

***Table A1.1** Summary of convergence assessment methods. U/M distribution: univariate/multivariate distribution. S/M chains: single/multiple chains.* $\boldsymbol{x}, \overline{\boldsymbol{x}}, \boldsymbol{q}$*: parameter, mean and quantile. "a" is the easiest to use (from Ye, 2011).*

In practice, we label the $\boldsymbol{t^{th}}$ observation in the chain $\boldsymbol{j}$ as $\boldsymbol{\theta_j^t}$, the process to calculate $\boldsymbol{\widehat{R}}$ is to firstly calculate the between-sequence variance $\boldsymbol{B}$ of the $\boldsymbol{m}$ chains as

$$B = \frac{n}{m-1}\sum_{j=1}^{m}\left(\overline{\theta_j^{\cdot}} - \overline{\theta_{\cdot}^{\cdot}}\right)^2, \tag{A1.14}$$

where

$$\overline{\theta_j^{\cdot}} = \frac{1}{n}\sum_{t=n+1}^{2n}\theta_j^t \text{ and } \overline{\theta_{\cdot}^{\cdot}} = \frac{1}{m}\sum_{j=1}^{m}\overline{\theta_j^{\cdot}}. \tag{A1.15}$$

The within-sequence variance, W, is estimated by:

$$W = \frac{1}{m}\sum_{j=1}^{m}s_j^2, \tag{A1.16}$$

where

$$s_i^2 = \frac{1}{n-1}\sum_{t=n+1}^{2n}\left(\theta_j^t - \overline{\theta_j^t}\right)^2 \tag{A1.17}$$

and the variance of θ in the target distribution $\hat{V}$ is estimated by:

$$\hat{V} = \frac{n-1}{n}W + (1+\frac{1}{m})\frac{B}{n} \tag{A1.18}$$

and the PSRF,

$$\hat{R} = K\frac{\hat{V}}{W}, \tag{A1.19}$$

where K is a calibration term and is set to 0.95 by default. When $n \to \infty$, the total variance $\hat{V}$ decreases, while the W increases and $\hat{R}$ is getting close to 1. If $\hat{R}$ is greater than 1, it indicates the need for more samples. This method is implemented in the seis2sim inversion. Because it requires multiple chains, some trial runs are usually launched to determine the typical length of convergent Markov chains.

Appendix 2

Practical implementation of the seis2sim and CtL workflows

The seis2sim is developed on a similar basis to the in-house sim2seis package of ETLP (Amini, 2014), with which it shares some common functions. Generally, the implementation of the seis2sim and CtL is carried out over a number of software platforms, in three stages: pre-processing and sim2seis, seis2sim and CtL (see Figure A2.1).

Pre-processing includes the reservoir simulation performed by the Schlumberger ECLIPSE reservoir simulator. An in-house Fortran code is used to extract the static and dynamic reservoir parameters after simulation. The extraction converts the data into a so-called ETLP format, which is used by sim2seis and seis2sim. Wavelets are required for both forward modelling and inversion, therefore the CGG Hampson-Russell package is used to conduct well-ties, which provide the sim2seis and seis2sim with wavelets at various offsets. The necessary petro-elastic model (PEM) and rock-physics analysis is calculated in MATLAB, with a manual script. Calibration of the PEM has been discussed in Chapter 3 and 5 when demonstrating the Heidrun and Girassol examples. The rock-physics analysis will define the bounds for the later inversion, as well as providing the relationship between inverted elastic parameters (V_P, V_S and ρ) and the petro-physical parameters (ϕ and NTG), as discussed in Chapters 4 and 6.

The sim2seis predictions need to be introduced into seis2sim as *a priori* information and EC (engineering consistent) constraints. To perform this, a MATLAB script is coded which inputs the sim2seis predictions, and outputs them as matrices of the means and covariances of 4D changes (see Chapters 2, 3 and 5). Practically, seis2sim is firstly carried out at well locations to verify the settings and constraints. This quick test is executed by a MATLAB version of seis2sim which is fully consistent with the parallel version (coded in C language with GNU OpenMPI), with additional options to

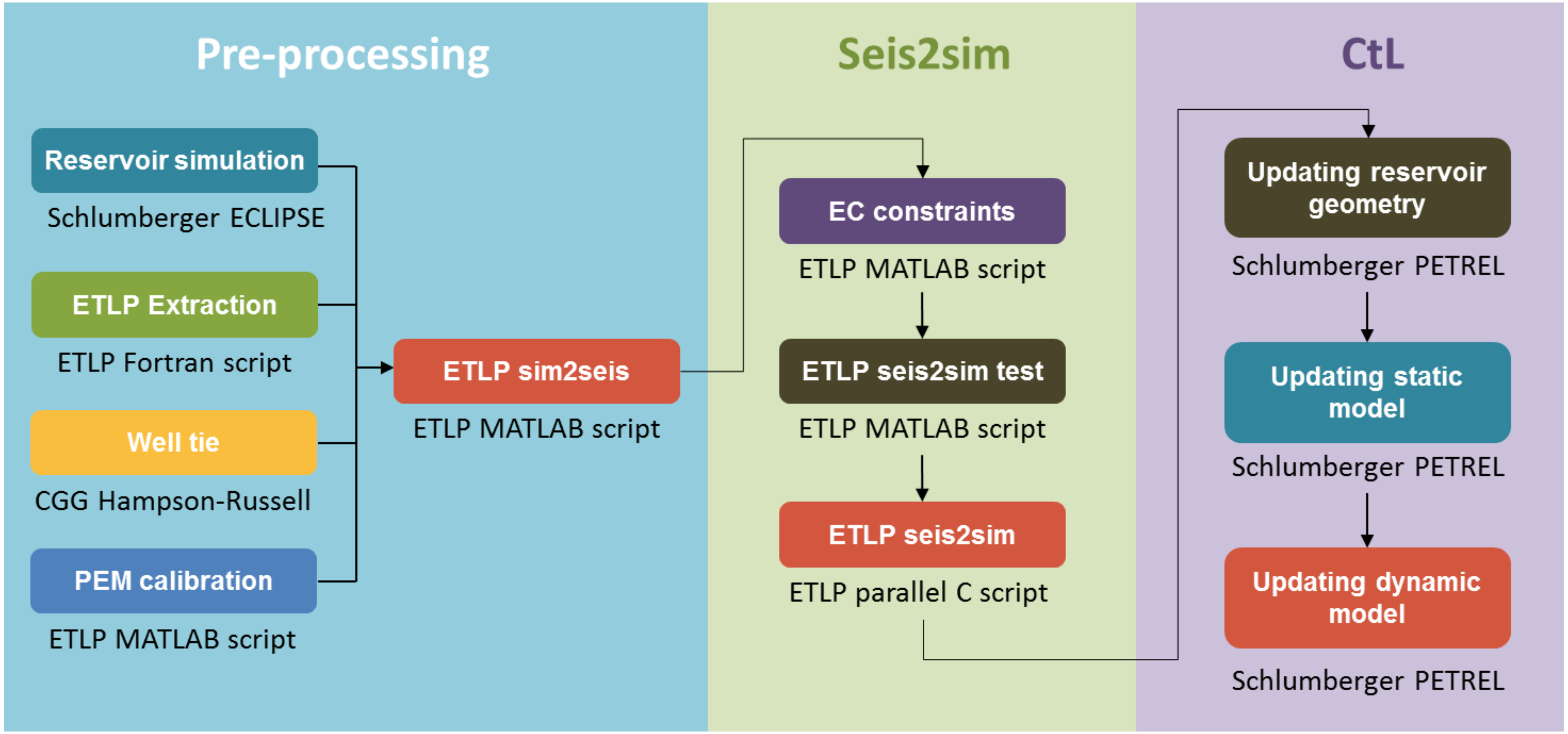

Figure A2.1 *The practical workflows for the seis2sim and CtL implementation.*

output intermediate results for QC and visualization purposes.

The seis2sim results are automatically written in the Generic ECLIPSE Grid Properties format, which can be directly loaded by the Schlumberger PETREL package. This is where the CtL workflow is primarily carried out at the model updating stage. With the sim2seis and seis2sim results stored on the same reservoir model grid, the reservoir loop, static loop and dynamic loop can be closed by performing cell-by-cell comparisons. The results of the CtL update can be directly visualised by PETREL by re-launching the sim2seis process with updated parameters in the reservoir model.

In addition, the practical proceedings for the 3D and 4D seis2sim can be found on pages 40 and 53, for future practitioners to replicate the workflow.

References

Almaskeri, Y., MacBeth, C. (2006). Location and Evaluation of Flow Barriers with 4D Seismic. *First Break, v.24, No 11*.

Amini, H. (2014). A pragmatic approach to simulator to seismic modelling for 4D seismic interpretation. *Ph.D. thesis, Heriot Watt University*.

Annor, P. D., and Routh, P. S. (2007). A new 4D workflow for legacy seismic data. In 2007 SEG Annual Meeting. Society of Exploration Geophysicists.

Arts, R.J., Chadwick, R.A., Eiken, O., Trani, M. and Drotland S. (2007). Synthetic versus real time-lapse seismic data at the Sleipner CO_2 injection site. *77th SEG meeting, San Antonio, USA, Expanded Abstracts, 2974-2978*.

Avseth, P., Mukerji, T., and Mavko, G. (2005). Quantitative Seismic Interpretation: Applying Rock Physics Tools to Reduce Interpretation Risk , *University Press*.

Ayzenberg, M., and Theune, U. (2010). Stratigraphically constrained seismic 4D inversion. *72nd EAGE conference & exhibition, extended abstract*.

Barclay, F., A. Bruun, K. B., Rasmussen, J. Camara Alfaro, A. Cooke, D. Salter, R.Godfrey, D. Lowden, S. McHugo, H. Ozdemir, S. Pickering, F. Gonzalez Pineda, J. Herwanger, S. Vlterrani, A. Murineddu, A. Rasmussen, and R. Roberts (2008). Seismic inversion: Reading between the lines. *Oilfield Review, 20, no. 1, 42-63.*

Barkved, O. I. (2012). Seismic Surveillance for Reservoir Delivery. *In EAGE Annual Meeting.*

Batzle, M., and Wang, Z. (1992). Seismic properties of pore fluids. *Geophysics, 57(11), 1396-1408.*

Benguigui, A. (2010). Quantitative evaluation of structural compartmentalization in the Heidrun field using time-lapse seismic data. *Ph.D. thesis, Heriot Watt University.*

Blanchard, T.D. and Thore, P. (2013). Breaking the limitations of pressure and saturation inversion with a new dynamic constraint. *75th EAGE conference & exhibition, extended abstract.*

Bouchet, R., Levallois, B., Mfonfu, G., Authier, J.F. (2004). Girassol field optimized development. *AAPG International Conference, extended abstract.*

Boutte, D. (2007). Seismic-to-simulation arrives. *Hart's E&P J (July 2007).*

Brevik, I. (1997). The effect of pore pressure and brine saturation on seismic properties in the Heidrun Fangst reservoir Unit. *F&U-LoU 97S241041.*

Buckley, S. E., & Leverett, M. C. (1941). Mechanism of fluid displacement in sands. *Trans. AIME, 146.*

Buland, A. and Omre, H. (2003). Bayesian linearized AVO inversion. *Geophysics, 68(1), 185–198. doi: 10.1190/1.1543206.*

Buland, A. and Omre, H. (2003). Joint AVO inversion, wavelet estimation and noise-level estimation using a spatially coupled hierarchical Bayesian model. *Geophysical Prospecting 51 (6), 531-550.*

Buland, A. and El Ouair, Y. (2006). Bayesian time-lapse inversion. *Geophysics, 71(3), R43–R48. doi: 10.1190/1.2196874.*

Broucke, O., Temple, F., Rouby, D., Robin, C., Calassou, S., Nalpas, T., Guillocheau, F. (2004). The role of deformation process on the geometry of mud-dominated turbiditic system, Oligocene and Lower-Middle Miocene of the Lower Congo basin (West African Margin). *Marine and Petroleum Geology v. 21, p. 327-348.*

Carcione, J. M., Kosloff, D., and Kosloff, R. (1988). Viscoacoustic wave propagation simulation in the earth. *Geophysics, 53(6), 769-777.*

Castagna, J. P., and Smith, S. W. (1993). Comparison of AVO Indicators: A Modeling Study. *Geophysics 59.12 (1994): 1849-1855.*

Calvert, R. (2005). Insights and methods for 4D reservoir monitoring and characterization. *SEG/EAGE Distinguished instructor short course, 8.*

Castro, S., Caers, J., Otterlei, C., Hoye, T., Anderen, T., and Gornel, P. (2006). A probabilistic integration of well log, geological information, 3D/4D seismic, and production data: application to the Oseberg Field. *SPE Annual Technical Conference and Exhibition, San Antonio, Texas, September 24-27, 2006, SPE 103152.*

Chib, S. and Greenberg, D. (1995). Understanding the Metropolis-Hastings algorithm. *American Statistician, 49:327-335.*

Chierici, G.L. (1992). Economically improving oil recovery by advanced reservoir management. *Journal of Petroleum Science and Engineering 8 (3): 205-219. DOI: 10.1016/0920-4105(92)90034-X.*

Christie, M.A. and Blunt, M.J. (2001). Tenth SPE comparative solution project: a comparison of upscaling techniques. *SPE72469-PA SPEREE 4(4), p308-317.*

Chu, D., Burger, J., and Medema, G. (2011). Using Time Strain Volume for Improved 4D Interpretation: Methods and Case Studies. *Society of Exploration Geophysicists.*

Coats, K. H. (1989). Implicit compositional simulation of single-porosity and dual-porosity reservoirs. *Paper SPE, 18427, 6-8.*

Crane, A. A., and Lemoine, J. (1977). An introduction to the regenerative method for simulation analysis. *New York: Springer-Verlag.*

De Gennaro, S., Grandi, A., Escobar, I., Onaisi, A., Ben-Brahim, L., Joffroy, G., Tindle, C. and Neillo, V. (2008). Integrating 4D seismic, geomechanics and reservoir simulations in the Elgin and Franklin fields. *70th EAGE conference & exhibition, extended abstract.*

Durrer, E. J., & Slater, G. E. (1977). Optimization of petroleum and natural gas production-A survey. *Management Science, 24(1), 35-43.*

Dubrule, O. (2003). Geostatistics for seismic data integration in earth models. *EAGE Distinguished Instructor Series 6, 282.*

Dubucq, D., Lefeuvre, F., and Bertini, F. (2003). Deep Offshore Seismic Monitoring: the Girassol Field, a West Africa Textbook Example. *Society of Exploration Geophysicists.*

Dutry, J.-C. (2013). Towards more reliable reservoir models by integrating the 4D seismic information example of Mobim and Bilondo fields. *EAGE West Africa workshop, extended abstract.*

Eide, A.L., More, H., Ursin, B. (2002). Prediction of reservoir variables based on seismic data and well observations. *Journal of the American Statistical Association 97 (457), 18-28.*

Eidsvik, J., Omre, H., Mukerji, T., Mavko, G., Avseth, P. (2002). Seismic reservoir prediction using Bayesian integration of rock physics and Markov random fields: a North Sea example. *The Leading Edge 21 (3), 290-294.*

El Quair, Y., Lygren, M., Osdal, B., Husby, O., Springer, M. (2005). Integrated reservoir management approach: from time-lapse acquisition to reservoir model update at the Norne Field. *IPTC 10894.*

El Ouair, Y. and Stronen, L.K. (2006). Value creation from 4D seismic at the Gullfaks field: Achievements and new challenges. *76th Annual International Meeting, SEG, Expanded Abstracts, 3250-3254.*

Fahimuddin, A., Aanonsen, S. I., and Skjervheim, J.-A. (2010). Ensemble Based 4D Seismic History Matching: Integration of Different Levels and Types of Seismic Data. *Society of Petroleum Engineers. doi:10.2118/131453-MS*

Fanchi, J. R. (1999). Predicting 4D Seismic Performance Using an Integrated Flow Model. *Society of Petroleum Engineers. doi:10.2118/56517-MS*

Floricich, M., Jenkins, G., McComirck, D., Copp, J., Martin, K., Allan, P., Day, S., Fletcher, J., Macdonald, C., Mannini, A., Gilham, R. and Boundy, F. (2010). Probabilistic seismic inversion of a West of Shetlands deepwater turbidite field. *72nd EAGE conference & exhibition, extended abstract.*

Floricich, M., Jenkins, G. and McComirck, D. (2012). Probabilistic inversion of multiple 4D seismic as applied on Schiehallion field. *74th EAGE conference & exhibition, extended abstract.*

Floricich, M., Large, S., Jones, D., Helmi, A. and Lörtzer, G. (2011). Conditioning reservoir model and aiding well planning using probabilistic seismic inversion in a Central North Sea field. *73rd EAGE conference & exhibition, extended abstract.*

Fürre, A. K., Munkvold, F. R. and Nordby, L. H. (2003). Improving Reservoir Understanding Using Time-Lapse Seismic at the Heidrun Field. *65th Meeting of the European Association of Geoscientists and Engineers.*

Fürre, A. K., Nordby, L. H. and Bakken, E. (2004). Heidrun time-lapse interpretation project 2004. *Statoil report HNO HD PTEK 0124.*

Fürre, A-K., Bakken, E., and Nordby, L. H. (2005). Heidrun Time-Lapse 2001-2004 – Further Improvement of Reservoir Understanding. *67th Meeting, EAGE, Expanded Abstracts.*

Fürre, A. K., Bakken, E., Kløv, T. and Nordby, L.H. (2006). Heidrun 2001-2004 time lapse seismic project: integrating geophysics and reservoir engineering. *First Break, 24, 33-39.*

Hajizadeh, Y., Christie, M., & Demyanov, V. (2011). Ant colony optimization for history matching and uncertainty quantification of reservoir models. *Journal of Petroleum Science and Engineering, 77(1), 78-92.*

Hampson, D., & Galbraith, M. (1981, January). Wavelet extraction by sonic log correlation. *In GEOPHYSICS (Vol. 46, No. 9, pp. 1341-1341). 8801 S YALE ST, TULSA, OK 74137: SOC EXPLORATION GEOPHYSICISTS.*

Hanssen, T. H., E. Bakken, and Nordby, L. H. (2004). Time-lapse seismic and real options: new measures are required to show value of creation. *Search and Discovery Article 40117.*

Huang, Y., MacBeth, C., Barkved, O.I., and van Gestel, J.P. (2011). Enhancing dynamic interpretation at the Valhall field by correlating well activity to 4D seismic signatures. *First Break v. 29(3),37-44.*

Huang, Y., MacBeth, C. (2012). Direct correlation of 4D seismic with well activity for a clarified dynamic reservoir interpretation. *Geophysical Prospecting, 60(2), 293-312.*

Jørstad, A., Furre, A-K. and Al-Najjar, N. F. (2000). Heidrun IOR Pilot Reservoir Monitoring Project. *Statoil Summary report, HD-PETEK-U 00060.*

Kleemeyer, M., Gelderblom, P., Altintas, A., and Foreste, K. (2012). 4D Close-the-loop Using Probabilistic Seismic Inversion on the Astokh Field, Offshore Sakhalin. *In 74th EAGE Conference & Exhibition.*

Kumar, D. (2006). A Tutorial on Gassmann Fluid Substitution. *Geohorizons.*

Gavalas, G.R., Shah, P.C., Seinfeld, J.H. (1976). Reservoir history matching by Bayesian estimation. *SPE Journal. 16(6), 337–350*

Gelman, A. and Rubin, D. (1992). Inference from iterative simulation using multiple sequences. *Statistical Science, 7(4):457-472.*

Gonzalez-Carballo, A., Guyonnet, P., Levallois, B., Veillerette, A. and Deboiasne, R. (2006). 4D monitoring in Angola and its impact on reservoir understanding and economics. *The Leading Edge, v.25, p. 1150-1159.*

Gonzalez-Carballo, A., Guyonnet, P.-Y., Levallois, B., Veillerette, A., and Deboiasne, R. (2006). Repeated 4D Monitoring of the Girassol Field (Angola): Impact on Reservoir Understanding and Economics. *Offshore Technology Conference. doi:10.4043/18221-MS*

Gosselin, O., van den Berg, S., and Cominelli, A. (2001). Integrated History-Matching of Production and 4D Seismic Data. *Society of Petroleum Engineers. doi:10.2118/71599-MS*

Gouveia, W.P., Johnston, D.H., and Solberg, A. (2004). Remarks on the estimation of time-lapse elastic properties: The case for the Jotun field, Norway. *74th Annual International Meeting, SEG, Expanded Abstracts, 2212-2215.*

Guderian, K., Kllemeyer, M., Kjeldstaad, A., Pettersson, S.E., and Rehling, J. (2003). Draugen field: Successful reservoir management using 4D seismic. *65th EAGE Conference & Exhibition, Expanded Abstract.*

Gunning, J. (2000). Constraining random field models to seismic data: getting the scale and the physics right. *ECMOR VII: Proceedings, Seventh European Conference on the Mathematics of Oil Recovery, Baveno, Italy, p. M-20.*

Gunning, J. and Glinsky, M. (2004). Delivery: an open-source model-based Bayesian seismic inversion program. *Computers & Geosciences, Volume 30, Issue 6, July 2004, Pages 619-636, ISSN 0098-3004.*

Haas, A. and Dubrule, O. (1994). Geostatistical inversion “a sequential method of stochastic reservoir modelling constrained by seismic data”. *First Break, 12, 11, 561-569.*

Haaland, N.A., Gjerding, K., Skjei, N., Riste, P., Coleou, T., and Machecler, I. (2008). 4D petrophysical seismic inversion on the Troll West Field. *EAGE 70th Conference and Exhibition.*

Huang, X., Meister, L., & Workman, R. (1998). Improvement on the Quantitative Seismic History Matching. In 1998 SEG Annual Meeting. Society of Exploration Geophysicists.

Hubans, C., and Berthet, P. (2007). 4D seismic monitoring of the Girassol field (Angola): enhanced interpretation of production mechanisms through impedance inversion. *10th International Congress of the Brazilian Geophysical Society, extended abstracts.*

Jack, I. (1997). Time-lapse seismic in reservoir management. *Society of Exploration Geophysicists.*

Jansen, J.D., Brouwer, D.R., Naevdal, G. and van Kruijsdijk, C.P.J.W. (2005). Closed-loop reservoir management. *First Break 23: 43-48.*

Jansen, J.D., Brouwer, D.R., and Douma, S. G. (2009). Closed Loop Reservoir Management. *Society of Petroleum Engineers. doi:10.2118/119098-MS*

Kleemeyer, M., Gelderblom, P., Altintas, A. and Foreste, K. (2012). 4D close-the-loop using probabilistic seismic inversion on the Astokh field, offshore Sakhalin. *74th EAGE conference & exhibition, extended abstract.*

Kumar, D., Landa, J.L. (2008). A reliable 4D seismic attribute for joint inversion of seismic and production data. *SEG Annual meeting, Expanded Abstract.*

Kretz, V., Valles, B., and Sonneland, L. (2004). Fluid Front History Matching Using 4D Seismic and Streamline Simulation. *Society of Petroleum Engineers. doi:10.2118/90136-MS.*

Lafet, Y., Duboz, P., Deschizeaux, B., Lefeuvre, F. and Hubans, C. (2005). 4D stratigraphic inversion of the Girassol field – Towards a more quantitative approach. *67th Conference and Exhibition, EAGE, Extended Abstracts, C018.*

Lafet, Y., Roure, B., Doyen, P.M. and Buran, H. (2009). Global 4-D seismic inversion and time-lapse fluid classification. *79th Annual International Meeting, SEG, Expanded Abstracts, 3830-3834.*

Lancaster, S. and Whitcombe, D. (2000). Fast-track coloured inversion. *Society of Exploration Geophysicists, 1572-1575.*

Landa, J. L., and Horne, R. N. (1997). A procedure to integrate well test data, reservoir performance history and 4D seismic data into a reservoir description. *SPE Annual Technical Conference and Exhibition, Expanded Abstract.*

Landrø, M (1999). Discrimination between pressure and fluid saturation changes from time-lapse seismic data. *69th SEG International Exposition and Annual Meeting, Expanded Abstract, 1651–1654.*

Landrø, M. (2001). Discrimination between pressure and fluid saturation changes from time lapse seismic data. *Geophysics 66, 836-844.*

Lefeuvre, F., Kerdraon, Y., Peliganga, J., Medina, S., Charrier, P., Houtellier, R., and Dubucq, D. (2003). Improved Reservoir Understanding Through Rapid And Effective 4D: Girassol Field, Angola, West Africa. *73rd Meeting, Society of Exploration Geophysicists, Expanded Abstract.*

Leguijt, J. (2001). A promising approach to subsurface information integration. *63rd EAGE Conference & Exhibition.*

Leguijt, J. (2009). Seismically constrained probabilistic reservoir modeling. *The Leading Edge, 28, 1478–1484.*

Lerat, O., Nivlet, P., Doligez, B., Lucet, N., Roggero, F., Berthet, P., … Vittori, J. (2007). Construction of a Stochastic Geological Model Constrained by High-Resolution 3D Seismic Data - Application to the Girassol Field, Offshore Angola. *Society of Petroleum Engineers. doi:10.2118/110422-MS.*

Liu, N., Oliver, D. S. (2005). Ensemble Kalman filter for automatic history matching of geologic facies. *Journal of Petroleum Science and Engineering*, 47(3), 147-161.

Lu, R., Lazaratos, S., Wang, K., Cha, Y. H., Chikichev, I., & Prosser, R. (2013, June). High-resolution elastic FWI for reservoir characterization. *In 75th EAGE Conference & Exhibition incorporating SPE EUROPEC 2013.*

MacBeth, C., Floricich, M., Soldo, J. (2006). Going quantitative with 4D seismic analysis. *Geophysical Prospecting, v.54, p. 303-317.*

Machecler, I., Coléou, T., Gjerding, K., Skjei, N., Haaland, A. N., Riste, P. (2009). *4-D petrophysical seismic inversion on the Troll West field. In 2009 SEG Annual Meeting. Society of Exploration Geophysicists.*

Marvillet, C., Hubans, C., Thore, P., Desegaulx, P., Al-Mehairi, Y.S., Shuaib, M. and Al-Shaikh, A. (2007). Seismic monitoring feasibility on Bu-Hasa field. *IPTC No. 11640.*

Meadows, M. (2001). Enhancements to Landro's method for separating time-lapse pressure and saturation changes. *71st SEG International Exposition and Annual Meeting, Expanded Abstract, 1652-1655.*

Metropolis, N., Rosenbluth, A., Rosenbluth, M., Teller, A. and Teller, E. (1953). Equations of state calculations by fast computing machines. *J. Chem. Phys., 21:1087-1091.*

Menke, W. (1984). Geophysical data analysis: discrete inverse theory. *Academic press*.

Mohaghegh, S. D. (2006, January). Quantifying uncertainties associated with reservoir simulation studies using a surrogate reservoir model. *In SPE Annual Technical Conference and Exhibition. Society of Petroleum Engineers.*

Mohamed, L., Christie, M. A., & Demyanov, V. (2010, January). Reservoir Model History Matching with Particle Swarms: Variants Study. *In SPE Oil and Gas India Conference and Exhibition. Society of Petroleum Engineers.*

Muskat, M. (1945). The Production Histories of Oil Producing Gas‐Drive Reservoirs. *Journal of Applied Physics, 16(3), 147-159.*

Muskat, M., & Taylor, M. O. (1946). Effect of Reservoir Fluid and Rock Characteristics on Production Histories of Gas-Drive Reservoirs. *Transactions of the AIME, 165(01), 78-93.*

Navarre, J., Claude, D., Liberelle, E., Safa, P., Vallon, G., and Keskes, N. (2002). Deepwater turbidite system analysis, West Africa: Sedimentary model and implication s for reservoir model construction. *The Leading Edge, v.21, no. 11, p. 1132-1139.*

Nur, A. (1982). Seismic imaging in enhanced recovery. *SPE/DOE 10680, 99-109.*

Nur, A., Tosaya, C., and Vo-Thanh, D. (1984). Seismic monitoring of thermal enhanced oil recovery processes. *54th Annual International Meeting, SEG, Expanded Abstract, 337-340.*

Nur, A., and Wang, Z. (1987). In-situ seismic monitoring EOR. *The petrophysical basis: SPE 16865.*

Oliver, D.S., Reynolds, A.C., Liu, N. (2008). Inverse Theory for Petroleum Reservoir Characterization and History Matching. *1st edn. Cambridge: Cambridge University Press,* Omre, H., Tjelmeland, H. (1997). Petroleum Geostatistics. *Geostatistics Wollongong 96. Kluwer Academic, Dordrecht, The Netherlands, pp. 41-52.*

Pendrel, J. (2006). Seismic Inversion—A Critical Tool in Reservoir Characterization. *Scandinavian Oil-Gas Magazine, No. 5/6, 2006, p. 19-22 .*

Pillar, N. (2012). A short course in modern seismic inversion techniques. *74th EAGE conference & exhibition incorporating SPE EUROPEC.*

Reid, B.E., Høyland, L.A., Olsen, S.R. and Petterson, O. (1996). The Heidrun Field – Challenges in Reservoir Development and Production. *Offshore Technology Conference, OTC 8084 Houston.*

Retail, P., Thane, L., and Liberelle, E. (2002). Well interference test on Girassol. In Offshore Technology Conference. Offshore Technology Conference.

Robert, C. and Casella, G. (1999). Monte Carlo statistical methods. *Springer texts in statistics, v. 27.*

Roggero, F., Ding, D. Y., Berthet, P., Cap, J., Schreiber, P.E. (2007). Matching of production history and 4D seismic data – Application to the Girassol Field, offshore Angola. *SPE Annual Technical Conference and Exhibition, paper no. 109929.*

Roggero, F., Lerat, O., Ding, D. Y., Berthet, P., Lefeuvre, F., Perfetti, P., & Bordenave, C. (2008). Constraining Reservoir Models to Production And 4D Seismic Data - Application to the Girassol Field, Offshore Angola. *World Petroleum Congress.*

Sagitov, I., and Stephen, K. D. (2013). Optimizing the Integration of 4D Seismic Data in History Matching: Which Data Should We Compare? *Society of Petroleum Engineers. doi:10.2118/164852-MS.*

Sarkar S., Gouveia W. and Johnston D. (2003). On the inversion of time-lapse seismic data. *SEG Annual International Meeting, Expanded Abstract, 1489-1492.*

Sen, M. K., Datta-Gupta, A., Stoffa, P. L., Lake, L. W., & Pope, G. A. (1995). Stochastic reservoir modeling using simulated annealing and genetic algorithm. *SPE Formation Evaluation,* 10(01), 49-56.

Shah, P.C., Gavalas, G.R., Seinfeld, J.H. (1978). Error analysis in history matching: the optimum level of parameterization. *SPE Journal. 18(6), 219–228*

Shahin, A., Stoffa, P.L., Tatham, R.H. and Seif, R. (2011). Accuracy required in seismic modelling to detect production-induced time-lapse signatures. *81st SEG meeting, San Antonio, USA, Expanded Abstracts, 2860-2864.*

Shuey, R. T. (1985). A simplification of the Zoeppritz equations. *Geophysics 50 (9): 609–614. Bibcode:1985Geop...50..609S. doi:10.1190/1.1441936.*

Skjervheim, J.A., Van Lanen, X., Hulme, D., Røine Stenerud, V., Zachariassen, E., Liu, S., Hove, J. and Evensen, G. (2012). Integrated workflow for consistent model building from depth conversion to flow simulation – North Sea Field Case. *74th EAGE conference & exhibition, extended abstract.*

Staples, R., Stevens, T., Leoutre, E., Jolley, S., and Marshall, J. (2005). 4D seismic history matching – The reality. *67th EAGE Conference & Exhibition, Extended Abstracts.*

Stephen, K. D., Shams, A., and Macbeth, C. (2009). Faster Seismic History Matching in a United Kingdom Continental Shelf Reservoir. *Society of Petroleum Engineers. doi:10.2118/107147-PA.*

Stephen, K.D., Soldo, J., MacBeth, C., and Christie, M. (2006). Multiple-model seismic and production history matching: a case study: *SPE Journal, v.11, p. 418-430.*

Tarantola, A., and Bernard, V. (1982). Inverse Problems = Quest for Information. *Journal of Geophysics 50: 159–170.*

Tarantola, A. (2005). Inverse Problem Theory and Methods for Model Parameter Estimation. *SIAM. ISBN 978-0-89871-572-9.*

Theune, U. (2013). Quantitative 4D reservoir property determination. *75th EAGE conference & exhibition, extended abstract.*

Thore, P. (2006). Accuracy and limitations in seismic modeling of reservoir. *In 76th Annual International Meeting (pp. 1674-1677).*

Tierney, L. (1994). Markov chains for exploring posterior distributions (with discussion). *Annals of Statistics, v. 22: 1701-1762*.

Thore, P. (2011). A 4-D seismic inversion scheme ready-to-use for updating reservoir grid. *EAGE/SPE Joint Workshop - Closing the Loop: Reservoir Simulation & Geophysical Measurements, Istanbul, Turkey.*

Toinet, S., Maultzsch, S., Souvannavong, V., and Colnard, O. (2011). 4D pre-stack inversion workflow integrating reservoir model control and lithology supervised classification. *First Break, v.29.*

Tolstukhin, E., Lyngnes, B., and Sudan, H. H. (2012). Ekofisk 4D Seismic - Seismic History Matching Workflow. *Society of Petroleum Engineers. doi:10.2118/154347-MS*

Tura, A., and Lumley, D.E. (1999). Estimating pressure and saturation changes from time-lapse AVO data. *69th Annual Internat. Mtg., Soc. Expl. Geophys., Expanded Abstracts, pp. 1655-1658.*

Turpin, P., Gonzalez-Carballo, A., Bertini, F., and Lefeuvre, F. (2003). Velocity Volume And Time/Depth Conversion Approach During Girassol Field Development. *Society of Exploration Geophysicists.*

Villegas, R., Macbeth, C., and Paydayesh, M. (2009). Permeability Updating of the Simulation Model Using 4D Seismic Data. *Society of Petroleum Engineers. doi:10.2118/125632-MS.*

Waggoner, J. R., and Huang, X. (1999). Integrating Time-Lapse Seismic and Reservoir Simulation for Improved Asset Management. *Offshore Technology Conference. doi:10.4043/10786-MS.*

Watkins, A. J., Parish, R. G. (1992). Computational aids to reservoir history matching. *In Petroleum Computer Conference. Society of Petroleum Engineers.*

Whiley, M., and Wilson, S. P. (2004). Parallel algorithms for Markov chain Monte Carlo methods in latent spatial Gaussian models. *Statistics and Computing, 14(3), 171-179.*

Willcox, P. J., and Riley, H. G. (1975). Performance Matching for a North Sea Gas Field. *Society of Petroleum Engineers. doi:10.2118/5535-MS.*

Williamson, P.R., Cherrett, A.J., Sexton, P.A. (2007). A New Approach to Warping for Quantitative Time–Lapse Characterization. *EAGE, Expanded Abstracts*.

van Wijngaarden, A. J., Couleou, T., Haaland, A. N., Formento, J. L., & Ona, R. (2007). Petrophysical Seismic inversion applied to the Troll field. *In 3rd North African/Mediterranean Petroleum & Geosciences Conference & Exhibition.*

Ye, J. (2011). Efficient, concurrent Bayesian analysis of full waveform LaDAR data. *Heriot-Watt University, Ph.D. thesis.*

Ye, J., Wallace, A. M., Al Zain, A., and Thompson, J. (2013). Parallel Bayesian inference of range and reflectance from LaDAR profiles. *Journal of Parallel and Distributed Computing, 73(4), 383-399.*

Zachariassen, E., Meisingset, H., Otterlei, C., Andersen, T., Hatland, K., Hoye, T., Liestol, F. (2006). Method For Conditioning The Reservoir Model On 3D And 4D Elastic Inversion Data Applied To A Fluvial Reservoir In The North Sea. *Society of Petroleum Engineers. doi:10.2118/100190-MS.*

Zhang, M. (2005), Simultaneous inversion of time-lapse seismic data. *M.Sc thesis, University of Alberta*.

Zhang, M., Mauricio, D., Sacchi, R. (2005). Simultaneous inversion of time-lapse seismic data. *CSEG National Convention, Expanded Abstracts*.

Zhdanov, M. S. (2002). Geophysical inverse theory and regularization problems. *(Vol. 36). Elsevier*.